ROZPRAWA DOKTORSKA

Institute of Physical Chemistry
Polish Academy of Sciences
Kasprzaka 44/52
01-224 Warsaw, Poland

Effect of boundary conditions on self-assembly

Jakub Pękalski

Supervisors:

Prof. dr hab. Alina Ciach and **Dr. Noé García Almarza**

This dissertation was prepared within the International PhD Studies at the Institute of Physical Chemistry of the Polish Academy of Sciences in Warsaw

Project operated within the Foundation for Polish Science International PhD Projects Programme co-financed by the European Regional Development Fund, Operational Program Innovative Economy 2007-2013.

NATIONAL SCIENCE CENTRE POLAND

INNOVATIVE ECONOMY
NATIONAL COHESION STRATEGY

FNP
Foundation for Polish Science

EUROPEAN UNION
EUROPEAN REGIONAL DEVELOPMENT FUND

Warsaw, August 2015

To my beloved Kasia and Adam

and

the memory of my mother.

Acknowledgments

I would like to express my deep gratitude to Professor Alina Ciach and Doctor Noé García Almarza, my research supervisors, for their patience, guidance and support. Thank you for being a lot more than just supervisors.

During my studies, I have been a member of two research groups: a group of Dr. Wojciech T. Góźdź at the Institute of Physical Chemistry in Warsaw and a group of Prof. Enrique Lomba at the Instituto de Química Física in Madrid. I would like to thank all the members of the groups for their assistance and a family atmosphere.

Finally, I would like to thank my wife Kasia for the support she gives me, and my Father for an inspiration to become a scientist.

Financial support

- This work was realized within the International Ph.D. Projects Programme of the Foundation for Polish Science, cofinanced from European Regional Development Fund within Innovative Economy Operational Programme "Grants for innovation".
- The author received funding for the preparation of the doctoral dissertation from the National Science Center in the funding of Ph.D. scholarships on the basis of the decision number DEC-2014/12/T/ST3/00647.
- Part of the work presented in the dissertation was financially supported by the National Science Center under Contract Decision
  No. DEC-2013/09/N/ST3/02551.

Abstract

Nanoscale self-assembly is a process in which initially disordered particles spontaneously organize into thermodynamically stable patterns. In the bulk, structure and symmetries of the patterns are determined only by the interaction potential between the components, while in the case of confined systems the impact of the system size and component-wall interaction play an important role. In the thesis we study these effects of boundary conditions on the self-assembly at nanoscale.

We start the study with comparison between two classes of self-assembling systems in the bulk. The first class consists of systems with spherically symmetric particles which interact *via* an isotropic potential with competing short range attraction and long range repulsion (SALR). Such interactions can be observed in e. g. colloidal suspensions, protein solutions or between quantum dots. The second class is characterized by amphiphilic interactions, that is anisotropic interactions present between e. g. lipids which have hydrophilic heads and hydrophobic tails, or block copolymers with building blocks of different chemical properties. We solve the two models exactly by the transfer matrix method in one dimension, perform Monte Carlo simulations and numerical calculations of the mean-field type. The comparison made between the equations of state, correlation functions, heat capacities and the ground states indicates striking similarities between these systems and significant differences between them and simple fluids. Thus, further studies in a two dimensional (2d) space were carried out only for the model with the SALR potential. In 2d we have obtained the first complete phase diagram for the system with SALR type of potential. In particular, we have discovered the "molten lamella" phase which was not previously included in the phase diagrams of systems with the SALR potential.

Knowing the bulk properties of the SALR system, we have focused further studies on the effects of confinement. We have assumed that the system has geometry of a slit and considered one- and two-dimensional models. In the case of 1d model with permeable walls we have found exact solutions for the density profiles and the effective interactions between the walls, i. e. the solvation potential. In the case of impervious walls we have studied density profiles and equation of state by

Monte Carlo simulations. In both cases rigid and elastic walls were considered. In the case of rigid walls the impact of the system size which is not favorable for the bulk ground state structures has been analyzed. In particular, we have discovered anomalies which do not occur in simple fluids, and qualitative differences between cluster distributions in canonical and grand canonical ensembles for the same thermodynamic conditions. The study of elastic confinement led us to discovery of a new way in which a complex system may spontaneously change its size. Namely, we have found that if the system self-assembles into periodic structures, then the fluid induced force between the walls may compete with the elastic force of the confinement in such a way, that two system sizes can be equally probable. Moreover, the two stable sizes may differ by as much as a period of the ground state pattern.

The 2d model with slit geometry revealed the ordering effects of the confinement. In contrast to the bulk, in which the ground state is strongly degenerated, in the case of confined system the ground state patterns are unique. We have found that the presence of walls may induce defects in the bulk patterns either locally (in the close neighborhood of the walls in the cluster phase), or globally (across the whole slit in the lamellar phase). Interestingly, the defects appear in an organized manner not only at zero temperature, but also at low temperatures.

The majority of the results have been published in the following papers:

1. **J. Pękalski**, A. Ciach, N. G. Almarza,
   Periodic ordering of clusters in a one-dimensional lattice model,
   J. Chem. Phys. **138**, 144903 (2013). (Sec. 2.1.1)

2. **J. Pękalski**, A. Ciach,
   Simple one-dimensional lattice model for lipids in water,
   Trans. R. Now. Soc. Sci. Lett. **3** , 29-39 (2014).
   Invited article (Sec. 2.1.2)

3. **J. Pękalski**, P. Rogowski, A. Ciach,
   Self-assembly of lipids in water. Exact results from a one-dimensional lattice model,
   Mol. Phys. **113:9-10**, 1022-1032 (2014). Invited article (Sec. 2.1.2)

4. **J. Pękalski**, A. Ciach, N. G. Almarza,
   Periodic ordering of clusters and stripes in a two-dimensional lattice model. I. Ground state, mean-field phase diagram and structure of the disordered phase,
   J. Chem. Phys. **140**, 114701 (2014). (Sec. 2.2.1)

5. N. G. Almarza, **J. Pękalski**, A. Ciach,
   Periodic ordering of clusters and stripes in a two-dimensional lattice model. II. Results of Monte Carlo simulation,
   J. Chem. Phys. **140**, 164708 (2014). (Sec. 2.2.1)

6. **J. Pękalski**, A. Ciach, N. G. Almarza,
   Bistability in a self-assembling system confined by elastic walls: Exact results in a one-dimensional lattice model,
   J. Chem. Phys. **142**, 014903 (2015). (Sec. 3.1)

7. **J. Pękalski**, N. G. Almarza, A. Ciach,
   Effect of rigid or adaptive confinement on self-assembling systems. Fixed vs. fluctuating number of confined particles,
   J. Chem. Phys. **142**, 204904. (2015). (Sec. 3.2)

Contents

Abbreviations

1d	one-dimenisonal space
2d	two-dimenisonal space
CE	Canonical Ensemble
CF	Cluster Fluid
EOS	Equation of State
F	Fluid
GCE	Grand Canonical Ensemble
GS	Ground state (T=0)
MC	Monte Carlo
MF	Mean-Field
ML	Molten Lamella
OR	Ordered Rhombuses
PBC	Periodic Boundary Conditions
RBC	Rigid Boundary Conditions
SALR	Short range Attraction and Long range Repulsion
TCP	Tricritical point
TI	Thermodynamic Integration
TP	Triple point

Symbols

β	Inverse $k_B T$
δ^{Kr}	Kronecker delta function
∇	Nabla operator, gradient
λ_i	i-th (in the absolute value) eigenvalue of the transfer matrix
μ	Chemical potential
Ξ	Grand statistical sum
ξ	Correlation length
$\hat{\rho}$	Occupancy operator
$\bar{\rho}(x)$	Mean-field average density at the site x
σ	Colloidal particle diameter, equal to the lattice constant
σ_N	Standard deviation of the number of particles
Ψ	Effective wall-wall interaction
Ω	Grand thermodynamic potential
c_V	Heat capacity per particle at constant volume
G	Correlation function
H	Hamiltonian in the Grand Canonical Ensemble
H_{W2d}	Grand Canonical Hamiltonian of the two-dimensional system with slit geometry
h^*	dimensionless energy of the wall-particle interaction
J_1	Energy of attraction between the nearest neighbours
J_2	Energy of repulsion between the third neighbours
k_B	Boltzmann constant
L	Length of the system
L_1	Length of the two-dimensional slit in direction parallel to the confining walls
L_2	Distance between confining walls of the two-dimensional slit

M	Number of triple sites in the one-dimensional slit
N	Number of particles
$mod(m,n)$	reminder after division of m by n
p	Pressure
S	Entropy
$sgn(x)$	Sign function
T	Temperature
$\mathbf{T}$	Transfer matrix
U	Hamiltonian in the Canonical Ensemble
V	Volume of the system
$V(\Delta x)$	The interaction potential between the particles at distance Δx
X^*	$= X/J_1$ for any quantity X which has dimension of energy
x	Space variable in the one-dimensional model (scalar)
$\mathbf{x}$	$= (x_1, x_2)$ space variable in the two-dimensional model

Chapter 1

Introduction

1.1 The self-assembly phenomena

In the fluid state of matter particles can freely diffuse without any constraints put on their positions or orientation, while in the solid state only vibrations about fixed average positions are allowed. The class of soft condensed matter systems lays in the middle between the solid and the fluid states - it is characterized by large groups of particles (aggregates) which can move only collectively. Spontaneous formation of such aggregates, termed **self-assembly**, is a process in which initially disordered components spontaneously organize into thermodynamically stable structures, often of very complex nature. It occurs at all the length scales and it is ubiquitous in chemistry, biology or material science [1, 2]. Typical examples of self-assembling systems are colloidal crystals [3, 4], microphase-separated or ionic layered polymers [5], lipid bilayers and films [6], globular proteins [7] (e. g. insulin [8]), block copolymers [9], lyotropic liquid crystals [10] or almost monodisperse mixed aggregates of polyelectrolytes and surfactants [11]. Exemplary spontaneously formed patterns are presented in Fig. 1.1.

Because of the ubiquity, the term "self-assembly" is not uniquely defined among different scientific fields. It is sometimes used in a broaden sense, which includes

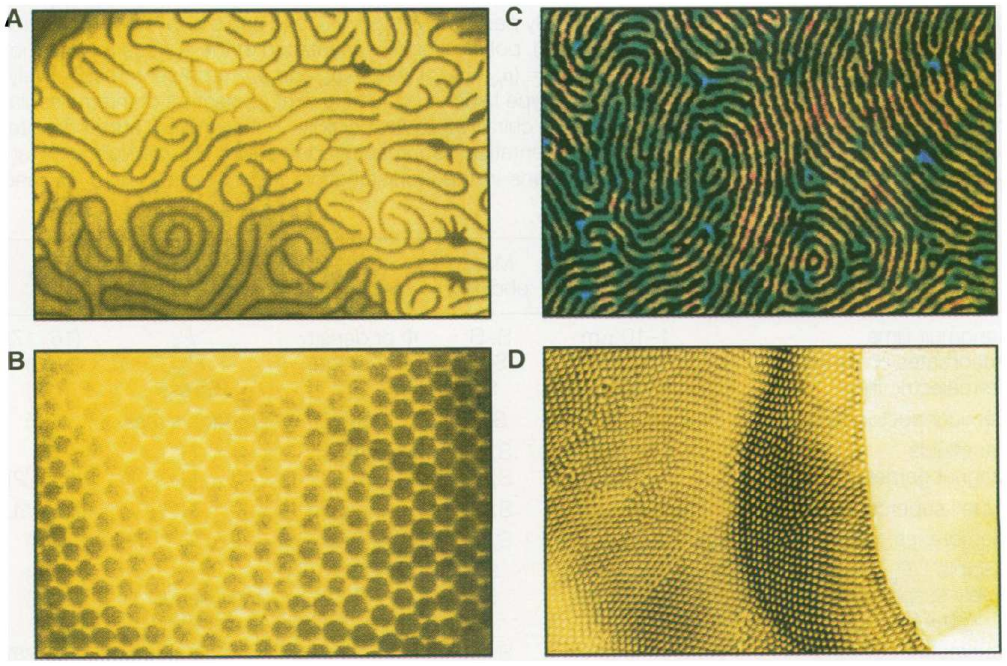

FIG. 1.1: This figure is taken from Ref. [12] and it presents lamellar and bubble phases in organic systems. Left panels show monomolecular two dimensional organic Langmuir film seen by fluorescence microscope. Panels C and D present solvent-cast film of block copolymers imaged by transimission electron microscopy. The periods of the observed structures are $\sim 3.5\,\mu m$ (panel A) and $\sim 20\,\mu m$ (panel B), $\sim 40\,nm$ (panel C) and $\sim 16\,nm$ (panel D). The panels are adapted from [13–17].

also systems out of the thermodynamic equilibrium [1]. In such sense, systems which dissipate energy, like e. g. oscillating reaction-diffusion systems, are also referred as self-assembling. However, such systems are said to self-assemble in a *dynamic* manner (or to self-organize). In that sense the object of the thesis is a *static self-assembly*, in which a system is at global or local equilibrium and does not dissipate energy.

The process of self-assembly is observed along all length scales, but we focus on nano- and microscale systems e.g. when ions adsorb on solid substrates, colloid particles self organize on interfaces between two fluid phases or ligands bind to biological membrane receptors. In that case spontaneous organization is possible only if the components interact with one another and can diffuse. While the diffusion simply results from the thermal fluctuations, the shape of the effective pair interaction potential is often a sum of many different factors with lyophobic, Van der Waals, entropic or electrostatic interactions among them. The effective interactions uniquely determine morphology and symmetries of the aggregated structures in a

given thermodynamic state, but only if the process takes place in the *bulk*, i.e. the boundaries of the system do not influence the self-assembled structure. However, if for example the confinement and the self-assembled structure have different symmetries, or incommensurability between characteristic lengths of the ordered phase and the system size occurs, then one should expect that the boundaries will have a significant effect on the self-assembly. Possible effects of boundary conditions on the self-assembly are e. g. stabilization of new morphologies, anomalies in the equation of state, or in the case of elastic boundaries a bistability in the system size distribution. The study of these effects, preceded by a proper description of self-assembling systems in the bulk, are the aims of the thesis.

In Sec. 1.2 we will present theoretical and computer simulation studies aimed at description of self-assembling systems. We will focus on two classes of effective pair interaction potentials which lead to self-assembly into inhomogeneous structures, namely amphiphilic potentials (Sec. 1.2.1) and isotropic potentials with competing interactions (Sec. 1.2.2). In Sec. 1.3 we will discuss the known similarities between these two systems and show their possible origin. In Sec. 1.4 the current state of knowledge on effects of boundary conditions on the self-assembly will be presented, and finally in Sec. 1.5 the remaining open questions and the specific aim of the thesis will be formulated.

1.2 Self-assembly into inhomogeneous patterns in the bulk

In this section we will discuss two classes of pair interaction potentials which lead to self-assembly into inhomogeneous structures. Firstly, based on Ref. [9, 18] we will discuss self-assembly of amphiphilic molecules as a representative example of components with *anisotropic* interactions. Secondly, we will focus on *isotropic* interaction with competition between a short-range attraction part leading to aggregation of the particles, and a long-range repulsion term which induces separation of the aggregates.

1.2.1 Amphiphilic interaction potentials

Amphiphiles are chemical compounds in which two separate building blocks with different chemical properties can be distinguished. In water solution usually one of the blocks is hydrophilic while the other one is hydrophobic. A typical example of an amphiphilic molecule is a block copolymer, that is a molecule which consists of at least two chemically joined blocks of different monomers (Fig. 1.4). Because of the immiscibility of the blocks, the system spontaneously tends to separate the monomers of different kind. The tendency to minimize the contact between the monomers of a different kind leads to self-assembly of the components into structures well organized in space. On the other hand, such energy minimization is inhibited by the associated loss of entropy, and thus either defects in the ordered structures occur, or different morphologies are stabilized.

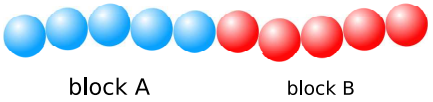

FIG. 1.2: Schematic representation of a diblock copolymer.

The competition between entropy and energy is a common origin of inhomogeneities in the self-assembled structures for all amphiphilic systems with solutions of lipids in water [19] and Janus particles [20] among them. The common origin and similar chemical structure of the components result in topologically equivalent mean-field phase diagrams (Upper left panel of Fig. 1.3). The possible origin of such universality within the class of systems characterized by amphiphilic interactions, is that all of them can by described by the same Landau-Brazovskii functional [12, 21–24]. In the context of amphiphilic systems the free energy density $\mathcal{L}_B[\phi]$ is a functional of a local difference between concentrations of hydrophilic and hydrophobic components. The form of $\mathcal{L}_B[\phi]$ suitable for all amphiphilic systems is

$$\mathcal{L}_B[\phi] = \int d\mathbf{r}\Big[f(\phi(\mathbf{r})) + \frac{\beta V_2}{2}|\nabla\phi(\mathbf{r})|^2 + \frac{\beta V_4}{4!}\Big(\nabla^2\phi(\mathbf{r})\Big)^2\Big], \tag{1.1}$$

where $V_2 < 0$ and $V_4 > 0$, $\beta = 1/(k_B T)$, k_B is the Boltzmann constant and T is the temperature. The inhomogeneous structure is favored and disfavored by the second and the third term in (1.1) respectively. Competition between these terms leads to a finite length scale of inhomogeneities, $2\pi/k_b$, with $k_b^2 = -6V_2/V_4$ [25].

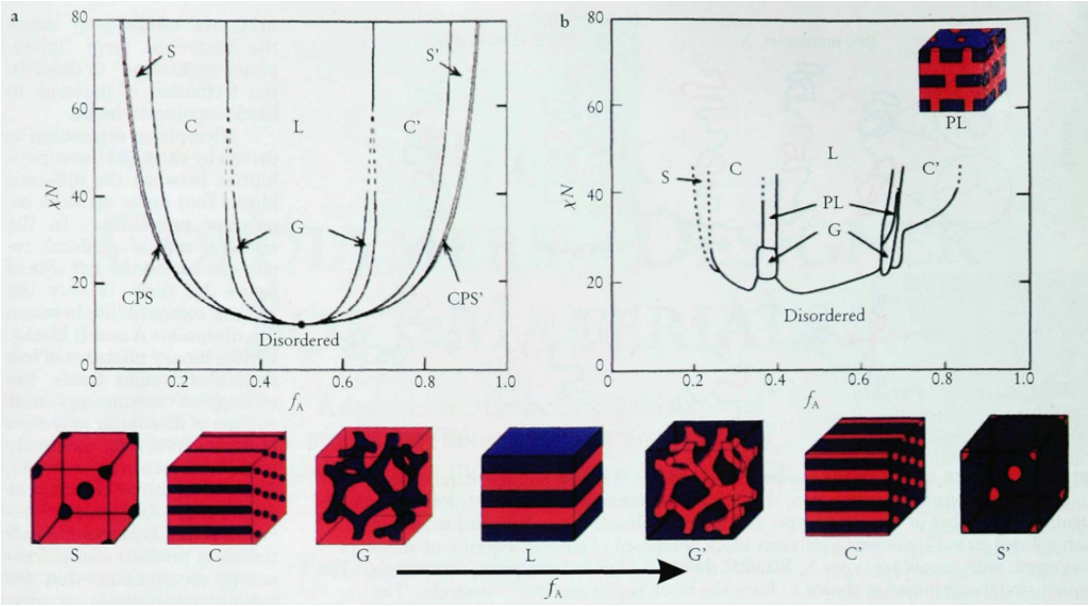

FIG. 1.3: Phase diagrams of diblock copolymer system (adapted from Ref.[9]). Left upper panel presents theoretical results based on calculations within the self-consistent mean-field theory. The theoretical phase diagram predicts stability of four different morphologies which change with the value of the composition parameter f_A and the combination parameter χN, where χ is the segment-segment interaction energy in $k_B T$ units, and N is the number of all monomers per macromolecule. With increasing f_A and for intermediate values of χN the following morphologies are stable: spherical (S), cylindrical (C), gyroid (G) and lamellar (L). Right upper panel presents experimental phase diagram obtained in [26] for system of poly(isoprene-styrene) diblock copolymers. The lower panel shows schematically equilibrium structures for different values of f_A with blue color corresponding to monomers of type A, and red color to monomers of type B.

What is more, the theoretical phase diagram reproduces very well the experimental results (Upper right panel of Fig. 1.3). In both cases the lamellar (L) phase stabilizes when the copolymer blocks are composed of nearly the same number of monomers. If one type of monomers significantly dominates, than the system self-assembles into structures with shorter blocks of copolymers packed together, what ensures more configurational space for the longer blocks, and thus maximizes the entropy. At low temperatures and with increasing fraction of monomers of one type the copolymers form the following phases: hexagonally packed cylinders (C), body-centered cubic spheres (S) and finally close-packed spheres (CPS). Apart from these phases at intermediate temperatures a periodic bicontinuous gyroid phase (G) stabilizes. Unlike the other phases present at the block copolymers phase diagram, the gyroid phase is characterized by domain boundaries with negative Gauss curvature (saddle shape surfaces). Even though its mathematical description seems uncommon, the

structure of the gyroid phase is ubiquitous in soft condensed matter systems.

The theoretical phase diagram is only an approximation, thus discrepancies between the theory and experiment occur. First of all, the phase diagram for a poly(isoprene-styrene) block copolymers presented in Fig. 1.3 is not symmetric, mostly because the monomers in the two blocks have different size and shape. Another important difference is the presence of the perforated layers (PL) phase in the experimental phase diagram. However, it turned out that this discrepancy is just an artifact of the method, since it was shown later both theoretically [27] and experimentally [28] that the PL phase is metastable. The last discrepancy we need to mention concerns the border region of stability of the disordered phase. The theoretical results predict that all transition lines meet in a critical point and thus the disordered phase coexists only with the CPS phase, while the experimental phase diagram clearly shows that transitions from the disordered phase to various ordered phases are possible. This difference occurs because in the mean-field approximation one neglects fluctuations of the composition, which in the case of inhomogeneous systems tend to destroy the periodic order [25].

For experimentalists block copolymers are of great importance because of the potential use in the semiconductor industry, for which miniaturization is an everlasting issue. Currently, the well established procedures with highly optimized costs use the "top-down" photolitography, hence their use at *nano* scale is limited by optical diffraction. A possible way to overcome such limitation is a "bottom-up" strategy based on self-assembling materials. In 2007 a first-ever application of self-assembly to chip manufacturing was reported [29] - the researchers of the IBM used self-assembly of poly(styrene-b-methyl methacrylate) block copolymers to fabricate a nanoporous template with trillions of uniform holes with 20 nanometers in diameter. At that time the top result of the lithography technique was 100 nm. Even though, the range of structures or symmetries offered by block copolymer self-assembly is somewhat limited, the promise of low costs of the technique is a key motivation for its fast development. Different morphologies and shorter length scales (up to *ca.* 0.5-10 nm) are of course also possible, but they require more complex structure of the components, which are out of the scope of the thesis.

1.2.2 Isotropic effective competing interaction potentials

Integral membrane proteins bind to the lipid bilayer by hydrophobic forces which besides adsorbing them to the surface cause the short-range protein-protein attraction. A mismatch between the shape of the proteins and the surface geometry, or electrostatic interactions can be the origin of the long-range protein-protein repulsion. The form of the effective interaction potential can vary depending on the proteins, solvent and the membrane structure, but mostly it takes the form of the **s**hort-range **a**ttraction and **l**ong-range **r**epulsion (SALR) potential [7, 30, 31].

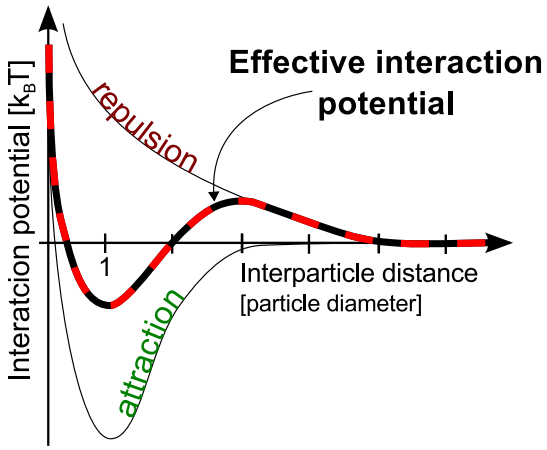

FIG. 1.4: An example of the SALR effective interparticle potential.

The SALR type of potential can also describe the interaction in the colloid suspensions. The colloid particles are often charged, and repel each other with the screened electrostatic potential. Repulsion is also present when the nanoparticles are covered with polymeric brushes [31]. The attractive part of the potential consists of the Van der Waals and the solvophobic forces. Moreover, depletion attraction appears when nonadsorbing polymers with a much smaller radius of gyration are added to the solution. In addition, when the particles are amphiphilic, they become adsorbed at the interface between the polar and organic liquids. By adjusting the charge, solvent (dielectric constant, solvophobic interactions), the size and concentration of the depletion agents, one can tune the strengths and the ranges of the competing attractive and repulsive parts of the SALR potential [7, 32]. If there are not too many particles and the potential is suitably tuned, then the particles can form patterns similar to the patterns formed by the macromolecules bound to the lipid membrane.

A series of theoretical and simulation studies of self-assembly driven by the SALR potential started with the report on spontaneous patterning of quantum dots at the

air-water interface [33]. The quantum dots seen by the Transmission Electron Microscope (TEM) self-assembled into circular or stripe domains depending on their concentration. Using Monte Carlo techniques of computer simulation it was shown that the probable origin of the inhomogeneities is the isotropic pair interaction potential which leads to microsegregation. The proposed model for the effective pair interactions consisted of a hard core repulsion, and a term of the SALR shape. The assumption of the hard-core repulsion followed from the inability of the dots to interpenetrate, while the SALR part was the effective potential resulting from summation of the dispersion attraction and the electrostatic repulsion. The SALR potential in Ref. [33] had the following form of the double Kac potential

$$u_{2K}(r) = -\epsilon_a \gamma_a^2 exp(-\gamma_a r) + \epsilon_r \gamma_r^2 exp(-\gamma_r r), \tag{1.2}$$

where $\epsilon_a, \epsilon_r > 0$ and $\gamma_r^{-1} > \gamma_a^{-1}$. Similar interaction potentials were used later in [34–41] in the context of soft-matter systems, with colloidal suspensions as a typical example. In the case of three dimensional systems the authors preferred to use the Yukawa functions

$$u_{2Y}(r) = -\frac{\epsilon}{r}\exp(-z_1 r) + \frac{A}{r}\exp(-z_2 r). \tag{1.3}$$

The extensive investigation of the SALR systems focused mainly on a determination of the phase diagram. Because of extremely high complexity of the energy landscapes, which for the SALR systems exhibits a large number of local minima, only approximate results were obtained so far. In the studies presented in [37–42] the authors used the density functional theory (DFT) which neglects the fluctuations of density, hence only regions of stability of homogeneous or periodic structures can be distinguished. It turned out that the topology of the phase diagram is preserved for values of the interaction potential parameters which assure the same sign of $I \equiv \int u_{2K}(\mathbf{r})\, d\mathbf{r}$. The sign of the parameter I is crucial for the phase diagram topology, because it holds the information on how a trial particle would effectively interact with neighboring uniformly distributed particles. Thus the sign of I determines whether the system tends to expand or shrink.

In the case of $I \geq 0$ the phase diagram obtained for the three-dimensional system is presented in the $(\rho\sigma^3,\ k_B T/\epsilon_a)$ representation in Fig. 1.5. The heterogeneous phases where found below the bell shaped curve. With increasing density ρ the

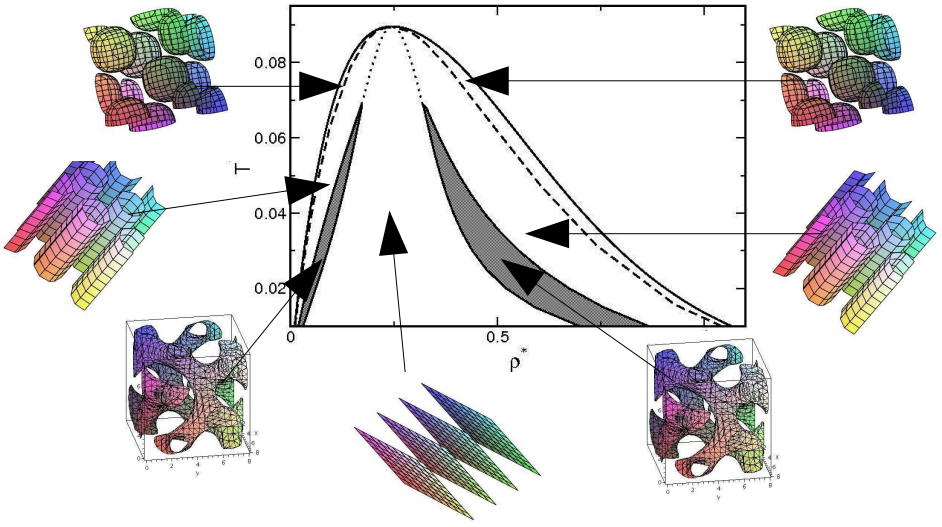

FIG. 1.5: Phase diagram in the SALR-potential system obtained in Refs.[41, 42]. $\rho^* = 6\eta/\pi$, where η is the volume fraction of particles and $I > 0$. The structure of the phases stable in regions separated by the solid, dashed and dotted lines is illustrated by the corresponding surfaces placed arround the phase diagram. Inside the regions enclosed by these surfaces the density is enhanced or depleted compared to ρ^* when $\rho^* < 0.25$ or $\rho^* > 0.25$ respectively.

heterogeneous phases are: body centered cubic crystal phase, hexagonally ordered cylinders phase, the gyroid phase and the lamellar phase. For higher densities analogous "inverse" phases are stabilized, that is the patterns which at low densities were formed by particles, at high densities are formed by bubbles (regions with depleted density).

In the case of $I = 0$ described in [35, 39] for a two-dimensional system, with increasing ρ the order in which the stable phases were found is: homogeneous phase of low density - hexagonally ordered clusters - stripes - hexagonally ordered voids - homogeneous phase of high density. In [39] the authors used the DFT method, while in [35] Monte Carlo simulations were performed. Unfortunately, in a presence of thermal fluctuations it was not trivial to distinguish the disordered and the ordered phases when structural defects were present in the latter. It was assumed that at the transition between the disordered and the ordered phases the specific heat assumes a maximum. The ordered phases were distinguished on the basis of the form of the structure factor. The obtained sketch of the phase diagram (Fig. 1.6) was similar to the DFT result. The main differences are: (i) a stability of a disordered cluster phase between the ordered cluster phase and the homogeneous fluid (ii) a reentrant melting of the ordered cluster phase upon increasing density for high temperatures, and

the ordered clusters – disordered – stripes transitions instead of the ordered clusters – stripes transition obtained in the DFT.

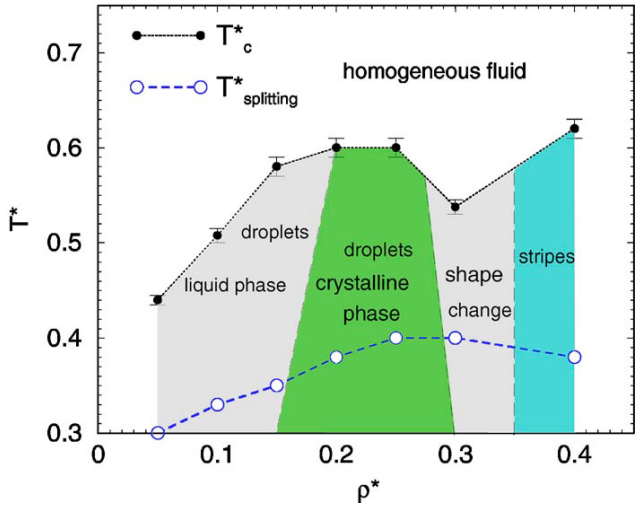

FIG. 1.6: Phase diagram in the SALR-potential system obtained in Ref.[35] with $I = 0$, by Monte Carlo simulations. The transition points correspond to a maximum of the specific heat.

The case of $I < 0$ was analyzed in Ref. [40] within the DFT and Landau theory. The authors used the same double Yukawa potential as in Refs. [35, 39], but they assumed that the density profile varies only in one spatial dimension, hence all the ordered phases were treated as a single periodic phase. The obtained phase diagram differed from the previous ones as it predicted a gas-liquid transition below a certain temperature T_t (Fig. 1.7).

Note that the case of $I > 0$ corresponding to formation of small clusters, was investigated only by approximate theories and only in three-dimensional space. For this reason in Chapter 2 we will consider the case of $I > 0$ in two-dimensional space using both the mean-field theory and the Monte Carlo simulation techniques (see Fig. 2.52).

In comparison to amphiphilic self-assembly, spontaneous pattern formation of systems with the SALR potential is still barely understood and described. The so far obtained results for the phase diagram of the SALR systems are only sketches based on unverified assumptions[1] *or are obtained within an approximate theory which neglects fluctuations crucial for a proper description of the phase diagram topology. One of the goals of the*

[1] In Sec. 2.1.1.5 we show that a maximum of the specific heat for the SALR systems not necessarily indicates a phase transition, as was assumed to obtain the phase diagram presented in Fig. 1.6.

thesis is to obtain the first complete and accurate phase diagram of the SALR system in the bulk.

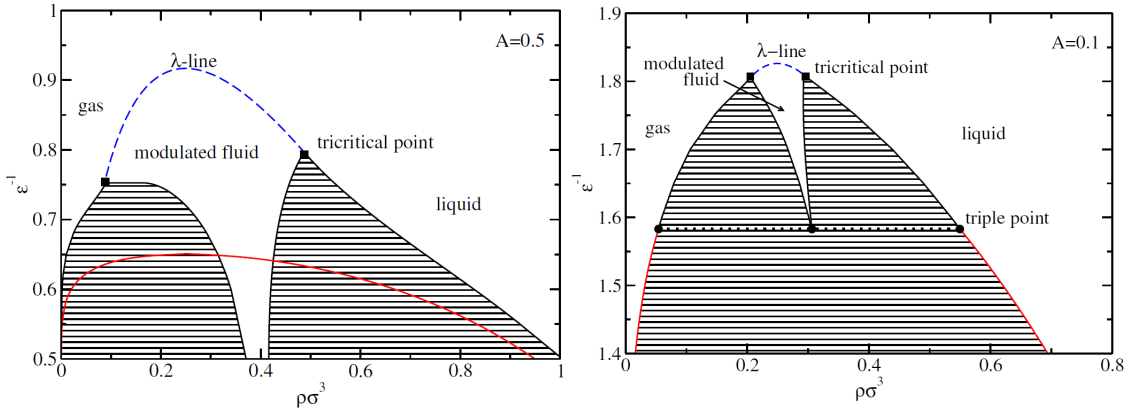

FIG. 1.7: Effectively one-dimensional phase diagrams for the SALR-potential system obtained in Ref.[40] with $I < 0$. The panels refer to different values of parameter A in Eq. 1.3. Left panel: $A = 0.5$, right panel $A = 0.1$.

1.3 Similarities between amphiphilic and colloidal self-assembly

Although the amphiphilic and the SALR systems from the first sight seem to have nothing in common, some striking similarities between these two systems have been noticed. In this section we will present results of q theoretical study on these similarities. We suggest that once a mapping between the mathematical models describing the systems is established, one can take advantage of a variety of the results obtained earlier for the amphiphilic system in studies of colloidal systems with competing interactions.

Most of the results discussed in this section were published in [43] and concern off-lattice systems. Although the thesis focuses on the lattice models, we present the studies in detail, because they strongly support the *universality* of the main dissertation results.

1.3.1 The origin of similarities

Interactions between amphiphilic molecules are strongly orientation-dependent, whereas effective interactions between spherical colloid particles usually depend only on the

distance between their centers. The purpose of the research presented in this section was to understand why despite different interaction potentials phase diagrams of amphiphilic systems and of systems interacting with the SALR type potentials are very similar (Figs. 1.3 and 1.5 respectively). *We focused on the question why the pattern formation and the sequence of ordered phases in quite different self-assembling systems are nearly the same.*

Case of simple systems

It is well known that the topology of the phase diagrams in systems undergoing separation into homogeneous phases is the same [44]. This universality is reflected in the generic free energy density functional [44]

$$\mathcal{L}[\phi] = \int d\mathbf{r}\Big[f(\phi(\mathbf{r})) + \frac{\beta V_2}{2}|\nabla\phi(\mathbf{r})|^2\Big], \tag{1.4}$$

where

$$f(\phi) = (A_2/2 + \beta V_0)\phi^2 + A_4\phi^4/4!, \tag{1.5}$$

$V_0 < 0$ is the measure of attraction, $A_n > 0$ and $V_2 > 0$. The term $\frac{1}{2}\beta V_2|\nabla\phi(\mathbf{r})|^2$ ensures that the equilibrium phases corresponding to the minimum of the functional (1.4) are homogeneous ($\nabla\phi(\mathbf{r}) = 0$).

Inhomogeneous systems

Because the functional (1.1) describes succesfully various inhomogeneus systems, it is plausible that the generic model for systems with competing interactions has the same form, with $\phi(\mathbf{r})$ denoting local excess volume fraction of particles. However, it is not obvious apriori if the functional (1.4) with $V_2 > 0$ or (1.1) with $V_2 < 0$ is appropriate for a given form of interactions. Thus, it is necessary to find the relation between the coefficients in the functional and the form of the interaction potential. Such a relation can be reliably obtained when the functional (1.1) is derived from a microscopic theory.

1.3.2 Approximate expressions for the internal energy

Let us focus on the internal energy (configurational part),

$$\mathcal{U} = \frac{1}{2}\int d\mathbf{r}\int d\Delta\mathbf{r}\ \rho(\mathbf{r})\rho(\mathbf{r}+\Delta\mathbf{r})V(\Delta r)g(\Delta r) \tag{1.6}$$

where $V(\Delta r)$ and $g(\Delta r)$ are the interaction potential and the pair distribution function for particles located at $\mathbf{r}$ and $\mathbf{r}+\Delta\mathbf{r}$, and $\rho(\mathbf{r})$ is the local average density of the particles. We focus on systems inhomogeneous on a mesoscopic length scale and on weak ordering, therefore we assume that g depends only on Δr, and $\rho(\mathbf{r})$ is a slowly varying function.

We consider short-range interaction potentials, whose moments $\int d\mathbf{r}V(r)r^n$ are finite at least for $n = 4$. We Taylor expand $\rho(\mathbf{r}+\Delta\mathbf{r})$ about $\mathbf{r}$, integrate by parts (see Appendix 6.1) and obtain the following approximate expression for the internal energy (1.6)

$$\mathcal{U} \approx \int d\mathbf{r}\Big[V_0\eta(\mathbf{r})^2 + \frac{V_2}{2}|\nabla\eta(\mathbf{r})|^2 + ...\Big] \tag{1.7}$$

where $\eta(\mathbf{r}) = \rho(\mathbf{r})v$ is the local volume fraction, $v = \pi\sigma^3/6$ is the particle volume, and

$$V_n = \frac{2\pi(-1)^{n/2}}{(n+1)v^2}\int_0^\infty dr\, r^{2+n}V(r)g(r). \tag{1.8}$$

For attractive interactions ($V(r) < 0$) homogeneous phases are energetically favored, because $V_2 > 0$, and the second term in (1.7) leads to an *increase* of $\mathcal{U}$ for $\nabla\eta(\mathbf{r}) \neq 0$. Note that $g(r) > 0$ and either oscillates around 1 in crystals or exhibits oscillatory decay to 1 in liquids. Thus, repulsion at large distances ($V(r) > 0$) can lead to $V_2 < 0$, and hence to a *decrease* of $\mathcal{U}$ for $\nabla\eta(\mathbf{r}) \neq 0$, i.e. to spatial inhomogeneities.

For $V_2 < 0$ the Taylor expansion of $\rho(\mathbf{r}+\Delta\mathbf{r})$ should be truncated at the fourth order term (see Appendix 6.1), and (1.7) should be replaced by

$$\mathcal{U} \approx \int d\mathbf{r}\Big[V_0\eta(\mathbf{r})^2 + \frac{V_2}{2}|\nabla\eta(\mathbf{r})|^2 + \frac{V_4}{4!}\big(\nabla^2\eta(\mathbf{r})\big)^2\Big]. \tag{1.9}$$

From (1.8) it follows that $V_4 > 0$ if $V_2 < 0$, and the above functional is stable. Note

the similarity between the last two terms in Eqs.(1.9) and (1.1). Spatial inhomogeneities favored by Eq.(1.9) for $V_2 < 0$ are consistent with preferential formation of clusters in the case of the SALR potential, with the size and the distance between the clusters determined by the range of attraction and the range of repulsion respectively.

1.3.3 Derivation of the Landau-Brazovskii functional

In order to find thermal equilibrium we need to compare grand potentials in systems with and without mesoscopic inhomogeneities. A particular form of the volume fraction on the mesoscopic scale, $\eta(\mathbf{r})$, imposes a constraint on the volume occupied by the particles in mesoscopic regions [41]. Let us consider the grand potential in the presence of the constraint $\eta(\mathbf{r})$,

$$\Omega_{co}[\eta] = U[\eta] - TS[\eta] - \bar{\mu}\int d\mathbf{r}\eta(\mathbf{r}), \tag{1.10}$$

where $U[\eta]$ and $S[\eta]$ are the configurational parts of the internal energy and the entropy, $\bar{\mu} = [\mu - k_B T \ln(\Lambda/\sigma)^3]/\nu$, where μ is the chemical potential and Λ is the thermal wavelength. We assume that $U[\eta]$ is given by (1.7) or (1.9).
When $\eta(\mathbf{r})$ varies on a length scale larger than σ, then we can make the local density approximation for the entropy, $-TS \approx \int d\mathbf{r}[f_h(\eta(\mathbf{r}))]$, where $f_h(\eta)$ is the configurational part of the free energy density of the hard-sphere reference system with the volume fraction η. $f_h(\eta_0 + \phi(\mathbf{r}))$ can be Taylor expanded and for weak ordering ($\phi(\mathbf{r}) \ll 1$) $f_h(\eta)$ can be approximated by the polynomial in ϕ.
From (1.10), (1.7), (1.9) and the above we can see that the change of $\beta\Omega_{co}$ associated with creation of the mesoscopic inhomogeneity,

$$\mathcal{L}_{\eta_0}[\phi] = \beta\Omega_{co}[\eta_0 + \phi] - \beta\Omega_{co}[\eta_0], \tag{1.11}$$

takes the form of the functional (1.4) or (1.1) for $V_2 > 0$ or $V_2 < 0$ respectively, with

$$f(\phi) = \sum_{n\geq 1} \frac{1}{n!} \frac{d^n \beta f_h(\eta)}{d\eta^n}|_{\eta=\eta_0} \phi^n + 2\eta_0 \beta V_0 \phi + \beta V_0 \phi^2 - \beta\bar{\mu}\phi. \tag{1.12}$$

Thus, we have shown that self-assembly in amphiphilic systems and in systems with competing interactions can be described by the same functional (1.1). This explains

striking similarity of the phase diagrams and supports the hypothesis that these systems belong to the same universality class.

It should be stressed, however that the description by the Landau-Brazovskii functional is valid only in the case of weak ordering, that is for high temperatures. The question whether the self-assembly in colloidal and amphiphilic systems remains similar at low temperature will be addressed in the results part of the thesis.

1.4 Effects of confinement

Spatial confinement has an impact on structural, thermodynamic and transport properties of the confined fluid [45]. In intracell compartments, in pores of a porous material or on geometrically patterned surfaces, the boundaries of the self-assembling systems can have an ordering or a disordering effect on the confined clusters or layers. The confinement has a significant effect on fluids when the separation between the confining surfaces is comparable with the characteristic structural length of the confined fluid [46, 47]. The key factor is the commensurability of the typical distance between the objects in the bulk, and the size of the compartment. Despite the fact that the confinement plays a very important role in biological systems, in pores of porous materials, and on patterned surfaces, the effects of confinement on the self-assembling systems have been much less studied than the bulk properties. In this section, we will briefly summarize the current state of knowledge about thermodynamical effects of confinement as well as about the impact of confining surfaces on the self-assembly driven either by the isotropic SALR potential or the amphiphilic interactions.

1.4.1 Thermodynamical effects of confinement

The bulk structures which organize spontaneously are free of internal stresses. Imposing geometrical bonds often introduces an internal stress which depends on the size and shape of the container, as well as on chemical and elastic properties at the walls. In simple liquids, characterized by very short correlation lengths, the effects of confinement are local and are present only close to the surfaces of the walls. In the case of complex liquids, for which the range of the correlations can be larger than the distance between the confining walls, the effects can be more pronounced

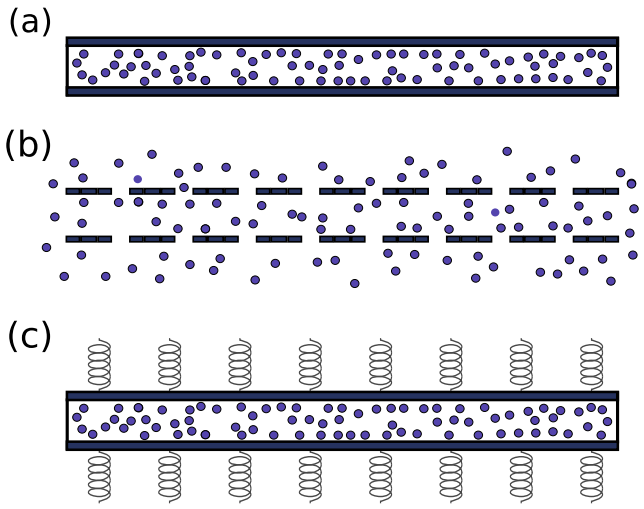

FIG. 1.8: Schematic representation of different types boundary conditions for system of slit geometry. The panels present: (a) rigid and impervious walls, (b) rigid and permeable walls, (c) elastic and impervious walls.

along the whole system. The key factor which determines whether significant effects of confinement will occur, is the distance between the confining walls. When the wall separation is commensurate with the period of the confined structure, the only expected effect is the order enhancement, which weakens the disordering effects of thermal fluctuations. On the other hand, if the wall-wall distance and the characteristic lengths are incommensurate, significant effects of confinement are expected.

The aim of the thesis is to study what kind of effects are expected for different kinds of boundary conditions. In Fig. 1.8 typical types of confinement are schematically presented. Panel (a) presents rigid walls which are separated by a fixed distance and are impervious, hence the volume and the total number of confined particles are fixed. Panel (b) presents a system with rigid and permeable walls, hence the system can exchange particles with the external environment, and the particle number inside the confinement is controlled by the chemical potential. In panel (c) the impervious and elastic boundary conditions are presented, the springs attached to the walls symbolize the ability of the confining material to adapt its size to the confined structures. A confinement with permeable and elastic walls is not presented, but is of course possible and should be imagined as a combination of the (b) and (c) schemes.

The permeability and rigidity of the boundaries influences the ordering or disordering effects of the confinement. In the case of impervious boundaries a fixed number

of confined particles may not match the number of particles required to form an ordered structure, hence defects in the stable structures are expected. If the boundaries are rigid, the disordering effect depends on the commensurability of the wall-wall distance and the characteristic lengths of the confined structure. On the other hand, in the case of elastic boundaries, adaptive features should enhance ordering effects and the situation is more complicated. For elastic boundaries the wall separation is determined by the equilibrium between two competing forces: the *elastic force* resulting from the deformation of the confining material and the *solvation force* resulting from the stress in the confined self-assembling system. Thus, the confinement effects result from properties of both the fluid and the walls.

The solvation force is the effective interaction between the walls and it occurs when the distance between the confining walls is comparable with the length of correlations between the particles. The value of the solvation force is associated with the excess of the grand potential in the confined system, $\Omega_{ex} \equiv \Omega - \Omega_b$, where Ω_b is the grand potential of the bulk system of the same volume. The confined system tends to minimize Ω_{ex}, which far from phase transitions can be described by the following formula:

$$\Omega_{ex} = \sum_i \sigma_i A_i + \sum_j \sigma^j_{dw} A^j_{dw} + \Psi, \tag{1.13}$$

where σ_i is the surface tension between the fluid and the i-th confining wall, A_i is the area of the wall, $\sigma^j_{dw} A^j$ is the sum of all domain-wall surface energies, with A^j denoting the area of the j-th domain wall, and Ψ is the solvation potential.

The fluid-wall surface tension is associated with all external walls and its contribution to Ω_{ex} is also known in the theory of simple liquids. On the other hand, the domains of liquid with different morphologies or orientation can occur only in complex liquids. The presence of the domains is a result of local structure deformations caused by the confinement (see the right panel of Fig. 1.9 for an example of domains with different orientation of the lamellas). Finally, the solvation potential in the case of simple liquids is nonzero only for very short wall separations, but in the case of self-assembling systems the solvation potential can decay very slowly as a function of the wall-wall distance [48]. How the solvation potential changes with the wall separation L can be seen from the shape of the $\Omega_{ex}(L)$ curve (Fig. 1.10), since for fixed (T, V, μ) and large L the values of Ψ and Ω_{ex} differ only by a constant.

More detailed description of Eq.1.13 as well as additional terms which should be

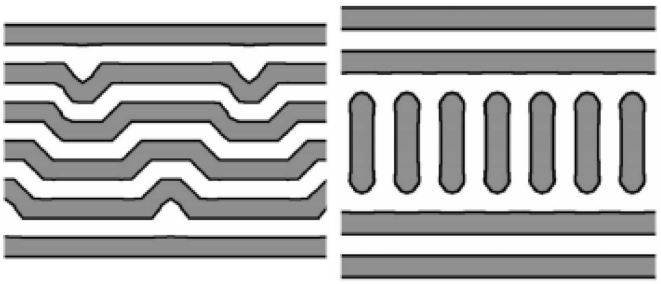

FIG. 1.9: Mean-field results for the average density in the CHS model [48]. The panels show a cross section of a three dimensional slit, where the shaded regions correspond to oil-rich domains, and white regions to water-rich domains. The thick lines are the local interfaces occupied by surfactant.

included close to phase transitions can be found in [49]. *The long-range solvation force in the self-assembling systems is an important effect of boundary conditions and will be further studied in the thesis.*

1.4.2 Amphiphilic systems

Because of the promising future use of amphiphilic systems in the industry focused on device miniaturization, the effects of confinement on those systems was intensively investigated both experimentally [18, 50, 51] and theoretically [48, 52–56]. Since a review on known confinement effects on amphiphilic self-assembly could be a topic of a separate monography (see Ref. 4-44 in [57]), here we will describe only a few significant reports on amphiphilic self-assembly, with a special care taken on the effects of confinement.

An extensive mean-field study of amphiphilic self-assembly was based on a model introduced by Ciach, Høye and Stell [58]. The CHS model for oil-water-surfactant solution studied in [48, 49, 58, 59] is a generic lattice model which predicts stability of lamellar phases in the bulk and in the confined systems of e. g. slit geometry. In [48] the authors focused on the role of two factors: the wall-liquid interactions and the ratio between the slit width and the period of the lamellar phase. A possible effect of incommensurability between the wall separation and the period of the bulk structure for a short-period lamellar phase is presented in Fig. 1.9. The figure shows how the stable morphology can change if the distance between the walls varies only by one lattice constant. Such structures, characterized by domains with different stripe orientation or by non straight stripes, are not stable in the bulk, thus their

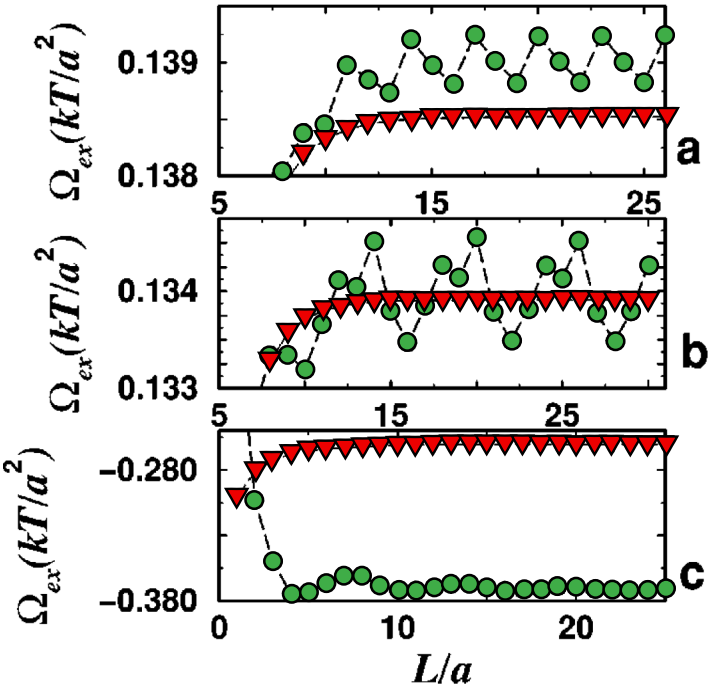

FIG. 1.10: Excess grand potential Ω_{ex} (Eg. 1.13) as a function of the wall separation L for the CHS model [48]. Red triangles (green circles) correspond to the lamellar phase with stripes perpendicular (parallel) to the slit wall. Panels present Ω_{ex} for different wall hydrophilicity with: (a) neutral walls, (b) weakly hydrophilic walls, and (c) strongly hydrophilic walls. The stable orientation for given L corresponds to the lower value of $\Omega_{ex}(L)$.

stability is an effect of confinement. In addition, the authors noticed that the orientation of the stripes in the slit depends on the period of the bulk phase. For longer periods the stripes are parallel to the walls independently of the wall separation, while for shorter periods the orientation of the stripes depends on hydrophilicity of the confining walls. The authors conclude that the short period phases are stiff and thus their response to the external stress is inelastic, while the swollen, long period phases behave more elastically. Interestingly, for intermediate periods it is possible that the orientation of the lamellar phase changes with the wall separation (Fig. 1.10).

In [60] the authors studied self-assembly of block copolymers in a nanopore confinement of a cylindrical shape. For that purpose they used simulated annealing technique and a lattice model proposed in [61] and [62]. In the model it was assumed that the block of the copolymer consists of 10 monomers, each of which can occupy only one site of the cubic lattice. The authors assumed non-zero interactions only between neighboring monomers of different kind, which were separated by 1

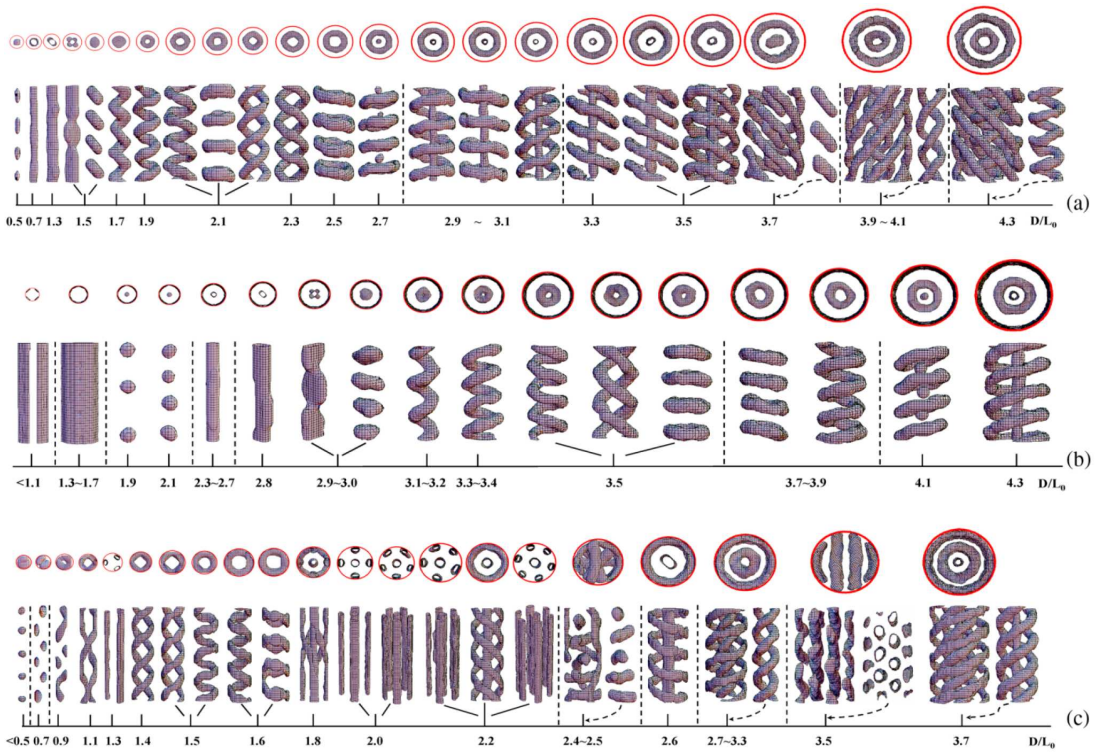

FIG. 1.11: This figure is taken from [60] and it presents different morphologies of self-assembled block copolymers for different ratio between the pore diameter to bulk cylinder spacing. First row:the wall attracts majority blocks, middle row: the walls attracts minority blocks, bottom row: neutral walls assumed. Copyright 2006 American Physical Society.

or $\sqrt{2}$ lattice units.

What was found is that, unlike for colloidal systems [36], the presence of confinement may induce structural frustration which leads to stabilization of totally novel structures (Fig. 1.11), not seen in the bulk. The authors claim that the formation of new structures such as helices and stacked toroids is connected with the very small ratio between the pore diameter and the bulk cylinder spacing. Probably for that reason no new morphologies were reported in [36], where the bulk period of the stripe phase and the stripe width were comparable. Thus, one can expect that a further research on effects of confinement on colloidal systems with different characteristic lengths of periodic structures can lead to determination of new stable morphologies which are not stabilized in the bulk.

The study of the impact of the cylinder-shape confinement on diblock copolymers was later carried out for asymmetric block copolymers [63, 64] and also reports stability of new morphologies.

In [57] the authors reported a study of the impact of soft confinement on diblock

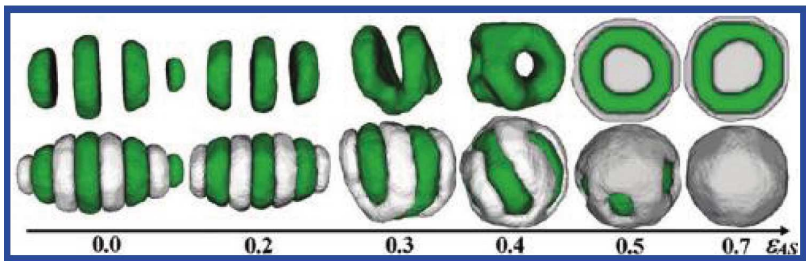

FIG. 1.12: This figure is taken from [57] and it presents different morphologies of self-assembled symmetric block copolymers for different solvent-copolymer strength of intraction ϵ_{AS}. In the upper row only A domains of the copolymer are shown, while in the lower row both domains are presented, with green color indicating domain A and gray color domain B.

copolymers morphologies. Since in Chapter 3 we are also exploring effects of this type of confinement, in what follows we are going to discuss this work in more detail. Soft type of confinement, in contrast to hard confinement used in the aforementioned research, allows the system to change the shape of the confining geometry upon internal forces or external environment. The typical example of such system is a biological cell. In [57] the soft confinement is realized by the formation of polymer droplets in a poor solvent environment. The authors report that the effective shape of the confinement as well as the morphology of the internal self-assembling system inside depend on two competing factors: the solvent-copolymer interactions and the tendency of copolymers to aggregate into bulk structures. If the solvent is neutral or weakly selective, than the systems prefers the bulk morphology of the copolymer, while the strongly selective solvent favors spherical aggregates. In that case spherical or nearly spherical aggregates contain internal morphologies of lamellar, gyroid or cylinder shapes. In Fig. 1.12 the dependence of the stable morphologies on the solvent-copolymer interaction is presented in case of symmetric diblock copolymers, which in the bulk self-assemble into lamellar structure.

1.4.3 Colloidal self-assembly

In the case of the SALR potential the impact of a slit-type confinement (a system with two parallel walls) on thermodynamically stable patterns was studied in the Canonical Ensemble by Monte Carlo simulations [36] and in the Grand Canonical Ensemble by the density functional theory [39]. All of the authors reported qualitative differences between the properties of the self-assembling system in the bulk and in the confinement.

In Ref. [36] Imperio and Reatto studied microseparation of particles interacting *via* the hard-core double Kac potential. They assumed that the particles form a monolayer confined by smooth parallel walls and focused their attention on the lamellar phase. They have shown that in the case of neutral hard walls the internal energy per particle as a function of the distance between the walls is non-monotonic and exhibits a number of minima and maxima corresponding to different patterns (Fig. 1.13). They stressed that if the wall separation is too large to fit one stripe parallel to the walls, the stripes align perpendicularly until the width is large enough for two parallel stripes to fit. For larger separations the minima of the energy profile correspond to stripes parallel to the walls, while the maxima to structures characterized by stripes perpendicular to the walls in the middle of the slit and parallel in the neighborhood of the walls. Note that such lamellar structure, with separate stripes aligned perpendicularly, is not stable in the bulk, hence its stabilization is a pure effect of confinement. Moreover, it was found that unlike in the bulk, in the presence of neutral walls a switch from the cluster to the lamellar morphology with increasing temperature is possible.

Similar effect characterized by switches between structures with different stripe orientations upon change of the wall-wall distance was observed in the CHS model (Figs. 1.10b and 1.9). Interestingly, also the curves of the internal energy of the SALR system and the excess grand potential of the CHS model are similar.

In Ref.[39] Archer used the same form of the SALR interparticle potential as had been used in [36], and also studied an impact of hard neutral walls. In order to compare the results with those of Imperio and Reatto, the Grand Canonical DFT calculations were made for fixed average density. The author focused on determining the sequences of stable structures for increasing distance between the walls at a given temperature and fixed density. He confirmed that the change of the distance can lead to the change of the stable-phase morphology, especially if the period of the structure stable in the bulk and the width of the slit are incommensurate.

In [39] the comparison with the results obtained in [36] is concluded with a statement that the DFT method “appears to be qualitatively reliable” and “seems to at least be able to describe some of the sequences of structures that are observed in the confined fluid”. More detailed study of the reliability of the DFT method is one of the goals of the thesis and will be described in the next chapters.

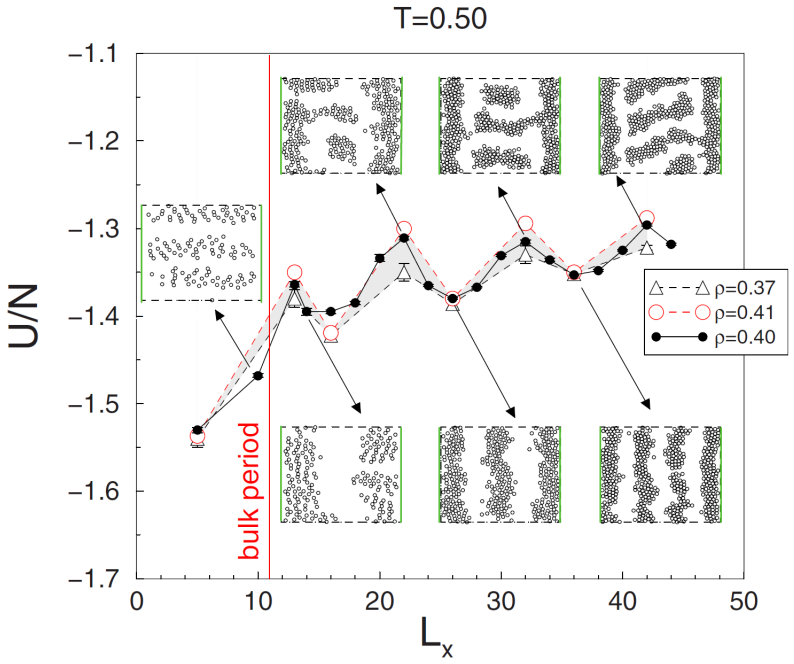

FIG. 1.13: This figure is taken from [36] and it presents potential energy per particle as a function of wall separation for three densities (0.37 marked by triangles, 0.41 marked by red circles and 0.40 marked by black dots). The insets show snapshots of different morphologies for the density 0.4. The neutral walls are vertically oriented. Copyright 2007 American Physical Society.

1.5 Open questions, scope and plan of the thesis

The shapes of the effective interaction potentials in various self-assembling systems can be very similar if the distance is measured in units of the diameter σ of the system components (ions, membrane proteins or colloid particles). In such a case similar patterns can be expected for the same volume fractions η of the particles and for the same temperature measured in appropriate reduced units. Thanks to the scaling, one can obtain information on pattern formation on different length scales from a suitably designed generic model. In order to gain general knowledge about the process of self-assembly under confinement we decided to use an approach which has not been considered before in the context of self-assembling systems. We introduced a **generic lattice model** which does not require a specific function to model interactions, but only ratios of interaction energies and their ranges.

One of the main problems that a researcher have to face while studying the self-assembly process is the extraordinarily complex free energy landscape. One way of dealing with such an obstacle is the mean-field approximation used in [37–42]. The

MF approximation allowed to determine the phase diagrams for systems which exhibit pattern formation driven by the isotropic SALR competing interaction potential (Figs. 1.5 and 1.7) and the amphiphilic interaction potential of block copolymers (left panel of Fig. 1.3). The comparison of the MF phase diagram for block copolymers with experimental results has shown that the MF approximation significantly influenced the diagram. The question how the MF approximation influenced the results for the SALR potential remains open. How neglecting the density fluctuations changed the phase diagram of the system? Were all the stable phases found? What is more, if we cannot be sure of completeness of the diagram - can we draw conclusions about the effects of boundary conditions? **In order to bypass such doubts we have decided to develop a model which in one dimension can be solved exactly and in two-dimensional space allows for a solid investigation by computer simulation techniques. Thus, for the first time a complete phase diagram for a system with particles interacting via the SALR potential can be obtained and validity of the MF approximation can be verified.**

Determination of the bulk properties of a self-assembling system is the first step required to draw conclusions about the effects of boundary conditions. After verifying that the amphiphilic and SALR systems in the bulk share many features also at low temperatures, we have decided to study the effects of confinement only for the SALR self-assembly which at the moment are far less described. Since the boundary conditions may be imposed in the variety of ways, we focused our attention on the role of **permeability** and **rigidity** or **elasticity** of the confining walls.

Suppose that a cell membrane at given temperature confines a system with a given density. Should the confined structure be the same for permeable and impervious confinement ? From the point of view of statistical physics this question is associated with the problem of *statistical ensembles equivalence*. If the system has impervious rigid walls and its temperature is fixed, then the thermodynamically stable configurations minimize the Helmholtz free energy. On the other hand, if the rigid walls are permeable and the system is in an environment acting as a reservoir of particles, then for a fixed temperature stable configurations minimize the grand thermodynamic potential. These cases correspond to the system descriptions in the canonical and in the grand canonical ensembles respectively. For simple fluids the two ensembles are equivalent in the thermodynamic limit and if the values of the thermodynamic parameters are relatively far from phase transitions. Close to the phase transition

the equivalence breaks due to large fluctuations of the number of particles. **It is of interest to compare the ensembles in the case of complex liquids. The question how the self-assembly is coupled with the fluctuation of the number of particles is open. We compare the two ensembles in different thermodynamic conditions in the core of a confined one-dimensional system, which does not exhibit phase transitions.**

Rigidity of the confinement plays an important role in the process of self-assembly. If for an empty system the distance between the walls is incommensurate with the characteristic lengths of the bulk structure, then depending on the confinement rigidity different effects of confinement are possible. We will study these effects in the case of rigid and elastic confinement with both permeable or impervious walls. In the case of rigid walls we will focus on the defects introduced in the bulk structure and on the shape of the equation of state, while for elastic walls a **new phenomena concerning thermally induced switches of the system size** will be described.

Specific questions to be addressed

In the thesis, by a deep analysis of generic models for spontaneous pattern formation, we address the following questions:

1. What are the properties of the self-assembling systems in the bulk ?
   - What is the bulk phase diagram of a system with particles interacting *via* the SALR potential ?
   - What is the impact of the mean-field approximation on the phase diagrams of the SALR self-assembling systems ?
   - Which properties of colloidal and amphiphilic self-assembling systems are common at low temperatures ?
2. What are the effects of boundary conditions on the self-assembly in the SALR system ?
   - What is the impact of the incommensurability between the system size and the period of the bulk structure ?
   - What is the impact of the rigidity and the permeability of the confinement on mechanical, thermal and structural properties ?

Research and thesis plan

The research presented in the thesis starts with a study of one-dimensional lattice models for the SALR and the amphiphilic systems in the bulk (Sec. 2.1). Both models are solved exactly. In addition, the investigation of the SALR system was further extended by the comparison with the results obtained within the mean-field approximation. Because of the similarities between the amphiphilic and SALR systems, which as it turned out occur not only at high-T (as was shown in Sec. 1.3), but also at low temperatures, for further investigation in the two-dimensional bulk we used only the SALR system (Sec. 2.2.1). The two-dimensional bulk model was studied in mean-field and by computer Monte Carlo simulation techniques. After an extensive investigation of colloidal self-assembly in the bulk, the effects of different types of confinement are studied in Chap. 3 and 4. Chapter 3 concerns the one dimensional SALR model with permeable and impervious walls which can be either rigid or elastic, Chap. 4 presents the effects of slit confinement in the two dimensional SALR model with rigid boundary conditions. In Chap. 5 the thesis is summarized.

Chapter 2

Self-assembly in the bulk

In this Chapter we present the results of our investigation of the self-assembly at a nanoscale *in the bulk*, that is, when the system boundaries do not influence the properties of the confined fluid. In Sec. 2.1, we introduce and carefully study one-dimensional (1d) generic models for the colloidal (Sec. 2.1.1) and the amphiphilic (Sec.2.1.2) self-assembly. The results of both systems are compared in Sec. 2.1.3. We choose the model of the colloidal self-assembly for further studies in a two-dimensional (2d) space (Sec. 2.2). The 2d colloidal self-assembly model investigation consists of derivation of: the ground state (Sec. 2.2.2), the MF phase diagram (Sec. 2.2.3) and the phase diagram obtained *via* Monte Carlo (MC) simulations (Sec. 2.2.4).

2.1 One-dimensional models

A great advantage of studying one-dimensional (1d) models is that often they can be solved exactly. In this section two 1d generic models will be studied. We will present and compare their ground states as well as the exact solutions for the equation of state, the average density, the correlation function. The investigation of the model for the colloidal self-assembly will be further extended by comparison of the

exact results with the phase diagrams obtained within the mean-field approximation which were described in the authors Master Thesis [65].

2.1.1 Self-assembly of colloidal particles with competing interaction potential

We start the study of the one-dimensional self-assembly by considering the model for particles interacting *via* competing interaction potential. The model, apart from yielding general information on periodic ordering in the SALR-potential systems, describes several physical systems that are interesting by their own. In the first place it can represent charged particles in a presence of depletant at a three phase coexistence line, or adsorbed at nanotubes or microtubules. Another example is a linear backbone polymer with monomers containing sites binding particles or ions that attract or repel each other when bound to first or third neighbors on the backbone, respectively. Our model can answer the question of spontaneous formation of ordered periodic patterns on linear substrates.

2.1.1.1 Introduction of the SALR model

We consider an open system in equilibrium with a reservoir with temperature T and chemical potential μ_p. The interaction h between the particles and the nanotubes, microtubules or binding sites plays analogous role as the chemical potential, and we introduce $\mu = \mu_p + h$. The particles can occupy lattice sites labeled by x taking integer values, $1 \leq x \leq L$, and we assume periodic boundary conditions (PBC), i.e. $L+1 \equiv 1, 0 \equiv L$. Each microstate is described by $\{\hat{\rho}(x)\} \equiv (\hat{\rho}(1), ..., \hat{\rho}(L))$, where the occupancy operator $\hat{\rho}(x) = 1$ or $\hat{\rho}(x) = 0$ when the site x is occupied or empty respectively. The probability of the microstate $\{\hat{\rho}(x)\}$ is given by

$$p[\{\hat{\rho}(x)\}] = \frac{e^{-\beta H[\{\hat{\rho}(x)\}]}}{\Xi}, \tag{2.1}$$

where Ξ is the normalization constant, and $\beta \equiv (k_B T)^{-1}$ with k_B denoting the Boltzmann constant. We have introduced for convenience the thermodynamic Hamiltonian containing the energy and the chemical potential term,

$$H[\{\hat{\rho}\}] = \frac{1}{2}\sum_{x=1}^{L}\sum_{x'=1}^{L}\hat{\rho}(x)V(x-x')\hat{\rho}(x') - \mu\sum_{x=1}^{L}\hat{\rho}(x), \tag{2.2}$$

where the pair interaction potential V is of the SALR type, that is

$$V(\Delta x) = \begin{cases} -J_1 & \text{for } |\Delta x| = 1, \\ +J_2 & \text{for } |\Delta x| = 3, \\ 0 & \text{otherwise.} \end{cases} \tag{2.3}$$

That is, the particles attract each other with the energy J_1, if they are nearest neighbors and repel with the energy J_2 if they are 3-rd neighbors (Fig. 2.1). The nearest-neighbor attraction is the standard assumption in the lattice-gas models. In the case of charged particles in electrolyte the assumed range of repulsion ($\sim 2.5\sigma$) should be of order of the Debye screening length, $2.5\sigma \sim \lambda_D$. Since in various solvents with weak ionic strength $\lambda_D \sim 1 - 100nm$, the model is suitable for charged molecules, nanoparticles or globular proteins [66].

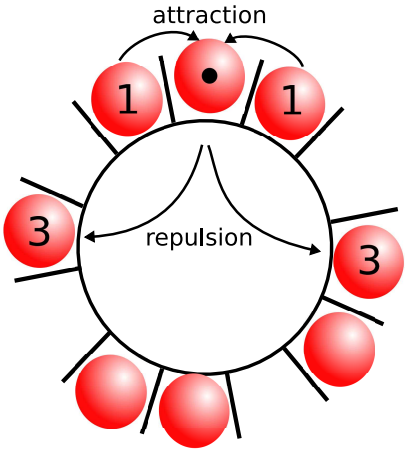

FIG. 2.1: Schematic presentation of the one-dimensional lattice model with periodic boundary conditions.

The Hamiltonian (2.2) can be rewritten in terms of the "unoccupancy" operator $\hat{\nu}(x) = 1 - \hat{\rho}(x)$ ($\hat{\nu}(x) = 1, 0$ for an empty and full site x respectively)

$$H[\{\hat{\nu}\}] = \frac{1}{2}\sum_{x=1}^{L}\sum_{x'=1}^{L}\hat{\nu}(x)V(x-x')\hat{\nu}(x') + (\mu - V_0)\sum_{x=1}^{L}\hat{\nu}(x) + L\Big(\frac{V_0}{2} - \mu\Big) \tag{2.4}$$

where $V_0 = \sum_x V(x) = 2(J_2 - J_1)$. Note that Eq.(2.2) in terms of $\hat{\rho}$ and Eq.(2.4) in terms of $\hat{\nu}$ have the same form for $\mu = V_0/2$. Moreover, the probability of the microstate $\{\hat{\rho}(x)\}$ for $\mu = V_0/2 - \Delta\mu$ is the same as the probability of the "negative" of this microstate, $\{1-\hat{\rho}(x)\}$, for $\mu = V_0/2 + \Delta\mu$. Because of the above particle-hole symmetry the phase diagrams must be symmetric with respect to the symmetry axis $\mu = J_2 - J_1$.

We choose J_1 as the energy unit and introduce dimensionless variables for any quantity X with dimension of energy as $X^* = X/J_1$, in particular

$$T^* = k_B T/J_1, \quad J^* = J_2/J_1, \quad \mu^* = \mu/J_1. \tag{2.5}$$

2.1.1.2 The ground state

The grand potential

$$\Omega = -pL = -k_B T \ln \Xi = U - TS - \mu N \tag{2.6}$$

where p, U, S, N are pressure, internal energy, entropy and average number of particles respectively, reduces to the minimum of $H[\{\hat{\rho}(x)\}]$ for $T = 0$ and fixed L. In the case of periodic phases the bulk properties must be determined for $L = ln$, where l is the period of density oscillations and n is a positive integer. We consider $\omega^* = -p^* = H^*[\{\hat{\rho}(x)\}]/(ln)$ for two homogeneous phases, one with all sites empty (gas) and the other one with all sites occupied (liquid) and for a periodic phase where 3 occupied neighboring sites are followed by $l-3$ empty sites with $l \geq 6$. For these phases we have

$$\omega^* = \begin{cases} 0 & \text{empty lattice (gas)} \\ -\frac{2+3\mu^*}{l} & \text{periodic phase, } l \geq 6 \\ J^* - 1 - \mu^* & \text{full occupancy (liquid).} \end{cases}$$

Two phases can coexist for thermodynamic states such that ω^* in these phases takes the same value. The (J^*, μ^*) phase diagram for $T^* = 0$ is shown in Fig.2.2.

Note that for $\mu^* = -2/3$ the ω^* of the periodic phase is independent of l if $l \geq 6$. This is because when in the empty lattice 3 neighboring cells become occupied, the associated change of H^* is $-2-3\mu^*$. Since the interaction range is 3, for $\mu^* = -2/3$ a triple of occupied cells can be separated from another triple of occupied cells by $l-3$

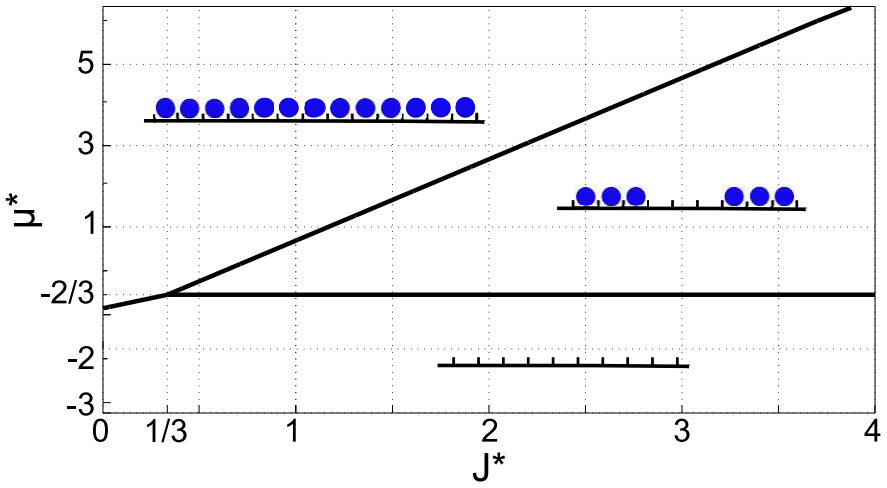

FIG. 2.2: Ground state of the considered model. The repulsion to attraction ratio J^* and the chemical potential μ^* are dimensionless (see (2.5)). The coexistence lines are $\mu^*_{gas-cond} = -1 + J^*$, $\mu^*_{gas-per} = -2/3$ and $\mu^*_{cond-per} = -4/3 + 2J^*$. Schematic illustration of the three phases is shown in the insets inside the region of stability of each phase.

empty cells for any $l \geq 6$. Such a state can be interpreted as a cluster fluid that can be stable, however, only for a single value of the chemical potential, $\mu^* = -2/3$. When $2 + 3\mu^* > 0$, the lowest value of ω^* corresponds to $l = 6$, and the periodic phase with period 6 is stable. The gas and periodic phases coexist for $\mu^* = -2/3$. Because of this coexistence, arbitrary separation between the clusters, whose number is also arbitrary (but smaller than $L/6$), can be interpreted as arbitrarily small droplets (larger than 6 in the case of the periodic phase) of these phases. As a result, an arbitrary number of interfaces can be formed. This is possible when the surface tension between the gas and the periodic phases vanishes.

Similarly, creation of a triple of empty sites in the fully occupied lattice leads to the change of H^* which is $\Delta H^* = -6J^* + 4 + 3\mu^*$. At the coexistence between the fully occupied lattice and the periodic phase $6J^* - 4 - 3\mu^* = 0$, hence the separation between the three empty neighboring cells (bubbles) can be arbitrary (but ≥ 3). Again, such a state can be interpreted as a fluid of bubbles, or as a coexistence between the liquid and periodic phases in the case of vanishing surface tension. Note the similarity between this property of our model and the very low surface tension between water- or oil- rich phases and microemulsion. At $T^* = 0$ formation of the microemulsion is associated with vanishing surface tension in the lattice model for the water-oil-surfactant mixture[67].

2.1.1.3 Mean-field approximation

Short background

In the self-consistent mean-field (MF) approximation the Hamiltonian (2.2) is approximated by

$$H_{MF}[\{\hat{\rho}(x)\}] = \sum_x \Big[-(h(x)+\mu)\hat{\rho}(x) + \frac{1}{2}h(x)\bar{\rho}(x) \Big] \tag{2.7}$$

where the mean-field acting on the site x is

$$h(x) = -\sum_{x'} V(x-x')\bar{\rho}(x') \tag{2.8}$$

and the MF average density satisfies the self-consistent equation

$$\bar{\rho}(x) = \frac{e^{\beta(h(x)+\mu)}}{1+e^{\beta(h(x)+\mu)}}. \tag{2.9}$$

The grand statistical sum

$$\Xi_{MF} = \prod_x \Big[e^{-\frac{\beta}{2}h(x)\bar{\rho}(x)} \Big(1 + e^{\beta(h(x)+\mu)} \Big) \Big] \tag{2.10}$$

together with (2.9) after some algebra leads to the grand potential of the form [68]

$$\begin{aligned} \Omega_{MF} &= \sum_{x_1=1}^{L}\sum_{x_2=1}^{L} \frac{1}{2}\bar{\rho}(x_1)\bar{\rho}(x_2)V(x_1-x_2) \\ &+ \sum_{x=1}^{L} f_h(\bar{\rho}(x)) - \mu\sum_{x=1}^{L}\bar{\rho}(x). \end{aligned} \tag{2.11}$$

where in the lattice models

$$f_h(\bar{\rho}) = -k_B T s(\bar{\rho}) = k_B T \Big[\bar{\rho}\ln(\bar{\rho}) + (1-\bar{\rho})\ln(1-\bar{\rho}) \Big]. \tag{2.12}$$

Local minima of (2.11) satisfy Eq.(2.9) (see Ref.[68]).
Eq.(2.9) can be solved by iterations for different initial conditions. Stability regions of different phases and first-order transitions between them can be obtained by comparing $\omega_{MF} = \Omega_{MF}/(ln)$ for different forms of $\bar{\rho}(x)$. In practice systems with the size l and PBC represent one period of the phases with the period l, and we have

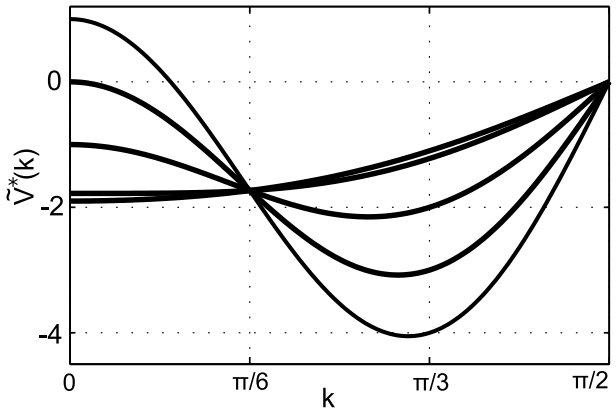

FIG. 2.3: $\tilde{V}^*(k)$ given by (2.16). $J^* = 0.05, 1/9, 0.5, 1, 1.5$ from the bottom to the top line on the left.

considered $6 \leq l \leq 50$.

Stability analysis

Boundary of stability of the disordered phase can be found by analyzing the second derivative of $\beta\Omega_{MF}$ with respect to the density profile $\bar{\rho}(x)$. The disordered fluid is stable as long as this derivative,

$$C_{MF}(x,x') = \frac{\partial^2 \beta\Omega_{MF}}{\partial\bar{\rho}(x)\partial\bar{\rho}(x')}, \tag{2.13}$$

is positive definite. The disordered phase is at the boundary of stability when the smallest eigenvalue of (2.13) vanishes for $\rho(x) = const$. For interactions depending only on $x - x'$ the quadratic part of $\beta\Omega_{MF}$ (bilinear form) is diagonal in Fourier representation, and the eigenvalues of C are given by

$$\tilde{C}_{MF}(k) = \beta^*\tilde{V}^*(k) + \frac{1}{\bar{\rho}(1-\bar{\rho})}, \tag{2.14}$$

where

$$\tilde{V^*}(k) = \sum_x V^*(x)e^{ikx}. \tag{2.15}$$

In this model

$$\tilde{V^*}(k) = -2\cos k + 2J^*\cos 3k. \tag{2.16}$$

$\tilde{C}_{MF}(k)$ assumes the smallest value $\tilde{C}_{MF}(k_b)$ for given T^* and μ^* for $k = k_b$ corresponding to the minimum of $\tilde{V}(k)$. We obtain

$$k_b = \begin{cases} 0 & \text{if } J^* < 1/9, \\ \arccos\sqrt{\frac{1+3J^*}{12J^*}} & \text{otherwise,} \end{cases}$$

and

$$\tilde{V}^*(k_b) = \begin{cases} 2(J^*-1) & \text{if } J^* < 1/9, \\ -2J^*\left(\frac{1+3J^*}{3J^*}\right)^{3/2} & \text{otherwise.} \end{cases}$$

The boundary of stability of the disordered phase obtained from $\tilde{C}_{MF}(k_b) = 0$,

$$T^*_\lambda = -\tilde{V}^*(k_b)\bar{\rho}_0(1-\bar{\rho}_0), \tag{2.17}$$

represents the spinodal line of the gas-liquid separation when $k_b = 0$ ($J^* < 1/9$). The MF boundary of stability of the disordered phase with respect to density waves with finite wavelengths $2\pi/k_b$ is termed λ-line in literature [37, 38, 69], to distinguish it from the spinodal line where the disordered phase is unstable with respect to phase separation. In this model the MF instability with respect to periodic ordering with the wavelength $2\pi/k_b$ with $k_b > 0$ occurs when $J^* > 1/9$ (see Fig.2.3).
It is interesting to find the λ-line and the spinodal in the (μ^*, T^*) phase space. From the form of the chemical potential for $\bar{\rho} = const$, $\mu^* = 2(J^*-1)\bar{\rho} + T^* \ln[\bar{\rho}/(1-\bar{\rho})]$, we obtain the boundary of stability of the homogeneous phase

$$\mu^* = (J^*-1)(1\pm q) + T^* \ln\left(\frac{J^*}{2T^*}\left(\frac{1+3J^*}{3J^*}\right)^{3/2}(1\pm q)^2\right) \tag{2.18}$$

where

$$q = \sqrt{1 + 2\frac{T^*}{J^*}\left(\frac{3J^*}{1+3J^*}\right)^{3/2}}. \tag{2.19}$$

The shapes of the spinodal and λ-lines for various J^* are shown in Fig.2.4.
In the case of attraction dominated system ($J^* < 1/9$), the two branches of the spinodal line separate the region where Ω_{MF} assumes two minima for two different constant densities (low-T^* side of the lines) from the region with one minimum on the high-T^* side of the lines. This is usual behavior associated with the gas-liquid separation.
For $1/9 < J^* < 1$ the branches of the line of instability intersect and form a loop for high T^*. The homogeneous phase is unstable for any density inside the loop. Note

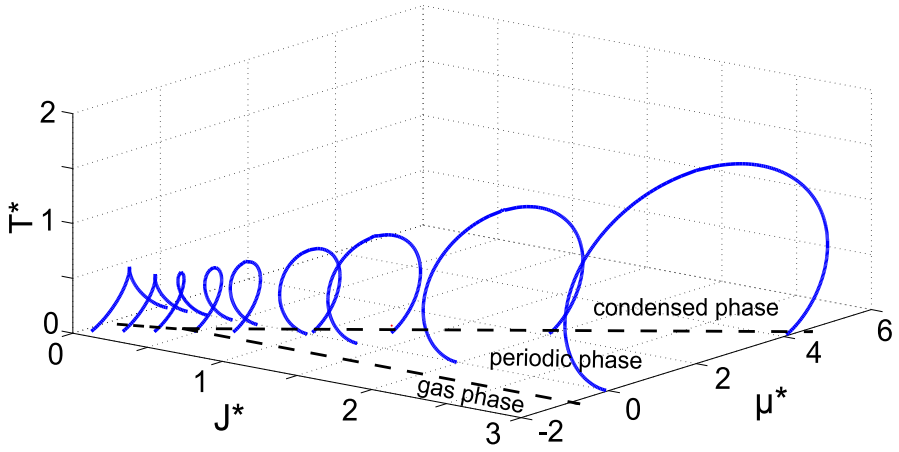

FIG. 2.4: Lines of instability (solid) of the homogeneous phase in the (μ^*, T^*) variables for a range of J^*. Similar behavior was obtained in Ref.[70]. The coexistence lines at $T^* = 0$ are shown as dashed lines.

that when the loop is present, then for decreasing T^* or increasing μ^* there may exist a sequence of phases: disordered - periodic - disordered. Such a sequence agrees with observations of the reentrant melting [71, 72]. For the repulsion-dominated system ($J^* > 1$) only the loop is present (Fig.2.4), and coexistence between homogeneous phases is not expected.

Our stability analysis is incomplete, because we did not study the boundary of stability of the periodic phase.

Mean-field phase diagrams

The continuous transitions between the disordered and ordered phases coincide with the critical point or with the λ-line determined above for $J^* < 1/9$ or $J^* > 1/9$ respectively. The transitions become first order for $T^* < T^*_{tcp}$, where the tricritical point (TCP) is calculated analytically in Appendix 6.2. The TCPs exist only for $1/9 < J^* < 1$. For $J^* = 1/9$ the two TCP (one for $\rho < 1/2$, the other one for $\rho > 1/2$) merge into the critical point at $\rho = 1/2$. For $J^* = 1$ we obtain $T^*_{tcp} = 0$. The locations of the first-order transition lines have been obtained by calculating the grand potential (2.11) for the average densities that are self-consistent solutions of Eq.(2.9). The method of determining the transition lines is shown schematically in Fig.2.5.

We obtain four qualitatively different phase diagrams for $J < 1/9$, $1/9 < J < 1/3$, $1/3 < J < 1$ and $J > 1$. In the first case standard gas-liquid separation occurs. For

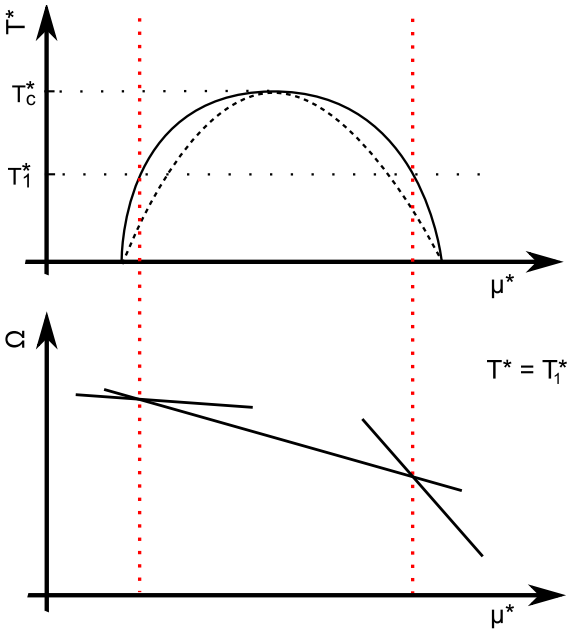

FIG. 2.5: Illustration of the method used for obtaining the phase coexistence. In the bottom panel the left, central and right line corresponds to the gas, periodic and disordered liquid phases respectively.

$1/9 < J < 1/3$ we find gas-liquid coexistence at low T^*, next a triple point where the two phases coexist with the periodic phase, and the first-order transition between the periodic phase and the fluid becomes continuous at the tricritical points. This type of phase diagram is shown in Fig.2.6 for $J^* = 1/4$. Similar phase diagram was obtained for very weak repulsion in Ref.[40], where only one-dimensional density oscillations were assumed in the Landau-type and density-functional theories. Moreover, when electrostatic repulsion is added to the Landau functional, similar phase diagram is obtained [73].

For $1/3 < J < 1$ there is no coexistence between the gas and liquid phases. Instead, the gas - periodic phase transition, followed by the periodic phase - liquid transition occur for increasing chemical potential. The transitions are first order below and continuous above (in temperature) the tricritical points. The phase diagram for $J^* = 1/3$ is shown in Fig.2.7. Similar phase behavior was obtained in Ref.[40] for medium-strength repulsion.

Finally, for $J^* > 1$ the tricritical points disappear and the transition between the disordered and periodic phases is continuous. This seems to be inconsistent with the presence of the first-order transition between the periodic and the fluid phases at $T^* = 0$. This apparent inconsistency follows from the presence of two periodic phases for $J^* > 1$. One of them is the same as the phase stable at $T^* = 0$. It has

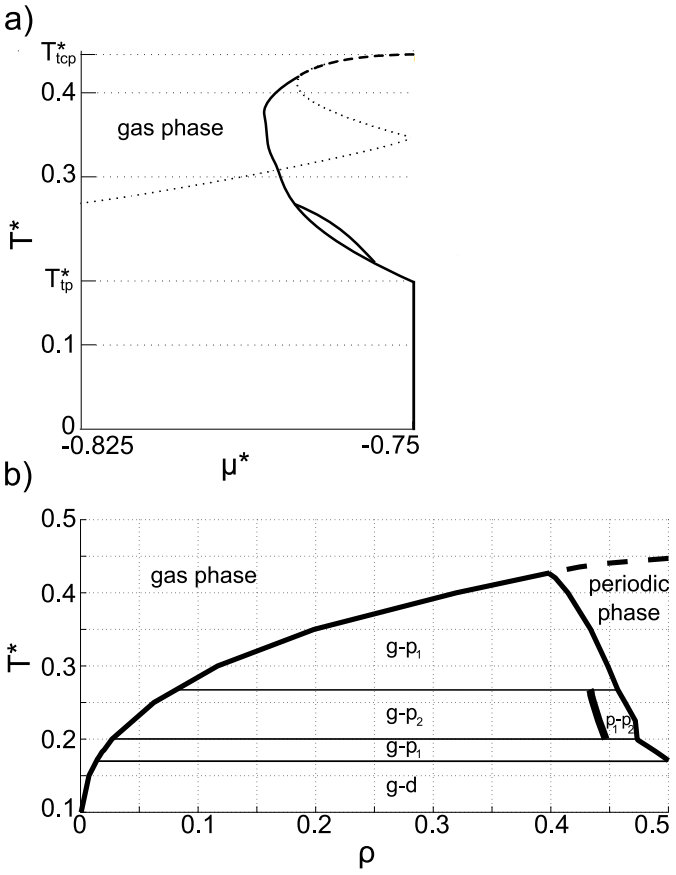

FIG. 2.6: MF phase diagram for $J^* = 1/4$ in variables (μ^*, T^*) (a) and (ρ, T^*) (b). The symmetry axis in (a) is $\mu^* = -3/4$ and $\rho = 1/2$ in (b). Only half of the phase diagram is shown because of the symmetry. Dash and solid lines represent continuous and first-order transitions. The dotted line is the λ-line. The coexisting phases in the two-phase regions in (b) are labeled by g for gas, d for dense fluid and p_1, p_2 for the periodic phases with the smaller and the larger period respectively. The density range of stability of the large-period phase is within the thickness of the line. The periodic phases in (a) are stable inside the lense (p_2) and inside the loop (p_1).

large amplitude of density oscillations and the period $l = 6$. The other phase appears inside the loop of the λ-line, has a period $2\pi/k_b$ and small amplitude of density oscillations. The two periodic phases coexist along the line which is a continuation of the coexistence line between the large-amplitude periodic phase and the homogeneous fluid, above the temperature at which this transition and the low-T^* branch of the λ-line intersect (see Figs. 2.4 and 2.8). The coexistence between the two periodic phases terminates at a critical point, where the densities, amplitudes and periods of the two phases become the same. The (μ^*, T^*) and (ρ, T^*) phase diagrams for $J^* = 3$ are shown in Fig.2.8. The amplitudes of the two periodic phases along their coexistence line and for $T^* = 0.347$ are shown in Fig.2.9 as functions of

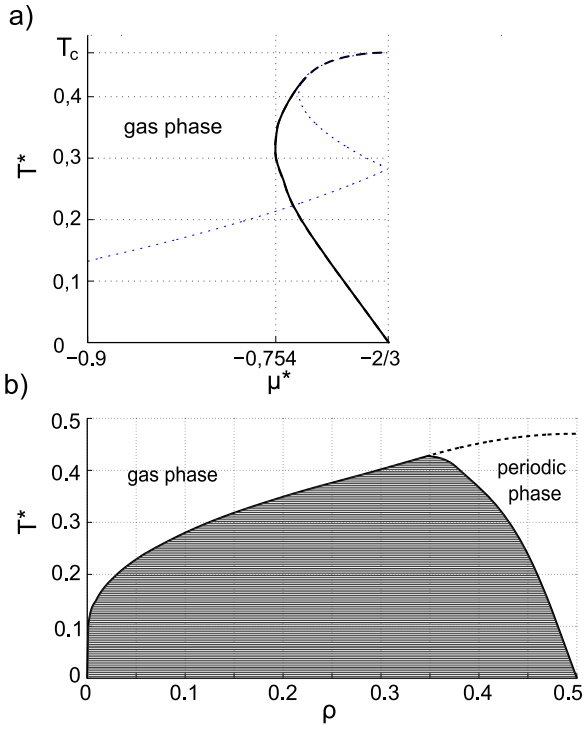

FIG. 2.7: MF phase diagram for $J^* = 1/3$ in variables (μ^*, T^*) (a) and (ρ, T^*) (b). The symmetry axis is $\mu^* = -2/3$ and $\rho = 1/2$ in (a) and (b) respectively. Only half of the phase diagram is shown because of the symmetry. Dash and solid lines represent continuous and first-order transitions between the disordered fluid and the periodic phase. The dotted line is the λ-line. The periodic phase in (a) is stable inside the loop (thick line). The two-phase regions in (b) are shaded.

T^* and μ^* respectively. The density profiles in the two periodic phases for selected thermodynamic states are shown in Fig.2.10. As far as we know, coexistence of two ordered phases with the same symmetry but different degree of order has not been reported yet.

2.1.1.4 Exact solution

Transfer matrix and exact expressions

Since the range of interactions is 3, we coarse-grain the lattice and introduce $L/3$ boxes consisting of three neighboring lattice sites, and labeled by integer $1 \leq r \leq L/3$. The microstates in the r-th box are

$$\hat{S}(r) = (\hat{\rho}(3r-2), \hat{\rho}(3r-1), \hat{\rho}(3r)). \tag{2.20}$$

There are 2^3 possible microstates in each box. We distinguish 4 states with the first site occupied and the remaining sites either occupied or empty, and denote such

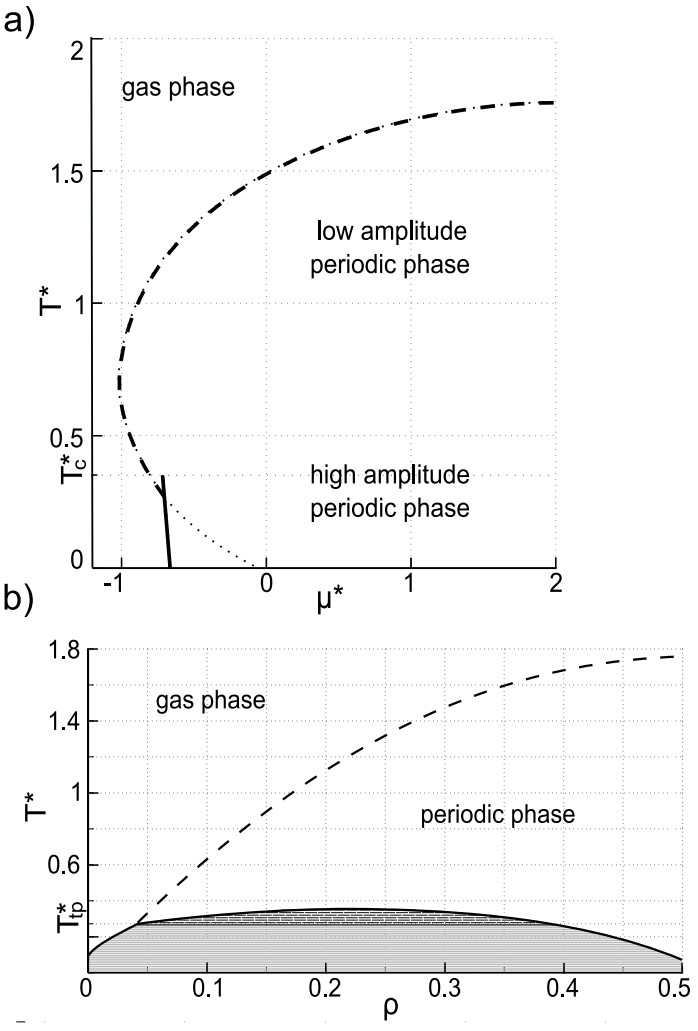

FIG. 2.8: MF phase diagram for $J^* = 3$ in variables (μ^*, T^*) (a) and (ρ, T^*) (b). The symmetry axis is $\mu^* = 2$ and $\rho = 1/2$ in (a) and (b) respectively. Only half of the phase diagram is shown because of the symmetry. Dash and solid lines represent continuous and first-order transitions. The dotted line is the λ-line. The two-phase regions in (b) are shaded with different shades for different phase equilibria. The *high-amplitude periodic phase* coexists with gas (for $\mu^* < 2$ or $\rho < 1/2$) or liquid (for $\mu^* > 2$ or $\rho > 1/2$) for $T^* < T^*_{TP}$, and with the *low-amplitude periodic phase* for $T^* > T^*_{TP}$. The coexistence line between the two periodic phases (short solid line above the dashed line in (a)) begins at $T^* = T^*_{TP}$ and terminates at the critical point with $T^*_c \approx 0.34713$. Note that the point where the transition between the disordered and the periodic phases changes order is not the TCP. The disordered phase coexists with one periodic phase for $T^* < T^*_{TP}$, and undergoes a continuous transition to the other periodic phase for $T^* > T^*_{TP}$, whereas at the TCP the transition between the same phases changes order.

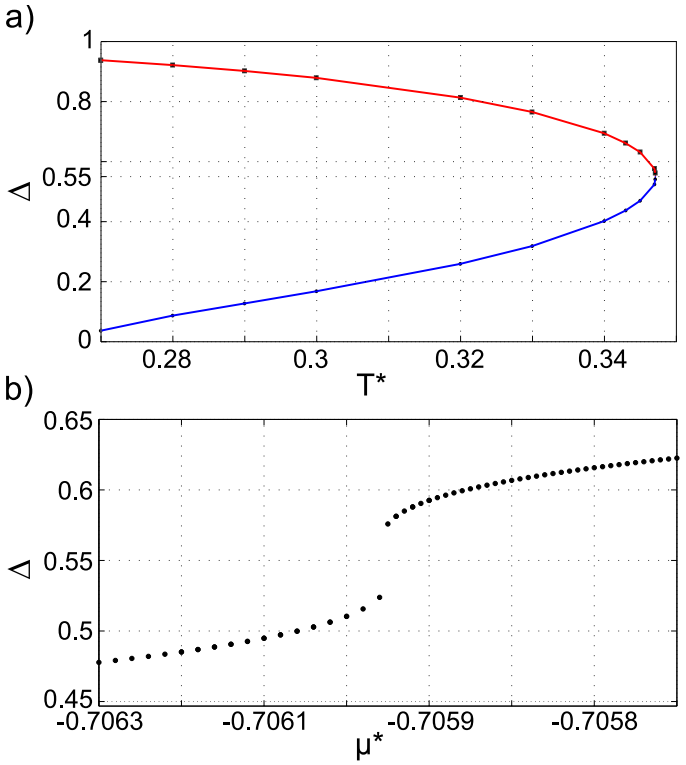

FIG. 2.9: Amplitudes of the density profiles in the two periodic phases for $J^* = 3$. (a) as a function of temperature along the coexistence line (the lines meet at $T_c^* \approx 0.34713$) (b) as a function of μ^* for $T_c^* = 0.347$.

states by $\hat{S}_1(r) = (1, \hat{\rho}(3r-1), \hat{\rho}(3r))$. Likewise, we denote states with the second site occupied by $\hat{S}_2(r) = (\hat{\rho}(3r-2), 1, \hat{\rho}(3r))$, and with the third site occupied by $\hat{S}_3(r) = (\hat{\rho}(3r-2), \hat{\rho}(3r-1), 1)$.

The Hamiltonian of the system with the PBC can be written in the form

$$H^*[\{\hat{\rho}(x)\}] = \sum_{r=1}^{L/3} H_t^*[\hat{S}(r), \hat{S}(r+1)] \tag{2.21}$$

where

$$H_t^*[\hat{S}(r), \hat{S}(r+1)] = \sum_{x=3r-2}^{3r} \left[-\hat{\rho}(x)\hat{\rho}(x+1) + J^*\hat{\rho}(x)\hat{\rho}(x+3) - \mu^*\hat{\rho}(x) \right]. \tag{2.22}$$

We introduce a 8×8 transfer matrix $\mathbf{T}$ with the matrix elements

$$T(\hat{S}(r), \hat{S}(r+1)) \equiv e^{-\beta^* H_t^*[\hat{S}(r), \hat{S}(r+1)]} = \sum_{i=1}^{8} P_i(\hat{S}(r)) \lambda_i P_i^{-1}(\hat{S}(r+1)), \tag{2.23}$$

where the eigenvalues of $\mathbf{T}$ are denoted by λ_i such that $|\lambda_i| \geq |\lambda_{i+1}|$, the elements

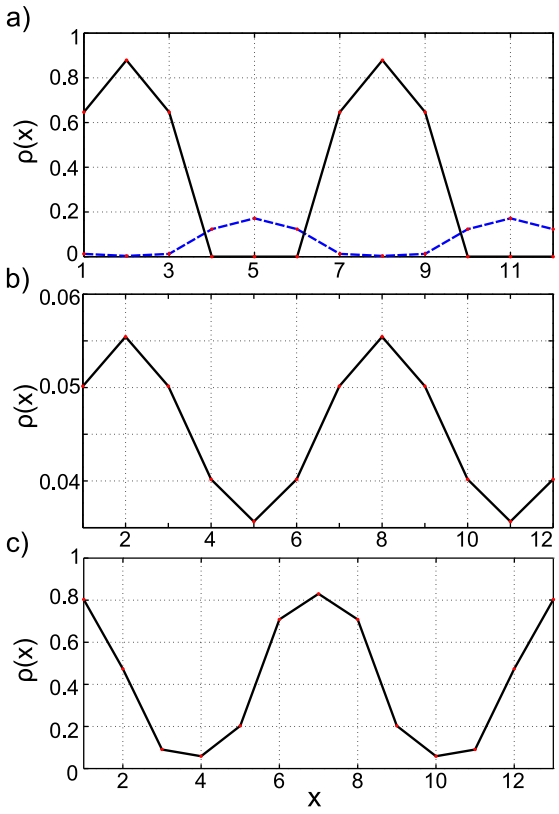

FIG. 2.10: Density profiles (a) in the coexisting high- and low-amplitude phases for $T^* = 0.3$. The lines are shifted horizontally for clarity. (b) in the low-amplitude phase close to the continuous transition to the fluid at $T^* = 0.3$ and (c) for $T^* = 1.3$ and $\mu^* = 1$. The quasi-periodic structure with a period incommensurate with the lattice is obtained from a density profile with a large-period when $2\pi/k_b$ is noninteger. The lines connecting the results for integer x are to guide the eye.

$(\hat{S}, i)$ of the matrix **P** transforming **T** to its eigenbasis are denoted by $P_i(\hat{S})$, and the elements $(i, \hat{S})$ of the matrix inverse to **P** by $P_i^{-1}(\hat{S})$. Note that **T** is not symmetric, hence pairs of complex-conjugate eigenvalues may occur. However, because **T** is a finite matrix with positive elements, from the Perron-Frobenius theorem it follows that the largest (in absolute value) eigenvalue is non-degenerate [74].

The grand statistical sum in terms of the transfer matrix takes the form

$$\Xi = Tr\mathbf{T}^{L/3} = \sum_{i=1}^{8} \lambda_i^{L/3} \tag{2.24}$$

and for the grand potential we obtain

$$\Omega^*/L = -p^* = -T^*\left[\frac{1}{3}\ln\lambda_1 + \frac{1}{L}\ln\left(1 + \sum_{i=2}^{8}\left(\frac{\lambda_i}{\lambda_1}\right)^{L/3}\right)\right] \simeq_{L\to\infty} -\frac{T^*}{3}\ln\lambda_1. \tag{2.25}$$

In the case of PBC the average density is independent of the position, $\rho = \langle\hat{\rho}(1)\rangle$. From the definition of the average density and from Eqs. (2.23) and (2.24) we obtain

$$\langle\hat{\rho}(1)\rangle = \frac{\sum_{\hat{S}_1(1)}\sum_{i=1}^{8}\lambda_i^{L/3}P_i^{-1}(\hat{S}_1(1))P_i(\hat{S}_1(1))}{\sum_{i=1}^{8}\lambda_i^{L/3}} \simeq_{L\to\infty} \sum_{\hat{S}_1(1)} P_1^{-1}(\hat{S}_1(1))P_1(\hat{S}_1(1)). \tag{2.26}$$

Let us consider the correlation function G for the sites separated by a distance $x = 3r + i$, where $r \geq 0$ and $i = 0, 1, 2$. Because the interaction range is 3, and the transfer matrix operates between triples of sites, we shall obtain different expression for $\langle\hat{\rho}(1)\hat{\rho}(1+x)\rangle$ for different $i = 0, 1, 2$. We introduce the notation

$$G(3r+i) = \langle\hat{\rho}(1)\hat{\rho}(1+3r+i)\rangle - \langle\hat{\rho}(1)\rangle^2. \tag{2.27}$$

From the definition of $\langle\hat{\rho}(x)\hat{\rho}(x')\rangle$ and from Eqs. (2.23) and (2.26) we obtain the asymptotic expression for $L \to \infty$

$$G(3r+i) = \sum_{n=2}^{8}\Big(\frac{\lambda_n}{\lambda_1}\Big)^r A_1^{(n)}B_{1+i}^{(n)} \tag{2.28}$$

where $i = 0, 1, 2$,

$$A_j^{(n)} = \sum_{\hat{S}_j} P_n(\hat{S}_j)P_1^{-1}(\hat{S}_j), \tag{2.29}$$

$$B_j^{(n)} = \sum_{\hat{S}_j} P_n^{-1}(\hat{S}_j)P_1(\hat{S}_j), \tag{2.30}$$

and $\hat{S}_j$ is defined below Eq.(2.20). The asymptotic decay of correlations for $r \gg 1$ is determined by the eigenvalue λ_2 with the second largest absolute value.
If λ_2 is real, then for $r \gg 1$ and $i = 0, 1, 2$ we can write

$$G(3r+i) = (sgn(\lambda_2))^r e^{-3r/\xi}A_1^{(2)}B_{1+i}^{(2)}, \tag{2.31}$$

where the correlation length is

$$\xi = 3/\ln\Big(\frac{\lambda_1}{|\lambda_2|}\Big). \tag{2.32}$$

Note the qualitatively different behavior for $\lambda_2 > 0$ and $\lambda_2 < 0$. For $\lambda_2 < 0$ the correlation function changes sign when the separation between the particles increases by 3, in analogy with the density of the periodic phase in the ground state. The case $\lambda_2 > 0$ corresponds to decay of correlations in the gas or liquid phases where no clusters consisting of three particles separated by 3 vacancies are formed.
If λ_2 is complex, then $\lambda_3 = \lambda_2^*$, $A_1^{(3)} = A_1^{(2)*}$ and $B_j^{(3)} = B_j^{(2)*}$. We introduce the notation

$$\lambda_2 = |\lambda_2|e^{i\lambda}, \qquad A_1^{(2)} = |A_1^{(2)}|e^{i\alpha_1}, \qquad B_j^{(2)} = |B_j^{(2)}|e^{i\beta_j}, \tag{2.33}$$

and for $r \gg 1$ and $i = 0, 1, 2$ obtain the asymptotic expression

$$G(3r+i) = \mathcal{A}_i e^{-3r/\xi}\cos\big(r\lambda + \theta_i\big) \tag{2.34}$$

where $\mathcal{A}_i = 2|A_1^{(2)}||B_{1+i}^{(2)}|$ and $\theta_i = \alpha_1 + \beta_{1+i}$, $i = 0, 1, 2$. Similar expression was proposed in Ref.[75] for a 1d and in Ref.[76] for a 3d system. The structure factor obtained in experiments and theory [7, 33–41, 66, 76, 77] is also consistent with this form. In general, $-\pi \le \lambda \le \pi$, and $2\pi/\lambda$ is noninteger. Except from $\lambda = \pm\pi$ (but in this case the imaginary part of λ_2 vanishes), the period of the exponentially damped oscillations is incommensurate with the lattice. This is similar to the results of the MF stability analysis and to the incommensurate density profiles obtained in MF for higher temperatures.
When $\lambda = \pm\pi \mp \epsilon$ with $\epsilon \ll 1$, then we can write Eq.(2.34) in the equivalent form

$$G(3r+i) = (-1)^r e^{-3r/\xi}\mathcal{G}(r,i), \tag{2.35}$$

with

$$\mathcal{G}(r,i) = \mathcal{A}_i\cos(6\pi r/w + \phi_i), \tag{2.36}$$

where the phase and the period of the amplitude modulations are $\phi_i = -\theta_i sgn(\lambda)$ and

$$w = \frac{6\pi}{|\lambda - sgn(\lambda)\pi|}. \tag{2.37}$$

The first factor in (2.35) changes sign when the distance increases by 3. The last factor describes the modulated amplitude with the wavelength of modulations $w \gg 6$ if $\lambda \to \pm\pi$.

We have obtained λ_i and the matrix **P** numerically for different J^*, μ^* and T^* and the results are presented in the next section.

Exact results

There are no phase transitions in a thermodynamic sense in one-dimensional systems with short range interactions and at finite temperature [78]. However, instead of a discontinuity, a rapid change of the density as a function of μ^* or p^* can occur. Moreover, instead of long-range order and the associated periodic density, a short-range order with exponentially damped oscillatory decay of correlations with very large correlation length may exist. In order to verify if such pseudo phase transitions occur in this model, we calculate density and pressure for several values of J^* for the range of μ^* and T^* corresponding to the phase transitions obtained in MF. In the next step we examine the correlation functions.

(A) Thermodynamic properties (Equation of state)

In Figs. 2.11-2.12 $p(\mu^*)$ and $\rho(\mu^*)$ obtained from Eqs.(2.25) and (2.26) are shown for $J^* = 3$ and $J^* = 1/4$ for $0.05 < T^* < 1$. By eliminating μ^* from Eqs. (2.25) and (2.26) we obtain the equation of state (EOS), and present several isotherms $\rho(p^*)$ in Figs.2.13 and 2.14. The chosen strengths of the repulsion to attraction ratio correspond to qualitatively different ground state and MF phase diagrams (see Figs.2.2, 2.6 and 2.8). Let us first discuss $J^* = 3$. For low T^* one can observe that although $p^*(\mu^*)$ is a smooth function, its slope changes rapidly for the two values of μ^* that correspond to the phase transitions at $T^* = 0$ and in MF. In accordance with this behavior the density changes from nearly 0 to 1/2 in a very narrow range of p^* and μ^*, remains nearly constant for large intervals of p^* and μ^*, and again changes rapidly from $\rho = 1/2$ to $\rho \approx 1$. Very large compressibility for $\rho \neq 1/2$ changes to very small compressibility for $\rho \approx 1/2$. It is necessary to substantially

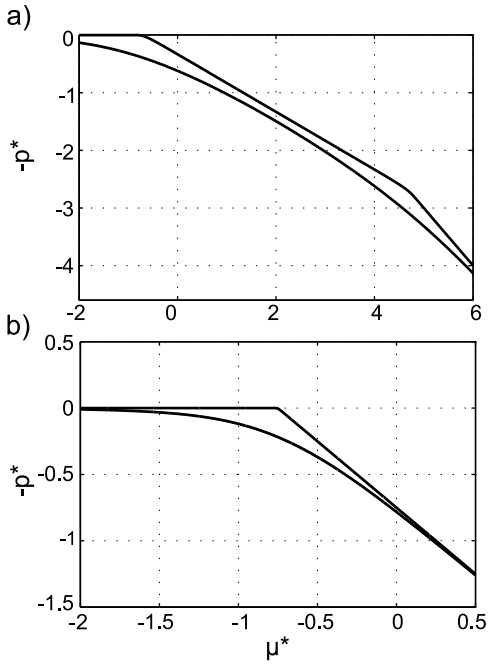

FIG. 2.11: $p(\mu^*)$ obtained from Eq.(2.25) (a) $J^* = 3$; top line: $T^* = 0.1$, bottom line: $T^* = 1$ and (b) $J^* = 1/4$; top line: $T^* = 0.05$, bottom line: $T^* = 0.5$.

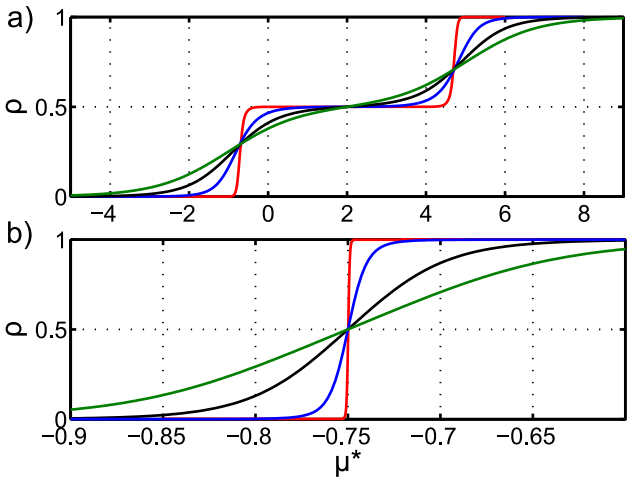

FIG. 2.12: $\rho(\mu^*)$ obtained from Eq.(2.26) for $J^* = 3$ and $T^* = 0.1, 0.4, 0.7, 1$ (top to bottom line on the right) (a) and $J^* = 1/4$ and $T^* = 0.005, 0.05, 0.1, 0.15$ (top to bottom line on the right) (b).

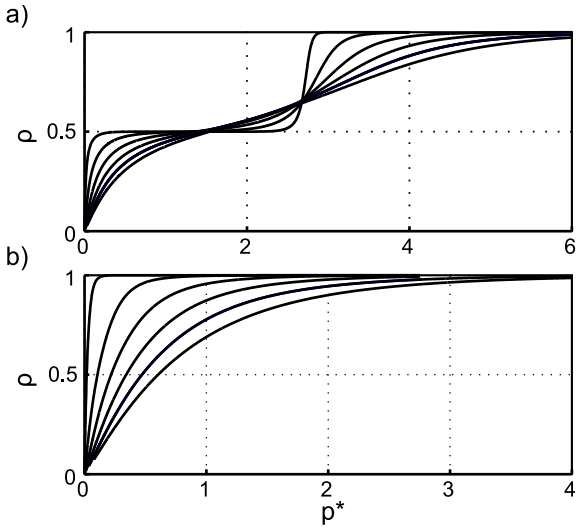

FIG. 2.13: EOS $\rho(p^*)$ isotherms obtained from Eqs.(2.25) and (2.26) for $T^* = 0.1, 0.2, 0.3, 0.4, 0.5$ and 1 (top to bottom line on the left) for $J^* = 3$ (a) and $J^* = 1/4$ (b).

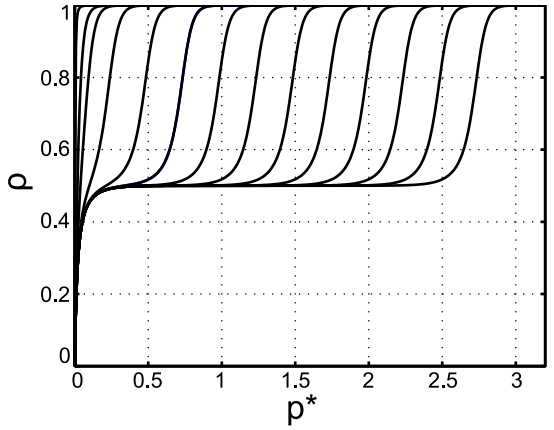

FIG. 2.14: EOS $\rho(p^*)$ isotherms obtained from Eqs.(2.25) and (2.26) for $T^* = 0.1$. From the left to the right line $J^* = 0.1, 0.25, 1/3, 0.5, 0.75, ..., 2.75, 3$.

increase the pressure in order to induce a slight increase of the density from $\rho = 1/2$, and a slight further increase of pressure is sufficient for a rapid compression to $\rho \approx 1$. When T^* increases from $T^* \approx 0.1$, the density changes from the gas density to $1/2$ more and more gradually. For $T^* > 0.5$ there are no abrupt changes of the slopes of the $\rho(p^*)$ and $\rho(\mu^*)$ lines, but the curvature of these lines is significantly smaller than in the one-phase region of a simple fluid. This is because the repulsion between the particles at the distance 3 leads to a significant increase of pressure for random distribution of particles. On the other hand, small pressure for $\rho < 1/2$ when T^* is low signals that in majority of states clusters made of at most 3 particles are separated by at least 3 empty sites. Similar behavior is observed for $1 < J^* < 3$

(Fig.2.14), but the range of μ^*, p^* and T^* for which $\rho \approx 1/2$ and remains nearly constant decreases with decreasing J^*. For $J^* < 1$ the plateau at the $\rho(\mu^*)$ and $\rho(p^*)$ curves for $\rho = 1/2$ disappears.

For $J^* = 1/4$ we can see in Fig. 2.11 b) a rapid change of the slope of the $p^*(\mu^*)$ line and in Fig. 2.12 the corresponding change of density from $\rho \approx 0$ to $\rho \approx 1$ when $T^* < 0.06$. For $T^* > 0.15$ the shapes of $p^*(\mu^*), \rho(\mu^*)$ and $\rho(p^*)$ (Fig.2.13) resemble the corresponding curves in the single-phase simple fluid. We thus see a pseudo-transition between the gas and liquid phases for very low T^*.

We conclude that the thermodynamic properties show no signature of the weakly-ordered periodic phase previously found in MF (Fig.2.6). By comparing Figs.2.13 a) and b) one can see the much lower pressure in this case than for the repulsion-dominated case of $J^* = 3$.

(B) Structure (correlation function)

Our aim in this section is to discuss the exact results for the correlation function for $J^* = 3$ and $J^* = 1/4$, corresponding to qualitatively different ground state (Fig.2.2) and MF phase diagrams (Figs.2.8 and 2.6). We particularly address the question for what parameters the periodic order occurs, and how the range and amplitude of the correlation function depends on μ^*, T^* and J^*.

For $J^* = 3$ we obtain complex λ_2 for the considered region of (μ^*, T^*). In this case the correlation function is given in Eq.(2.34), and presented in Figs.2.15 and 2.16. In Fig.2.15 μ^* corresponds to $\rho \approx 1/2$, where the periodic phase is predicted in MF, and in Fig.2.16 μ^* corresponds to $\rho \approx 0$ (homogeneous gas in MF).

The correlation length ξ (Eq.(2.32)) and the amplitude of the correlation function $\mathcal{A}_0$ (see below Eq.(2.34)) are shown in Figs.2.17 and 2.18 respectively. For $\mu \leq -2/3$ the wavenumber λ is shown in Fig.2.19 a), and for $\mu \geq -2/3$ the period w of modulations of the amplitude (see (2.35) and (2.36)) is shown in Fig.2.19 b).

From Fig.2.17 a) it follows that for $\mu^* < -2/3$ the correlation length ξ first increases slightly for decreasing T^*, but starting form T^* depending on μ^* decreases rapidly to 0 for T^* decreasing to 0. Analogous behavior is predicted for $\mu^* > 14/3$ by the model symmetry. For $-2/3 < \mu^* < 14/3$ (stability of the periodic phase for $T^* = 0$) the correlation length increases for decreasing T^*. For given T^* the correlation length increases with increasing μ^* when $\mu^* < 2$ and assumes a maximum for $\mu^* = 2$. The maximum of ξ is very large for $T^* < 0.15$. For $\xi \sim 10^5$ the range of the 'short-range order' is in fact macroscopic. For particles with a diameter $10nm$ the periodic

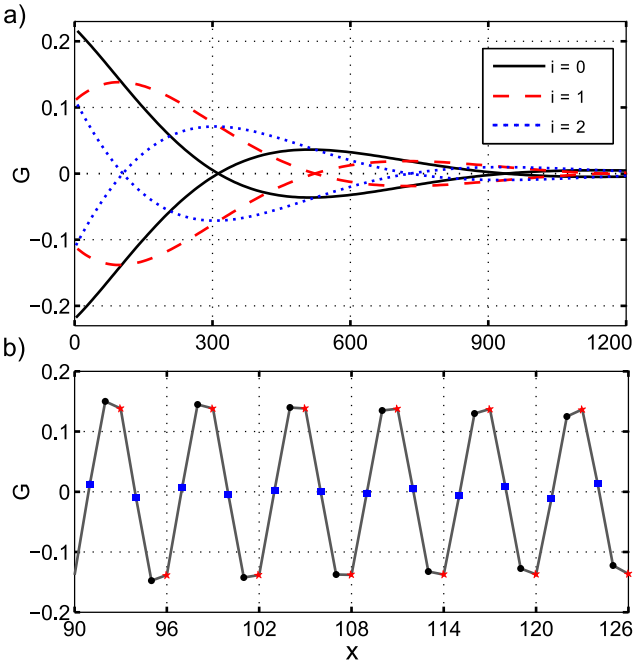

FIG. 2.15: The correlation function $G(x)$ for $x = 3k + i$ with $i = 0, 1, 2$ (Eq.(2.34)) for $J^* = 3$, $\mu^* = 0$ and $T^* = 0.1$ (inside the MF stability region of the periodic phase). Solid line and the circles (black), dashed line and the asterisks (red) and dotted line and the squares (blue) correspond to $i = 0, 1, 2$ respectively. The bottom panel shows a small portion of the upper panel.

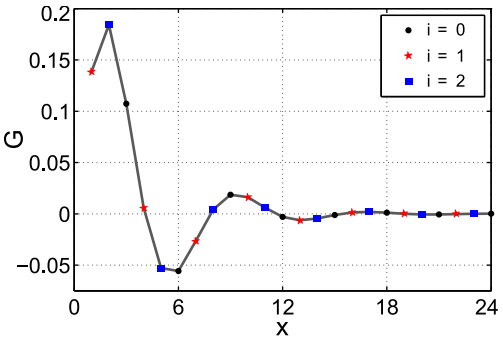

FIG. 2.16: The correlation function $G(x)$ for $x = 3k + i$ with $i = 0, 1, 2$ (Eq.(2.34)) for $J^* = 3$, $\mu^* = -0.7$ and $T^* = 0.1$ (outside the MF stability region of the periodic phase). Black (circle), red (asterisk) and blue (square) symbols correspond to $i = 0, 1, 2$ respectively.

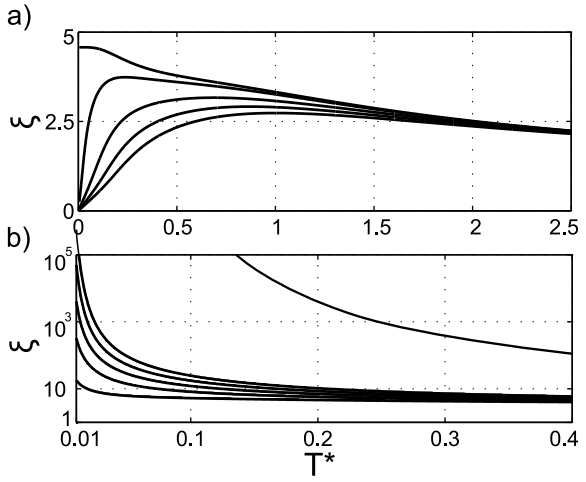

FIG. 2.17: The correlation length ξ (Eq.(2.32)) for $J^* = 3$ as a function of T^* (a) outside the MF stability region of the periodic phase. From the top to the bottom line $\mu^* = -2/3, -0.7, -0.8, -0.9, -1$ and (b) inside the MF stability region of the periodic phase. From the bottom to the top line $\mu^* = -0.65, -0.6, -0.55, -0.5, -0.45$ and 2.

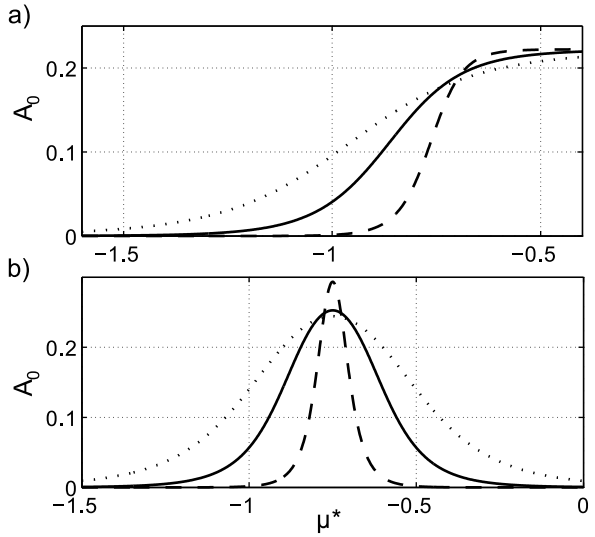

FIG. 2.18: The amplitude $\mathcal{A}_0$ of the correlation function (see Eq.(2.34) and below) as a function of μ^*. Dash, solid and dotted lines correspond to $T^* = 0.1, 0.2, 0.3$ respectively. $J^* = 3$ (a) and $J^* = 1/4$ (b).

arrangement persists to distances $\sim 1mm$. The amplitude of the correlation function for $T^* \leq 0.1$ increases sharply from a very small value for $\mu^* < -1$ to ~ 0.2 for $\mu^* > -0.7$ (see Fig.2.18a). The period w of the modulations of the correlation function (Eqs.(2.35)- (2.37)) increases for decreasing T^*, indicating more and more ordered structure (see Fig. 2.19b). All these results confirm a qualitative change of the structure along the lines $\mu^* = -2/3, 14/3$ for low T^*. For $-2/3 < \mu^* < 14/3$ quasi long-range order with the very large correlation length and the amplitude that

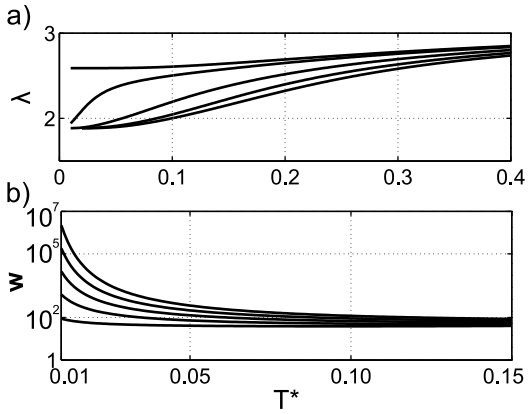

FIG. 2.19: (a) the wavenumber λ of the correlation function (Eq.(2.34)). $J^* = 3$ and $\mu^* = -2/3, -0.7, -0.8, -0.9, -1$ from the top to the bottom line (b) the period w (Eqs.(2.35)-(2.37)) of the amplitude modulations. $J^* = 3$ and $\mu^* = -0.65, -0.6, -0.55, -0.5, -0.45$ from the bottom to the top line.

for low T^* rapidly decreases at the boundaries of this region exists. From Figs.2.17 and 2.18 we can see that the increasing correlation length and amplitude for increasing T^* when $-1 < \mu^* < -2/3$ indicates a change from a less to a more ordered structure when T^* increases. The rapid increase of the amplitude as a function of μ^* for $\mu^* \approx -2/3$ near T^* corresponding to the maximum of ξ resembles the transition between the periodic phases with weak and strong order found in MF (compare Figs. 2.18a and 2.9b). When T^* further increases, the properties of the correlation function change more gradually and the correlation length becomes short, in consistency with the continuous transition between the ordered and disordered phases found in MF for high T^*. Despite the absence of the phase transition in the strict sense, we can see a change from a quasi-ordered periodic structure to the structure with much lower degree of order.

For $J^* = 1/4$ we obtain λ_2 that is a real number on the low-T^* side of a line $T^*_{cross}(\mu^*)$, and a complex number for T^* above this line. As a result, a monotonic decay of correlations is found for $T^* < T^*_{cross}(\mu^*)$, and an oscillatory decay sets in for $T^* > T^*_{cross}(\mu^*)$. The derivatives of the correlation length ξ and the wavenumber λ with respect to T^* have a discontinuity when the imaginary part of λ_2 appears (see Fig.2.20). The amplitude of the correlation function (Fig.2.18b) increases from a very small value for $\mu^* < -1$ to ~ 0.3 for $\mu^* = -0.75$ for $T^* = 0.1$. For larger T^* the increase of the amplitude is more gradual. The correlation function shown in Fig. 2.21 confirms that for low T^* the correlations decay monotonically, whereas for higher T^* the oscillatory decay of correlations is present. The correlation length,

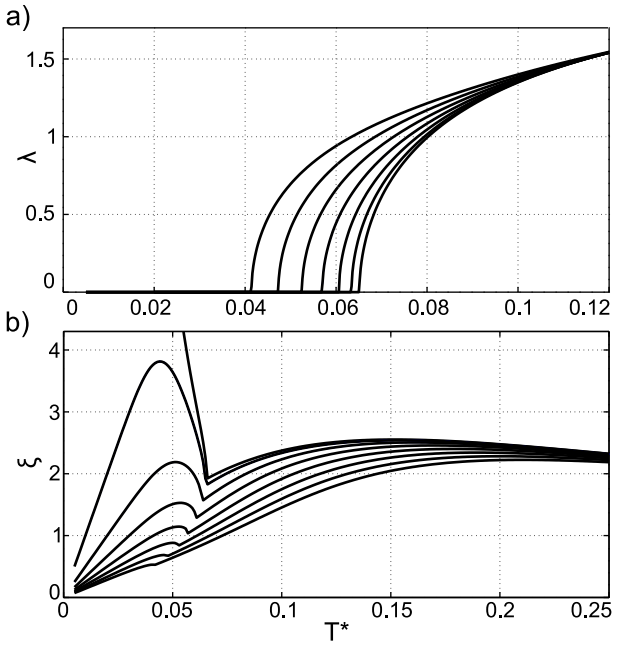

FIG. 2.20: The wavenumber λ (a) and the correlation length ξ (Eq. (2.32)) (b) of the correlation function (Eq.(2.34)) as a function of T^* for $J^* = 1/4$. From the bottom to the top line in (a) and from the top to the bottom line in (b) $\mu^* = -0.75, -0.75 \pm 0.01, -0.75 \pm 0.02, \ldots, -0.75 \pm 0.07$.

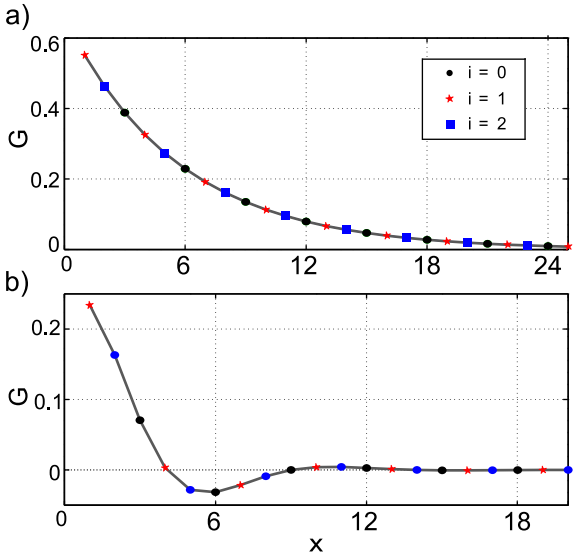

FIG. 2.21: The correlation function $G(x)$ for $x = 3k + i$ with $i = 0, 1, 2$ (Eq.(2.34)) for $J^* = 1/4$ and $\mu^* = -3/4$ for $T^* = 0.05$ (a) and $T^* = 0.2$ (b). Black (circle), red (asterisk) and blue (square) symbols correspond to $i = 0, 1, 2$ respectively.

however, is rather short, as shown in Fig.2.20. The monotonic decay of correlations for low T^*, and oscillatory decay of correlations at higher T^* together with a rather rapid increase of the amplitude of the correlation function from a very small to a rather large value for some range of μ^* around $\mu^* = -3/4$ bear some similarity to the MF phase diagram. However, due to the much shorter correlation length than for $J^* = 3$, we can conclude that the weak periodic order (small amplitude of density oscillations) found in MF for relatively large T^* does not resemble an ordered phase in 1d.

2.1.1.5 Monte Carlo simulations in the Canonical Ensemble

In the previous section we have shown that the disordered phase in systems with competing interactions is characterized by the EOS and the correlation function that for strong repulsion are completely different than in simple fluids. In this section we would like to determine how the pretransitional ordering into clusters whose positions can be correlated over very large distances is reflected in the measurable thermal properties such as the constant-volume specific heat. Since analytical calculations in the Canonical Ensemble are very difficult, we perform MC simulations. The basic step in the sampling is made as follows: Given the current configuration of the system one chooses at random with equal probability one of the occupied positions, x (with $\hat{\rho}(x) = 1$), and one of the empty positions x' (with $\hat{\rho}(x') = 0$), the trial configuration is then constructed by swapping the states between the positions x and x'. Considering the energies of the current and the trial configurations one applies the Metropolis criterion [79] to decide whether the trial configuration is accepted as the new configuration of the system or not. The energies of the system in the Canonical Ensemble are given by the Canonical Hamiltonian U

$$U[\{\hat{\rho}\}] = \frac{1}{2}\sum_{x=1}^{L}\sum_{x'=1}^{L}\hat{\rho}(x)V(x-x')\hat{\rho}(x'). \tag{2.38}$$

The heat capacity per particle, $c_v = (\partial(U/N)/\partial T)_{N,L}$, is computed using the fluctuation formula:

$$c_v = \frac{1}{Nk_BT^2}\left[\langle U^2\rangle - \langle U\rangle^2\right], \tag{2.39}$$

where the angular brackets indicate averages in the Canonical Ensemble.

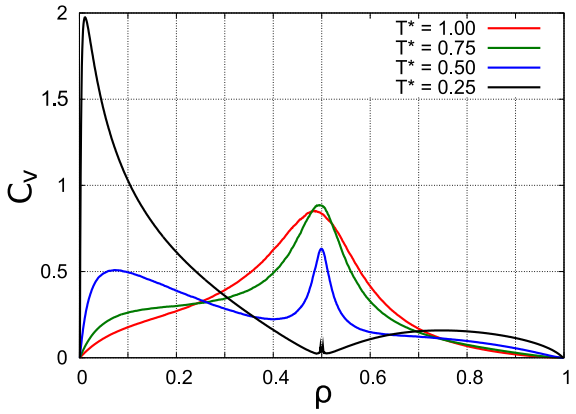

FIG. 2.22: The specific heat per particle (in k_B units) as a function of density (dimensionless) for $J^* = 3$. From the top to the bottom line on the left $T^* = 0.25, 0.5, 0.75, 1$ with $L = 1200$.

For $J^* = 3$ the specific heat is shown in Fig.2.22. The results for $J^* = 0.25$ are shown in Fig. 2.23. For both values of J^* we can observe the presence of a peak at low density. On cooling the system the height of this peak increases, and the density where it appears is shifted to lower values. This maximum in the heat capacity at low temperature can be explained as an effect of the equilibrium between isolated particles and clusters of several particles. Given the Hamiltonian of the model, these clusters are likely to be triples in the case of $J^* = 3$. At low temperature and low density the loss of entropy due to the formation of clusters is compensated by the energetic effect due to the attractive interaction between the nearest neighbors.

There are, however, significant differences between the heat capacities curves for $J^* = 0.25$ and $J^* = 3.0$, especially for $\rho \simeq 1/2$. These differences are consistent with the results for the EOS and the correlation function that indicate periodic ordering of clusters only for strong enough repulsion. For $J^* = 3.0$, at low temperature, we can observe a basin around $\rho = 1/2$, and a narrow peak centered also at $\rho = 1/2$. Focusing in the region $\rho \leq 1/2$, the ground state configurations are formed by triples of occupied positions. Each triple of occupied cells is separated at least by three empty positions from another triple. Since the triple-triple interaction is repulsive at short distances, the system does not show any trend to exhibit a pseudo phase separation to form large regions of occupied and empty positions, and therefore the small energy fluctuations lead to small values of the heat capacity. Notice, however that for $J^* < 1/3$ and low temperature the dominant attractive interactions lead to a condensation of particles in large clusters of occupied cells. In this case neither the basin at low T^* nor the peak near $\rho = 1/2$ is present.

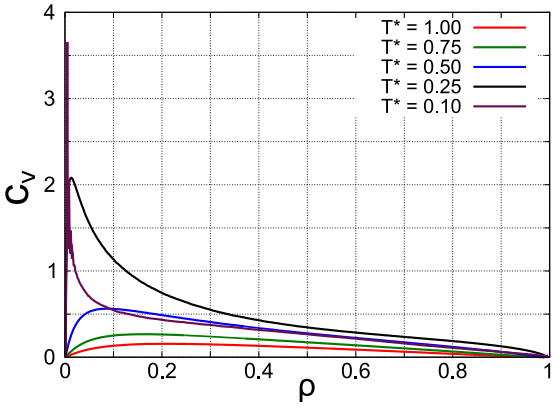

FIG. 2.23: The specific heat (in k_B units) as a function of density (dimensionless) for $J^* = 1/4$. From the top to the bottom line on the left $T^* = 0.1, 0.25, 0.5, 0.75, 1$ with $L = 840$.

The peak of $c_v(\rho)$ at $\rho \simeq 1/2$ for $J^* = 3$ can be interpreted as a signature of a pseudo-phase transition between an ordered (or quasi-ordered) phase (periodic phase with $l = 6$ for $\rho = 1/2$) and a high temperature disordered phase. Notice that as one approaches $\rho = 1/2$ the degeneracy of the ground state reduces sharply, then we can describe this peak as produced by the competition between the ground state (with very low entropy values when $\rho \to 1/2$) and *disordered* states (with higher values of energy and entropy). This ordered *pseudo*-phase lies between the fluid of small droplets ($\rho < 1/2$, $T \to 0$) and the fluid of bubbles ($\rho > 1/2$, $T \to 0$). In spite of the lack of real phase transitions for one-dimensional models with short range interactions, the periodic pseudo phase with density $\rho = 1/2$ resembles to some extent the low-density crystalline phases that appear in core-softened models [80].

2.1.1.6 Short summary & comparison of the exact and the mean-field results

We have developed a generic model for self-assembly of systems with isotropic competing interactions. The 1d model was solved exactly and within the MF approximation for the whole range of the repulsion to attraction ratio J^*. We have found exact solutions for the equation of state, average density and the correlation function. The mean-field phase diagrams obtained in [65] were also discussed. In addition, MC simulations for specific heat have been performed. The main results are:

- The ground state ($T^* = 0$) shows a sequence of phases: fluid (gas) - periodic - fluid (liquid) for increasing μ^* when $J^* > 1/3$, while for weaker repulsion only gas and liquid phases are stable (Fig. 2.2).

- Ordering on mesoscopic length scale induces qualitative changes in the equation of state (EOS) in comparison to that of simple fluids (see Fig.2.13): very large compressibility for the range of densities where the pseudo-phase transitions between the fluid and the periodic phase are expected, and extremely small compressibility where quasi-periodically distributed clusters are formed.
- The correlation length of self-assembling particles may be several orders of magnitude larger than the particle diameter (see Fig.2.17).
- The exact solution for the correlation function showed that counterintuitively monotonic decay can change upon heating to oscillatory decay (Fig. 2.21).
- The pseudo-phase transition to the periodically distributed clusters is associated with a peak in the specific heat (Fig. 2.22).
- The range of μ for which the periodic phase is stable is broaden within the MF approximation at $T > 0$, than predicted by the exact results at $T = 0$. (see e. g. Fig. 2.6)
- The MF phase diagrams exhibit re-entrant melting, i. e. for increasing T at constant μ^* a sequence of phases: fluid-periodic-fluid appears. (Figs. 2.6, 2.7 and 2.8).
- The MF phase diagram for strong repulsion (Fig. 2.8) predicts coexistence of two periodic phases with different amplitude of oscillations, while the MF phase diagram for weak repulsion(Fig. 2.6) predicts coexistence of two periodic phases with different periods of oscillations .

The aforementioned results will be discussed in more detail in Sec. 2.1.3, where the comparison between the SALR and the amphiphilic systems is presented.

Utility of the MF approximation for 1d self-assembling systems

The mean-field approximation is a common tool used for investigation of complex systems. However, in the case of self-assembling systems it is not known how it affects the results. Since we were able to obtain the exact solution of the model, we can comment on what is the connection between the exact results for the ground state, equation of state and the correlation function and the mean-field phase diagram.
The exact result for the ground state ($T^* = 0$) shows stability of the periodic phase for intermediate values of the chemical potential and for sufficiently strong interparticle repulsion. The MF solution is consistent with the exact results when $T^* \to 0$,

but for intermediate temperatures the MF phase diagram shows existence of the periodic phase for a range of μ^* and J^* that is broader than at $T^* = 0$. In particular, the periodic phase appears in the MF phase diagrams for $J^* > 1/9$, while at $T^* = 0$ only for $J^* > 1/3$.

What is more, the MF phase diagram shows that for increasing temperature at constant chemical potential a sequence of phases: fluid-periodic-fluid appears. The found re-entrant melting, leads to counterintuitive conclusion, that upon the increase of temperature more ordered structure is formed. This phenomenon, however, is not a pure artifact of the MF approximation. We have found that it is reflected in the qualitative change of the correlation function properties. For the chemical potential values that in the ground state correspond to the gas or liquid, we observe that the correlation length assumes a maximum for some finite T^*, indicating *an increase of order upon heating*. Moreover, for such T^* the amplitude of the correlation function changes from a very small value to a much larger value for a narrow range of the chemical potential, and stays large for the range of the chemical potential similar to the stability region of the periodic phase found in MF. Thus, the surprising MF result and the predicted MF phase diagram are related with some particular features of the model exact solution.

We need to stress, however, that in one-dimensional systems at $T > 0$ no phase transitions are present, thus the MF approximation should only be used if the exact solution is out of reach. The validity of the MF approximation in 2d self-assembling systems is discussed in Sec. 2.2.5.

2.1.2 Self-assembly of amphiphilic molecules

In Sec. 1.3 we have shown why colloidal and amphiphilic self-assembly in the bulk are similar if one assumes weak ordering. These results, however, do not answer the question of similarity at low temperature. In order to compare colloidal and amphiphilic self-assembly at low temperatures, in this section we will introduce and carefully study a one-dimensional generic model of amphiphiles in a polar solvent. Determining the exact solution of the model will allow us to compare the colloidal and amphiphilic self-assembly without the limitation for the temperature range. Such comparison is presented in Sec. 2.1.3.

This section is organized as follows: we introduce the model in Sec. 2.1.2.1, its ground state (T=0) is presented in Sec. 2.1.2.2, while the analysis at $T > 0$ is first carried out within the MF approximation in Sec. 2.1.2.3 and next the exact results are derived and studied in Sec. 2.1.2.4. Conclusions from the investigation on amphiphilic self-assembly in 1d are in Sec. 2.1.2.5.

2.1.2.1 Model Introduction

Amphiphilic molecules consist of a hydrophilic head and a hydrophobic tail, therefore the interactions between them depend on their relative orientations. In the case of a two-component mixture of a polar solvent and amphiphilic molecules, for example lipids, we assume that the solvent molecules attract the polar head, and effectively repel the hydrophobic tail of the amphiphilic molecule. We neglect orientational degrees of freedom of the solvent molecules. In a one-dimensional model the continuum of different orientations of amphiphiles is reduced to just two orientations (Fig.2.24). We assume that the molecules occupy lattice sites, and the lattice constant a is of order of the length of the amphiphilic molecule in this model. If the solvent molecules are much smaller than the amphiphilic molecules, we assume that the site is occupied by a cluster of several solvent molecules.
We assume nearest-neighbor interactions. The absolute value of the energy of two clusters of solvent molecules that occupy the nearest-neighbour sites, $-b$, is taken as the energy unit. We assume that the interaction between the cluster of solvent molecules and the amphiphilic molecule in the favorable (unfavorable) orientation is $-cb$ $(+cb)$, and the interaction between two amphiphilic molecules in the favorable and unfavorable orientation is $-gb$ and $+gb$ respectively. The orientations of two amphiphilic molecules are favorable when they are oriented either head-to-head or tail-to-tail. The neighborhood of the polar head and the hydrophobic tail is unfavorable. The energies of different pairs of occupied sites are shown in Fig. 2.24. The model is similar to the lattice model of ternary oil-water-surfactant mixtures introduced in Ref.[58] and to a continuous model of binary mixtures with amphiphiles [68].

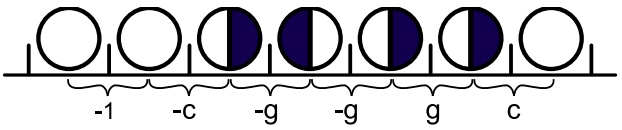

FIG. 2.24: The interacting pairs of occupied sites in the 1d model. The open circle represents the solvent molecule, and the light and dark semicircles represent the head and the tail of the amphiphilic molecule respectively. The unit of the inscripted energies is the absolute value of the solvent-solvent interaction energy.

Different values of the parameters b, c, g may correspond to different particular mixtures. We are interested in general aspects of the amphiphilic self-assembly, especially in similarities between ordering on the mesoscopic length scale in the amphiphilic and colloidal systems, and in origin of these similarities. For this reason we shall not try to fit the model parameters to any particular mixture. A representative example of a system described by this model is a mixture of lipids and water. We should stress that water is a complex liquid [81–84], and micro-heterogeneities are present in aqueous solutions of polar molecules [85, 86]. However, on the mesoscopic length scale of tens or hundreds of nanometers the ordering of the water molecules plays a subdominant role.

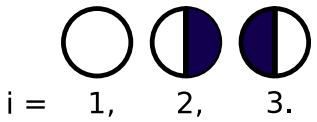

FIG. 2.25: Presentation of the used notation: $i = 1$ corresponds to cluster of solvent molecules, $i = 2$ corresponds to amphiphilic molecules with the head on the left, while $i = 3$ corresponds to the amphiphilic molecules with the head on the right.

We introduce the microscopic densities $\hat{\rho}_i(x)$ with $i = 1, 2, 3$ denoting the cluster of solvent molecules, and the amphiphile with the head on the left and on the right respectively (Fig. 2.25). $\hat{\rho}_i(x) = 1$ when the site x is in the state i and $\hat{\rho}_i(x) = 0$ otherwise. Multiple occupancy of the lattice sites is excluded. We further restrict our attention to the liquid phase and assume close-packing, i. e. for any site x

$$\sum_{i=1}^{3} \hat{\rho}_i(x) = 1. \tag{2.40}$$

The Hamiltonian of an open system, with the chemical-potential contribution included, can be written in the form

$$H'_{am}[\{\hat{\rho}_i\}]/b = \frac{1}{2}\sum_{x=1}^{L}\sum_{x'=1}^{L}\hat{\rho}_i(x)V'_{ij}(x,x')\hat{\rho}_j(x') - \sum_{x=1}^{L}\mu\hat{\rho}_1(x), \tag{2.41}$$

where $V'_{ij}(x,x')$ is the interaction potential between the i-th and j-th states at sites x and x' respectively, and the Einstein summation convention[1] for repeated indices is used, L is the system size, $\mu = \mu_1 - \mu_s$, $\mu_1 b$ is the chemical potential of the solvent, and the chemical potential of amphiphiles, $\mu_s b = \mu_2 b = \mu_3 b$, is independent of orientations of the molecules. In order to mimic properties of the bulk we assume periodic boundary conditions, $L+1 \equiv 0$. According to the above discussion of interactions the interaction potential $\mathbf{V}'$ is

$$\mathbf{V}'(x,x+1) = \begin{bmatrix} -1 & -c & c \\ c & g & -g \\ -c & -g & g \end{bmatrix} \tag{2.42}$$

and $V'_{ij}(x,x-1) = V'_{ji}(x,x+1)$, $V'_{ij}(x,x+k) = 0$ for $|k| > 1$. In the liquid phase we can neglect density fluctuations (Eq.(2.40)), hence $\hat{\rho}_1(x) = 1 - \hat{\rho}_2(x) - \hat{\rho}_3(x)$ and there are two independent densities. In a disordered phase $\langle\hat{\rho}_i(x)\rangle = \rho_i$, and $\rho_1 = 1 - \rho_s$ with $\rho_s = 2\rho_2 = 2\rho_3$ denoting the average amphiphile concentration. Thanks to the close packing assumption we can eliminate $\hat{\rho}_1(x)$ in the energy contribution, and the Hamiltonian takes the form (up to a state-independent constant)

$$H_{am}[\{\hat{\rho}_i\}]/b = \frac{1}{2}\sum_{x}\sum_{x'}\hat{\rho}_i(x)V_{ij}(x,x')\hat{\rho}_j(x') - \sum_{x}\bar{\mu}_1\hat{\rho}_1(x) \tag{2.43}$$

where $i,j = 2,3$, $\bar{\mu}_1 = \mu_1 + 2 - \mu_s$ and

$$\mathbf{V}(x,x+1) = \begin{bmatrix} -1+g & -1-g-2c \\ -1-g+2c & -1+g \end{bmatrix}. \tag{2.44}$$

Again, $V_{ij}(x,x-1) = V_{ji}(x,x+1)$ and $V_{ij}(x,x+k) = 0$ for $|k| > 1$.

[1] If expression contains repeated subscripted variables, then the subscripted variables are assumed to be summed over.

2.1.2.2 The ground state

At $T = 0$ the stable structure corresponds to the global minimum of the Hamiltonian. The Hamiltonian in Eq.(2.43) for given interactions c and g takes the minimum for the densities $\hat{\rho}_i(x)$ that depend on $\bar{\mu}$. Apart from the water-rich and lipid-rich phases we expect stability of the periodic phase where lipid bilayers are separated by water layers. In the lipid-rich phase the lipids are oriented head-to-head and tail-to-tail when $g > 0$. The values of H_{am} per lattice site, $h = H_{am}/L$, in these phases are

$$h/b = \begin{cases} -1-\bar{\mu}_1 & \text{water} \\ -\frac{l-1+\bar{\mu}_1 l+2c+g(2n-1)}{l+2n} & \text{periodic} \\ -g & \text{lipid.} \end{cases} \tag{2.45}$$

In the periodic phase l water occupied sites are followed by $2n$ sites occupied by properly oriented lipid molecules. The coexistence lines obtained by equating h/b in these phases are

$$\bar{\mu}_1 = \begin{cases} g-1 & \text{water-lipid} \\ \frac{2c+g-3}{2} & \text{water-periodic} \\ 2(g-c) & \text{periodic-lipid.} \end{cases} \tag{2.46}$$

The three phases coexist along the triple line $g = 2c-1$ and $\bar{\mu}_1 = 2(c-1)$.
Note that for the periodic phase we can write Eq.(2.45) in two equivalent forms,

$$h/b = \begin{cases} -(1+\bar{\mu}_1) + \frac{2n(\bar{\mu}_1+1-g)+1-2c+g}{l+2n} \\ -g + \frac{l(g-1+\bar{\mu}_1)+g-2c+1}{l+2n}. \end{cases} \tag{2.47}$$

In the stability region of the periodic phase h/b in this phase is smaller than in the other two phases, therefore the second terms in both expressions in (2.47) must be negative. From the top line in (2.47) it follows that the lowest value of h/b is assumed for $l = 1$, and from the bottom line it follows that $n = 1$ in the stable structure. However, at the coexistence with the water phase the numerator in the second term in the top line in (2.47) vanishes. Since the periodic phase must be more stable than the pure lipid phase and therefore $n = 1$ (see the second line in (2.47)), we obtain that at the water-periodic phase coexistence the separation l between the lipid bilayers can be arbitrary. Thus, the ground state is strongly degenerated.

Similar degeneracy occurs at the periodic-lipid phase coexistence. In this case $l = 1$ (the periodic phase is more stable than water). At the periodic-lipid coexistence the nominator in the second term in the bottom line in (2.47) vanishes, therefore the separation $2n$ between the water occupied sites is arbitrary.

The (c, g, μ) ground state is shown in Fig. 2.26. The water-amphiphile coexistence occurs for small values of c. When $g \leq 2c - 1$ the periodic structure of solvent-separated bilayers may be present for some range of μ and the sequence of the stable phases for increasing μ at fixed c and g is: amphiphiles-bilayers-solvent.

Note that the arbitrary separation between the bilayers can be interpreted as the sponge or the disordered lamellar phase. On the other hand, the arbitrary separation between the bilayers is possible only at the coexistence between the water and the periodic phase, and can be interpreted as an arbitrary number of coexisting droplets of the two phases, which in addition can have an arbitrary size. This in turn signals vanishing surface tension between the periodic and the water phases. Precisely the same properties, namely the coexisting droplets of the periodic and the lipid phases, and the associated vanishing surface tension, are found at the coexistence between the periodic and the lipid phases.

Thus, the ground state is strongly degenerate and the entropy per site does not vanish, at these periodic-lipid phase coexistences.

Similar degeneracy of the ground state was found earlier for the lattice model of microemulsion [67]. The very low surface tension at the coexistence between the microemulsion and the water-rich phases was attributed to the amphiphilic nature of lipid molecules.

2.1.2.3 Mean-field stability analysis

The grand thermodynamic potential in the MF approximation takes the form

$$\beta\Omega^{am}_{MF} = \frac{1}{2}\sum_{x}\sum_{x'}\rho_i(x)\beta V_{ij}(x,x')\rho_j(x') - \mu^*\sum_{x}\rho_1(x) + \sum_{x}\sum_{n=1}^{3}\rho_n(x)\ln\rho_n(x) \tag{2.48}$$

where the indices in the first term are $i, j = 2, 3$ and summation convention is used for this term, $\rho_1(x) = 1 - \rho_2(x) - \rho_3(x)$, V_{ij} is defined in Eq.(2.44), $\mu^* = \beta\bar{\mu}_1$, and in thermal equilibrium the densities correspond to the minimum of Ω^{am}_{MF}, i.e. $\delta\Omega^{am}_{MF}/\delta\rho_i(x) = 0$ for $i = 2, 3$. The last term in (2.48) is the entropy contribution.

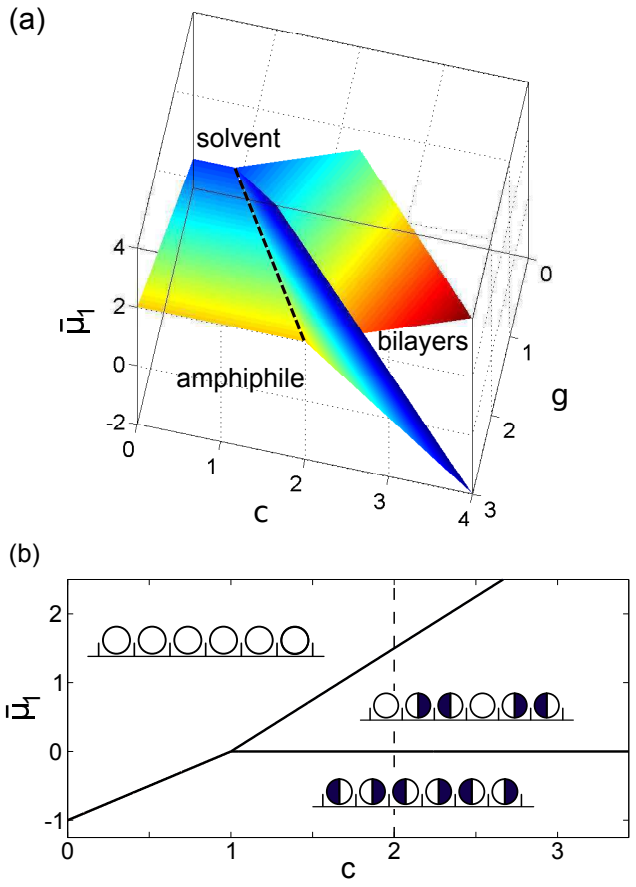

FIG. 2.26: The ground state of the model in the variables $(c, g, \bar{\mu}_1)$ (panel (a)) and in the plane $(c, \bar{\mu}_1)$ for $c = g$ (panel (b)). The surfaces in panel (a) represent coexistence between the phases, while the black dashed line represents the triple points where all the three phases coexist. The triple point for $g = c$ is at $(c, \bar{\mu}_1) = (1, 0)$. On the (b) panel a schematic illustration of the three phases is shown in the insets inside the region of stability of each phase. At the coexistence with the solvent-rich phase the layers of solvent, l, can have an arbitrary length, and at the coexistence with the amphiphile-rich phase the layers of amphiphilic molecules can have the thickness $2n$ with arbitrary n. The dashed line corresponds to $c = g = 2$ for which the EOS, the correlation function and the specific heat are calculated in the following sections.

In this section we shall determine the stability of the disordered phase with respect to concentration waves with the wavenumber $0 \leq k \leq \pi$. Macroscopic separation of water- and lipid-rich phases corresponds to $k = 0$. In the crystalline lipid phase the particles are oriented head-to-head and tail-to-tail. This phase corresponds to the concentration wave with $k = \pi$, i.e. the period Φ is $2\pi/k = 2$. There are two sublattices in this phase. The sites of the first one are numbered with even x, and of the second one with odd x. $\rho_2(x) - \bar{\rho}_2 > 0$ for x belonging to one of the sublattices, whereas $\rho_3(x) - \bar{\rho}_3 > 0$ on the sites of the other sublattice, where $2\bar{\rho}_2 = 2\bar{\rho}_3 = \rho$ is

the space-averaged density of lipids. For $0 < k < \pi$ the fluctuating bilayers of lipids oriented tail-to-tail are separated by layers of water. At the instability with respect to the k-mode

$$\det \tilde{\mathbf{C}}(k) = 0, \tag{2.49}$$

where

$$\tilde{C}_{ij}(k) = \frac{\delta^2 \beta \Omega^{am}_{MF}}{\delta\tilde{\rho}_i(k)\delta\tilde{\rho}_j(-k)}, \tag{2.50}$$

for $i, j = 2, 3$ and $\tilde{\rho}_j(k) = \sum_x \rho_j(x)\exp(ikx)$, with similar convention (tilde) for the Fourier transforms of the remaining functions. From (2.48) and (2.44) we obtain

$$\tilde{C}_{ij}(k) = \beta\tilde{V}_{ij}(k) + f_{ij}, \tag{2.51}$$

where

$$\tilde{V}_{ii}(k) = 2\beta^*(g-1)\cos k, \tag{2.52}$$

$$\tilde{V}_{23}(k) = \tilde{V}_{32}(k) = -2\beta^*\Big[(1+g)\cos k + 2ic\sin k\Big], \tag{2.53}$$

and

$$f_{ij} = \Big(\frac{2}{\rho} + \frac{1}{1-\rho}\Big)\delta^{Kr}_{ij} + \Big(\frac{1}{1-\rho}\Big)(1-\delta^{Kr}_{ij}). \tag{2.54}$$

From (2.49) we obtain the explicit expression for the reduced temperature T^* at the instability with respect to the density wave with the wavenumber k for given ρ

$$T^*(\rho, k) = -\rho\Big[P\cos k \mp \sqrt{4c^2(1-\rho) - Q\cos^2 k}\Big], \tag{2.55}$$

where

$$P(g, \rho) = g - 1 + \rho, \tag{2.56}$$

$$Q(c, g, \rho) = 4(1-\rho)(c^2 - g) - P^2(g, \rho). \tag{2.57}$$

At the domain boundaries, i.e. for $\cos k = \pm 1$ we obtain

$$T^*(\rho, k) = \begin{cases} 2\rho(1-\rho) & \text{for } k = 0 \\ 2g\rho & \text{for } k = \pi. \end{cases} \tag{2.58}$$

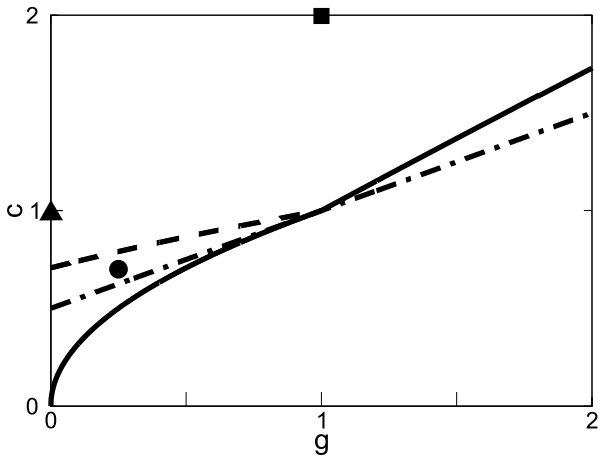

FIG. 2.27: The plane of the interaction parameters in units of the water-water interaction (see (2.42)) with indicated regions corresponding to different types of ordering. Above the solid line the disordered phase can become unstable with respect to oscillatory density with the period $\Phi = 2\pi/k_b \neq 2$ for some range of densities $\rho_{min} < \rho < \rho_{max}$ (formation of the amphiphilic bilayers). Above the dashed line the instability with respect to periodic ordering occurs for $0 < \rho < \rho_{max}$. Below the dashed line the separation into water-rich and lipid phases occurs for $\rho < \rho_{min}$. The dash-dotted line is the projection of the three-phase line at $T = 0$ on the (c, g) plane. For the points marked by triangle $(1, 0)$, square $(2, 1)$ and circle $(c, g) = (0.7, 0.25)$ the MF instability lines $T^*(\rho, k_b)$ and the period of density oscillations along the line are presented at Figs. 2.28, 2.29 and 2.30 respectively.

For given ρ the boundary of stability of the disordered phase corresponds to $T^*(\rho, k_b)$ such that $T^*(\rho, k)$ assumes a maximum for $k = k_b$. From the necessary condition $\partial T^*(\rho, k)/\partial k = 0$ we obtain

$$\cos^2 k_b = R, \qquad R = \frac{c^2 P^2(g, \rho)}{(c^2 - g) Q(c, g, \rho)}. \tag{2.59}$$

The corresponding temperature is

$$T^*(\rho, k_b) = 4c\rho(1-\rho)\sqrt{\frac{(c^2 - g)}{Q(c, g, \rho)}}. \tag{2.60}$$

The boundary of stability of the disordered phase for given density corresponds to $\max(T^*(\rho, 0), T^*(\rho, \pi), T^*(\rho, k_b))$. The instability with respect to $k_b \neq 0, \pi$ can occur provided that $0 \leq R \leq 1$. The R (see Eq.(2.59)) is a positive number less than 1 for $\rho \in (\rho_{min}, \rho_{max})$, where the boundaries depend on the strengths c, g of the interactions. For $1 > \rho > \rho_{max}$ and for $0 < \rho < \rho_{min}$ the instability with respect to the k_b mode does not occur. For $0 < \rho < \rho_{min}$ the instability of the disordered phase is given by $T^*(\rho, 0)$, and for $1 > \rho > \rho_{max}$ by $T^*(\rho, \pi)$. The boundaries of

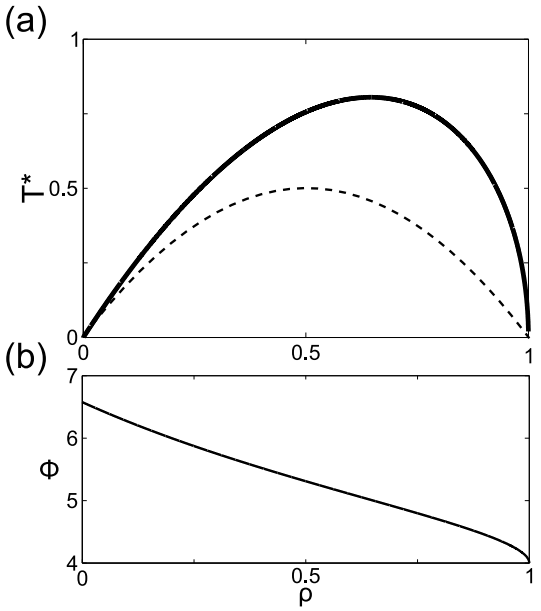

FIG. 2.28: Panel (a): The $T^*(\rho, k_b)$ (solid), $T^*(\rho, 0)$ (short-dash) lines of MF instability with respect to formation of the lamellar phase (Eq.(2.60)) and water-lipid phase separation (Eq.(2.58)). The actual instability of the disordered phase is indicated by the thick line. Panel (b): The period Φ of the density oscillations along the line of instability $T^*(\rho, k_b)$ as a function of the density of lipids. On both panels $(c, g) = (1, 0)$.

the interval (ρ_{min}, ρ_{max}) are found to be

$$\rho_{min} = \begin{cases} 1 - \frac{g^2}{2c^2 - g} & \text{if } c^2 < g < 2c^2 \\ 1 - 2c^2 + g & \text{if } g < c^2 \text{ or } g > 2c^2 \end{cases} \tag{2.61}$$

and

$$\rho_{max} = \begin{cases} 1 - 2c^2 + g & \text{if } c^2 < g < 2c^2 \\ 1 - \frac{g^2}{2c^2 - g} & \text{if } g < c^2 \text{ or } g > 2c^2. \end{cases} \tag{2.62}$$

We have found that $T^*(\rho, k_b) > T^*(\rho, 0), T^*(\rho, \pi)$ for $\rho_{min} < \rho < \rho_{max}$ and $0 < k_b < \pi$ when $c^2 > g$ and $2c^2 > g + g^2$.

The density interval (ρ_{min}, ρ_{max}) with the above properties does not exist for g, c located below the solid line in Fig. 2.27. For such parameters the instability is with respect to water-lipid phase separation or with respect to ordering of lipids into a stack of oppositely oriented bilayers.

Figs. 2.28(a), 2.29(a) and 2.30(a) show the lines of instability for the parameters from different regions in Fig. 2.27, whereas Fig. 2.28(b), 2.29(b) and 2.30(b) show

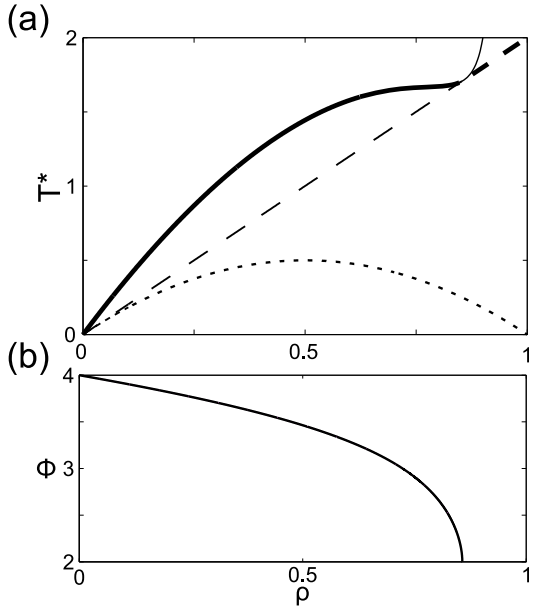

FIG. 2.29: Panel (a): The $T^*(\rho, k_b)$ (solid), $T^*(\rho, \pi)$ (long-dashed) and $T^*(\rho, 0)$ (short-dash) lines of MF instability with respect to formation of the lamellar phase (Eq.(2.60)), crystallization of lipids, and water-lipid phase separation (Eq.(2.58)) respectively. The actual instability of the disordered phase is indicated by the thick line. Panel (b): The period Φ of the density oscillations along the line of instability $T^*(\rho, k_b)$ as a function of the density of lipids. On both panels $(c, g) = (2, 1)$.

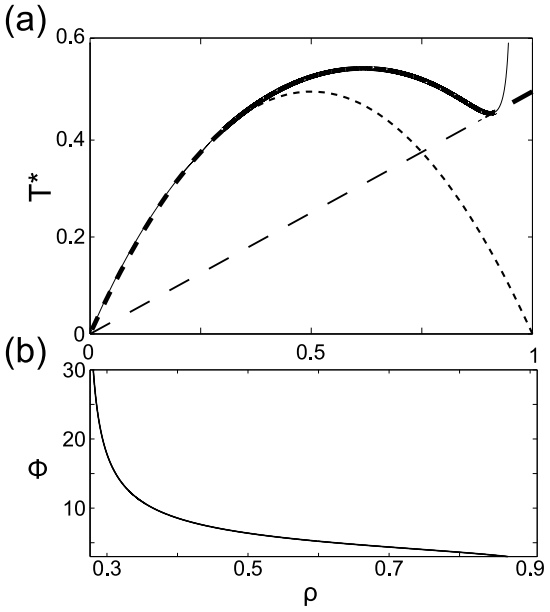

FIG. 2.30: Panel (a): The $T^*(\rho, k_b)$ (solid), $T^*(\rho, \pi)$ (long-dashed) and $T^*(\rho, 0)$ (short-dash) lines of MF instability with respect to formation of the lamellar phase (Eq.(2.60)), crystallization of lipids, and water-lipid phase separation (Eq.(2.58)) respectively. The actual instability of the disordered phase is indicated by the thick line. Panel (b): The period Φ of the density oscillations along the line of instability $T^*(\rho, k_b)$ as a function of the density of lipids. On both panels $(c, g) = (0.7, 0.25)$.

corresponding periods of density oscillations.

2.1.2.4 Exact solution

In this section we introduce the transfer matrix and develop exact expressions for the grand thermodynamic potential, the average density of each component and for the correlation function. In the first paragraph the expressions are derived, whereas in further paragraphs the exact results are analyzed.

Exact expressions

The elements of the transfer matrix **T** are given by

$$\mathbf{T}_{ij} \equiv \exp\left\{-\beta^*\left(V_{ij} - \mu\delta_{i1}^{Kr}\right)\right\}, \tag{2.63}$$

The partition function for a system with periodic boundary conditions is

$$\Xi_{am} = \sum_{\hat{\rho}(1)} \cdots \sum_{\hat{\rho}(L)} \prod_{n=1}^{L} \exp\left\{-\beta^*\left[\hat{\rho}^T(n)\mathbf{V}\hat{\rho}(n+1) - \mu\hat{\rho}_1(n)\right]\right\}. \tag{2.64}$$

where **V** is given by Eq. 2.42, $\hat{\rho}(x)^T = (\hat{\rho}_1(x), \hat{\rho}_2(x), \hat{\rho}_3(x))$ denotes the microscopic state at the site x, and is transverse to the columnar vector $\hat{\rho}(x)$. At each lattice site there can be one of the 3 microscopic states $(1,0,0)$, $(0,1,0)$, or $(0,0,1)$. In terms of the transfer matrix Ξ_{am} takes the form

$$\Xi_{am} = Tr\mathbf{T}^L = \lambda_1^L + \lambda_2^L + \lambda_3^L, \tag{2.65}$$

where λ_i is the eigenvalue of the transfer matrix. If we denote $\lambda_1 = max_{i\in\{1,2,3\}}(|\lambda_i|)$, the partition function for the system size $L \gg 1$ takes the even simpler asymptotic form

$$\Xi_{am} \simeq \lambda_1^L. \tag{2.66}$$

In the thermodynamic limit the grand potential in b units, $\Omega_{am}^* = \Omega_{am}/b$, is given by the exact formula

$$\lim_{L\to\infty} \Omega_{am}^*/L = -p^* = -T^* \lim_{L\to\infty} \frac{\ln \Xi_{am}}{L} = -T^* \ln \lambda_1, \tag{2.67}$$

where p^* is 1d pressure in b/a units.

The average density of the i-th state is independent of x because of the translational invariance, and is given by

$$\langle\hat{\rho}_i(1)\rangle = \frac{1}{\Xi_{am}}\sum_{\hat{\rho}(1)}\cdots\sum_{\hat{\rho}(L)}\prod_{n=1}^{L}\hat{\rho}_i(1)\exp\left\{-\beta^*\left[\hat{\rho}^T(n)\mathbf{V}\hat{\rho}(n+1)-\mu\hat{\rho}_1(n)\right]\right\}. \quad (2.68)$$

If we change the basis of $\mathbf{T}$ with a help of the invertible matrix $\mathbf{P}$ such that $\mathbf{P}^{-1}\mathbf{T}\mathbf{P}$ is diagonal, then the average density in thermodynamic limit is given by the following expression:

$$\langle\hat{\rho}_i\rangle = \langle\hat{\rho}_i(1)\rangle = \lim_{L\to\infty}\frac{1}{\Xi_{am}}\mathbf{P}^{-1}_{1i}\lambda_1^L\mathbf{P}_{i1} = \mathbf{P}^{-1}_{1i}\mathbf{P}_{i1}. \quad (2.69)$$

The correlation function $G_{ii}(n)$ between two sites in the same state i separated by n sites is given by

$$G_{ii}(n) = \langle\hat{\rho}_i(1)\hat{\rho}_i(n+1)\rangle - \langle\hat{\rho}_i(1)\rangle\langle\hat{\rho}_i(n+1)\rangle, \quad (2.70)$$

where

$$\langle\hat{\rho}_i(1)\hat{\rho}_i(n+1)\rangle = \frac{1}{\Xi_{am}}\mathbf{T}^n[\hat{\rho}_i(1),\hat{\rho}_i(n+1)]\mathbf{T}^{L-n}[\hat{\rho}_i(n+1)\hat{\rho}_i(1)]. \quad (2.71)$$

We change the basis to the one in which $\mathbf{T}$ is diagonal, take the thermodynamic limit and obtain the exact formula,

$$\begin{aligned} <\hat{\rho}_i(1)\hat{\rho}_i(n+1)> &= \sum_{k=1}^{3}\Big(\frac{\lambda_k}{\lambda_1}\Big)^n\mathbf{P}_{ik}\mathbf{P}^{-1}{}_{ki}\mathbf{P}_{i1}\mathbf{P}^{-1}_{1i} \\ &= <\hat{\rho}_i>^2 + \sum_{k=2}^{3}\Big(\frac{\lambda_k}{\lambda_1}\Big)^n A_i^{(k)}B_i^{(k)}, \end{aligned} \quad (2.72)$$

where

$$A_i^{(k)} = \mathbf{P}_{ik}\mathbf{P}^{-1}_{1i}, \quad B_i^{(k)} = \mathbf{P}^{-1}_{ki}\mathbf{P}_{i1} \quad (2.73)$$

From (2.70) and (2.72) we obtain the correlation function

$$G_{ii}(n) = \sum_{k=2}^{3}\Big(\frac{\lambda_k}{\lambda_1}\Big)^n A_i^{(k)}B_i^{(k)}. \quad (2.74)$$

Eq. (2.74) can be further simplified for $n \gg 1$. In such a case we can neglect the smallest components of the sum in Eq.(2.74). If the second largest (in absolute

value) eigenvalue λ_2 is a pure real number, then $G_{ii}(n) = \left(\frac{\lambda_2}{\lambda_1}\right)^n A_i^{(2)} B_i^{(2)}$, but if the λ_2 has a non-zero imaginary part, then we have to take into account also the eigenvalue λ_3, complex conjugate to λ_2. Let us introduce the notations

$$\lambda_2 = Z_\lambda e^{\lambda i} \qquad A_1^{(2)} = Z_\alpha e^{\alpha i} \qquad B_1^{(2)} = Z_\gamma e^{\gamma i} \tag{2.75}$$

and

$$\xi_{am} = \Big[\ln\Big(\frac{\lambda_1}{Z_\lambda}\Big)\Big]^{-1}. \tag{2.76}$$

In terms of these parameters the correlation function for large separations between the particles in an infinite system takes the asymptotic form

$$G_{11}(n) \overset{n\gg 1}{\simeq} 2Z_\alpha Z_\gamma e^{-n/\xi_{am}} \cos\Big(n\lambda + \alpha + \gamma\Big). \tag{2.77}$$

Equation of state

We choose stronger interactions between the amphiphilic than between the solvent molecules, $c = g = 2$. For such interaction parameters the periodic phase is present on the ground state (GS) (see the dashed line in Fig. 2.26b). In Fig.2.31 we show the concentration ρ_s (average density of the amphiphile) as a function of the reduced chemical potential difference μ. Note the rounded steps for $\mu \approx 0$ and $\mu \approx 1.5$. The steps occur for the values of μ corresponding to the GS phase transitions between the periodic and the amphiphile-rich or solvent-rich phases respectively. Between the steps the plateaus for the three densities, $\rho_s = 1, 2/3, 0$ occur. For increasing T^* the $\rho_s(\mu)$ lines become smoother, but the inflection points exist up to $T^* \approx 0.2$.

In Eqs.(2.67) and (2.69) the pressure and the average density are expressed in terms of T^* and the reduced chemical potential difference μ. By eliminating μ we can obtain the dependence of the amphiphile density on p^*. We present $\rho_s(p^*)$ in Fig.2.32. Note that although there are no phase transitions in the strict sense in 1d, for low T^* there is a rapid change in ρ_s between $\rho_s = 1$ and $\rho_s = 2/3$ for a very small p^* interval near $p^* \approx 2$, almost constant amphiphile density between $p^* \approx 2$ and $p^* \approx 2.5$, and again a rapid change of ρ_s between $2/3$ and nearly 0 for $p^* \approx 2.5$. This behavior suggests the pseudo-phase transitions between the amphiphile-rich and the periodic

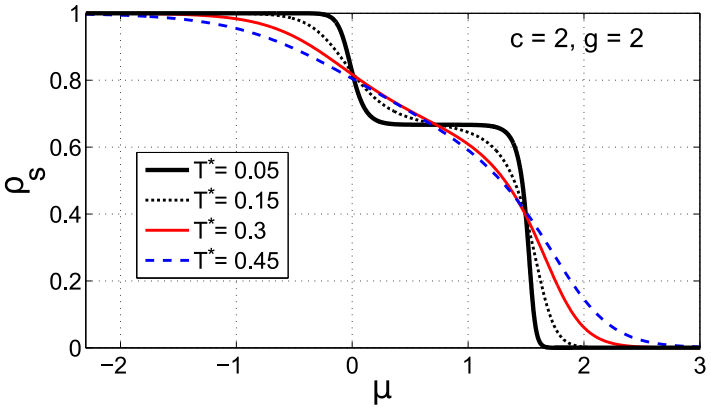

FIG. 2.31: Average density of the amphiphile, $\rho_s = 1-\rho_1 = \rho_2+\rho_3$, for $c = g = 2$ at $T^* = 0.05, 0.15, 0.3, 0.45$ as a function of the reduced chemical potential difference μ.

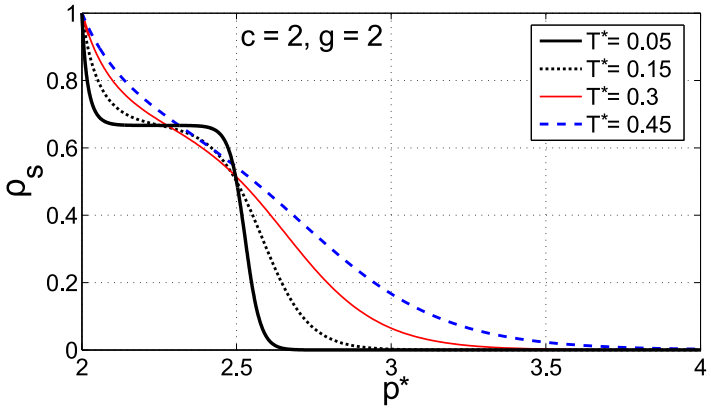

FIG. 2.32: Average density of the amphiphile as a function of pressure $p*$, $\rho_s = 1-\rho_1 = \rho_2+\rho_3$, for $c = g = 2$ at $T^* = 0.05, 0.15, 0.3, 0.45$. As the energy unit we choose the interaction b between the two solvent molecules, and the length unit is the lattice constant a. We assume that a is of order of the size of the amphiphilic molecules. In the case of lipids $a \sim 2nm$.

pseudo-phase with the density $\rho_s \approx 2/3$ (see Fig.2.26b) and next between the periodic pseudo-phase and the solvent-rich pseudo-phase. For increasing temperature the changes of the slope of the $\rho_s(p^*)$ line for increasing p^* become smaller. This result should be contrasted with the pressure-concentration dependence shown in Fig.2.33 for the interaction parameters such that the periodic phase is not stable at the GS.

Correlation function

In the case of the periodic boundary conditions the system is translationally invariant, and the assembly into bilayers should be reflected in the shape of the correlation function. When the bilayers are formed, then the correlation function for

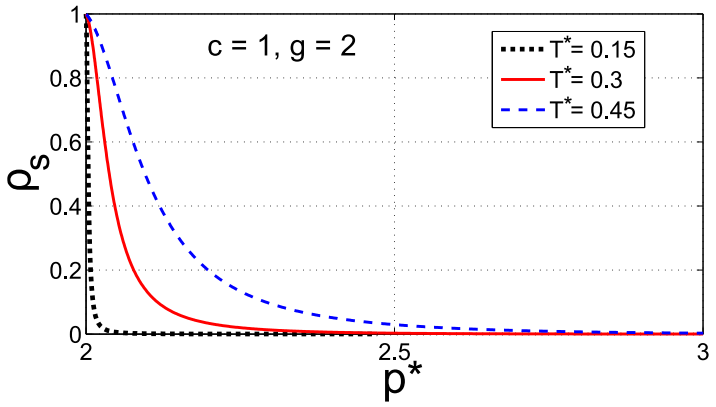

FIG. 2.33: Average density of the amphiphile, $\rho_s = 1 - \rho_1 = \rho_2 + \rho_3$, for $c = 1$ $g = 2$ and $T^* = 0.15, 0.3, 0.45$. As the energy unit we choose the interaction b between the two solvent molecules, and the length unit is the lattice constant a. We assume that a is of order of the size of the amphiphilic molecules. In the case of lipids $a \sim 2nm$.

the solvent, $G_{11}(x)$ should be negative for two subsequent values of x, where the properly oriented amphiphilic molecules should appear with larger probability than the solvent molecule. The exact results for $G_{11}(x)$, given in Eq.(2.74), are shown in Fig.2.34 for $\mu = 1$, i.e. for the GS stability of the periodic phase, for a few rather high temperatures. We can see the oscillatory decay of correlations, with the period 3 as in the case of the concentration in the GS periodic phase. The decay length decreases with increasing temperature. Only for short distances $G_{11}(x) < 0$ for two subsequent values of x, however.

In Figs.2.35 and 2.36 we show $G_{11}(x)$ for very low T^* and a few values of μ close to the GS coexistence between the periodic and the solvent- or amphiphile-rich phases. Very large correlation length, 3 orders of magnitude larger than the molecular size, can be seen inside the GS stability of the periodic phase.

The correlation length ξ_{am} (see Eq. 2.76) and the period of the damped oscillatory decay (see Eq. 2.77) are shown in Fig.2.37. We can see that $\xi_{am} \to 0$ beyond the GS stability of the periodic phase, i.e. for $\mu < 0$ and $\mu > 1.5$. Moreover, for $0 < \mu < 1.5$ the period of the damped oscillations is $2\pi/\lambda \approx 3$.

Let us focus on the structure for the interaction parameters corresponding to the absence of the periodically distributed bilayers in the GS. We choose $c = 0.623$ and $g = 0.25$. The correlation length ξ_{am} and the period $2\pi/\lambda$ of the damped oscillatory decay for $c = 0.623$ and $g = 0.25$, and different temperatures are shown in Fig.2.38. For $T^* \leq 0.2$ the eigenvalue λ_2 is a pure real number for any value of the chemical

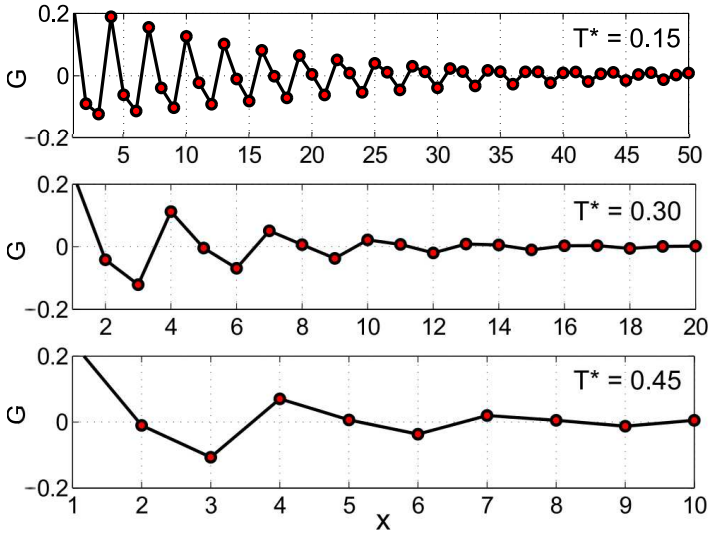

FIG. 2.34: Correlation function between the solvent molecules at $T^* = 0.15, 0.3, 0.45$ for $g = c = 2$ and $\mu = 1$.

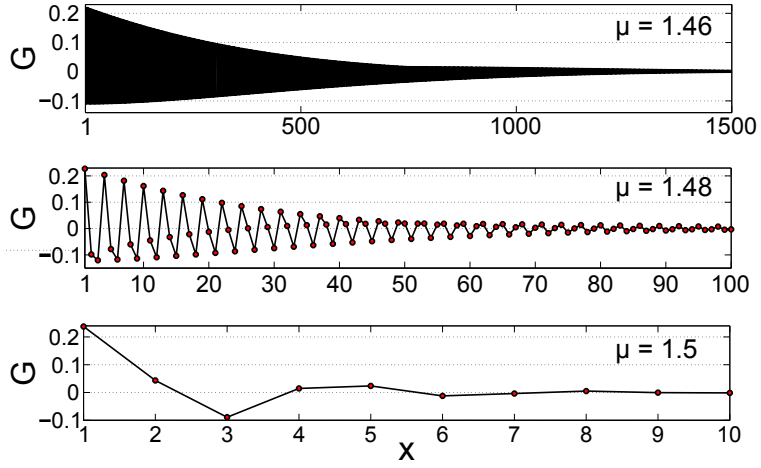

FIG. 2.35: Correlation function between the solvent molecules at $T^* = 0.005$ for $g = c = 2$ and $\mu = 1.46$ (a), $\mu = 1.48$ (b), $\mu = 1.5$ (c), with $\mu = 1.5$ being the value of the chemical potential at the coexistence between the periodic and the solvent-rich phases at the GS.

potential, and the correlation function decays monotonically. The change of the ξ_{am} slope around $\mu = -0.39$ at $T^* = 0.2$ indicates the point where λ_2 changes sign. The period of the oscillatory decay jumps from zero to infinity at this point. Both cases correspond to the monotonic decay of correlations, but at this point ($\mu = -0.39$ and $T^* = 0.2$) an oscillatory decay for $T^* > 0.2$ and a range of μ around $\mu = -0.39$ begins. This is because for $T^* > 0.2$ there are two discontinuities of the derivative of ξ_{am} (e.g. at μ_1 and μ_2 for $T^* = 0.3$). Between the two points of discontinuity of $\partial\xi_{am}/\partial\mu$, the λ_2 is a complex number, and hence for this interval of μ the correlation function has an oscillatory decay. Note that for $c = 0.623, g = 0.25$ the periodic

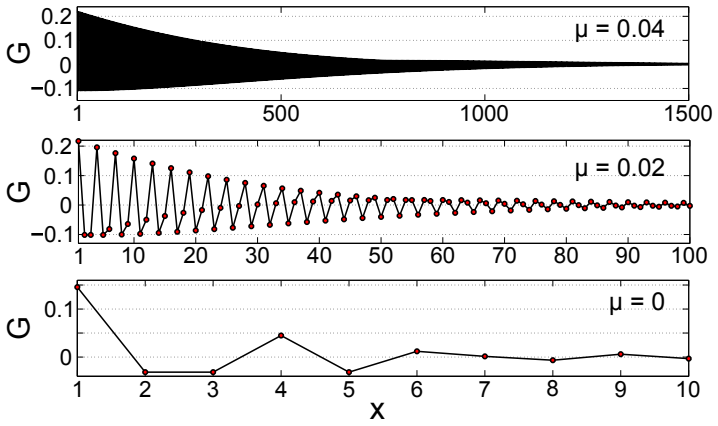

FIG. 2.36: Correlation function between the solvent molecules at $T^* = 0.005$ for $g = c = 2$ and $\mu = 0.04$ (a), $\mu = 0.02$ (b), $\mu = 0$ (c), with $\mu = 0$ being the value of the chemical potential at the coexistence between the periodic and the amphiphile-rich phases at the GS.

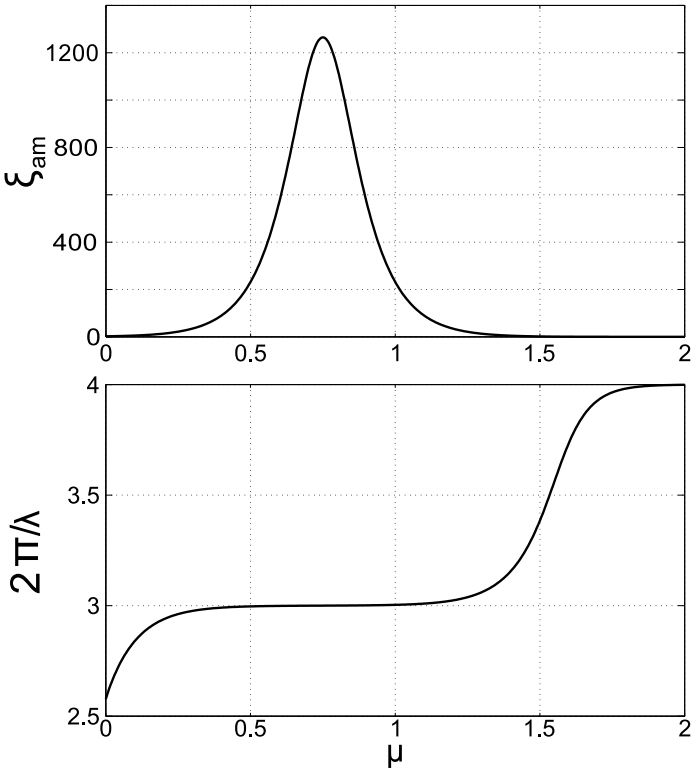

FIG. 2.37: The correlation length ξ_{am} and the period of the oscillatory decay of correlations (Eqs.(2.76) and (2.77)) for $g = c = 2$ and $T = 0.1$. For $\mu = 0$ and $\mu = 1.5$ the periodic phase coexists with the amphiphile and the solvent respectively at $T^* = 0$.

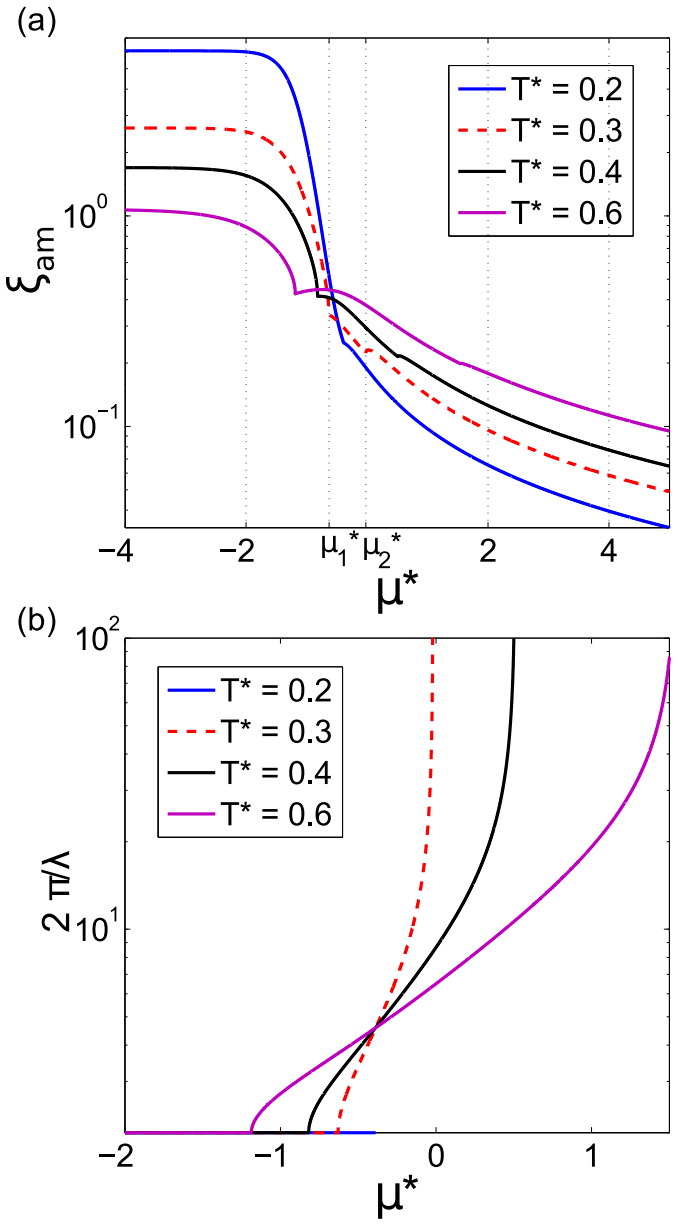

FIG. 2.38: The correlation length ξ_{am} and the period of the oscillatory decay of correlations for $c = 0.623, g = 0.25$ at $T^* = 0.2, 0.3, 0.4, 0.6$. For $\mu = -0.75$ the amphiphile and the solvent coexist at $T^* = 0$. For $T^* < 0.2$ the monotonic decay of correlations between the solvent molecules is obtained. At $T^* = 0.2$ the period of the oscillatory decay jumps from zero to infinity for $\mu \approx -0.39$. For $T^* > 0.2$ the correlation function for the solvent exhibits an oscillatory decay for some range of μ. In the case of $T^* = 0.3$ the oscillatory decay occurs for $\mu_1 < \mu < \mu_2$. Note the logarithmic scale on the vertical axis.

phase is not stable on the GS, and counterintuitively the oscillatory decay of $G_{11}(x)$ occurs at higher T^*. However, the correlation length is smaller than the period of the damped oscillations.

Specific heat

In this section we consider the specific heat for a fixed concentration. Fixed concentration imposes a global constraint on the microstates, therefore exact analytical calculations directly in the Canonical Ensemble are more difficult. To overcome this difficulty, we first calculate the specific heat for fixed chemical potential and then by using thermodynamic relations between the ensembles we compute the specific heat for fixed concentration. For verification we perform Canonical Ensemble Monte Carlo simulations.

The specific heat of a mixture with fixed number of all particles and fixed chemical potential difference between the components, μ, is given by

$$c_\mu = -\frac{T}{L}\left(\frac{\partial^2 \Omega^*_{am}}{\partial T^2}\right)_{\mu,V}, \tag{2.78}$$

where the exact expression for Ω^*_{am} is given in Eq. 2.67. We compute c_v using the following relations,

$$c_v = c_\mu - T\left(\frac{\partial \rho_\mu}{\partial T}\right)^2 \left(\frac{\partial \rho_\mu}{\partial \mu}\right)^{-1} \tag{2.79}$$

and

$$\rho_\mu(T,\mu) = -\frac{1}{L}\left(\frac{\partial \Omega^*_{am}}{\partial \mu}\right)_{T,V}. \tag{2.80}$$

In order to verify the exact calculations based on the Grand Canonical Ensemble, we performed MC simulations in the Canonical Ensemble with the sampling procedure based on the Metropolis algorithm [35]. The sampling is made with two kinds of MC steps: (i) the exchange of lipid and water molecules positions (ii) the change of lipid molecule orientation. The specific heat per lattice site is computed using the fluctuation formula:

$$c_v = \frac{1}{Lk_B T^2}\left[\langle U^2_{am}\rangle - \langle U_{am}\rangle^2\right], \tag{2.81}$$

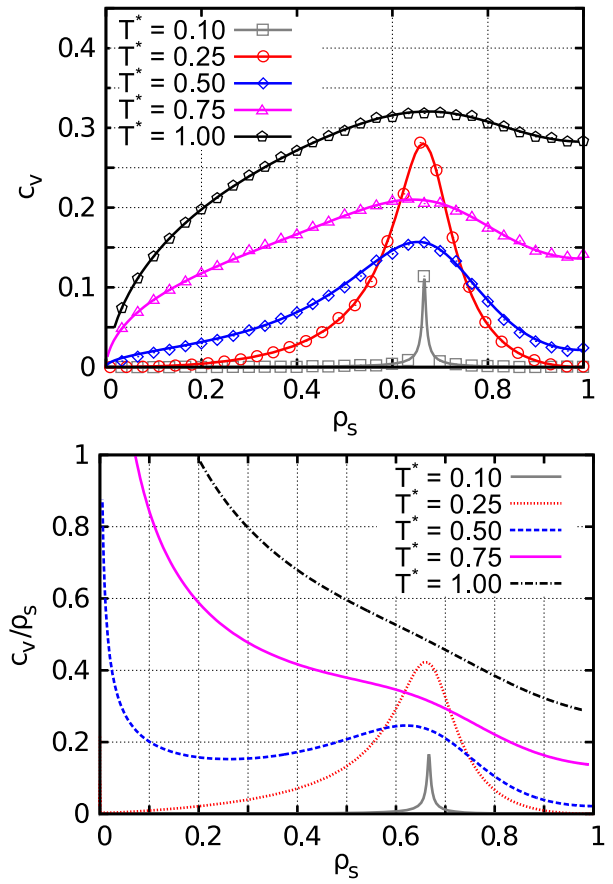

FIG. 2.39: The specific heat for fixed concentration ρ_s as a function of ρ_s for $c = g = 2$ and different temperatures. Top: per unit volume (c_v). Bottom: per amphiphilic molecule (c_v/ρ_s). Symbols denote the results of the Monte Carlo simulations for $L = 4800$, and lines represent the analytical results in thermodynamic limit (Eqs. (2.78)- (2.61) and (2.67)).

where $\langle\cdot\rangle$ is the average over the microstates in the Canonical Ensemble and U_{am} is the Canonical Hamiltonian

$$U_{am}[\{\hat{\rho}_i\}]/b = \frac{1}{2}\sum_{x=1}^{L}\sum_{x'=1}^{L}\hat{\rho}_i(x)V_{ij}(x,x')\hat{\rho}_j(x'), \tag{2.82}$$

where the Einstein summation convention for repeated indices is used. The simulations were performed for $L \leq 4800$. We verified that the finite size effects are negligible for $L = 4800$ (see Fig.2.39a).

The results of the specific heat calculations are presented in Fig.2.39. The specific heat assumes a maximum for the density or concentration corresponding to the GS periodic phase. In addition, the specific heat per amphiphilic molecule increases for decreasing number of amphiphilic molecules. This behavior is associated with the equilibrium between the bilayers (or micelles) and isolated amphiphiles.

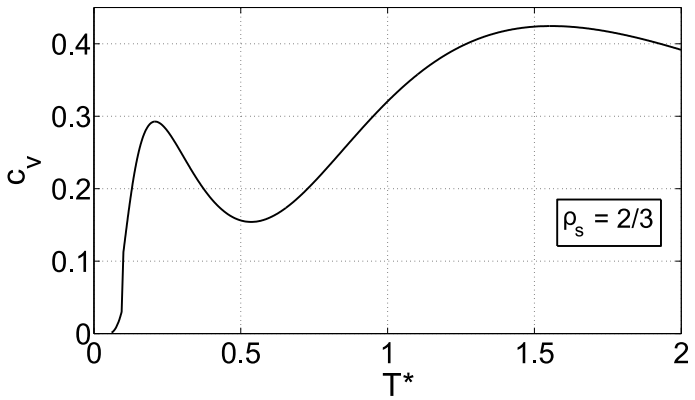

FIG. 2.40: The specific heat for fixed concentration ρ_s as a function of temperature for $c = g = 2$.

From Figs.2.40 and 2.41 it follows that the dependence of c_v on T for fixed ρ_s is nontrivial, and differs qualitatively from $c_v(T)$ in the lattice gas or Ising model. In the latter models a single maximum of $c_v(T)$ occurs, whereas in this model two maxima separated by a minimum are present. The simulation snapshots indicate formation of solvent-separated bilayers at low T^* for $\rho_s \leq 1/3$. Between the two maxima of $c_v(T)$ the amphiphiles, oriented head-to-head or tail-to-tail, form larger domains separated by domains of solvent. At the second maximum random positions and orientations of the amphiphiles appear. The two maxima of $c_v(T)$ are present even for c, g such that only the pure solvent and pure amphiphiles are present at the GS. In such a case phase-separated solvent and amphiphiles, or random positions and orientations are present for low T^* or for high T^* respectively, whereas between the two maxima of $c_v(T)$ domains of solvent and properly oriented amphiphiles are formed.

2.1.2.5 Summary

We have developed a simple lattice model for water-lipid mixtures. The ground-state and the MF stability analysis as well as the exact results show that the model predicts the key properties of aqueous solutions of amphiphilic molecules. It also helps to understand the relation between the low surface tension and the degeneracy of the ground state. The main results are:

- The ground state ($T^* = 0$) shows a sequence of phases: lipid - periodic - water for increasing μ^* when the attraction between the water and properly

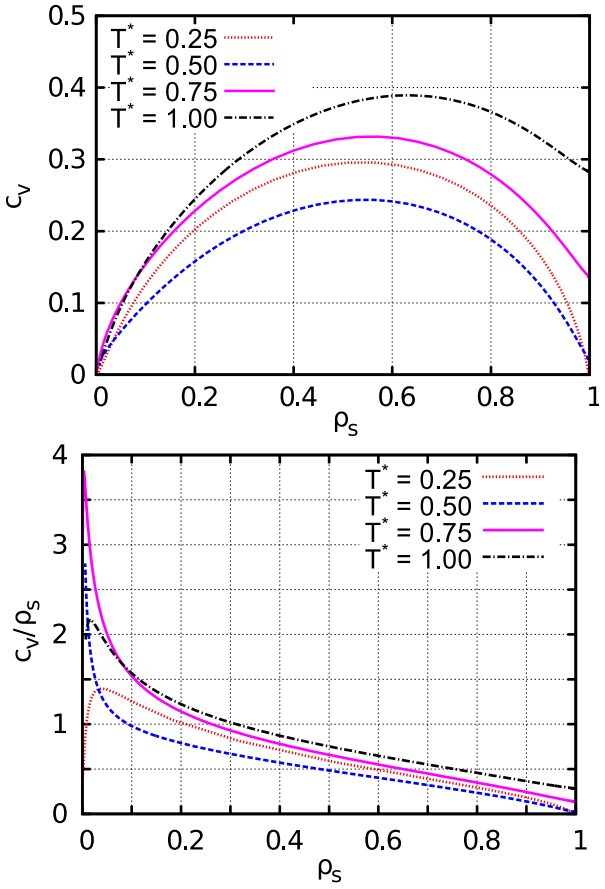

FIG. 2.41: The specific heat for fixed concentration ρ_s as a function of ρ_s for $c = 1$ and $g = 2$ and different temperatures. Top: per unit volume (c_v). Bottom: per amphiphilic molecule (c_v/ρ_s). Lines represent the analytical results in thermodynamic limit (Eqs. (2.78)- (2.61) and (2.67)).

oriented amphiphilic molecules is sufficiently strong, otherwise only lipid and water phases are stable (Fig. 2.26).

- System consisting only of amphiphiles self-assemble into a lamellar structure with periodic order.
- The equation of state exhibits significant slope changes for thermodynamic parameters values close to phase transitions at $T = 0$.
- At $T > 0$ the correlation function for μ corresponding to the GS stability of the periodic phase oscillates, what indicates stability of alternating layers of the solvent and the properly oriented amphiphiles.
- The correlation length at low T and μ corresponding to GS stability of the periodic phase is several orders of magnitude larger than the molecular size.
- The pseudo-phase transition to the periodic phase is associated with a peak in the specific heat.

2.1.3 Comparison of the SALR and the amphiphilic self-assembly

The colloidal system with the SALR competing interaction potential and the system of amphiphiles, despite qualitatively different potentials share many properties, with the topology of the high-T phase diagram among them (see Sec. 1.3). In what follows, we discuss the common structural, mechanical and thermal features of the SALR and amphiphilic systems at low-T, based on the results obtained in Sec. 2.1.1 and 2.1.2.

The ground states of the model for colloidal (Fig. 2.2) and amphiphilic (Fig. 2.26) self-assembly show strong similarities. The phases with oscillatory density or concentration occur when the repulsion in the case of colloids or attraction between the water and properly oriented amphiphilic molecules are strong. When the above interactions are weak, only two phases are present in the ground state - the gas and liquid in the SALR case and the water- and amphiphile rich phases in the amphiphilic system. This behavior agrees with the reentrant melting observed experimentally in several systems [71, 72]. In both models the surface tension between the water and the periodic phase vanishes for $T = 0$, and the ground state is strongly degenerated. Arbitrary number of arbitrarily small droplets of the coexisting phases can be present at the phase coexistence. This degeneracy of the ground state means that the macroscopic separation of the two phases at $T = 0$ is not possible, since the formation of an interface does not lead to any increase of the grand potential. At the same time, because of the microscopic size of the droplets, one can interpret the degenerated ground state as a disordered phase. The region of the ground state corresponding to the stability of this phase is of zero measure, however, in contrast to the remaining, ordinary phases. The properties of this phase resemble the sponge phase in the amphiphilic model or a cluster fluid in the case of the model of colloids. Note that the inhomogeneous density, leading to the formation of the clusters, micelles or bilayers results from competing tendencies in the interactions, and not exclusively from the amphiphilic nature of the molecules.

The exact results for the models of amphiphilic and colloidal self-assembly show that the low surface tension is a more general property of systems with competing interactions, and is not limited to amphiphilic molecules. This confirms the observation of

universality of the periodic ordering on the mesoscopic length scale that was derived under the assumption of weak ordering (see Sec. 1.3).

Moreover, we have found strong similarity between **the equations of state**, that is the pressure-density isotherm in the colloidal system (Fig. 2.13) and the pressure-concentration isotherm in the model of the amphiphilic mixture (Fig. 2.32). The characteristic feature of these lines is the *plateau* in the density or concentration as a function of pressure, which does not occur in simple fluids. Similar shapes have also the density - chemical potential and the concentration - chemical potential lines (Figs. 2.12 and 2.31 respectively). The *plateau* occurs when the density or concentration takes the value corresponding to the periodic distribution of the clusters or the bilayers, and indicates extremely low system compressibility. For the corresponding range of the chemical potential and the temperature **the correlation functions** in both models exhibit exponentially damped oscillatory decay with a very large correlation length. The *plateau* is limited by regions with high slopes, which indicate high system compressibility.

A surprising phenomenon of **ordering upon heating** associated with the properties of the correlation function was reported in both models. We have found that if the repulsion between the colloids or the interactions between water and amphiphiles are relatively weak, then the correlation function can cross over from a *monotonic decay* at low T^* to an *oscillatory decay* for higher T^*. The unusual appearance of the periodic short-range order at intermediate temperatures that for weak repulsion *is neither energetically nor entropically* favored is a surprising and interesting *exact* result. It means that for competing interactions the inhomogeneities may appear as a compromise between the macroscopic phase separation that is energetically favorable but entropically unfavorable, and the disordered structure that is favorable entropically and unfavorable energetically.

The **thermal properties** of the models are also similar, but in order to compare them we should note that in the case of the colloidal self-assembly the specific heat was calculated per colloid particle, and the solvent was disregarded. The specific heat per unit volume calculated for the model of the amphiphilic mixture is a different quantity, therefore in Fig.2.39b we present c_v/ρ_s representing the specific heat per

amphiphilic molecule. Note that for the model of amphiphilic self-assembly the specific heat of the pure solvent (i.e. for $\rho_s = 0$) vanishes, since the energy does not fluctuate when all the sites are occupied by the solvent. In this respect the solvent is analogous to the disregarded solvent in the SALR model. Thus, to compare the thermal effects of the amphiphilic and the colloidal self-assembly, we shall compare c_v/ρ_s and the specific heat per colloid particle.

Let us first discuss the specific heat for such values of the interaction parameters that three phases are present on the GS. In the amphiphilic model at $T = 0$ for $c = g = 2$ the stable phases are: the solvent-rich for $\rho_s = 0$, the periodic array of bilayers for $\rho_s = 2/3$ and the amphiphile-rich for $\rho_s = 1$. The formation of the periodic phase at $T^* > 0$ is indicated by the c_v/ρ_s peak for $\rho_s = 2/3$ that becomes narrower for decreasing temperature (Fig.2.39a). In Fig. 2.39b an increase of c_v/ρ_s for $\rho_s \to 0$ can be observed for the range of ρ_s that increases with increasing T^*. This behaviour may be associated with an equilibrium between bilayers and isolated amphiphilic molecules. In the SALR system the qualitative behavior of the specific heat is similar. For sufficiently strong repulsion ($J^* > 1/3$) three phases are stable in the ground state: the gas ($\rho = 0$), the periodic ($\rho = 1/2$), and the liquid phase ($\rho = 1$). The peak for the density corresponding to the stability of the periodic phase ($\rho \approx 1/2$) that becomes narrower for decreasing temperature, and another maximum for a very small density are both present (Fig. 2.22). Analogously as in the model for amphiphilic self-assembly the presence of the maximum for small densities can be explained as an effect of the equilibrium between isolated particles and clusters of several particles. Given the Hamiltonian of the model, these clusters are likely to be triples in the case of $J^* = 3$. At low temperature and low density the loss of entropy due to the formation of clusters is compensated by the energetic effect due to the attractive interaction between the nearest neighbors.

Let us focus now on the specific heat for such values of the interaction parameters that only two phases are present on the GS. In the case of the model for amphiphilic self-assembly for $c = 1$, $g = 2$ only the solvent-rich and the amphiphile-rich phases are stable, while in the case of model of colloids for $J^* < 1/3$ the only two stable phases at the GS are the gas and the liquid. For both models the absence of the periodic phase in the GS leads to a lack of the peak in the specific heat for the densities corresponding to the periodic phases (i. e. $\rho_s = 2/3$ and $\rho = 1/2$). However, still an increase of the specific heat for decreasing ρ_s and ρ can be observed (Figs.

2.23 and 2.41). The above signals that precursors of the ordered phase (present for $T^* = 0$) have a strong effect on the thermal system properties.
In both models the specific heat as a function of temperature has two maxima for the densities corresponding to the ground state periodic phases (Fig. 2.40). The maxima at lower temperatures are associated with the phase transitions which occur at $T^* = 0$, whereas the higher-T maxima correspond to structural changes of the system which are not coupled with a phase transition.

We conclude that measurements of the specific heat in self-assembling systems can give information on the formation and properties of clusters or bilayers for very small densities, and on formation of phases (or pseudo-phases) with periodically ordered structures for higher densities. While in the latter case thermal properties are consistent with the EOS and the correlation function, for very small densities **they provide additional information on the equilibrium between isolated particles and clusters or bilayers.**

The stability analysis shows that the main difference between the self-assembly in the amphiphilic and colloidal systems concerns the periodic ordering of the pure amphiphiles into the lamellar structure that is absent in the colloidal systems. Because of this crystal-like order of amphiphiles, the characteristic shape of the line of instability, similar to the spinodal line of the phase separation, is only found for $g = 0$, where the amphiphiles do not order in the absence of water. For $g > 0$ the shape of the line of instability in this model is similar to the corresponding line in the SALR system only for low volume fraction of amphiphiles.

To conclude, the exact results in the model for amphiphilic systems and in the lattice model for the SALR systems demonstrate close similarity between different types of self-assembly.

2.2 Two-dimensional model

In the previous section we have shown that the colloidal and the amphiphilic self-assembling systems have similar equations of state, structural and thermal properties, as well as the same topology of the ground state. For this reason, from the two generic models studied in 1d, for further studies we choose only one model - the one which was by now much less investigated that is the model of colloidal self-assembly. In this section we introduce a model of the colloidal self-assembly at an interface between two phases, that is in two-dimensional space (Sec. 2.2.1). The model was developed in order to mimic colloidal self-assembly, however it can be also related with self-assembly of particles on a solid substrate that has hexagonal topology, or self-assembly of proteins on a lipid membrane. We derive the ground state of the model (Sec. 2.2.2) and present the results for the phase diagram within approximate theories (2.2.3), and Monte Carlo simulation (Sec. 2.2.4).

2.2.1 Introduction of the SALR model on a triangular lattice

We consider a system in equilibrium with a bulk reservoir with temperature T and chemical potential μ_p. The interaction h of the particles with the binding sites on a solid substrate, or with the lipids in the membrane plays analogous role as the chemical potential, and we introduce $\mu = \mu_p + h$. This time we assume that the particles can occupy sites of a *triangular lattice*. We assume that the lattice constant is comparable with the diameter of the adsorbed particles σ. This way we allow for close packing of the particles. Because of this property the triangular lattice can yield more realistic results than the square lattice. In the case of adsorption on a solid substrate the model is appropriate for a triangular lattice of adsorption centers. The lattice sites are $\mathbf{x} = x_1\mathbf{e}_1 + x_2\mathbf{e}_2$, where $\mathbf{e}_1$, $\mathbf{e}_2$ and $\mathbf{e}_3 = \mathbf{e}_2 - \mathbf{e}_1$ are the unit lattice vectors on the triangular lattice, i.e. $|\mathbf{e}_1| = |\mathbf{e}_2| = |\mathbf{e}_1 - \mathbf{e}_2| = 1$ (in σ-units), and x_i are positive integers. We assume $1 \leq x_i \leq L$, where L is the size of the lattice in the directions $\mathbf{e}_1$ and $\mathbf{e}_2$. We also assume periodic boundary conditions.

In order to mimic the SALR interactions and to stay consistent with assumptions made in the 1d case, we assume that the nearest-neighbors attract each other, then the interaction changes sign for the next-nearest neighbors, becomes repulsive for the third neighbors, and vanishes for larger separations (see Fig.2.42).

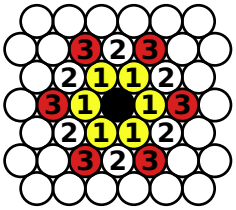

FIG. 2.42: The interactions in the lattice model. The occupied central site (black) attracts each one of the occupied nearest-neighbor sites labelled 1 (yellow) and repels each one of the occupied third-neighbor sites labelled 3 (red). The interactions between the central site and the remaining sites vanishes. The strength of the attraction is J_1 and the strength of the repulsion is J_2.

The Hamiltonian and the interaction potential have analogous forms as those defined in Sec. 2.1.1.1, but this time the distance is measured in a two-dimensional space, hence the Hamiltonian is

$$H = \frac{1}{2}\sum_{\mathbf{x}}\sum_{\mathbf{x}'}\hat{\rho}(\mathbf{x})V(\mathbf{x}-\mathbf{x}')\hat{\rho}(\mathbf{x}') - \sum_{\mathbf{x}}\mu\hat{\rho}(\mathbf{x}), \tag{2.83}$$

where $\hat{\rho}(\mathbf{x}) = 1$ (0) when the site $\mathbf{x}$ is (is not) occupied, and the interaction energy between the occupied sites $\mathbf{x}$ and $\mathbf{x}+\Delta\mathbf{x}$ is given by

$$V(\Delta\mathbf{x}) = \begin{cases} -J_1 & \text{for } |\Delta\mathbf{x}| = 1, \\ +J_2 & \text{for } |\Delta\mathbf{x}| = 2, \\ 0 & \text{otherwise,} \end{cases} \tag{2.84}$$

where $-J_1$ and J_2 represent the attraction well and the repulsion barrier respectively. The grand potential is expressed in terms of the grand statistical sum

$$\Xi = \sum_{\{\hat{\rho}(\mathbf{x})\}} \exp(-\beta H[\{\hat{\rho}(\mathbf{x})\}]) \tag{2.85}$$

in the standard way

$$\Omega = -k_B T \ln \Xi = -p a_0 L^2, \tag{2.86}$$

where $a_0 = \sigma^2\sqrt{3}/2$ is the area per lattice site, L^2 is the number of sites and p is 2d pressure.

Because the probability of the state $\{\hat{\rho}(\mathbf{x})\}$ for $\mu = \tilde{V}(0)/2 - \Delta\mu$ is the same as the probability of the state $\{1-\hat{\rho}(\mathbf{x})\}$ for $\mu = \tilde{V}(0)/2 + \Delta\mu$ (see Sec. 2.1.1.1), where

$$\tilde{V}(0) = \sum_{\mathbf{x}} V(\mathbf{x}) = 6(J_2 - J_1), \tag{2.87}$$

we expect symmetry of the phase diagram with respect to the symmetry axis $\mu = \tilde{V}(0)/2 = 3(J_2 - J_1)$.

As previoulsy, we choose J_1 as the energy unit, and use the notation $X^* = X/J_1$ for any quantity X with dimension of energy.

2.2.2 The ground state

The ground state of the lattice gas (Ising) class of models on a triangular lattice is of interest since the middle of the previous century, because in the case of a repulsion between the nearest neighbors it violates the Nernst's theorem (non-zero entropy at zero temperature limit) [87–93]. All the ground state configurations for the lattice gas models on the triangular lattice with interactions up to the third nearest-neighbors were determined by Kaburagi and Kanamori [89, 91], but only for vanishing external field and for a few fixed values of the particle density. The ground state of the lattice gas model in a presence of the external field was found in Ref.[90], but only interactions between the first and the second neighbors were taken into account. The GS for various interactions on the triangular lattice were studied in detail by Dublenych [91–93]. In the particular case of our model, however, the GS in the (J^*, μ^*) variables was not presented in the literature.

The grand potential for $T = 0$ reduces to the minimum of $H^*[\{\hat{\rho}(\mathbf{x})\}]/L^2$. We have calculated $H^*[\{\hat{\rho}(\mathbf{x})\}]/L^2$ for a number of various periodic structures. The structure for which $H^*[\{\hat{\rho}(\mathbf{x})\}]/L^2$ takes the lowest value is the stable one for given μ^* and T^*. Two phases can coexist when $H^*[\{\hat{\rho}(\mathbf{x})\}]/L^2 = -p^*$ in these phases takes the same value (equal to the global minimum). We have found that apart from the empty and fully occupied lattices five periodic structures are stable in different regions on the (J^*, μ^*) diagram. The stable structures agree with those found in Ref.[89]. We have verified that no other ordered structures appear by MC simulations for low T^*. The GS and the structure of the stable phases are shown in Fig.2.43 and 2.44. The topology of the ground state is similar to the one found before in the 1d version

of the model (Sec. 2.1.1.2) and the one found for the 2d model with interactions between the first and the second nearest-neighbors [90, 91].

Let us decribe the GS. For weak repulsion, $J^* < 1/2$, the vacuum ($p_v^* = 0$) and the fully occupied lattice ($p_d^* = -3 + 3J^* - \mu^*$) coexist for $\mu^* = 3J^* - 3$. For $J^* > 1/2$ the stability regions of the two homogeneous phases are separated by the region of stability of the following periodic structures: hexagonally ordered clusters of rhomboidal (OR) or hexagonal (HC) shape, the stripe (lamellar) phase (L) and hexagonally ordered rhomboidal (RB) or hexagonal (HB) bubbles. By the model symmetry, the bubble phases are "negatives" (i.e. $\hat{\rho}(\mathbf{x}) \to 1 - \hat{\rho}(\mathbf{x})$) of the cluster phases.

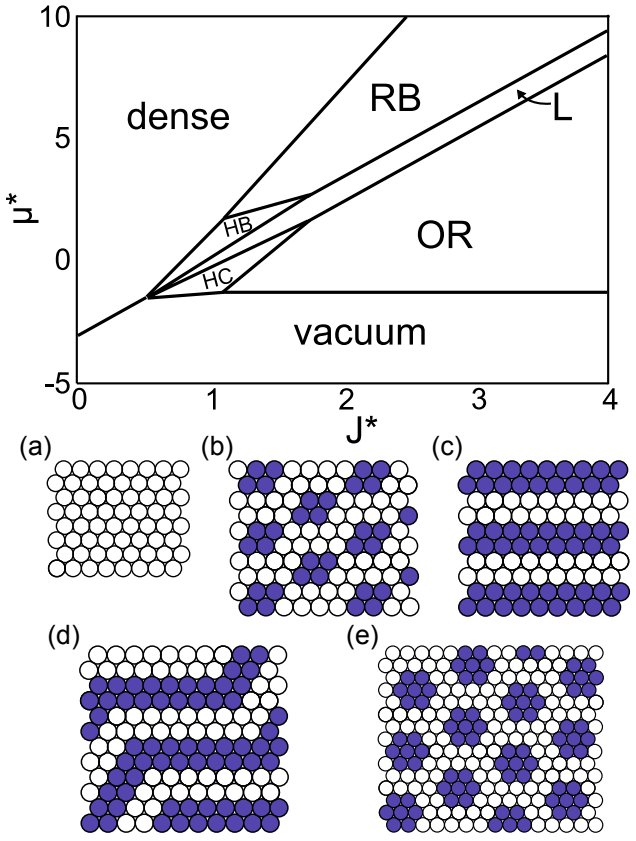

FIG. 2.43: Ground state of the model. μ^* and J^* denote the chemical potential and the third-neighbor repulsion respectively, both in units of the nearest-neighbor attraction. The structures of the stable phases are shown in the panels (a)-(e), with: (a) vacuum, (b) ordered rhomboidal clusters (OR), (c) and (d) lamellar phase (L), (e) hexagonal clusters (HC). Dense phase, hexagonal bubble phase (HB) and rhomboidal bubble phase (RB) are "negatives" of the phases (a), (b) and (c) respectively, i.e. the occupied sites are replaced by the empty ones and vice versa. The symmetry line is given by $\mu^* = 3J^* - 3$. Configurations stable at the coexistence lines are shown in Fig. 2.44.

For $J^* > 1/2$ the ground state is strongly degenerated at the coexistence lines, and the entropy per lattice site does not vanish for such state points. This can be easily

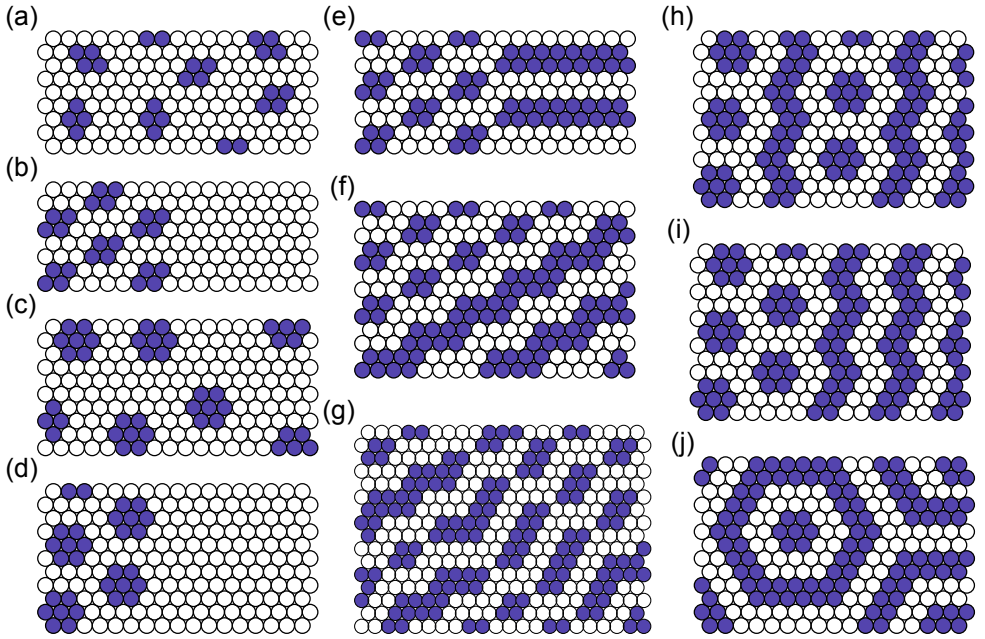

FIG. 2.44: Examples of the ground state structures stable at the coexistence lines. Left panels: vacuum - OR phase coexistence (a)-(b) and vacuum - HC phase coexistence (c)-(d). Central panels: OR - lamellar phase coexistence. Right panels: HC - lamellar phase coexistence.

shown for the coexistence between the vacuum and the OR or HC phases. In the vacuum $H^* = 0$. The change of $H^*[\{\hat{\rho}(\mathbf{x})\}]$ when a single rhomboidal or hexagonal cluster appears in the vacuum is $-5-4\mu^*$ or $-12+3J^*-7\mu^*$, respectively. For $\mu^* = -5/4$ or $\mu^* = (-12+3J^*)/7$ the Hamiltonian does not change if an arbitrary number of noninteracting rhomboidal or hexagonal clusters appears in the system. The clusters do not interact if the distance between them is sufficiently large. There are no more restrictions on the positions and orientations of the clusters in the states with $H^* = 0$ at the vacuum - OR and vacuum - HC phase coexistences (Fig.2.44a,c). For this reason the entropy per lattice site does not vanish. Note that the surface tension between the vacuum and the OR phases as well as between the vacuum and the HC phases vanishes, because $H^* = 0$ when the interface between the two phases is present (Fig.2.44b,d). For $-5-4\mu^* < 0$ and $-12+3J^*-7\mu^* < 0$ the OR and HC phases respectively are more stable than the vacuum. In these phases the noninteracting clusters are packed as densely as possible (Fig.2.43 b and e).

The HC and OR phases coexist with the lamellar phase for $\mu^* = (13J^*-14)/5$ and $\mu^* = 3J^*-7/2$ respectively, which can be easily verified by comparing p^* for these structures.

Note that p^* takes the same value in the lamellar phase shown in Fig.2.43c, and in

the zig-zag lamellar phase shown in Fig.2.43d. There are many configurations of the zig-zag stripes having thickness 2 in one of the lattice directions and separated by empty regions of the same shape. In what follows we will describe how the GS lamellar structures can be constructed and characterized. This description will allow us to make an estimation of the entropy of this phase, which will be useful later to find the phase transitions. Let us consider lamellas with periodicity in direction $\mathbf{e}_3$, as shown in Fig. 2.45. We start by setting three occupied positions defining an elementary triangle on the left end of the lattice (labelled as 1 in Fig 2.45). In order to proceed, after setting this first triangle (or whatever triangle with an odd label) we occupy a lattice position that closes an adjacent triangle (chosen between those labelled with even numbers in Fig. 2.45, which are those at the top or at the right of the previous triangle). Then after each triangle with even index is added the next triangle has to be that on its right, since the choice of the one on the left would break the periodicity in direction $\mathbf{e}_3$.

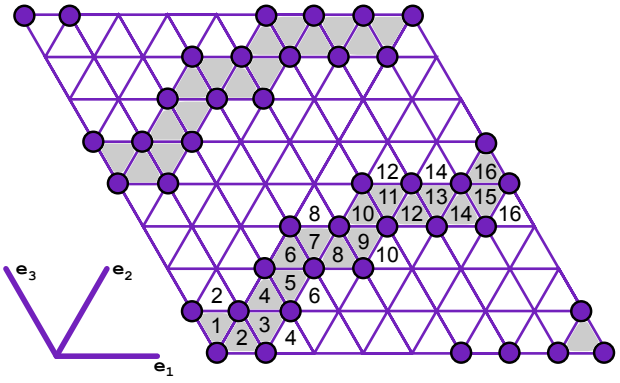

Fig. 2.45: Sketch of the construction of the ground state lamellar structures.

Once we get the reference lamellar stripe following the simple rules given above, it is straightforward to build up the GS lamellar structure by replicating each piece with translations. The occupied sites are $\mathbf{x} = \mathbf{x}_0 + 4k\mathbf{e}_3$, where $\mathbf{x}_0$ is the position of the site at the reference stripe and $k > 0$ is an integer number. The structures generated in this way fulfill $\rho = 1/2$, and their internal energy per particle is $-2 + J^*$.

Taking into account the procedure to construct the GS lamellas it is possible to compute the entropy of this phase at $T^* = 0$. PBC add some restrictions to the building procedure. If we follow one lamella stripe through PBC, it is clear that the number of choices of growing the reference lamella stripe in the vertical direction must be zero or a multiple of four. In addition, L must be a multiple of four.

Taking into account the number of ways of creating lamellar structures with translational order in, at least, one direction, and the restrictions due to PBC, we can estimate the entropy of the system as

$$S/L^2 = \frac{k_B}{L^2} \ln Q \simeq \frac{k_B \ln 2}{L} + O(L^{-2}). \tag{2.88}$$

where Q is the number of ways of building up the ordered lamellar structures following the previous procedure. The correction term $O(L^{-2})$ includes the translational degeneracy from the location of the triangle 1 in Fig. 2.45; the possibility of considering three directions in the construction of the reference lamella stripe; the overcounting of straight lamellas, that show periodicity of length four in two directions; and the restrictions due to the PBC, that eliminate about 3/4 of the reference stripes.

At the coexistence between the lamellar and the ordered cluster phases there exists a large number of disordered states with the same value of p^* as for the two coexisting ordered phases. Characteristic examples of such states are shown in Fig.2.44 e-j. Note that these states include the interface between the ordered cluster and the lamellar phases (Fig.2.44 e,f,i). In Fig.2.44g closely packed zig-zag clusters of different length are present. The thickness of the clusters in direction $\mathbf{e}_3$ is 2 except at the two opposing vertices where the thickness is 1. In Fig.2.44j the clusters are surrounded by lamellar rings. Structures with a few closely packed clusters surrounded by one or a few lamellar rings are stable too. All the clusters, layers or rings are packed as densely as possible under the constraint that the neighboring objects do not repel each other. More precisely, the polygons obtained by surrounding the clusters or stripes by a single layer of empty sites must cover the whole lattice. This requirement follows from the negative value of the grand potential per site in the L, HC and OR phases, and from equal values of p^* in the coexisting phases. We call the phase stable along the coexistence between the lamellar and the OR phases a 'molten lamella'. The GS at the HC - OR coexistence, $\mu^* = (36J^* - 49)/8$, is not degenerated.

The strong degeneracy of the GS at the coexistence lines between different structures was observed before by Dublenych [91]. Unlike Dublenych, we interpret the collection of the disordered states present at the coexistence between two ordered phases as a distinct, disordered phase. At $T^* = 0$ the cluster fluid and the molten lamella are

stable only at the phase coexistences, i.e. for a single value of the chemical potential for a given interaction strength. As we will show later by the preliminary investigation of the effects of fluctuations (Sec. 2.2.3.4) and by MC simulations (Sec. 2.2.4), these disordered phases remain stable for $T^* > 0$ for some interval of μ^*. Let us finally note that the degeneracy of the GS at the phase coexistence and the vanishing surface tension are closely related, as observed previously in 1d. An arbitrary number of interfaces can appear when the surface tension vanishes. As a result, the number and the size of the droplets of the coexisting phases can be arbitrary. This leads to disordered states that can be considered as fluids of clusters or stripes.

2.2.3 Mean-field phase diagram

In this section we present the MF phase diagram obtained by the methods described in Sec. 2.1.1.3. Note, however that although the notation used here is consistent with that of Sec. 2.1.1.3, the space argument of the considered functions is no longer a scalar, x, but a vector denoting a point on the triangular lattice, $\mathbf{x}$.

2.2.3.1 The structure of the disordered phase

In MF the structure factor in the disordered phase (with $\bar{\rho} = const.$) is obtained from the relations $\tilde{G}_{MF}(\mathbf{k}) = 1/\tilde{C}_{MF}(\mathbf{k})$ [94], where $\tilde{C}_{MF}(\mathbf{k})$ is given by Eq. (2.14) and the vector in the dual space $\mathbf{k}$ in the case of the triangular lattice is $\mathbf{k} \equiv (k_1, k_2) = k_1\mathbf{f}_1 + k_2\mathbf{f}_2$, where the unit vectors of the dual lattice satisfy $\mathbf{f}_i \cdot \mathbf{e}_j = \delta_{ij}^{Kr}$ and $|\mathbf{f}_i| = 2/\sqrt{3}$, where $\mathbf{x} \cdot \mathbf{y}$ is the standard scalar product in $\mathbb{R}^2$ and $|\cdot|$ is a norm induced by it. The interaction potential (Eq. 2.84) in the Fourier representation is

$$\beta\tilde{V}(\mathbf{k}) = \sum_{\mathbf{x}} \beta V(\mathbf{x}) e^{i\mathbf{k}\cdot\mathbf{x}} = 2\beta^*\Big[J^*\Big(\cos(2k_1)+\cos(2k_2)+\cos(2(k_1-k_2))\Big) - \cos k_1 - \cos k_2 - \cos(k_1-k_2)\Big]. \tag{2.89}$$

For $J^* < 1/4$ the function given by Eq.(2.89) assumes the minimum for $\mathbf{k} = \mathbf{0}$, whereas for $J^* \geq 1/4$ the minimum occurs for $k_1 = 2k_2 = k_b$ with

$$k_b = 2\arccos\Big(\frac{J^* + \sqrt{J^{*2} + 2J^*}}{4J^*}\Big). \tag{2.90}$$

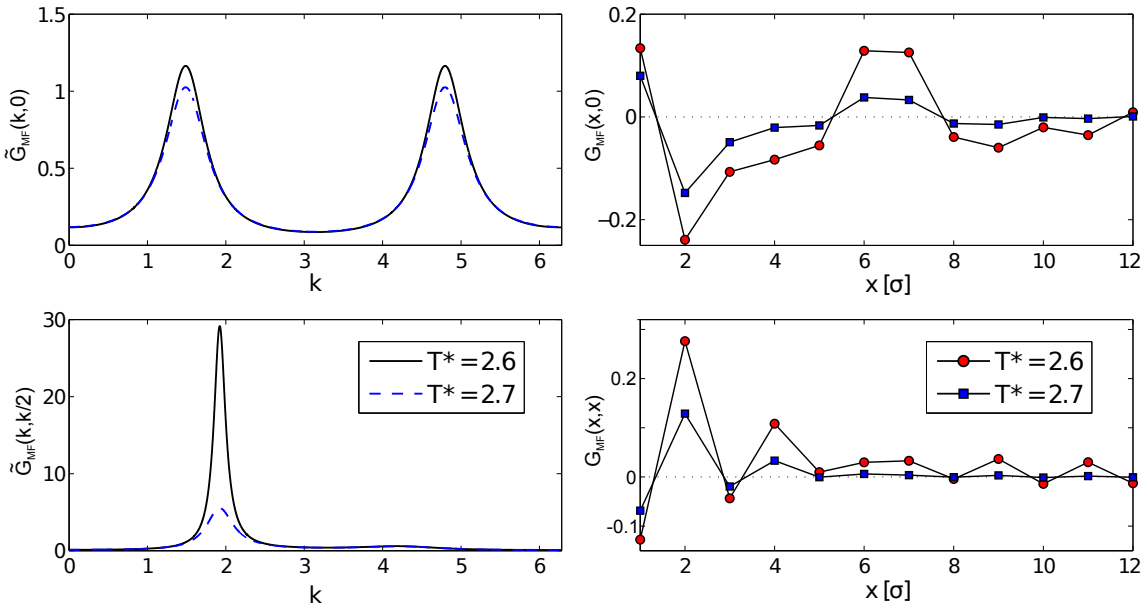

FIG. 2.46: The correlation function for $J^* = 3$ and $\rho = 0.5$. Red circles and solid lines correspond to $T^* = 2.6$ while blue squares and dashed lines to $T^* = 2.8$. Left column: G in Fourier space; top panel: $\tilde{G}_{MF}(k,0)$, bottom panel: $\tilde{G}_{MF}(k,k/2)$. Right column: G in real space; top panel: $G_{MF}(x,0)$, i.e. for points $\mathbf{x} = x\mathbf{e}_1$, and bottom panel: $G_{MF}(x,x)$, i.e. for points $\mathbf{x} = x\mathbf{e}_1 + x\mathbf{e}_2$. The temperature of the λ-line is $T^*_\lambda = 2.575$.

By symmetry of the lattice there are two other minima of the same depth. Thus, $\tilde{V}(\mathbf{k})$ takes the global minima for the wavevectors

$$\mathbf{k}_b^{(i)} = k_b \mathbf{e}_i. \tag{2.91}$$

We used the relations $\mathbf{e}_1 = \mathbf{f}_1 + \frac{1}{2}\mathbf{f}_2$ and $\mathbf{e}_2 = \mathbf{f}_2 + \frac{1}{2}\mathbf{f}_1$. Note that the characteristic length $2\pi/k_b$ is noninteger. Thus, the period of damped oscillations in the correlation function is incommensurate with the lattice. Similar result was obtained by the exact transfer matrix method for the 1d version of our model (Sec. 2.1.1.4). In Figs.2.46 and 2.47 we show the correlation function G_{MF} in Fourier and real-space representation for $J^* = 3$ and $J^* = 1/4$ respectively.

2.2.3.2 Boundary of stability of the disordered phase

The disordered phase is unstable if the grand potential decreases when the density wave with an infinitesimal amplitude and some wavevector $\mathbf{k}$ appears, i.e. when $\tilde{C}_{MF}(\mathbf{k}) < 0$. The boundary of stability of the disordered phase is given by Eq. 2.17 in which for the Fourier transform of the interaction potential we use Eq. 2.89. In

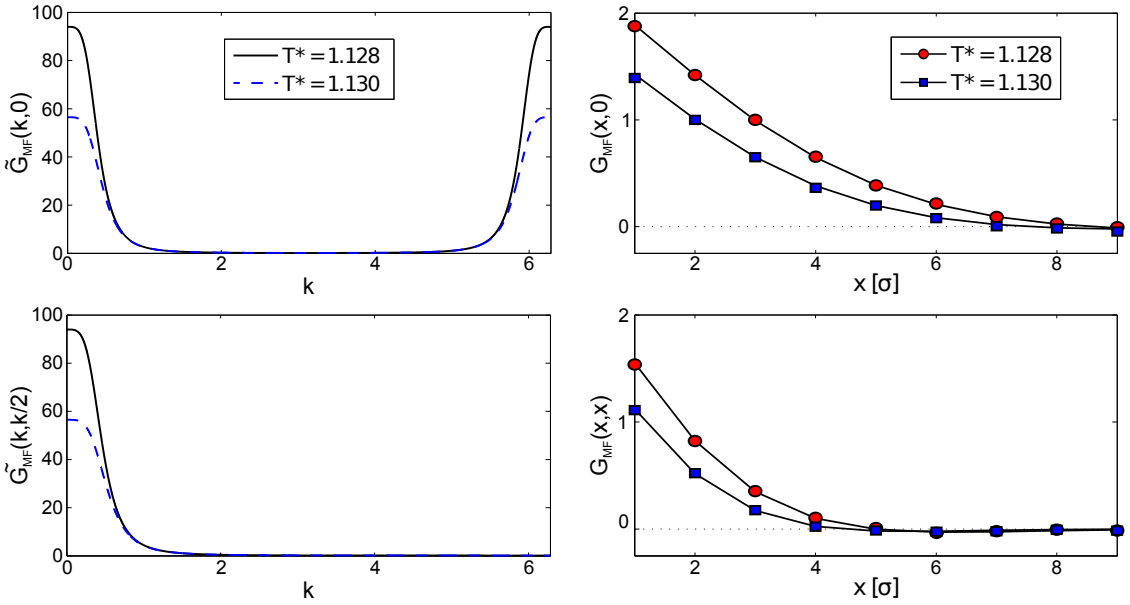

FIG. 2.47: The correlation function for $J^* = 1/4$ and $\rho = 0.5$. Red circles and black solid lines correspond to $T^* = 1.128$ while blue squares and dashed lines to $T^* = 1.13$. Left column: G in Fourier space; top panel: $\tilde{G}_{MF}(k,0)$, bottom panel: $\tilde{G}_{MF}(k,k/2)$. Right column: G in real space; top panel: $G_{MF}(x,0)$, i.e. for points $\mathbf{x} = x\mathbf{e}_1$, and bottom panel: $G_{MF}(x,x)$, i.e. for points $\mathbf{x} = x\mathbf{e}_1 + x\mathbf{e}_2$. The temperature of the λ- line is $T^*_\lambda = 1.124$.

the density waves that destabilize the disordered phase the density oscillates in the principal directions of the lattice (see (2.91)). In the case of the lamellar structure the layers of constant density are perpendicular to one of the unit lattice vectors $\mathbf{e}_i$ (three-fold degeneracy). In the case of the hexagonal structure the density is a superposition of 3 planar density waves in the principal lattice directions.

The shape of the λ-line in the (ρ, T^*) variables is the same as the shape of the spinodal line of the phase separation, except that the temperature scale is given by $-\tilde{V}(\mathbf{k}_b)$ rather than by $-\tilde{V}(\mathbf{0})$. This property is common for different forms of the SALR potential [39, 41]. However, in (μ^*, T^*) variables the shapes of the spinodal and the λ-lines differ significantly from each other. Moreover, the shape of the λ-line depends on J^* (Fig.2.48). For $J^* < 1/4$ the two branches of the spinodal form a cusp. On the low-T^* side of these lines there are two minima of Ω^*_{MF}, corresponding to the gas and liquid phases. For $J^* > 1/4$ the two branches form a loop for high T^*. The grand potential assumes a minimum for periodic structures for the state points inside the loop, while for the gas and liquid phases - inside the cusp below the loop. For increasing J^* the size of the loop increases, and for $J^* > 1$ the gas- and liquid branches of the instability line disappear. Since the instability and the

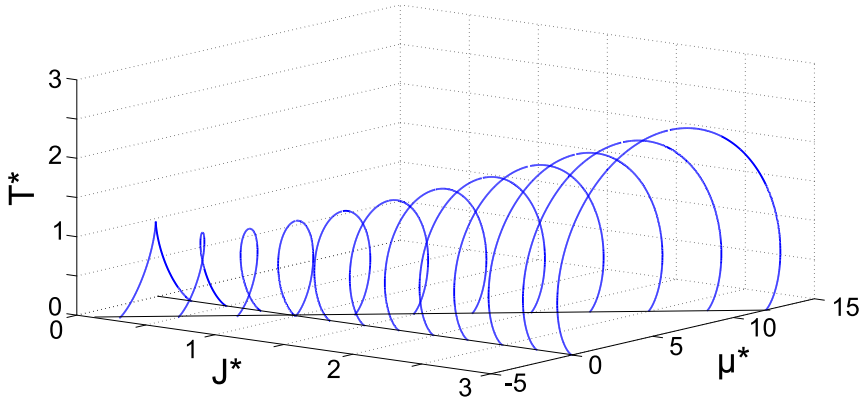

FIG. 2.48: MF lines of instability (solid) of the homogeneous phase in the (μ^*, T^*) variables for a range of J^*. We used $\partial\Omega_{MF}/\partial\rho = 0$, and 2d analogues of Eq. (2.11) and Eq. (2.17).

transition lines are not the same, the first-order gas-liquid transition may disappear for some different value of J^*. Similar shapes of the instability lines were obtained in the one-dimensional lattice model (Sec. 2.1.1.3) and in the three-dimensional model [70]. Thus, the above evolution of the MF lines of instability for increasing repulsion seems to be a generic property, independent of the particular shape of the SALR potential and dimensionality of the system.

2.2.3.3 First-order transitions

In order to determine the MF phase diagram we use the iterative method described in Sec. 2.1.1.3. We assume PBC and consider different values of L. This way structures with periods L/n where n is integer can be generated. We find very large number of metastable states, especially for high T^*, where the order is weak (small amplitude of the density oscillations). To overcome this problem we assume that when the amplitudes of the density oscillations in the periodic phases are small, the density has the form

$$\rho_p(\mathbf{x}) = \rho_0 + \delta\rho_p + \Phi_p g_p(\mathbf{x}). \tag{2.92}$$

In the above ρ_0 is the position-independent density corresponding to the extremum of Ω_{MF} for given μ^* and T^*. The $\delta\rho_p$ is the shift of the average density in the periodic phase p, and $g_p(\mathbf{x})$ is the normalized periodic function with the symmetry of the corresponding p phase, where $p = l, h$ for the lamellar and the hexagonal

phase respectively. For the densities of the form (2.92) the excess grand potential,

$$\Delta\Omega_p[\rho_p] = \Omega_{MF}[\rho_p] - \Omega_{MF}[\rho_0], \tag{2.93}$$

is a function of $\delta\rho_p$ and Φ_p. It takes a minimum for $\delta\rho_p$ and Φ_p corresponding to a stable or a metastable phase p. We limit ourselves to $\delta\rho_p \to 0$ and $\Phi_p \to 0$, and from the conditions $\partial\Delta\Omega_p/\partial\delta\rho_p = 0 = \partial\Delta\Omega_p/\partial\Phi_p$ obtain the approximate values of $\delta\rho_p$ and Φ_p, and of the excess grand potential in the lamellar and hexagonal phases. Next, from $\Delta\Omega_h = 0$ and $\Delta\Omega_h = \Delta\Omega_l$ we obtain the transitions between the disordered and hexagonal, and between the hexagonal and the lamellar phases respectively. These transition lines are shown as dashed lines in Fig.2.49. Some details of the calculation are given in Appendix 6.3.

The phase diagram obtained in the MF approximation described above is presented in Fig. 2.49 for $J^* = 3$. F, H, OR, L_1 and L_2 denote the disordered fluid, the high-T^* hexagonal phase, the ordered rhombus, and the low-T^* and high-T^* lamellar phases respectively. The MF density distribution in the H and L_2 phases is shown in Fig. 2.50, and the structure of the OR and L_1 phases for $T^* \to 0$ is shown in Fig.2.43b and Fig.2.43c,d respectively. In the H phase the clusters form a hexagonal pattern, but in contrast to the OR phase the orientation of the long axes of the rhombuses is not fixed. The OR phase can be present only in the case of small asymmetric clusters, i.e. for large repulsion. For $J^* = 1$ (hence for $\int d\mathbf{r}V(r) = 0$) hexagonal clusters appear for $T^* = 0$ (Fig. 2.43 e) and only positional ordering of the clusters can occur. In the L_2 phase the orientation of the lamellas differs from the ground-state orientations, and agrees with the orientation of the density waves that destabilize the homogeneous phase. Because of a very large number of metastable structures characterized by very similar values of the grand potential, it is likely that some details of the phase diagram are not reproduced in Fig.2.49 with full precision.

2.2.3.4 The effect of the degeneracy of the ground state on the phase diagram for $T^* > 0$ beyond mean-field.

In MF the self-assembled clusters and stripes are present only in the ordered phases, and for $T \to 0$ the density of the disordered phase at the coexistence with the OR phase is very small. This is because in the case of delocalized clusters the average density is position independent, and the repulsion contribution to the mean-field

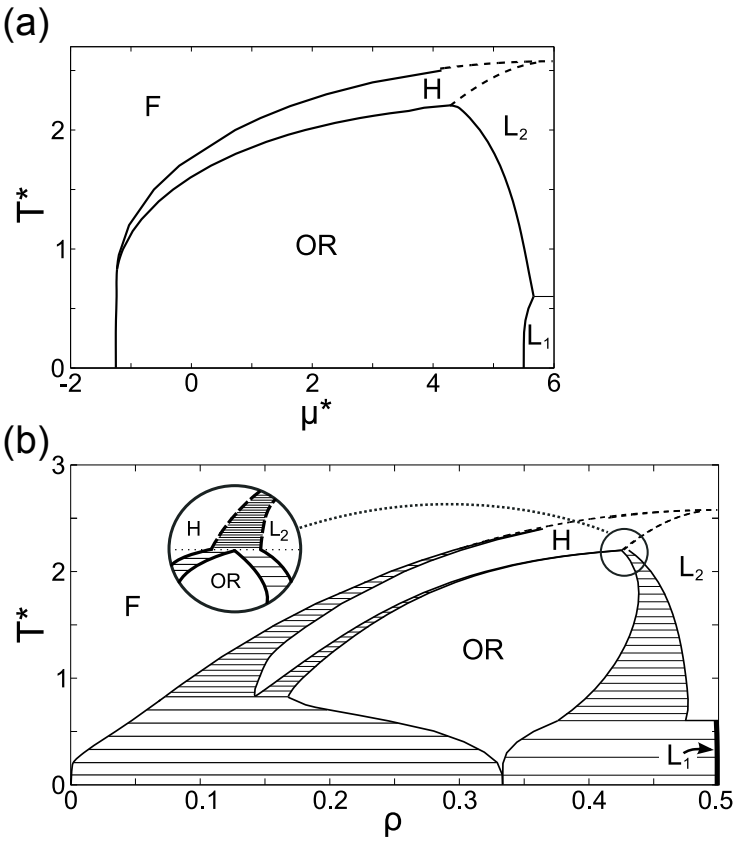

FIG. 2.49: Mean-field phase diagram for $J^* = 3$ in (μ^*, T^*) (Panel (a)) and (ρ, T^*) (Panel (b)) variables. F, H, OR, L_1 and L_2 denote disordered fluid, hexagonal phase, ordered rhombuses and low- and high temperature lamellar phases respectively. Typical microstates of the OR and L_1 phases are shown in Figs. 2.43b and 2.43c,d respectively. MF density profiles in the phases H and L_2 are shown in Fig.2.50. The L_1 lamellar phase is stable for $T^* < 0.65$ and $\rho \approx 0.5$ (the density interval is within the thickness of the line). When temperature rises ($T^* > 0.65$), the L_2 phase (see Fig.2.50b) becomes stable. The density ranges of the two-phase regions for temperatures $T^* > 2$ (dashed lines) are also within the thickness of the line.

grand potential for large position-independent density is large (see (2.11)). In the case of rhomboidal clusters separated by distances larger than the range of the repulsion, however, the repulsion contribution to the internal energy is absent. Therefore for low T^* the density of the disordered phase at the coexistence with the ordered cluster phase is significantly underestimated in the mean-field approximation. Here we take into account the degeneracy of the GS and present a semi-quantitative analysis of the disordered cluster fluid for $\beta^*(5 + 4\mu^*) \to 0$ and $\beta^* \gg 0$.

For $J^* > 1$ and the state points that satisfy $\beta^*(5+4\mu^*) \to 0^-$ all the microscopic states consisting of N noninteracting rhombuses are almost equally probable, since the probability of such states is proportional to $\exp[\beta^*(5 + 4\mu^*)N] \approx 1$, and for $\beta^* \gg 0$ the other states (with $H^* > 0$) are rare. We can obtain an upper bound for the grand

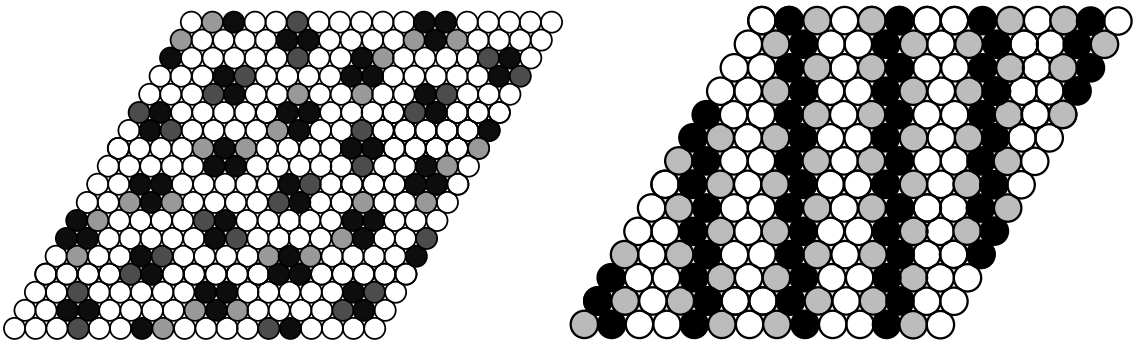

FIG. 2.50: A: Structure of the hexagonal phase H for $J^* = 3$, $T^* = 0.925$ and $\rho = 0.15364$. Site colors represent different ranges of probability for a particle to occur at the given site, namely: white - $(0, 0.065)$, light gray - $(0.206, 0.213)$, dark gray - $(0.37, 0.4)$, black - $(0.5, 0.57)$. B: Structure of the lamellar phase L_2 for $J^* = 3$, $T^* = 1$ and $\rho = 0.4905$. Sites colors represent different ranges of probability for a particle to occur at the given site, namely: white - $(0, 0.045)$, light gray - $(0.6758, 0.676)$, black - 0.9955.

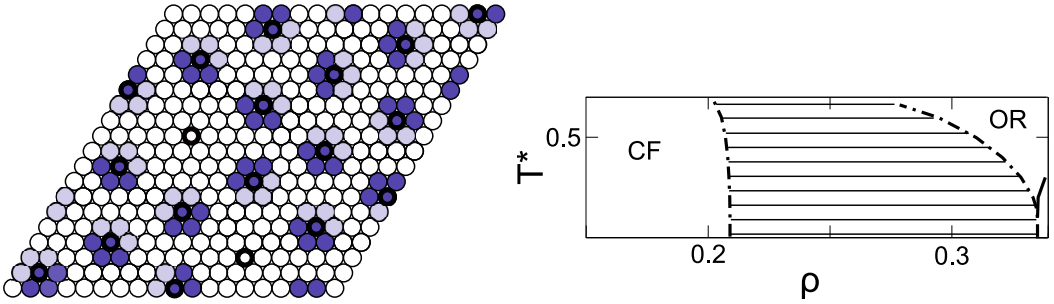

FIG. 2.51: Panel (a): The black solid circles represent sites of the sublattice considered in Sec. 2.2.3.4. The corresponding sites are occupied if they belong to a rhomboidal cluster. The dark blue color indicates one of the possible orientations of the rhomboidal clusters. Panel (b): A portion of the (ρ, T^*) phase diagram for $J^* = 3$ with the coexistence region between the cluster fluid (CF) and the OR phase (dash-dotted lines) estimated on the basis of the sublattice shown in panel (a).

potential of the cluster fluid by considering a subset of all such microscopic states. Let us consider the sublattice shown in Fig.2.51a. The sites of the sublattice can be empty, or occupied by noninteracting rhombuses. There are 6 possible orientations of the rhombuses at each site of the sublattice and the number of sublattice sites is $L^2/19$. The sublattice sites are occupied or empty independently of one another, and the grand potential and the average density can be obtained immediately,

$$\Omega^*/L^2 = -\frac{T^*}{19}\ln\left(1 + 6e^{\beta^*(5+4\mu^*)}\right) \tag{2.94}$$

and

$$\bar{\rho} = \frac{4}{19}\frac{6e^{\beta^*(5+4\mu^*)}}{1 + e^{\beta^*(5+4\mu^*)}}. \tag{2.95}$$

For $\beta^*(5+4\mu^*)=0$ we obtain $\bar{\rho}\approx 0.18$. This gives the order of magnitude of the density in the cluster fluid for $\mu^*=-5/4$. We compare the grand potential per lattice site, Eq. (2.94), with Ω^*_{MF}/L^2 calculated in the MF approximation for the OR phase. This way we obtain a rough estimate of the coexistence region between the cluster fluid and the OR phase. The corresponding portion of the phase diagram is shown in Fig.2.51b. Since only a subset of the microscopic states was considered and in the disordered phase the positions of the rhombuses are not restricted to the sublattice sites, the stability region of the CF phase is expected to be larger than shown in Fig.2.51b. By analogy we expect that the molten lamella phase found at the coexistence between the OR and lamellar phases for $T^*=0$ will remain stable for $T^*>0$ for the state points that satisfy $\beta^*(2\mu^*+5-6J^*)\to 0$.

2.2.4 Phase diagram - results of the Monte Carlo simulation

In this section we present the phase diagram obtained by the MC simulation methods. The techniques used for the derivation (the Metropolis algorithm, thermodynamic integration or parallel tempering scheme) are standard methods [95, 96]. However, for the clarity of the presentation they will be briefly described in Sec. 2.2.4.1. Sec. 2.2.4.2 is devoted to specific methods used for computation of phase equilibria between the OR and F phases, while Sec. 2.2.4.3 and Sec. 2.2.4.3 describe the lamellar phases: the order parameters used for their identification and the phase transitions.

2.2.4.1 Simulation methodology

Grand Canonical Monte Carlo procedure

The simulation procedures make use of the Metropolis criterion [97] implemented for two kinds of MC steps: *translations* of one particle and particle *insertions* or *deletions*. For each step a trial configuration is generated and it is accepted with the probability: $\min[1,\exp(-\beta\Delta H)]$, where ΔH is the change of the Hamiltonian in the trial step. The trial configuration for a particle *translation* is generated by moving a randomly chosen particle to a randomly chosen empty site, which is equivalent to choosing two sites of the lattice, x and x', so that $\hat{\rho}(x)\neq\hat{\rho}(x')$, and interchange their occupancy states, so that $\hat{\rho}^{trial}(x)=\hat{\rho}(x')$, and $\hat{\rho}^{trial}(x')=\hat{\rho}(x)$. A Monte Carlo step characteristic for the Grand Canonical simulations implies the *insertion*

or *deletion* of one particle, this is achieved by choosing at random one site of the lattice, x, and generating the trial configuration by *flipping* its occupancy state from its current value $\hat{\rho}(x)$ to the trial value $\hat{\rho}^{trial}(x) = 1 - \hat{\rho}(x)$.

Thermodynamic integration

According to the GS analysis for $J^* = 3$ and at low temperature we expect the presence of the lamellar phase with $\rho = 1/2$ for values of $\mu^* \approx 6$, and the ordered rhombus phase for $-5/4 < \mu^* < 11/2$. At high temperature, the state of the sites should be essentially dictated by the value of the chemical potential, i.e., we will have a disordered phase with the average density given as $\rho = e^{\beta\mu}/(1+e^{\beta\mu})$. Then we can expect some phase transition(s) connecting the high-temperature disordered phase with the low-temperature ordered phases. At low temperature and $\mu^* \approx -5/4$ we can expect to find the disordered CF phase composed of different aggregates of particles (mainly four particle clusters), while for increasing chemical potential the system should exhibit a phase transition into the OR phase. Similarly, for $\mu^* \approx 11/2$ the molten lamella (ML) phase present in the GS is expected to be stable for $T > 0$. Taking the above facts into account we have used thermodynamic integration (TI) techniques [95, 96, 98] to locate the phase transitions. These techniques are based on the numerical integration of thermodynamic potentials using simulation results. The integration of the grand potential is carried out as

$$\Omega(L,\beta,\mu_1) = \Omega(L,\beta,\mu_0) - L^2 \int_{\mu_0}^{\mu_1} \check{\rho}(L,\beta,\mu)\,\mathrm{d}\mu, \quad \text{where } \check{\rho} \equiv \frac{\langle N \rangle}{L^2}, \tag{2.96}$$

when the temperature is fixed, or:

$$\Omega(L,\beta_1,\mu) = \Omega(L,\beta_0,\mu) + \int_{\beta_0}^{\beta_1} H(L,\beta,\mu)\,\mathrm{d}\beta, \tag{2.97}$$

for fixed value of the chemical potential. The values of the grand potential in the thermodynamic limit are known for the ordered phases at low temperature, for the high-temperature limit $\beta = 0$, and for the vacuum system $\rho = 0$.

In the first attempt to compute the phase diagram we run sequences of simulations starting either from high temperatures ($\beta = 0$) or from low temperatures. In the latter case we used initial configurations of the corresponding stable phases at the GS. Then by applying TI we could get a draft of the shape of the phase diagram.

Parallel tempering

We found some features in the results which introduced some difficulty in the analysis. When considering the sequences of simulations starting from high temperature, we found non-monotonic behavior with the system size for different properties. In addition to the expected transitions corresponding to the *melting* of the GS ordered structures, we found signatures of a number of additional thermodynamic transitions, which seemed to be either continuous or weakly first-order. Moreover, in some cases the number of these apparent transitions depends on the system size: As one increases the system size for a given value of μ, the number of these transitions can increase. The presence of these transitions, and the atypical dependence of the results on the system size moved us to make use of parallel tempering (or replica exchange) MC sampling [99, 100] in order to improve the sampling quality of the simulation.

The aim of using the parallel tempering scheme is to allow the system for jumps over high potential barriers. This algorithm involves simulations of many system copies each with different temperature values. It allows for the exchange of configurations between the i-th and j-th copy with the probability of transition

$$p_t = min\big(1, e^{(H_i - H_j)(\beta_i - \beta_j)}\big). \tag{2.98}$$

Phase diagram

The phase diagram obtained *via* MC simulation is presented in Fig. 2.52. In order to get a reliable estimation of the phase diagram, we have focused the simulation effort into a relatively large system, $L = 120$. Other system sizes were also considered, but only for some representative values of the temperature and the chemical potential. We have found, however, that the topology of the phase diagram did not change and only minor displacements of the transitions loci are to be expected. In what follows we describe in detail the different phase equilibria shown in the diagram.

2.2.4.2 Ordered rhombus and fluid phases

We start the phase diagram presentation with the description of the phase transition between the ordered rhombus phase and the fluid phase. Firstly, we discuss the limit of low temperature where the standard MC algorithms described in Sec.2.2.4.1 are

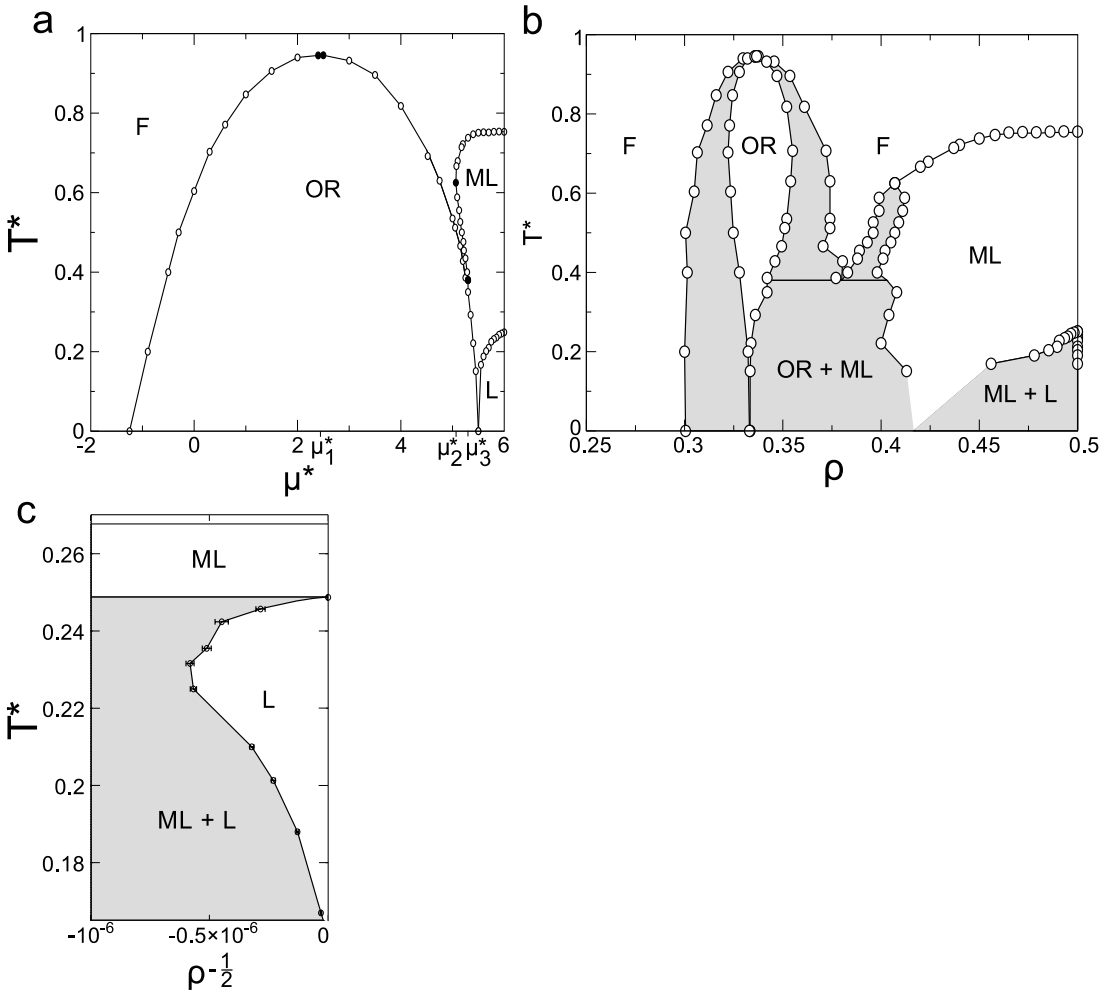

FIG. 2.52: Phase diagram in the temperature-chemical potential (a) and in the temperature-density (b) planes. OR stands for ordered-rhombus phase, F (fluid) for the disordered phase(s), L represents ordered lamellas, and ML molten lamellas.

inefficient and the use of different simulation technique was necessary. Secondly, we describe the results for the OR - F transition at finite temperature obtained with standard algorithms.

The limit of low temperature

It is possible to compute the phase equilibria between the OR and CF phases in the limit $T \to 0$ (for $\mu^* = -5/4$). In this limit the system is composed exclusively by noninteracting rhomboidal clusters. In order to analyze the possible phase transition of the system we consider the concavity/convexity properties of the entropy as a function of the density of these clusters (See Refs. [80, 101] for similar situations, in which a low density phase can appear due to the presence of repulsive interactions between particles). In short, we can simulate an athermal lattice gas model where

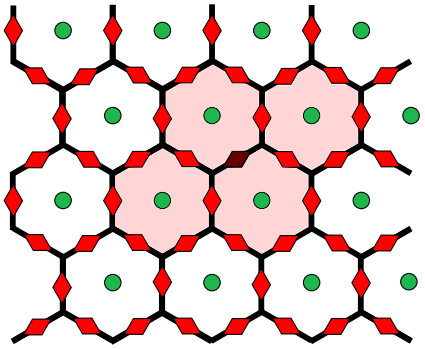

FIG. 2.53: The Kagomé lattice. The sites of the original triangular lattice are indicated by the filled green circles. Rhomboidal clusters (shaded region) are represented by the occupied nodes of the Kagomé lattice (filled red rhombuses).

the elementary units are four-particle clusters, with exclusion rules compatible with the lack of repulsive interactions between clusters in the SALR model. Such hard-core lattice gas model allowed us to compute the phase equilibria at conditions for which our standard MC algorithm is inefficient.

The possible positions of a rhomboidal cluster on the triangular lattice with L^2 sites can be described by considering the *bond* connecting the two sites of the rhombus that have three particles in the nearest neighbor positions. These *bond* positions define a Kagomé lattice [102] (See Fig.2.53). Each rhombus of the SALR model on the triangular lattice is mapped on a site of the Kagomé lattice (small solid rhombuses in Fig.2.53). Taking into account the interactions of the model it is easy to determine the exclusion rules on the new lattice, i.e. which sites cannot be occupied due to the presence of a *particle* (occupied site).

The simulation of the hard-core lattice model is performed using two types of moves: translations and changes of the number of particles. Translations are carried out by (1) Selection of a particle at random, (2) Deleting it from the system and updating the list of non-excluded positions, and (3) Inserting it back in one of the allowed positions (chosen at random with equal probabilities). The second type of moves involves changes in the number of particles. This is performed by choosing at random with equal probabilities either an insertion or a deletion attempt: If insertion is chosen and there are allowed positions, one of these allowed positions is selected at random, and acceptance rules are applied. If there are no allowed positions the insertion attempt is directly rejected. Deletion attempts are done by choosing at random a particle in the system to be removed.

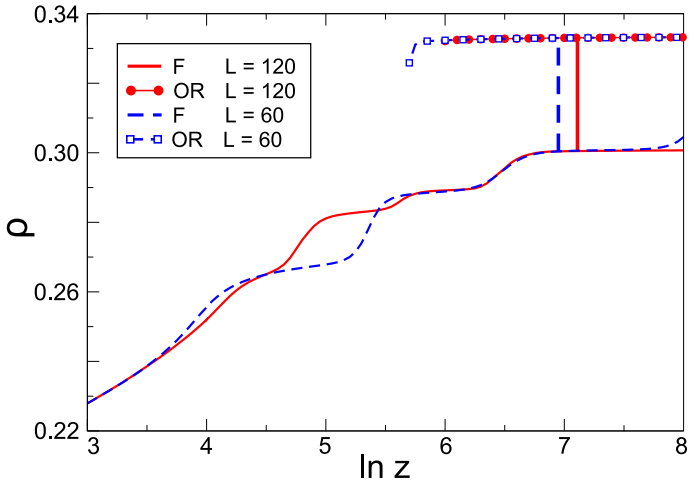

FIG. 2.54: Density as a function of the logarithm of the fugacity for the hard-core lattice gas model representing the F-OR equilibrium for $T \to 0$. Continuous line represents the results for the fluid phase and $L = 120$. Dashed lines are used for the fluid phase and $L = 60$. Lines with symbols mark the results for the OR phase (filled circles for $L = 120$, and squares for $L = 60$). Thick vertical lines mark the estimates for the F-OR transition ($\ln z \simeq 7$).

Considering detailed balance [96] the ratio between the acceptance probabilities, $A(N \to N')$ of an insertion and its reversal deletion move must fulfil

$$\frac{A(N \to N+1)}{A(N+1 \to N)} = \frac{(N+1)z}{N_{pos}(N)}, \tag{2.99}$$

where $z \equiv \exp[\beta\mu]$ is the fugacity, and $N_{pos}(N)$ is the number of non-excluded positions in the configuration with N particles. Using this simulation procedure for $L = 120$, coupled with parallel tempering and thermodynamic integration, we obtain the densities of the two phases at coexistence: $\rho_F \simeq 0.30$, and $\rho_{OR} \simeq 0.3330$. This result is consistent with the estimate $\rho > 0.2$ for the density in the CF phase at the coexistence with the OR phase obtained beyond MF (Sec. 2.2.3.4).

Interesting features appear at the plots of the density of the fluid phase as a function of z. For values of z close to the transition, but still in the region where the fluid phase is the stable one, the quantity: $(\partial\rho/\partial(\ln z))$ shows an oscillatory behavior. In the plot of ρ vs. $\ln z$ (Fig. 2.54) signatures of apparent weak transitions (steps-like changes in the density) can be seen. The number of these steps seems to increase with the system size, which implies that the results for the density of the fluid phase close to the transition depend on L. We cannot provide a definitive explanation of this behavior. It might occur that in the fluid phase, close to the transition, the system exhibits a short-range order, with small domains of rhombi arranged according to the

OR structure. The size of these domains is expected to increase with z, the growth of the domains might be conditioned by the effects of the PBC, which impose some correlations which might be relevant as the correlation length of the short-range order increases. Moreover, the use of a lattice model implies additional spatial and orientational correlations which might amplify the effects described above. Within this scenario we could expect that the lines ρ vs $\ln z$ will become smoother for larger system sizes.

Ordered rhombus - fluid transitions at finite temperature

For $T > 0$ we used the standard algorithms described in Sec. 2.2.4.1. The results showed that the OR phase melts irreversibly upon increasing T^*. However, the simulations give no evidence that the cluster fluid and the dilute gas are distinct phases. For this reason, at finite temperature F, instead of CF, will be used to denote the disordered phase.

In order to determine the loci of the OR melting transitions we firstly assumed that for $-1.25 < \mu^* \leq 5.50$ only the OR and the F phases can stabilize. Simulation results suggested that the above assumption was appropriate provided that $\mu^* < \mu_2^* \simeq 5.07$. For values in the range $\mu^* \in [\mu_2^*, 5.5]$, after the melting of the OR phase, the system can adopt structures with lamellar character that exhibit orientational order, but that case will be discussed later in Sec. 2.2.4.3.

For $\mu^* < \mu_1^* \simeq 2.4$ the F phase is less dense than the OR phase. As one increases the chemical potential from $\mu^* = -1.25$, the temperature at the phase equilibrium increases and for temperatures $T^* > 0.5$ the density of the fluid branch also increases. At $\mu^* = \mu_1^*$ the coexistence line reaches a maximum in temperature at $T_2^* \simeq 0.95$. At these conditions both phases have the same density $\rho \simeq 1/3$, however the OR-F phase transition is still first-order, with a discontinuity in the energy [80, 101]. For $\mu^* > \mu_1^*$ the density is larger in the F phase at F-OR coexistence.

The F phase shows different types of structures depending on the values of μ^*, and T^*. At low temperature, $T^* \lesssim 0.5$, and low values of μ^* the system can be described as a gas formed mostly by four-particle clusters (rhombuses, as in Fig. 2.44f), resembling the CF phase found for $\mu^* = -5/4$ at $T = 0$. These clusters are favored by energy considerations (Sec. 2.2.4.2) and they will be predominant for not too low densities. At higher temperature and density this phase appears as a mixture of

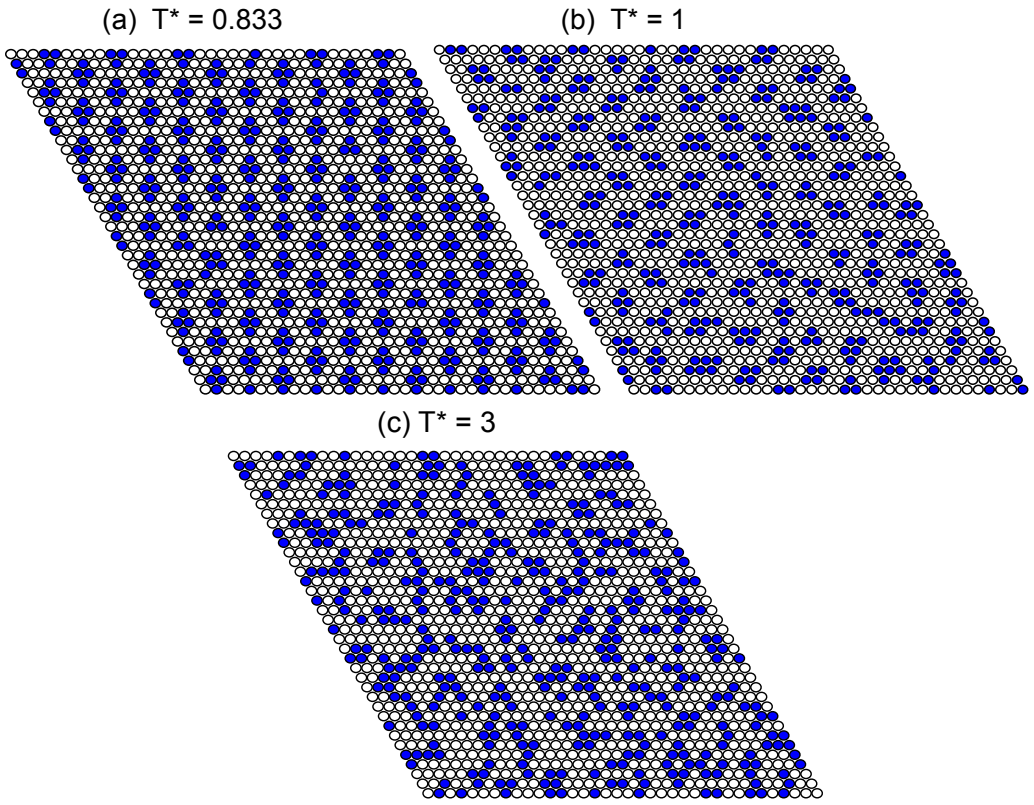

FIG. 2.55: Representative configurations for $\mu^* = 1$ with (a) $T^* = 0.833$ (OR), (b) $T^* = 1$ (fluid) and (c) $T^* = 3$ (fluid).

clusters of different sizes, which eventually percolate as the chemical potential approaches $\mu^* = 6$ [102]. Typical snapshots of the high-T OR and F phases for $\mu^* = 1$ are shown in Fig.2.55.

2.2.4.3 The lamellar phases

In this section we focus on the lamellar phases present in the phase diagram. In order to characterize them and determine the loci of the phase transitions we introduce two order parameters (OP): the translational OP which quantifies at what level the stable configuration consists of identical stripes, thus it says how much the stable configuration resembles the GS lamellar cofiguration (panel (c) and (d) of Fig. 2.43), and the orientational OP which describes if the particles self-assemble into structures with a dominant orientation. The simulation results show that the two OP have values close to one at low temperature lamellar phase L. Upon heating the system first looses the translational order and next the orientational order. We call the phase which has the orientational order, but lacks the translational order, *the molten lamella* phase and its description is one of the main thesis results.

Order parameters

An ordered lamellar phase, characterized by the long-range translational and orientational order, is stable at low temperature and for the chemical potential values close to $\mu^* = 6$. We have found that for this value of the chemical potential nontrivial qualitative changes of the stable structure occur if one changes the system temperature. In Fig. 2.56 we show representative configurations for the system at $\mu^* = 6$ and different temperatures. At high temperatures isotropic configurations of the system are stable (panel (a)). Note, however that although in panel (b) short lamella-like stripes and other cluster structures with local period of 4 in one direction are present, the structure has not any preferential orientation as well. A structure shown in panel (c) consists of lamellar pieces that have a preferential orientation, but since the structure has many defects it is still qualitatively different then the ground state lamellar phase. In panel (d) probably a metastable configuration of the same phase is plotted. Finally, at sufficiently low T an ordered lamellar structure with no defects stabilizes (panel (e)). In order to quantify these changes in the structures, and to analyze how the ordered structures are transformed, in what follows we define appropriate order parameters.

Translational order parameter

Translational order can be checked for a given set of simulation configurations, using the following procedure for each of the three main directions of the lattice: For each row $r = 0, 1, \ldots, L-1$ in the selected direction $\mathbf{e}_\alpha$, where $\alpha = 1, 2$ or 3, we consider the states of its j sites: $\hat{\rho}(r, j) \equiv \hat{\rho}(j\hat{\mathbf{e}}_\alpha + r\hat{\mathbf{e}}_\beta)$ for $j = 0, 1, 2, \cdots, L-1$ and $\beta \neq \alpha$. The four-site periodicity in the row r in direction α can be checked by computing the parameters $p_{r\alpha}(k)$

$$p_{r\alpha}(k) = \frac{1}{L}\left|\sum_{j=0}^{L-1}\{[2\hat{\rho}\,(r,j)-1]\,g_k(j)\}\right|, \tag{2.100}$$

where $g_k(i)$ takes the form of a square wave (Fig.2.57) with the values

$$g_k(i) = \begin{cases} 1 & ; \quad \text{if} \quad \text{mod}\,(i+k,4) < 2 \\ -1 & ; \quad \text{if} \quad \text{mod}\,(i+k,4) \geq 2, \end{cases} \tag{2.101}$$

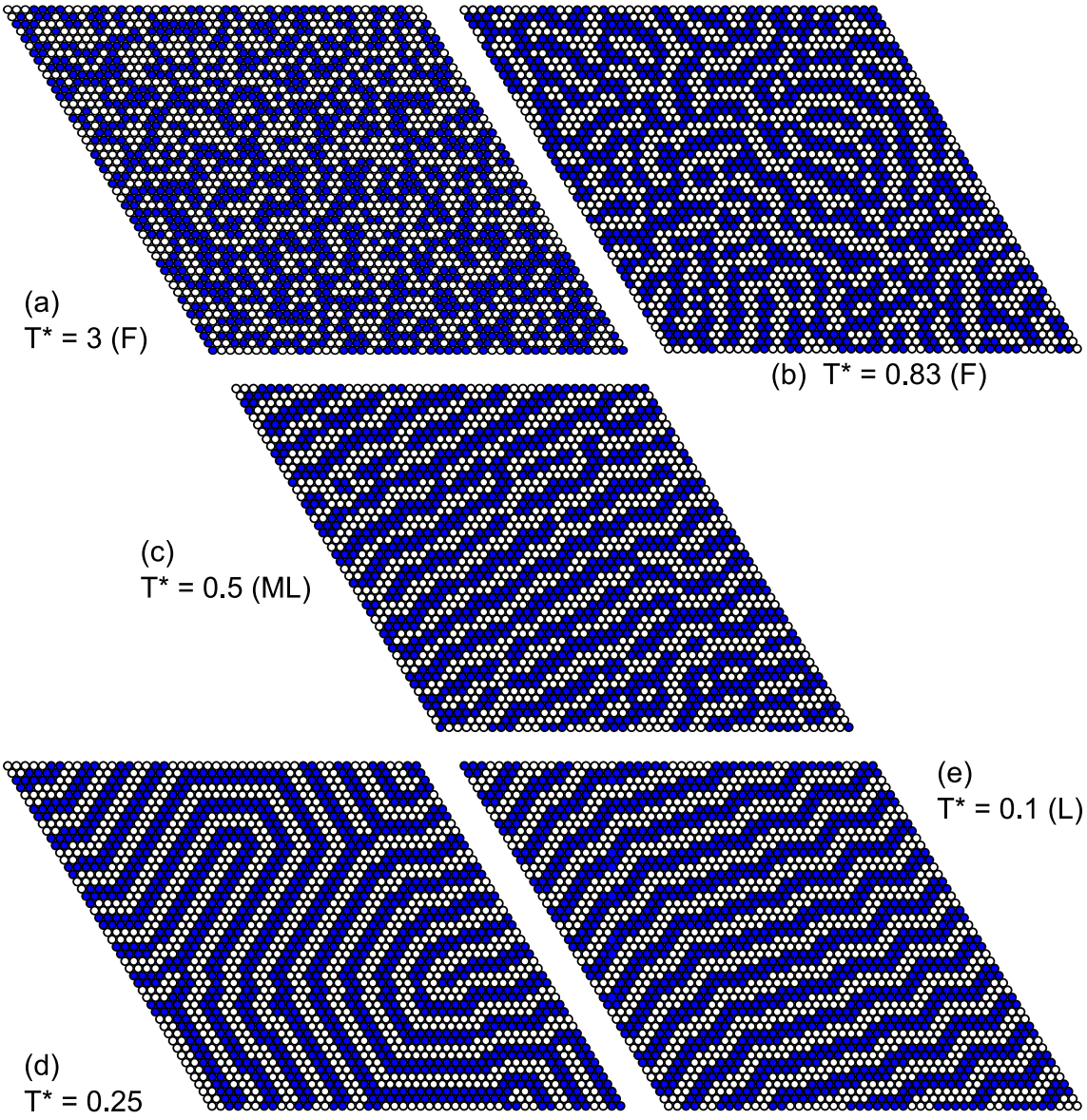

FIG. 2.56: Representative configurations for the lattice SALR model at $\mu^* = 6$ ($\langle\rho\rangle = 1/2$). The system size is $L = 48$.

where $k = 0$ or 1 and mod is the Modulo operation. A global translational order parameter can be defined for the selected direction, say $\mathbf{e}_\alpha$, by combining the results for $k = 0$ and $k = 1$:

$$P_\alpha = \frac{1}{L}\sum_{r=0}^{L-1} \max\left[p_{r\alpha}(0), p_{r\alpha}(1)\right]. \tag{2.102}$$

Lamellar structures with long-range translational order can be identified as those structures for which the order parameter P defined as

$$P \equiv \max[\langle P_1\rangle, \langle P_2\rangle, \langle P_3\rangle], \tag{2.103}$$

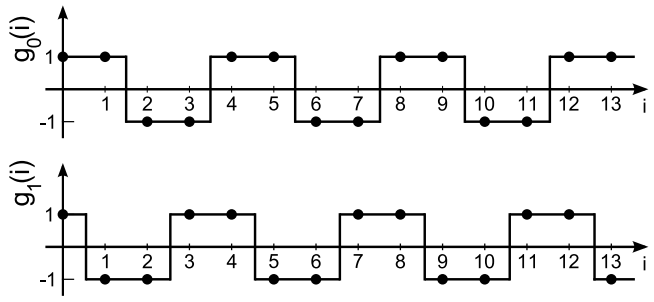

FIG. 2.57: The function $g_k(i)$ (see Eq.2.101)) for $k = 0$ (top) and $k = 1$ (bottom). The lines connecting values of the function for $i = 0, 1, 2, \ldots$ are to guide the eyes.

is close to 1.

Lamellar stripes and orientational order parameter

First, we need criteria to decide if a group of particles in a given region of the system belongs to a lamellar stripe. We consider sets of three sites forming elementary triangles on the lattice. The triangles are the units which we will characterize as either lamellar or non-lamellar. Only triangles with 3 sites occupied qualify to be lamellar, such triangles will by denoted as T_3. Given a T_3 triangle, we look at

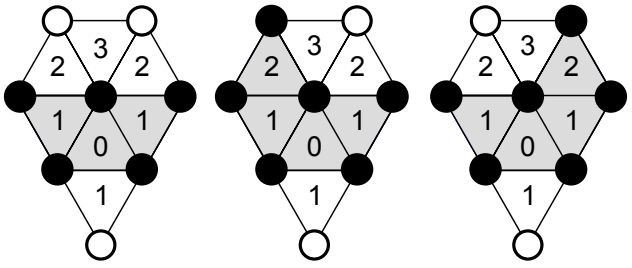

FIG. 2.58: Sketch of the definition of the lamellar triangle. Filled circles represent occupied sites, empty circles are vacant sites.

the structure of its neighbor triangles. Lets consider the triangle labelled as 0 in the local structures plotted in Fig. 2.58. The triangle 0 can be a lamellar triangle if precisely two of its nearest-neighbor triangles (labelled as 1 in the figure) have their three sites occupied. Thus, to be lamellar, a T_3 triangle must have 2 out of 3 neighbors that are also from the T_3 class. Note that the second criterion excludes the T_3 triangles which belong to the OR structure (Fig. 2.2b). Finally, in order to exclude the triangles which belong to seven-site hexagonal clusters, we consider the triangles labelled as 2 and 3. We say that the triangle 0 is a lamellar triangle if, in addition to the fulfillment of the previous conditions, the triangle labelled as 3 is not

fully occupied. According to these rules, the triangle 0 in all panels of Fig. 2.58 is lamellar.

In addition to classifying the fully occupied triangles as lamellar or non-lamellar, by checking which two out of the three nearest-neighbor triangles are fully occupied, this method also gives the orientation of the lamellar stripe. There are three possible orientations which coincide with the principal directions on the triangular lattice.

Taking into account the ground state structures for the lamellar phases, and the ability of the lamellar stripes to bend (See Fig. 2.45 and 2.56), we compute separately the number of lamellar triangles that exhibit one of the three possible orientations: $N_{LT}^{(1)}$, $N_{LT}^{(2)}$, and $N_{LT}^{(3)}$. If the orientational order exists, two of the orientations will be preferred by the lamellar triangles. Accordingly, we have defined the orientational order parameter for lamellas as:

$$O_L = \frac{N_{LT} - 3\left[\min\left(N_{LT}^{(1)}, N_{LT}^{(2)}, N_{LT}^{(3)}\right)\right]}{N_{LT}}, \tag{2.104}$$

where $N_{LT} = \sum_{i=1}^{3} N_{LT}^{(i)}$ is the total number of lamellar triangles. If no lamellar orientational order exists, then O_L will be close to zero, whereas it will approach $O_L = 1$ if the lamellar stripes exhibit preferential orientations.

Phase transitions of lamellas

At low temperatures the structure of the ordered lamellar phase hardly deviates from the GS, and therefore one can consider directly the ideal structure of this phase and its entropy to compute $\Omega(L, \beta, \mu)$. We found that the ordered lamellas melt irreversibly to produce a phase with orientational, but without translational order. In Fig. 2.59 we show some results for the case of $\mu^* = 6$ and $L = 120$. The melting temperature is relatively low ($T^* \approx 0.24$ for $L = 120$ and $\mu^* = 6$) and decreases for $\mu^* < 6$ (See Fig. 2.52).

Simulation results indicate that molten lamellas with only orientational order is a distinct phase (See Fig. 2.59). Looking at the variation of the order parameter O_L with temperature a sharp transition can be observed. The temperature where this transition occurs depends on μ, and on the system size L. At this transition the heat capacity $c_\mu \equiv L^{-2}(\partial H/\partial T)_{L,\mu}$, has a clear peak. The position and the height of this peak have non-monotonic dependences with L (in the range $24 \leq L \leq 120$), but the transition is observed for all the system sizes. In spite of the non-monotonic

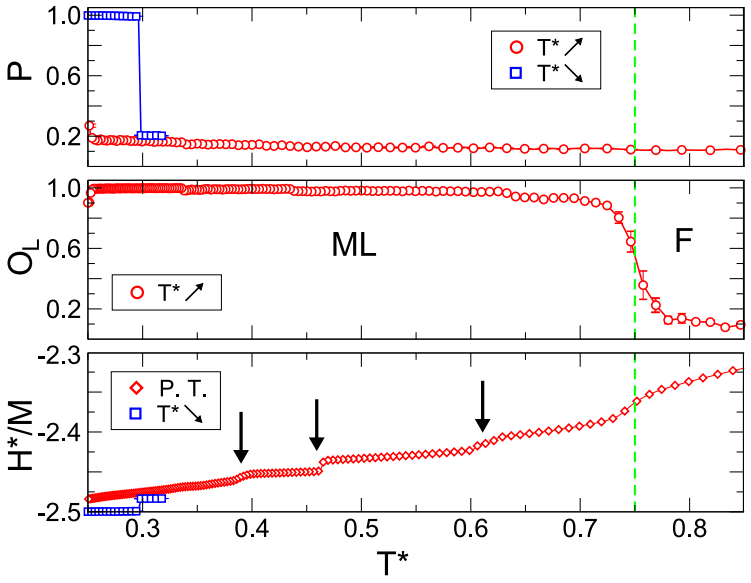

FIG. 2.59: Simulation results for the analysis of phase transitions in the lamella region. $\mu^* = 6$, $L = 120$. In the top panel we plot the translational order parameter, P (See Eq. (2.103)), as a function of the temperature: Circles mark the results for a sequence of simulations starting at high temperature, squares represent the results when starting at low T^* with the initial configuration corresponding to one of the GS lamellar microstates. Only in the latter case the system exhibits translational order, which is lost when the ordered lamella melts irreversibly at $T^* \simeq 0.3$. In the central panel the orientational order parameter for lamellas, O_L (See Eq. (2.104)) is plotted for a sequence of simulations starting at high temperature: the order-disorder transition at $T^* \simeq 0.75$, marked with the dashed vertical lines, can be clearly appreciated. Finally, in the lower panel the Grand Canonical Energy H^* per site is plotted: Diamonds mark the results obtained using the Parallel tempering scheme starting from disordered configurations, whereas squares represent the results for the sequence of simulations starting from the ground state configuration. The results from Parallel tempering exhibit signatures of a likely continuous transition at the temperature where the O_L indicated an order-disorder transition. In addition some step-like transitions (denoted by arrows) are observed below that temperature.

dependence of the local maximum value of the heat capacity $c_\mu^{\max}$(L) with L, the value of $c_\mu^{\max}$ seems to increase slightly with L (see Fig. 2.60). These results suggest that the transition is continuous in the range $5.5 < \mu^* \leq 6.0$. A weakly first-order transition, however, cannot be ruled out.

For temperatures below this order-disorder transition, a number of apparent weak transitions was found. As observed for the F phase close to the F-OR transition, the number of these transitions increases with the system size, whereas the individual jumps in H/L^2 and ρ (for $\mu^* < 6$) decrease with L. Visual inspection of the configurations (Fig.2.56) and of the plots of the order parameters as a function of the

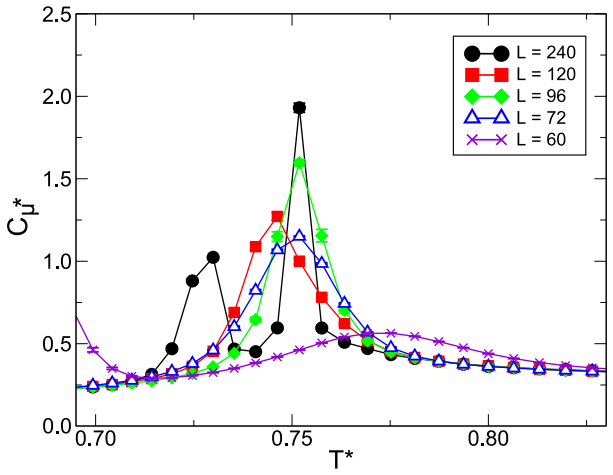

FIG. 2.60: The heat capacity at the constant chemical potential c_{μ^*} for $\mu^* = 6$ and different system sizes. c_{μ^*} exhibits a clear peak at the F-ML transition, but also non-monotonic behavior of its position and height for different system sizes. For $L = 240$ two peaks can be observed, the one at $T^* \approx 0.75$ corresponds to the F-ML phase transitions, whereas that appearing at $T^* \approx 0.72$ is associated with a step-like transition similar to the transitions shown in Fig. 2.59 for L =120.

temperature (Fig.2.59) did not provide any clear conclusion about the nature of these apparent transitions. As in the F case this behavior could be due to effects of compatibility of the stable patterns with the PBC, and the restrictions introduced by considering a lattice model. Note also that the MF stability analysis predicts noninteger period $2\pi/k_b$ of the density oscillations (Sec.2.2.3), which for the lattice system together with the PBC can lead to strong and nonmonotonic dependence on L.

The temperature of both the F-ML and the ML-L phase transitions depends on the chemical potential, and for both transitions assumes the maximum for $\mu^* = 6$.

The lines plotted on the (ρ, T) diagram for the threshold value of $\mu^* = 5.5$ have to be seen as conjectural. The simulation results showed that for $L = 48, 60$, the parallel tempering procedure reaches at low temperature configurations with the energy of GS and $\rho \approx 5/12$, which correspond to the ML phase shown in Figure. 2.43 h. However, for $L = 120$ the simulation scheme did not reach these GS configurations. Nevertheless, the trends of the properties suggest that also in this case the ML will be the stable phase.

A complex phase behavior was found for $\mu_2^* \leq \mu^* < 5.5$ (with $\mu_2^* \simeq 5.07$ for $L = 120$). Although the GS for this range of the chemical potential is the OR phase, on cooling the system at constant μ one finds a F $\rightarrow$ ML transition at some temperature $T_{F-ML}(\mu, L)$. Depending on the value of μ this ML phase can eventually melt again at a lower temperature, and the isotropic phase is recovered. Similar re-entrant melting

of the periodic phase was found in MF in the one-dimensional version of the present model (Fig. 2.49). This reentrant melting appears for $\mu_2^* \leq \mu \leq \mu_3^* \simeq 5.30$, and the transition seems to be discontinuous, with a finite change both in H/L^2 and in the density. Further cooling of the system transforms the fluid into the OR phase in a discontinuous transition.

The reentrant behavior of the F-ML tranistion can be observed in the (μ, T) representation of the phase diagram shown in Fig.2.52. The results for $L = 120$ suggest that the transition changes from a continuous to a weakly first order at a temperature $T^* \simeq 0.6$ (Fig.2.52b), and that this change occurs at, or close to, μ_2^*, i.e. the minimum value of the chemical potential with the F-ML equilibrium.

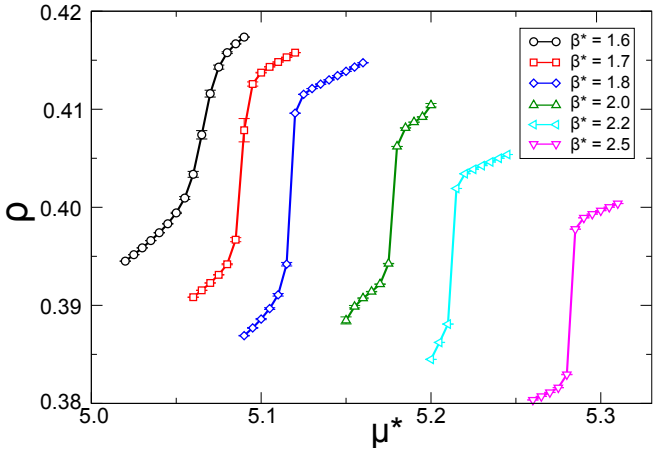

FIG. 2.61: Density as a function of the chemical potential for different values of β^*.

The calculation of the F-ML transition below $T^* \simeq 0.6$ was carried out by fixing the temperature and running parallel tempering MC simulation using several values of the chemical potential. The plots of the density as a function of the chemical potential indicated a continuous transition for $\beta^* = 1.60$, whereas for $\beta^* \geq 1.70$, a clear discontinuity was observed (Fig.2.61). From these plots it was possible to get estimates for both, the chemical potential at the transition, and the density of the two phases.

The topology of the phase diagram implies the existence of a triple point where the OR, F, and ML phases coexist. Using the results of simulations with $L = 120$ we have estimated the locus of this point as: $\mu_{TP}^* = \mu_3^* \simeq 5.3$, $T_{TP}^* \simeq 0.38$.

2.2.5 Comparison between phase diagrams obtained by the Mean-Field and the Monte Carlo techniques.

Let us compare the MF and the MC phase diagrams for the repulsion to attraction ratio $J^* = 3$. In the (μ^*, T^*) variables the phase diagrams (Fig. 2.49 and Fig.2.52) are similar for low T^*, except that in MC the stability region of the ML phase extends down to $T^* = 0$, while in MF the L_2 phase appears for $T^* > 0.65$. The relation between the ML and the L_2 phases obtained in MC and in MF respectively is not entirely obvious. In the L_2 phase the density oscillates in one of the lattice directions $\mathbf{e}_i$, i.e the distinguished directions in the L_2 and the ML phases are the same. The structure of the ML phase resembles the structure of the L phase with defects. The defects do not destroy the orientational order, but the translational order is lost (see Fig.2.56c). We attribute the stability of the ML phase for $T^* \to 0$ to the effect of the degeneracy of the GS that cannot be properly described within MF.

For high T^* the differences between the MF and MC phase diagrams in the (μ^*, T^*) variables are more pronounced. In MF the stability region of the ordered phases extends to much higher temperatures than found by MC simulation. Moreover, for high T^* the H (hexagonal) phase with translational and without orientational order of the rhomboidal clusters appears in the MF, but not in the MC phase diagram. Although we were not able to identify the H phase using MC simulation, we cannot rule out the physical significance of this MF result. Notice that in our analysis of the simulation results (see for instance Fig. 2.54) we found some anomalous behavior both in the equations of state (either $\rho(T)$ at constant μ, or $\rho(\mu)$ at constant T), and in the dependence of the results on the system size in the putative region of the F phase close to the transition to the OR phase. In this regard, it is interesting to point out that other models on the triangular lattice and related models containing competing interactions [91, 103–105] exhibit modulated structures, and the phenomenology of Devil's staircase [106]. Our simulation analysis cannot answer if it is the case for our lattice SALR model, but both the behavior of the fluid phase close to the transition to the OR phase, and the results in the region described as molten lamellas exhibit some similarities with those reported for this kind of systems.

Further differences between the phase diagrams concern the sequences of phase transitions for high T^*. In MF the L_2 phase coexists with the H phase for high T^*, and extends to higher T^* than the OR phase. In contrast, in MC we find that the

ML phase coexists with the disordered F phase for high T^*, and extends to lower T^* than the OR phase. We attribute the stability of the F phase between the OR and ML phases to the effects of fluctuations.

In our MC simulation we do not discriminate between possibly distinct fluid F phases, despite signatures of the phase transitions both in the density and in the energy. Thus, the region marked as F in Fig.2.52 might in fact represent stability of a few different phases (see the snapshots in Fig.2.56).

The differences between the MF and MC phase diagrams are even stronger in the (ρ, T^*) variables. The density ranges of the stability regions of the ordered phases and the two-phase regions are quite different in MF and in MC. The exception is the ordered L phase. It is stable for very narrow range of densities, $\rho \approx 1/2$ both in MF and in MC.

Based on the comparison of the MF and MC phase diagrams we conclude that if the amplitude of the density wave in an orderd phase is small in MF, then only a short-range order (such as in Fig 2.56b) is left in a presence of fluctuations. The MF ordered phases with a large amplitude of the density oscillations remain stable in a presence of fluctuations. However, instead of a coexistence of two different ordered phases, we find a transition between each of them and a less ordered phase above a triple point. We found the OR-ML-L triple point at $T^* = 0$, and the OR-F-ML triple point at $T^* \simeq 0.38$. We may observe that the temperature of the triple point is higher when the coexisting phases are less ordered.

2.2.6 Short summary

We have studied a model of the colloidal self-assembly at an interface between two phases, that is, in two-dimensional space. We have derived its ground state ($T^* = 0$) (Sec. 2.2.2) and presented the results for the phase diagram ($T^* > 0$) within approximate theories (2.2.3), and Monte Carlo simulation (Sec. 2.2.4). The main results are:

- The ground state shows stability regions of periodically distributed clusters, bubbles or stripes (Fig.2.44).
- The ground state at the coexistence between the vacuum and cluster phases, and between the cluster and stripe phases is strongly degenerated. The degeneracy leads to positive entropy per lattice site at $T^* = 0$ and vanishing

surface tension. We interpret the states stable at the coexistences as different disordered phases.

- The approximate theories predict stability of the cluster fluid phase at low T (Fig. 2.51), and the cluster phase with positional order, but without orientational order at high T (Fig. 2.49). Both cluster phases were not distinguished as distinct phases found by the MC simulation techniques, despite different structures visible in the snapshots.
- The phase diagram obtained *via* Monte Carlo simulations (Fig. 2.49) shows stability of two lamellar phases. The lamellar phase characterized by orientational and translational order, and the molten lamella phase which has only orientational order, but no translational order. Stability of the molten lamella phase is a novelty in comparison to previously published phase diagrams of the SALR systems [35, 39, 107].

2.3 Self-assembly in the bulk - summary

In order to investigate the impact of boundary conditions on self-assembling systems we have to know their general bulk properties. For that reason, we have developed two generic models with pair potentials that can lead to spontaneous pattern formation: the model for colloidal self-assembly induced by isotropic competing interactions and the model for amphiphilic self-assembly with anisotropic pair interactions. We have started our investigation by considering one-dimensional models. Our results reveal that the two systems, beside the common topology of the mean-field phase diagram at high T, share many properties at low T. We have shown that for the two systems the equation of state, the correlation function and the specific heat are qualitatively similar, and that the ground states also have the same topology. What is more, the systems share such specific property as infinite degeneration of the ground state at the coexistence lines, which for both models leads to vanishing surface tensions between the coexisting phases.

Because of the strong similarities between the properties of the amphiphilic system and the colloidal system with the SALR potential, we decided to continue the study of bulk properties of self-assembly only for the colloidal system. We have introduced a two-dimensional model for self-assembly of nanoparticles or proteins on surfaces,

interfaces or membranes. We have assumed nearest-neighbor attraction and third-neighbor repulsion. Such interaction ranges were found for example for lysozyme molecules in water [66]. We have determined the ground state of the model, the phase diagram within the mean-field approximation and the phase diagram obtained *via* Monte Carlo simulation.

The topologies of the ground states of the one- and two-dimensional models are similar, with the proviso that the region of stability of the 1d periodic phase in 2d is splitted between different inhomogeneous phases: periodically distributed clusters, bubbles or stripes. Independently of dimensionality, the ground state is strongly degenerated. The ground state of the 1d model is degenerated at the coexistence between the periodic and homogeneous phases, while the 2d model is degenerated additionally at the coexistence between ordered phases of different symmetry. Due to the infinite degeneracy, the entropy per site at the coexistence between different ordered phases does not vanish. We identify the disordered states stable at the phase coexistence between vacuum and hexagonally ordered clusters (Fig.2.44a,c) as a disordered cluster fluid. The disordered states stable at the coexistence between the ordered clusters and stripes (Fig.2.44e-j) correspond to a disordered phase called molten lamella. The structures stable at the above phase coexistences include the interface between the two phases. Thus, the surface tension vanishes. **We conclude that, because of its ubiquity, the vanishing surface tension at the ground state coexistence may be a universal property of self-assembling systems.**

The λ lines, which describe the MF boundary of stability of the disordered phase, have the same qualitative dependence on the strength of the repulsion for both 1d and 2d models (see Fig. 2.4 and 2.48 respectively). What is more, also for 3d axial next-nearest-neighbor Ising model similar dependence was found [70]. What seems to be surprising, in all the cases for a range of moderate repulsions the system is unstable with respect to a periodic ordering for high T^* and with respect to a gas-liquid separation for low T^*. However, the phase separation for low T^* and the periodic ordering for high T^* are consistent with the ground state, which is an exact result. Similar trend was observed before for different forms of the SALR potential for moderate repulsion in MF theories [40, 73]. The corresponding types of (μ, T) phase diagrams can be found in Ref. [108]. The periodic structures present only above a certain temperature are a compromise between the energetic and the entropic contributions to the grand potential. **The above evolution of the MF lines of**

instability for increasing repulsion is probably a generic property of SALR systems, which is independent of the particular shape of the potential and system dimensionality.

We have determined the phase diagram of the SALR model within the mean-field approximation. We have obtained the same sequence of the ordered periodic phases as in Ref.[39]. For increasing density the stable phases are: fluid, hexagonally ordered clusters, lamellar phase and hexagonally ordered bubbles. For high T^* the phase diagrams on the lattice and in continuum are very similar. However, on the lattice there are two lamellar phases with different orientations of the stripes w.r.t the lattice directions. For strong repulsion ($J^* = 3$) we obtain two hexagonal phases, with and without orientational ordering of the long axes of the rhomboidal clusters. The regions occupied by the ordered phases and the extent of the two-phase regions on the (ρ^*, T^*) phase diagram are also different than in Ref.[39]. For weak repulsion ($J^* = 1$, i.e. $\int d\mathbf{r}V(r) = 0$) the clusters are symmetrical and there is a single hexagonal phase, as in Ref.[39]. Unfortunately, in the mean-field approximation the effect of the degeneracy of the ground state cannot be correctly described. *In mean field the mesoscopic fluctuations are neglected, whereas in the SALR systems the displacements of the clusters or stripes lead to formation of the disordered cluster fluid or molten lamella.* The dominant role of mesoscopic fluctuations makes the studies of the SALR systems particularly difficult.

The phase diagrams obtained by the Monte Carlo simulation and the mean-field phase diagram differ significantly. The differences were discussed in Sec. 2.2.5. **The main novelty of the MC phase diagram is the stability of the molten lamella phase, which was not previously reported for the systems with the SALR potential [35, 39, 107].** The molten lamella phase denoted by ML on the phase diagram in Fig. 2.52 is characterized by global orientational order and lack of translational order, which are both present in the case of the lamellar phase. The typical particle configuration of the ML phase at high T and $\mu^* \approx 6$ consists of stripes with many defects of different kind, but with the same orientation in one of the main lattice directions (see Fig. 2.56c). At low T and μ^* corresponding to the coexistence of the lamellar and rhomboidal phases, the ML typical configuration is a mix of rhomboidal clusters and short zig-zag stripes oriented in the same direction (see Fig.2.44g for the ground state configuration of the ML phase). Such characterization was quantified by appropriate order parameters described in Sec. 2.2.4.3. The use of specific order

parameters was crucial and necessary to determine the loci of the phase transitions between the ML phase and other phases. In Ref. [39] Archer used the DFT, hence a period patterning was assumed and differentiation of the phase with structural defects was unreachable. On the other hand in Ref. [35] the phase transitions to the ML phase on the MC phase diagram could have been found, but the authors decided to determine the loci of phase transitions by maxima of the heat capacity, which in the case of the SALR systems do not necessarily indicate a transition. As we have shown, the heat capacity in the SALR system may have two maxima as a function of T even in one-dimensional system, where the peak in the heat capacity at lower temperature signals an approach to the transition at $T^* = 0$, while the maximum at higher temperature is not associated with any phase transitions. What is more, in Fig. 2.60 we have shown that the position and the hight of the heat capacity peak at the F-ML transition has nonmonotonic dependence on the system size, and thus cannot quantitatively determine the location of the phase transition.

It is worth noticing, that the 1d model with the SALR potential discussed in Sec. 2.1.1 to some extent can describe properties of the lamellar phases in a two-dimensional system. In such sense, the coexistence of the two periodic phases with different degree of order found within the MF approximation in 1d (Fig. 2.10), reflects the coexistence of the lamellar and molten-lamellar phases found in 2d space by the MC simulations. The change of the degree of order in a 1d system in the MF approximation captures to some extent the nature of the phase transitions in the 2d system, where the more ordered lamellar phase transforms to the less ordered molten lamella.

An interesting question is: to what extent the results for the lattice SALR model can be extrapolated to the corresponding models in the continuum? Regarding this point we could expect that the existence of low density ordered phases analogous to our OR phase might strongly depend on the details of the interaction potential. In the continuum, a low density cluster ordered phase could be expected only if the clusters formed at low temperature show little amount of polydispersity both in the number of particles and shape. On the other hand, the transitions involving isotropic phases and lamellar structures seem to appear easily for systems in the continuum [34–36, 39, 109]. We think that the presented results will provide a convenient framework to analyze the possible transitions between fluid and lamellar phases, and the possible order-disorder transition between different lamellar phases.

Chapter 3

Effects of confinement in the one-dimensional model of colloidal self-assembly

In this chapter we study colloidal self-assembly in confined systems. We focus on the effect of imposing rigid or elastic boundary conditions. In Sec. 3.1 permeable boundaries are assumed, while in Sec. 3.2 we study the effect of imposing a constrain on the number of confined particles. The results are compared in Sec. 3.3.

3.1 Open system

In this section we consider only permeable confining walls. Our first question is how the structural defects in the case of incommensurability between the system size and the period in the bulk phase depend on thermodynamic state and on the interaction with the surfaces. The second question concerns the fluid-induced effective interactions between the confining surfaces for different values of the chemical potential. The periodic order on the mesoscopic length scale can induce a periodic effective interaction between confining surfaces on the same length scale. This is analogous to the periodic solvation force on the atomic length scale in simple fluids [19, 47].

In contrast to the amphiphilic systems, where the effective interaction was intensively investigated both experimentally [50, 51] and theoretically [52–56, 110], in the case of the SALR potential it has not been studied yet.

In biological systems or in pores of a soft porous material the compartments are surrounded by lipid bilayers or by elastic material. The separation between the confining surfaces can be varied, and this change is associated with elastic energy. Mechanical equilibrium between the solvation force resulting from the stress in the confined self-assembling system, and the elastic force resulting from a deformation of the confining elastic material (eg. lipid bilayer) determines the equilibrium shape of the system boundary. Changes of a thermodynamic state, leading to the change of the solvation force, might lead to shape and/or size transformations. In this section we consider the equilibrium wall separation in a pore of an elastic material containing particles interacting with the SALR potential. It is interesting what is the equilibrium separation between the elastic walls when the equilibrium thickness of the pore in the absence of particles, and the period of the bulk phase are incommensurate.

In Sec. 3.1.1 we introduce the model for colloidal self-assembly between rigid permeable walls and give the exact expressions for the partition function, the average density and the effective interaction between the confining walls. In Sec. 3.1.2 we present asymptotic expressions for the local density and for the effective potential between the confining surfaces. We determine the range of validity of these formulas by comparison with exact results. In Sec. 3.1.3 we discuss the dependence of the distribution of the particles inside the pore on the chemical potential when the width of the slit and the period of the bulk structure are incommensurate. We also compare the shape of $\rho(\mu)$ for various slits with the result obtained in Sec. 2.1.1 for the bulk. In addition, we consider periodic boundary conditions in the case of incommensurability, in order to help to interpret simulation results. The effective interaction between the walls for different thermodynamic states, and the equilibrium width of a system with elastic boundaries are determined in Sec. 3.1.4.

3.1.1 Model introduction and exact results

3.1.1.1 Imposing rigid boundary conditions

In the case of the rigid boundary conditions (RBC) we assume that the confining walls are electrically neutral, hence they interact only with the particles located at the first and the last site of the system (see Fig. 3.1). The confining walls represent real physical confinement e.g. in a porous material or in a thin film on a solid substrate. The thermodynamic Hamiltonian which contains the energy and the chemical potential term is

$$H_W[\{\hat{\rho}\}] = \frac{1}{2}\sum_{x=1}^{L}\sum_{x'=1}^{L}\hat{\rho}(x)V(x-x')\hat{\rho}(x') + h_1\hat{\rho}(1) + h_L\hat{\rho}(L) - \mu\sum_{x=1}^{L}\hat{\rho}(x), \quad (3.1)$$

where the particle-particle interaction potential is the same as considered for the bulk (Eq. 2.44).

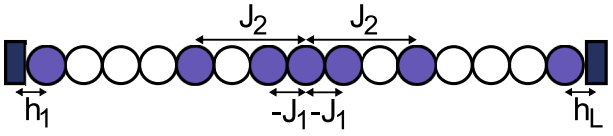

FIG. 3.1: Scheme of the model for a system of size $L = 15$. The lattice constant a is equal to the particle diameter σ. The particles attract or repel each other with the energy $-J_1$ or J_2 when they are the nearest or the third neighbors respectively. If a particle occupies the first or the last site of the lattice, then it interacts with the confining wall with the energy h_1 or h_L respectively.

3.1.1.2 Exact solution

We solve the model exactly by the transfer matrix method (see Sec. 2.1.1.4). Since the range of particle-particle interactions did not change, we use boxes consisting of three neighboring lattice sites defined in Eq. 2.20. For the system of size $L = 3M + j$, where $j = 0, 1, 2$, the boxes can be labeled by integer $r = 1, 2, \ldots M$. For $M > 1$ ($L \geq 6$) the Hamiltonian can be written in the form

$$H_W^*[\{\hat{\rho}\}] = \hat{\rho}(1)h_1^* + \hat{\rho}(L)h_L^* + H_j^*[\hat{S}(M)] + \sum_{r=1}^{M-1} H_t^*[\hat{S}(r), \hat{S}(r+1)]. \quad (3.2)$$

where H_t^* which contains the interaction between two neighboring boxes and the chemical potential term in the first box is given by Eq. 2.22 and

$$H_j^*[\hat{S}(M)]=\begin{cases} -(\sum_{i=0}^{1}\hat{\rho}(3M-i)\hat{\rho}(3M-i-1))-\mu^*(\sum_{i=0}^{2}\hat{\rho}(3M-i)), & \text{if } j=0 \\ -(\sum_{i=0}^{2}\hat{\rho}(3M+1-i)\hat{\rho}(3M-i))+J^*\hat{\rho}(3M-2)\hat{\rho}(3M+1) & \\ -\mu^*(\sum_{i=0}^{3}\hat{\rho}(3M+1-i)), & \text{if } j=1 \\ -(\sum_{i=0}^{3}\hat{\rho}(3M+2-i)\hat{\rho}(3M+1-i))+ & \\ J^*(\sum_{i=0}^{1}\hat{\rho}(3M-2+i)\hat{\rho}(3M+1+i))-\mu^*(\sum_{i=0}^{4}\hat{\rho}(3M+1-i)), & \text{if } j=2 \end{cases}$$

contains the particle-particle interactions between the particles which occupy the sites within the M-th box, and in addition the interactions between the particles at the sites labeled $3M+1$ and $3M+2$ (if such sites exist for given L). Finally, $\hat{\rho}(1)h_1^*$ and $\hat{\rho}(L)h_L^*$ are the energies of interaction between the particles and the two walls. For $M=1$ the Hamiltonian does not contain the last term in (3.2). We consider only $M>1$.

Partition function

The partition function in terms of the transfer matrix (Eq. 2.23) has the following form

$$\Xi_W=\sum_{\hat{S}(1)}\sum_{\hat{S}(M)}{}' e^{\beta^*\hat{\rho}(1)h_1^*}\mathbf{T}^{M-1}[\hat{S}(1),\hat{S}(M)]e^{\beta^*\hat{\rho}(L)h_L^*}e^{\beta^*H_j^*[\hat{S}(M)]}, \tag{3.3}$$

where $\sum'_{\hat{S}(M)}$ denotes

$$\sum_{\hat{S}(M)}{}' = \begin{cases} \sum_{\hat{S}(M)} & \text{if } j=0 \\ \sum_{\hat{S}(M)}\sum_{\hat{\rho}(3M+1)} & \text{if } j=1 \\ \sum_{\hat{S}(M)}\sum_{\hat{\rho}(3M+1)}\sum_{\hat{\rho}(3M+2)} & \text{if } j=2. \end{cases}$$

We transfer $\mathbf{T}$ to the base in which it is diagonal and the matrix elements of $\mathbf{T}^{M-1}$ can be easily expressed by the sum over the eigenvalues λ_i and the matrix elements $P_i(\hat{S}(n))$ of the matrix transforming $\mathbf{T}$ to its eigenbasis

$$\mathbf{T}^{M-1}(\hat{S}(n),\hat{S}(m)) \;=\; \sum_{i=1}^{8}P_i(\hat{S}(n))\lambda_i^{M-1}P_i^{-1}(\hat{S}(m)). \tag{3.4}$$

Hence the partition function is

$$\Xi = \sum_{\hat{S}(1)} {\sum_{\hat{S}(M)}}' \sum_{i=1}^{8} e^{\beta^* \hat{\rho}(1) h_1^*} P_i(\hat{S}(1)) \lambda_i^{M-1} P_i^{-1}(\hat{S}(M)) e^{\beta^* \hat{\rho}(L) h_L^*} e^{\beta^* H_j^*[\hat{S}(M)]}. \tag{3.5}$$

Average density

The framework of the transfer matrix allows us to find a formula for the average density at the site $x = 3n + l$, where n is the number of the triple to which the x-th site belongs and $l = 1, 2, 3$ is the label of the site within the triple. For $1 < n < M$ the average density at the x-th site is

$$\langle \hat{\rho}(x) \rangle = \frac{1}{\Xi} \sum_{\hat{S}(n)} \sum_{\hat{S}(1)} {\sum_{\hat{S}(M)}}' e^{\beta^* \hat{\rho}(1) h_1^*} \mathbf{T}^n(\hat{S}(1), \hat{S}(n)) \hat{\rho}(x) \mathbf{T}^{M-(n+1)}(\hat{S}(n), \hat{S}(M)) e^{\beta^* \hat{\rho}(L) h_L^*} e^{\beta^* H_j^*[\hat{S}(M)]}. \tag{3.6}$$

In terms of the eigenvalues it takes the form

$$\langle \hat{\rho}(x) \rangle = \frac{1}{\Xi} \sum_{\hat{S}(n)} \hat{\rho}(x) \left(\sum_{\hat{S}(1)} e^{\beta^* \hat{\rho}(1) h_1^*} \sum_{r=1}^{8} P_r(\hat{S}(1)) \lambda_r^n P_r^{-1}(\hat{S}(n)) \right) \times \left({\sum_{\hat{S}(M)}}' e^{\beta^* \hat{\rho}(L) h_L^*} e^{\beta^* H_j^*(\hat{S}(M))} \sum_{r=1}^{8} P_r(\hat{S}(n)) \lambda_r^{M-(n+1)} P_r^{-1}(\hat{S}(M)) \right). \tag{3.7}$$

Effective interaction between the walls

When the correlation length between the particles is comparable with the distance between the confining walls, then the distribution of the particles is influenced by both walls. This leads to the excess of the grand potential depending on the distance between the walls [46]. The thermodynamic effects of confinement are described by the excess grand thermodynamic potential

$$\Omega_{ex} \equiv \Omega_W - \Omega = \gamma_1 + \gamma_L + \Psi(L), \tag{3.8}$$

where $\Omega_W = -k_B T \ln \Xi_W$ is the grand potential in the slit, Ω is the grand potential in the bulk (Eq. 2.6), L is the size of these systems, γ_1 and γ_L are the wall-fluid surface tensions and $\Psi(L)$ corresponds to the effective interaction between the confining walls [46] (The effective force between the surfaces is $-\nabla\Psi(L)$).

In order to obtain the expressions for $\Psi(L)$ and γ_i we have to note that the grand thermodynamic potential for the bulk system of the size $L = 3M + j$, where $j =$

$0, 1, 2$, and $M \to \infty$ is

$$\beta\Omega \simeq_{M\to\infty} -\frac{L}{3M}\ln\lambda_1^M = -\ln\lambda_1^M - \frac{j}{3}\ln\lambda_1. \tag{3.9}$$

Whereas from Eq. 3.5 we get

$$\ln\Xi_W = \ln\Big(\sum_{r=1}^{8}\lambda_r^{M-1}C_r(j)\Big), \tag{3.10}$$

where

$$C_r(j) = \sum_{S(1)}\sum_{\hat{S}(M)}{}' e^{\beta^*\hat{\rho}(1)h_1^*}P_r(\hat{S}(1))P_r^{-1}(\hat{S}(M))e^{\beta^*\hat{\rho}(L)h_L^*}e^{\beta^*H_j^*(\hat{S}(M))}. \tag{3.11}$$

From (3.8)-(3.11) we obtain

$$\beta\Omega_{ex} \simeq \frac{3+j}{3}\ln\lambda_1 - \ln C_1(j) - \ln\Big(1+\sum_{r=2}^{8}\frac{C_r(j)}{C_1(j)}\Big(\frac{\lambda_r}{\lambda_1}\Big)^{M-1}\Big). \tag{3.12}$$

The sum of the surface tensions and the effective potential between the confining surfaces in Eq.(3.8) are given by

$$\beta(\gamma_1+\gamma_2) = \ln\lambda_1 - \ln C_1(0), \tag{3.13}$$

and

$$\beta\Psi(L) = -\ln\Big(1+\sum_{r=2}^{8}\frac{C_r(j)}{C_1(j)}\Big(\frac{\lambda_r}{\lambda_1}\Big)^{M-1}\Big) \tag{3.14}$$

respectively, since we have verified that the sum of the first two terms in Eq. (3.12) does not depend on j.

The exact expressions take much simpler asymptotic forms for $M \gg 1$ and $n \simeq M/2$. We present the asymptotic formulas for $M \gg 1$ for the density and for $\Psi(L)$, and compare them with the exact results in the next section.

3.1.2 Asymptotic expressions for large slits and the range of their validity

In the energetically favourable structure clusters composed of 3 particles are separated by 3 empty sites. For this reason the properties of the system confined in the slit of a large width $L = 3M + j$ depend on both, the number of the triples of sites, $M \approx L/3$, and the number of the additional sites, $j = 0, 1, 2$. Let us first consider the average local density in the central part of the slit of large width, $M \gg 1$. We divide the system into triples of sites. Each site x is characterized by the number of the triple to which it belongs, n, and the position inside the triple, l, so that $x = 3n + l$ with $l = 1, 2, 3$. The expression for $\langle\hat{\rho}(3n + l)\rangle$ depends on n and l, as well as on M and j. From the exact formulas derived in the previous section we obtain the asymptotic expression for $M \to \infty$ and $n \simeq M/2$ (central part of the slit)

$$\langle\hat{\rho}(3n+l)\rangle \simeq \bar{\rho} + A_1(l)\cos(n\lambda+\theta_1(l))e^{-3n/\xi} + A_L(l)\cos((M-n)\lambda+\theta_L(l))e^{-3(M-n)/\xi}. \tag{3.15}$$

The explicit expressions for $\bar{\rho}$, the amplitudes $A_1(l), A_L(l)$ and the phases $\theta_1(l), \theta_L(l)$ are given in Appendix 6.4 (these quantities depend also on M and j). The decay length ξ is given by the same expression as the correlation length in the bulk (Eq. 2.32),

$$\xi = 3/\ln\left(\frac{\lambda_1}{|\lambda_2|}\right), \tag{3.16}$$

where λ_1 and $\lambda_2 = |\lambda_2|\exp(i\lambda)$ are the largest and the second largest eigenvalues of the transfer matrix. The transfer matrix is not Hermitian, and some of the eigenvalues can be complex. The presence of the imaginary part of λ_2 depends on J^*, and on the thermodynamic state. The monotonic decay of the density near a single surface occurs when λ_2 is real and positive ($\lambda = 0$). The exponentially damped periodic structure with the period 6 occurs when λ_2 is real and negative, ($\lambda = \pi$). In most cases, however, including $J^* = 3$ for the range of μ^* studied in this work, λ_2 is complex and the period of the damped oscillations is noninteger.

The asymptotic formula for the effective interaction potential for $M \to \infty$ is

$$\beta\Psi(3M + j) \simeq A(j)\cos(\lambda M + \phi(j))e^{-3M/\xi}. \tag{3.17}$$

The explicit expressions for the amplitude $A(j)$ and the phase $\phi(j)$ are given in Appendix 6.4.

The asymptotic formulas are simply the exponentially damped periodic functions. Similar expressions, but without the amplitude modulations, were obtained in mean-field theories of confined self-assembling systems [24, 54, 111, 112]. These rather simple asymptotic forms are strictly valid for $M \gg 1$ and $n \simeq M/2$. We check the validity of the asymptotic expressions by comparing them with the exact results in case of strong repulsion, $J^* = 3$.

As shown in Fig.3.2, the agreement of the asymptotic expression for the local density with the exact result is very good already for $L = 42$, and the discrepancy between the exact and asymptotic expressions appears only very close to the surface. For $L = 30$ the accuracy of the asymptotic expression is less good but it is still satisfactory, except from the clusters adsorbed at the surfaces, where some discrepancy can be observed. Thus, the asymptotic formula is sufficiently accurate not only in the center, but inside the whole slit for slits containing 5 or more clusters.

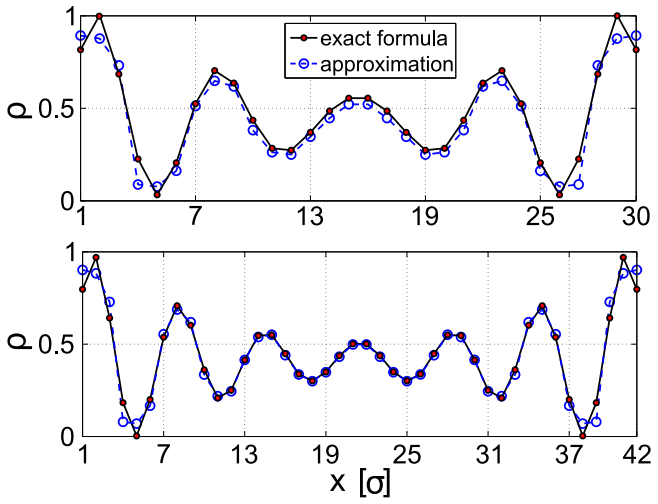

FIG. 3.2: Comparison of the exact (3.7) and approximate (3.15) formulas for the average density for $J^* = 3$, $\mu^* = 0, T^* = 0.5$ and $h_1^* = h_L^* = -1$. Upper panel $L = 30$, lower panel $L = 42$.

In the asymptotic expressions the decay length and the period of oscillations of the local density in the slit, and the correlation function in the bulk are the same. In Fig.3.3 we compare the exact results for the local density and for the correlation function. In order to compare the two functions, we add the average density of the bulk system to the linearly scaled correlation function, and obtain good agreement for the distance from the surface $x > 10$. We conclude that the correlation function

in the bulk describes very well the local structure (up to an amplitude that depends on the kind of the wall) except for the first cluster adsorbed at the surface.

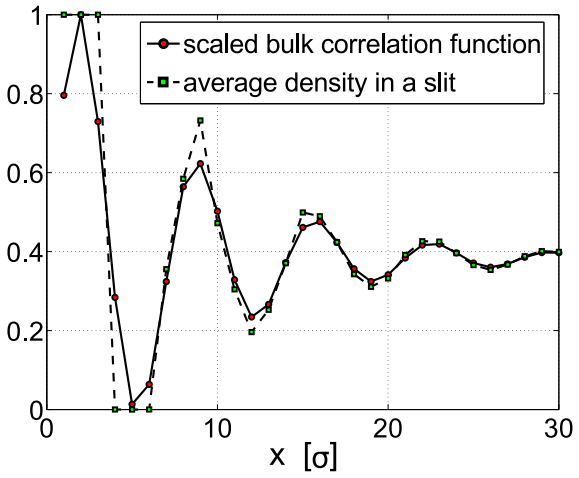

FIG. 3.3: Comparison of the density profile in a slit (dashed line) for $J^* = 3$, $\mu^* = -0.66$, $T^* = 0.0125$, $h_1^* = h_L^* = -1$ and $L = 96$, and the bulk correlation function obtained in Sec. 2.1.1.4 (solid line) for the same thermodynamic state. The correlation function was linearly scaled and shifted by the average density of the bulk system, $\rho = 0.3841$.

In Fig. 3.4 the exact and approximate results for the effective interaction between the walls are compared. As expected, the accuracy of the asymptotic formula improves with increasing system size. Close to the minima, i.e. near the equilibrium separations between the surfaces, the approximate formula works well also for small systems. On the other hand, for small and incommensurate system sizes the approximate formula highly underestimates the interaction potential, therefore for small systems it underestimates the effective force between the walls.

Notice that for some system sizes there is no clear minimum and $\Psi(L)$ takes almost equal values for two consecutive system sizes. However, for the exact and the approximate formulas this phenomenon occurs for different system sizes eg. in Fig. 3.4 for $L = 39, 40$ for the exact result, and for $L = 27, 28$ for the approximate formula.

3.1.3 Effects of incommensurability of the system size and the period of the bulk structure

In this section we study the effect of the incommensurability of the system size and the period of the bulk structure on the distribution of the particles and on the dependence of the average density on the chemical potential. Our aim is to verify how

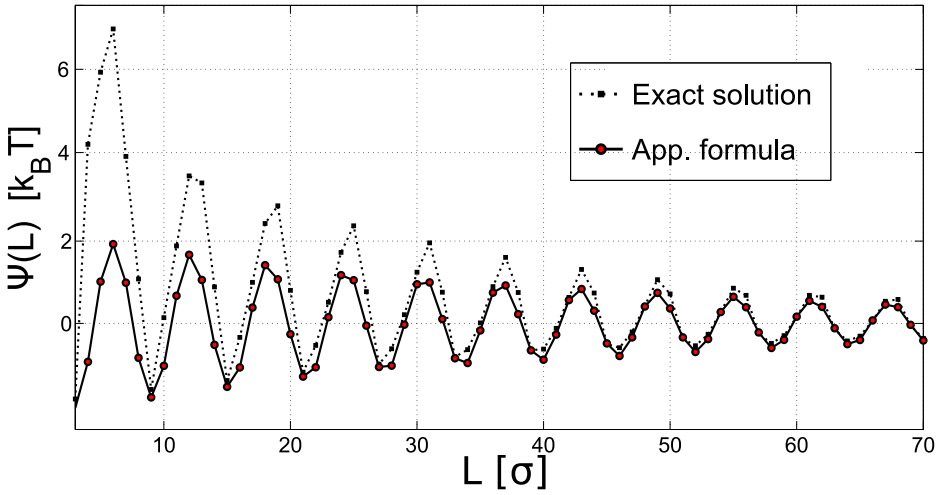

FIG. 3.4: The effective wall-wall interaction $\Psi(L)$ for $J^* = 3$, $\mu^* = 0$, $T^* = 0.2$ and $h_1^* = h_L^* = -1$. Dashed line with squares - the exact formula, Eq. (3.14). Solid line with circles - the approximate formula, Eq. (3.17).

$\rho(\mu^*)$ is influenced by the presence of structural defects that must be present in the case of the incommensurability. We first consider PBC, and next RBC.

3.1.3.1 The case of periodic boundary conditions (PBC)

We focus on L such that $\mod(L,6) = 3$, i.e. the remainder after division of L by 6 is 3 and thus the mismatch between L and 6 (the low-T period in the ordered phase) is the largest. Let us first investigate the ground state (GS), i.e. the case

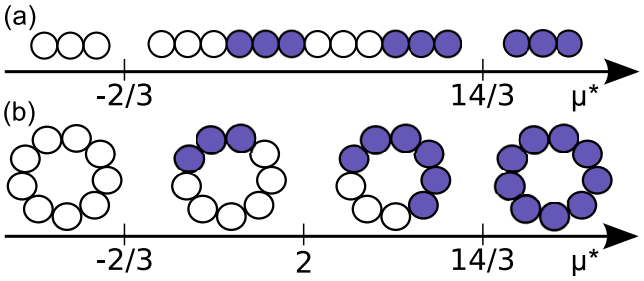

FIG. 3.5: Schematic representation of the ground state ($T^* = 0$) for $J^* = 3$ for the bulk system ($\mod(L,6) = 0$) (a) and for the system of size $L = 9$ (b). For $\mu^* < -2/3$ or $\mu^* > 14/3$ the stable phase is the vacuum or the fully occupied lattice. For $-2/3 < \mu^* < 14/3$ the periodic phase is stable in the bulk. For $L = 9$ the stability region of the periodic phase is split into $\mu^* < 2$ and $\mu^* > 2$ corresponding to enlarged void or cluster respectively.

of $T^* = 0$. For $\mod(L,6) = 3$ we may expect that in the periodic phase either a separation between some clusters is larger than 3, or some clusters are larger than 3 (see Fig.3.5). When the separation between the clusters is larger than 3 and we

add one particle to a cluster consisting of at least 3 particles, then the increase of the Hamiltonian is $\Delta H^* = -1 + J^* - \mu^*$. For $\mu^* < J^* - 1$ or $\mu^* > J^* - 1$ we have $\Delta H^* > 0$ or $\Delta H^* < 0$ respectively. Thus, in the GS corresponding to the minimum of the Hamiltonian H^* the voids in the first case and the clusters in the second case occupy 3 more sites. At $T^* = 0$ the average density jumps by $3/L$ for $\mu^* = J^* - 1$. The GS in the bulk (mod $(L,6) = 0$) and for $L = 9$ is shown in Fig.3.5 for $J^* = 3$. Note that we have $\Delta H^* = -1 + J^* - \mu^* = 0$ for $\mu^* = 2$ in this case, therefore for $\mu^* = 2$ the GS is degenerate, and the cluster can consist of either 3,4,5 or 6 particles. In Fig.3.6 we show $\rho(\mu^*)$ for $T^* = 0.15$. Note that the transition between the two types of defects, i.e. larger voids or larger clusters could be misinterpreted as a transition between different phases, because when a system undergoes a first-order phase transition, steps in $\rho(\mu^*)$ appear. The results of simulations in the case of systems with spatial inhomogeneities on a mesoscopic length scale should be interpreted with special care, especially when several periodic phases with different periods can appear. Our results show that in the case of structural defects the height of the step decreases as $\sim 1/L$ for increasing L, and for certain system sizes the step disappears (Fig.3.6).

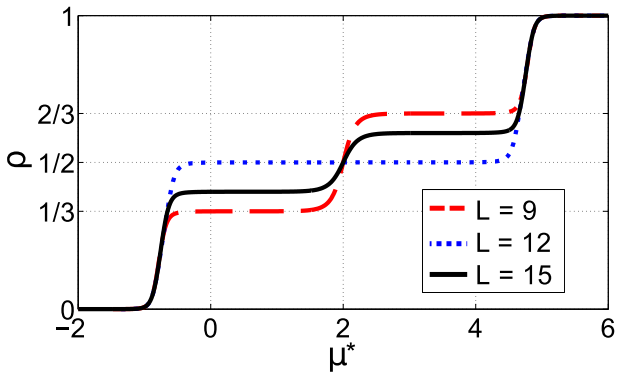

FIG. 3.6: The average density ρ^* as a function of the chemical potential μ^* for $J^* = 3$ and $T^* = 0.15$, for a system with PBC and $L = 9$ (red dashed line), $L = 12$ (blue dotted line) and $L = 15$ (black solid line).

3.1.3.2 The case of rigid boundary conditions (RBC)

We first focus on attractive surfaces. Let us consider the Hamiltonian for a single cluster composed of $n \leq 3$ particles adsorbed at the surface, $H^* = h_1^* - (n-1) - n\mu^*$. The adsorption of the cluster is energetically favourable compared to vacuum for $\mu^* > (h_1^* + 1 - n)/n$. In order to fix attention, we assume that the interaction

with the surfaces is the same as the particle-particle attraction, $h_1^* = h_L^* = -1$. In this case a cluster adsorbed at each attractive surface is energetically favourable for $\mu^* > -1$. Thus, for $\mu^* > -1$ the largest mismatch between the system size and the structure of the bulk periodic phase occurs for $mod(L,6) = 0$ when both surfaces are attractive. For mod $(L,6) \neq 3$ the GS of the system is degenerate in the whole stability region of the periodic phase, because the defects in the periodic structure that are caused by the incommensurability of the period and the system size are not localized. Moreover, the stability region of the periodic phase splits into 4 regions, corresponding to different numbers and sizes of the clusters present in the slit. We choose $L = 19$ and present typical microscopic states of the GS in Fig.3.7. For $\mu^* < 0$ there are 3 clusters in the slit. Each of them consists of 3 particles, and the neighboring clusters are separated by at least 3 empty sites. Apart from this limitation the position of the central cluster can be arbitrary. For $0 < \mu^* < J^* - 1$ there are 2 clusters consisting of 3 particles and 2 clusters consisting of 2 particles in the slit. The clusters do not repel each other, i.e. there are 3 empty sites between the neighboring clusters. For $J^* - 1 < \mu^* < 2(J^* - 1)$ there are 4 clusters consisting of 3 particles. Finally, for $\mu^* > 2(J^* - 1)$ there are 3 clusters separated by two voids composed of 3 empty sites, and each cluster consists of at least 3 particles.

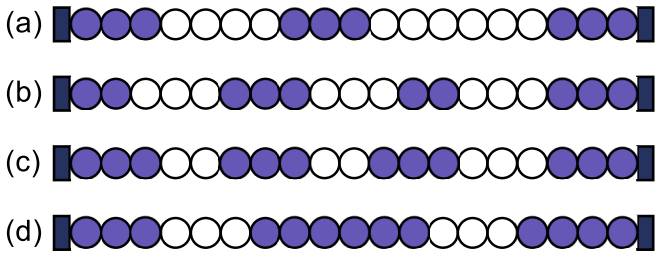

FIG. 3.7: Typical microstates in the degenerate GS for a slit of size $L = 19$ with attractive walls. The range of the chemical potential corresponding to the shown microstates is (a) $-2/3 < \mu^* < 0$, (b) $0 < \mu^* < J^* - 1$, (c) $J^* - 1 < \mu^* < 2(J^* - 1)$ and (d) $2(J^* - 1) < \mu^* < 2J^* - 4/3$.

In Fig.3.8 we present $\rho(\mu^*)$ for the slit with $L = 19$ at $T^* = 0.15$. The average densities corresponding to the plateaus are shown in the insets. Note the similarity between the average densities in the GS (Fig.3.7 (a)-(d)) and the insets (a)-(d) in Fig.3.8.

In the case of confinement in a slit the steps in $\rho(\mu^*)$ represent a physical effect, namely structural changes such as a jump of a number of the clusters or a change of their size as a function of the chemical potential. Such abrupt changes in a slit

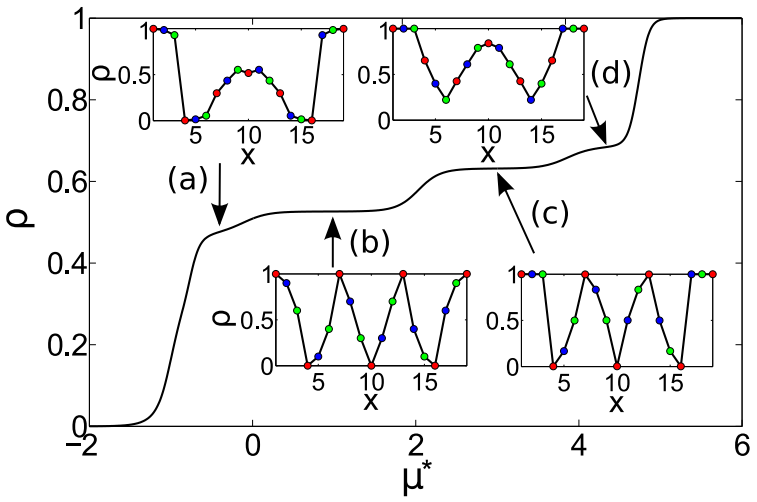

FIG. 3.8: Density ρ as a function of the dimensionless chemical potential μ^* for $J^* = 3$ and $T^* = 0.15$ in a slit of size $L = 19$ with attractive walls. For increasing μ^* we observe 4 plateaus. The plateaus from (a) to (d) correspond to the average densities shown in the insets. The steps between them occur for $\mu^* \approx 0, 2, 4$, i.e. near the GS coexistence between different structures in confinement (see Fig.3.7).

induced by small changes in the surroundings occur when the size of the system and the period of the bulk phase are incommensurate.

Let us focus on the role of the interaction with the confining surfaces. The attractive and repulsive surfaces are compared in Fig. 3.9 for a large slit. When the walls are attractive, we observe steps in $\rho(\mu^*)$ associated with adsorption of a particle or a cluster. The first step is present only if $h_1^*, h_L^* < -1$ and it originates from the adsorption of a single particle at each wall, while the second step corresponds to the adsorption of clusters. Note that for $\mu^* > -1$ the $\rho(\mu^*)$ curves are essentially the same for $h_1^* = h_L^* = -1$ and $h_1^* = h_L^* = -1.5$. This shows that for strong wall-fluid attraction the results are independent of h_1, h_L.

In the case of short-range interactions with the walls, the density profiles in the slits with attractive and repulsive surfaces are very similar for $-0.75 < \mu^* < -0.5$ (Fig. 3.9b). This rather surprising property follows from the fact that even though the clusters do not touch the repulsive surfaces, they are located very close to them. A significant difference between the attractive and repulsive surfaces appears only for $\mu^* > -0.45$ - there is one more cluster, and one more step in $\rho(\mu^*)$ in the slit with the attractive surfaces for $L = 20, 26, 32, \ldots$.

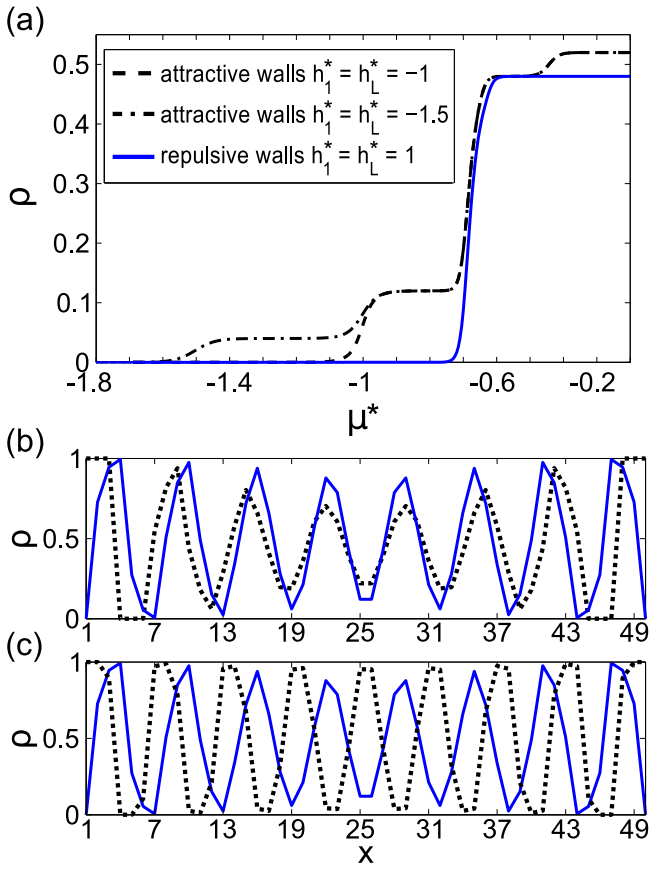

FIG. 3.9: Panel (a) $\rho(\mu^*)$ for $J^* = 3$, $T^* = 0.03$ and $L = 50$ for systems with PBC (red solid line), RBC with attractive walls for $h_1^* = h_L^* = -1$ (dashed line) and for and $h_1^* = h_L^* = -1.5$ (dash-dotted line), and RBC with repulsive walls for $h_1^* = h_L^* = 1$ (blue solid line). The rapid changes of the density at $\mu^* \approx -1.5$ and at $\mu^* \approx -1$ correspond to the adsorption of a particle and a cluster respectively at the attractive walls. Panels (b) and (c) show density profiles for $\mu^* = -0.55$ and $\mu^* = -0.4$ respectively for attractive (dotted lines) and repulsive (solid lines) surfaces. Note the change of the number of clusters for $\mu^* \approx -0.45$ when the walls are attractive.

3.1.4 Effective interaction between the confining walls and deformations of elastic containers

In this section we discuss the effective potential between the confining surfaces separated by the distance L. We first consider walls separated by a fixed distance. Next we assume that the walls are elastic, and the change of the wall separation is possible at the cost of elastic energy. When the equilibrium width of the empty slit, L_0, and the period of the ordered phase do not match, the elastic energy and the fluid-induced stress are in competition. We ask how the equilibrium width of the slit filled with the inhomogeneous fluid differs from L_0.

3.1.4.1 The case of fixed distance between the confining walls

The exact results for the effective potential between the confining walls separated by a fixed distance, $\Psi(L)$, are presented in Fig. 3.10 for the chemical potential corresponding to the GS stability of the vacuum, the periodic phase and the dense phase (see Fig.3.5). Note that the confined fluid leads to repulsion or attraction between the walls when the dilute or the dense pseudo-phase is stable in the bulk respectively. The repulsion may follow from the adsorption of the clusters at the surfaces, since the clusters repel each other. The oscillations of $\Psi(L)$ are present if the periodic distribution of clusters is thermodynamically preferred. These oscillations should be interpreted as follows: the minima of $\Psi(L)$ correspond to the system sizes commensurate with the periodic structure, therefore if we would allow the system to shrink or expand, then in order to suppress the internal stress the system would change its size to the value corresponding to the nearest minimum of $\Psi(L)$. The bigger is the slope of the oscillations, the stronger is the effective force leading to the nearest minimum of $\Psi(L)$.

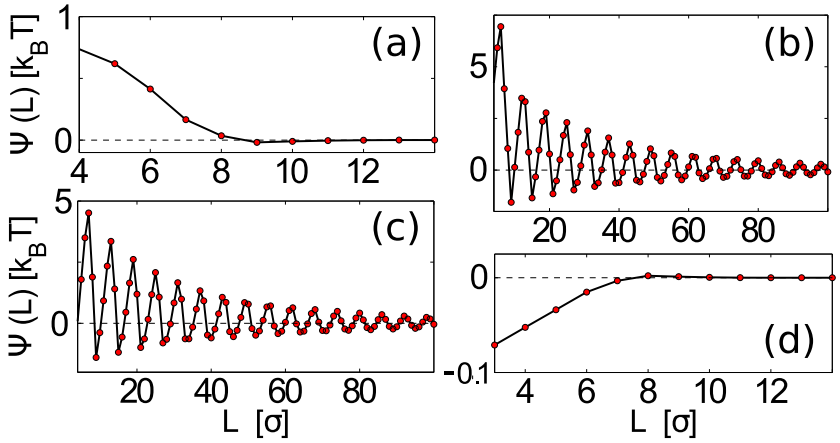

FIG. 3.10: $\Psi(L)$ for $J^* = 3$ and $T^* = 0.2$ for different values of the chemical potential μ^* and both walls attractive. (a) $\mu^* = -1$, (b) $\mu^* = 0$, (c) $\mu^* = 4$, (d) $\mu^* = 5$. L is in units of the particle diameter σ

For large L the decay rate of $\Psi(L)$, ξ, is equal to the bulk correlation length (see Eq.(3.17)). In Sec. 2.1.1.4 it was shown that the correlation length in the considered model can be a few orders of magnitude larger than the molecular size for μ^* corresponding to the stability region of the periodic phase on the GS ($-2/3 < \mu^* < 14/3$ for $J^* = 3$). In Fig. 3.11 we show that for $\mu^* = 2$, where ξ takes the maximum, $\Psi(L) \sim 0.1 k_B T$ even for system sizes 4 orders of magnitude larger than the particle diameter.

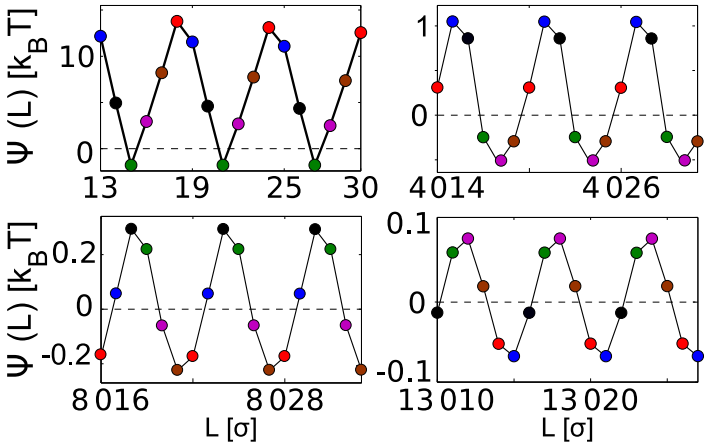

FIG. 3.11: $\Psi(L)$ for $J^* = 3$, $T^* = 0.2$ and $\mu^* = 2$ for non-interacting walls. L is in units of the particle diameter σ.

3.1.4.2 The case of elastic confining walls

We assume that the width L of the slit can oscillate around $L = L_0$, where L_0 is the equilibrium width in the absence of particles inside the slit. This oscillation can be controlled by a harmonic potential energy $U_w(L) = k \cdot (L - L_0)^2$ (see Fig. 3.12). Next we assume that when the slit is in contact with the reservoir of particles, and

FIG. 3.12: Illustration of the system with elastic walls with the spring constat k.

the chemical potential μ^* and temperature T^* are fixed, then in mechanical equilibrium the sum of $U_w(L)$ and the particle-induced effective potential $\Psi(L)$ reaches the minimum. In Fig. 3.13 we present the sum of Ψ and U_w as a function of the system size. Note that when L_0 corresponds to the maximum of $\Psi(L)$, i.e. to a large stress induced by the confined fluid, then $U_w(L) + \Psi(L)$ may have two minima of very similar depth for wall separations that differ approximately by the period of the bulk structure. The number of clusters in these two states differs by one. As can be seen in Fig.3.13, the barrier between the two minima is of order of $k_B T$ for the assumed elastic constant $k = 0.1 k_B T/\sigma^2$.

In Fig.3.14 we show how the bistability appears when the chemical potential changes from $\mu^* = 0$ or $\mu^* = 4$ towards $\mu^* = 2$. The barrier between the two minima decreases for increasing $|\mu^* - 2|$. Thus, by changing the concentration of particles in the surroundings we can change the hight of the barrier and induce or suppress the jumps between the two widths of the confined system.

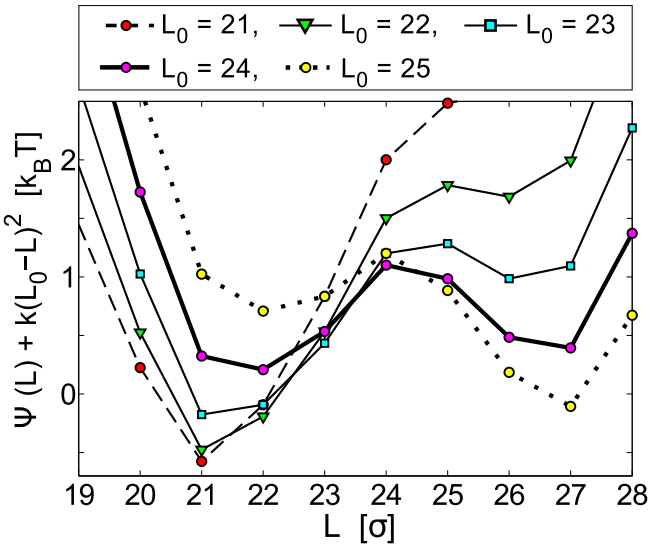

FIG. 3.13: The sum of the elastic energy of the confining boundaries, and the effective interaction induced by the confined self-assembling system for different equilibrium width of the empty slit L_0. $J^* = 3$, $T^* = 0.5$, $\mu^* = 2$, $h_1^* = h_L^* = -1$, and the spring constant $k = 0.1 k_B T/\sigma^2$, where σ is the particle diameter.

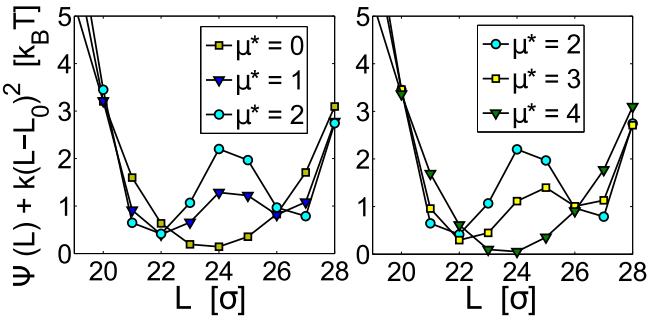

FIG. 3.14: The sum of the elastic energy of the confining boundaries and the effective interaction induced by the confined self-assembling system for various values of μ^*. $J^* = 3$, $T^* = 0.5$, $h_1^* = h_L^* = -1$, $L_0 = 24$, and the spring constant $k = 0.1 k_B T/\sigma^2$.

3.2 Fixed number of particles

Some membranes are permeable, while some other are not. Thus, a question arises if fluctuations of the number of confined particles have any effect on the properties of a self-assembling system confined by rigid or adaptive boundaries. This question motivates the study in this section. We ask how the effects of confinement on the self-assembling system depend on the contact with a reservoir of particles.

In the case of fixed boundaries we address the question of how the fluctuations of the positions and sizes of the clusters (their dynamical assembly and dissociation) are coupled with the fluctuations of the number of particles in the system. In the

case of inhomogeneous distribution of particles it is not a priori obvious that the largest fluctuations in the total number of particles lead to the largest differences between the density profiles in the canonical and grand canonical ensembles. We shall compare the density profiles and the pressure in the Grand Canonical Ensemble (GCE) and Canonical Ensemble (CE), with the average number of particles in the GCE equal to the number of particles N_0 in the CE. We shall pay particular attention to values of N_0 that are too small or too large for a given system size L for formation of periodically distributed layers of particles that minimizes the system energy. Roughly speaking, in the SALR systems the minimum energy is assumed when the individual clusters have the lowest energy (no intra-cluster repulsion), and are separated by the smallest distances corresponding to no inter-cluster repulsion. When the number of particles is too small or too large for a given L for formation of the optimal bulk structure, some structural deformations must occur. Our purpose is to compare these deformations and their effect on the mechanical properties in the GCE and CE.

In the case of permeable and elastic confinement we have shown in Sec. 3.1 that the system size fluctuations are accompanied by absorption or evaporation of a whole cluster. Clearly, for fixed number of particles such large size fluctuations are not possible. Hence, the permeability plays an important role in the case of elastic boundaries. In this section we verify if in the case of fixed number of particles the bistability of the system size can still exist due to some other mechanism.

This section is organized as follows: the simulation methods are presented in Sec. 3.2.2. The CE and GCE density profiles are compared in Sec. 3.2.3. The mechanical properties are discussed in Sec. 3.2.4. We compare the dependence of pressure on density in the CE (fixed N and varying L) and in the GCE for several fixed values of L and varying $\langle N \rangle$. The dependence of pressure on the system size for fixed N or $\langle N \rangle$ in the CE or GCE respectively is also discussed. In Sec. 3.2.5 we consider elastic boundaries and compute the average system size as a function of N for various elastic constants of the walls. For selected cases the histograms for the fluctuating width of the system are presented.

3.2.1 The model

In the current study we continue the investigation of the confined system with particles interacting *via* the pair potential given by Eq. (2.44). The confinement is

assumed to be electrically neutral, hence the interaction of the particles with the walls is short range. The Hamiltonian U in the Canonical Ensemble takes the form:

$$U[\{\hat{\rho}\}] = \frac{1}{2}\sum_{x=1}^{L}\sum_{x'=1}^{L}\hat{\rho}(x)V(x-x')\hat{\rho}(x') + h_1\hat{\rho}(1) + h_L\hat{\rho}(L) \qquad (\text{fixed } N); \quad (3.18)$$

The number of particles N (fixed in the Canonical Ensemble) is given by:

$$N = \sum_{x=1}^{L}\hat{\rho}(x). \quad (3.19)$$

As in Sec. 3.1, we assume that the confinement can be either rigid or elastic. For rigid boundary conditions the distance L between the confining walls is fixed, while in the case of elastic walls we assume that it may oscillate around L_0, which is the equilibrium width of an empty system. For the fixed number of particles the Hamiltonian takes the form:

$$\mathcal{U} = U + k(L-L_0)^2. \quad (3.20)$$

3.2.2 The simulation methods

In the current study we compare the exact solution obtained in the GCE with the results of MC simulation in the CE. In addition to the simulations in the CE we also carried out some runs in the GCE with the aim of cross-checking the consistency between the simulation codes and the numerical treatments based on the transfer matrix method.

The basic sampling steps follow the Metropolis scheme described in Sec. 2.2.4.1. For the GCE simulation both particle translations, deletion and insertion steps were carried, while for the CE simulation only the particle translation steps were performed. The computation of pressure from simulation of lattice models is usually carried out by means of the integration of the Grand Potential in the GCE, because the known relation for the Canonical Ensemble: $\beta p = -(\partial(\beta A)/\partial V)_{N,T}$ (where A is the Helmholtz free energy, and V the *generalized* volume) is hard to translate into an efficient numerical procedure due to the discreteness of the volume in lattice systems. We have found, however, that for our 1d system it is feasible to compute the pressure $p(N,L,T)$ in the CE, by an algorithm based on the discretization of the

derivative of $A(N,L,T)$ with respect to the system size as:

$$p_{\pm}(N,L,T) = \mp[A(N,L\pm 1,T) - A(N,L,T)]. \tag{3.21}$$

The pressure, in terms of the canonical partition function $Q(N,L,T)$ can be written as

$$p_{\pm}(N,L,T) = \pm\frac{1}{\beta}\ln\frac{Q(N,L\pm 1,T)}{Q(N,L,T)}. \tag{3.22}$$

The two ways of discretization, p_+ and p_-, lead to two different methods of computing the pressure, the *virtual expansion* and the *virtual contraction* respectively, from a direct analysis of the configurations from a simulation run at conditions (N,L,T). In the virtual expansion an empty site is added at a randomly chosen position of the system. For a confined system of size L, there are $L+1$ possibilities of performing such an insertion, namely $L-1$ cases where the inserted site is located between two sites of the system plus two insertions between the walls and the first or last site. Considering the $L+1$ possible ways of inserting an empty site on each of the microstates of the system of size L with N occupied sites (with $0 \le N \le L$), we get $L+1-N$ identical copies of each of the microstates of the system of size $L+1$ and N occupied sites (see Appendix 6.5). Let us denote by $\vec{\rho}_L$ a given configuration of the system with N particles and L sites, with potential energy given by $U(\vec{\rho}_L)$. If we define $\vec{\rho}_{L+1}(\vec{\rho}_L,k)$ as the configuration with N particles of a system with $L+1$ sites built from $\vec{\rho}_L$ by inserting a site at position k, and denote by $\sum_{\vec{\rho}_L}$ the sum over all possible microstates of this system with N particles and L sites, then we can write Eq. (3.22) as:

$$\begin{aligned} p_+(N,L,T) &= \frac{1}{\beta}\ln\frac{\sum_{\vec{\rho}_L}\exp[-\beta U(\vec{\rho}_L)]\sum_{k=0}^{L}\exp[-\beta U(\vec{\rho}_{L+1}(\vec{\rho}_L,k)) + \beta U(\vec{\rho}_L)]}{(L+1-N)\sum_{\vec{\rho}_L}\exp[-\beta U(\vec{\rho}_L)]} \\ &= k_B T \ln\left\langle \frac{L+1}{L+1-N}\exp[-\beta\Delta U_{ins}]\right\rangle_L, \end{aligned} \tag{3.23}$$

where $\langle\cdot\rangle_L$ is the average value of $\cdot$ when sampled on a system of size L, and ΔU_{ins} is the difference between the energies of the systems with $L+1$ and L sites. Analogously, a formula for pressure p_- computed by the *virtual contraction* scheme can be derived

$$p_-(N,L,T) = -k_B T \ln\left\langle \frac{L-N}{L}\exp[-\beta\Delta U_{del}]\right\rangle_L, \tag{3.24}$$

where $\Delta U_{del} = U(\vec{\rho}_{L-1}) - U(\vec{\rho}_L)$ is the variation of energy when a configuration $\vec{\rho}_{L-1}$, of N particles and $L-1$ sites is generated by eliminating one of the empty sites from the configuration $\vec{\rho}_L$ of a system with N particles and L sites. The virtual contraction method is inefficient at high densities, therefore we used it only for verification of the results obtained *via* the virtual expansion method, since by construction we expect:

$$p_+(N,L,T) = p_-(N,L+1,T). \tag{3.25}$$

In order to calculate properties of the system with elastic boundary conditions described by the Hamiltonian $\mathcal{U}$ given in Eq. (3.20), one needs to perform two additional types of MC steps. The first one is the *intercalation* of an empty site into a randomly chosen place of the system, the second one is the *removal* of a randomly chosen empty site of the system. The acceptance probability of the first move for system with L sites and N particles is

$$\mathcal{A}(L+1|L) = \min\Big\{1, \exp[-\beta\Delta\mathcal{U}]\frac{L+1}{L+1-N}\Big\}, \tag{3.26}$$

where $\Delta\mathcal{U}$ is the change of the energy after the size modification. Analogously the probability of acceptance of the move in which an empty site is removed is given by:

$$\mathcal{A}(L-1|L) = \min\Big\{1, \exp[-\beta\Delta\mathcal{U}]\frac{L-N}{L}\Big\}. \tag{3.27}$$

Notice that this procedure resembles a lattice version of isothermal-isobaric (NpT) simulation, in which the energy term introduced through the elastic force plays the role of the external field.

3.2.3 Distribution of particles between rigid walls

In this section we consider a system containing N_0 particles between rigid walls separated by a fixed distance L. The main question is how the particles self-assemble if N_0 is such that the equilibrium bulk structure is not possible. The distribution of particles for fixed N_0 will be compared with the distribution of particles in the open system, where the number of particles N fluctuates in such a way that $\langle N\rangle = N_0$.
In Fig.3.15 the density profiles obtained by the MC simulations in the CE are compared with the exact results obtained in the GCE by the transfer matrix method

described in Sec. 3.1. We chose $L = 50$, $T^* = 0.3$ and several values of N_0. In each case the chemical potential in the GCE was fixed to the value that corresponds to $\langle N \rangle = N_0$. We used the exact expression for density as a function of the chemical potential that was obtained in Sec. 3.1. For $L = 51$ the optimal number of clusters for the considered range of μ^* is 9 (hence $N = 27$), since the sequence of three occupied sites followed by three empty sites can be formed, with two clusters adsorbed at the attractive surfaces. The energy for such a structure assumes a minimum (there are as many attracting pairs as possible with no repulsion). For $L = 50$ only a small defect in the ordered structure occurs. We can see a very good agreement between the two ensembles for small as well as for large number of particles. For $N = 24$ corresponding to eight clusters, however, the number of maxima in the GCE is larger than in the CE. This result is even more surprising when we consider the fluctuation of the number of particles in the GCE (Fig.3.16). One can see that the largest discrepancy between the density profiles does not occur for the largest fluctuation of the number of confined particles in the GCE.

In order to understand why the distributions of the particles in the two ensembles are different when one cluster in the CE "is missing", let us consider the ground state (GS), $T^* = 0$. The microstates present in the GS for $L = 15$ and $N = 5, 6, 7$ are shown in Fig.3.17. The GS in Fig.3.17 shows that even small fluctuations of the number of particles - addition of one particle in our case - can lead to a significant change in the distribution of the particles. This is the case when $\langle N \rangle$ is a multiple of 3, and there is a free space for an extra cluster (with no cluster-cluster repulsion). When one additional particle enters the system, the energy change is J^*-1 when one of the clusters grows to contain 4 particles, or 0, when the new particle is sufficiently far from the clusters, or one of the clusters together with the new particle form two clusters composed of two particles. In Fig.3.17, bottom row, the two latter cases are shown. The states shown in Fig.3.17 are energetically favorable for $J^* > 1$. Thus, in the GCE with $\langle N \rangle = 6$ such microstates will appear quite often. As a result, an additional maximum in the average density profile occurs.

The above simple considerations show that spatial distribution of particles in the CE and GCE can be qualitatively different. This qualitative difference is not present for the largest fluctuation of the number of particles in the GCE. Even a small fluctuation of the number of particles can lead to a change of the number of clusters, because the sizes of the clusters can fluctuate, especially when N is not a multiple of 3. When

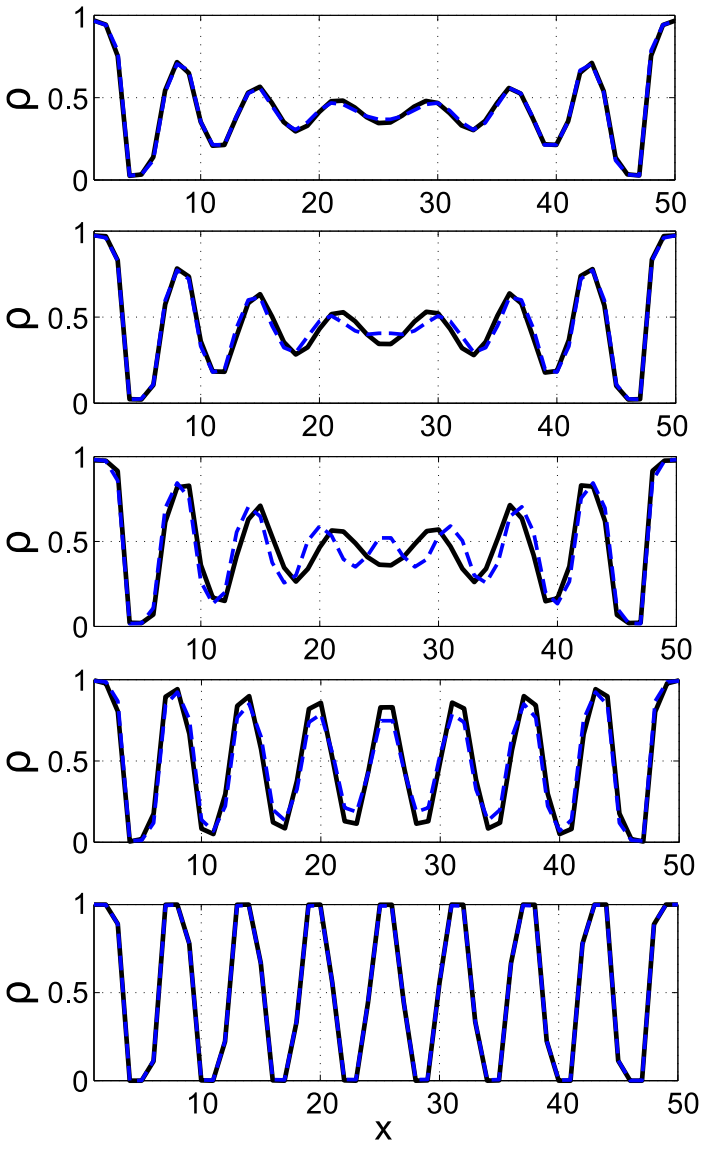

FIG. 3.15: Comparison of the GCE (dashed line) and the CE (solid line) density profiles for $L = 50$ at $T^* = 0.3$ and $N_0 = 22$ or $\mu^* = -0.33904$ (a), $N_0 = 23$ or $\mu^* = -0.21127$ (b), $N_0 = 24$ or $\mu^* = -0.02632$ (c), $N_0 = 25$ or $\mu^* = 0.22159$ (d), $N_0 = 26$ or $\mu^* = 1.08857$ (e). Repulsion to attraction ratio $J^* = 3$ and attractive walls with $h_1^* = h_L^* = -1$ are considered for all the cases.

$\langle N \rangle$ is small enough, the additional clusters can occupy the empty space and no inter-cluster repulsion appears.

3.2.4 Equation of state in a system confined by rigid walls

In this section we compute the pressure for fixed number of confined particles N_0 as a function of the distance between the confining surfaces L. From these results we obtain the pressure as a function of density, $p(\rho)$, for given N_0. For comparison we

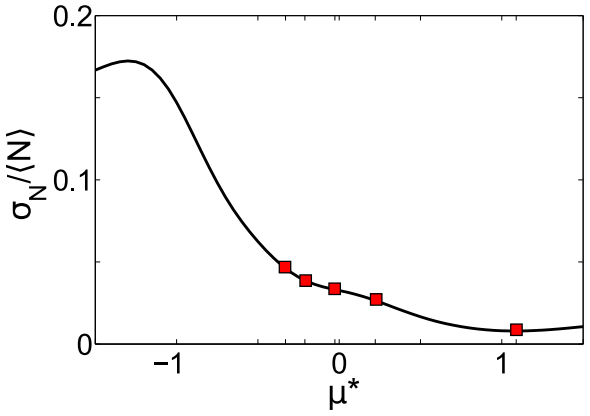

FIG. 3.16: The standard deviation of the number of particles σ_N divided by the average number of particles $\langle N\rangle$ for $L = 50$, $T^* = 0.3$, $J^* = 3$ and attractive walls with $h_1^* = h_L^* = -1$. The red squares indicate the values of the chemical potential taken for the density profiles in Fig. 3.15.

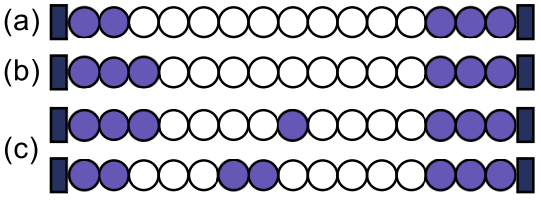

FIG. 3.17: Typical microscopic states present in the GS of the model with $J^* = 3$, attractive walls with $h_1^* = h_L^* = -1$ and $L = 15$ in the CE with $N = 5$ (a), $N = 6$ (b) and $N = 7$ (c). For $N = 5, 7$ the GS is degenerate.

present $p(\rho)$ calculated exactly in the GCE by the transfer matrix method described in Sec. 3.1. In the GCE we consider fixed L and μ, and calculate $p(\mu)$ and $\rho(\mu)$ to obtain $p(\rho)$ for given L. The shape of $p(\rho)$ in the GCE depends on the commensurability between L and the period of the energetically favorable structure. We shall compare the results obtained in the CE for fixed N_0 with the $p(\rho)$ lines obtained in the GCE for six system sizes L.

In Fig. 3.18 the results for the reduced pressure as a function of the average density for CE and GCE are presented. Note the discrepancy between the CE and GCE for $\rho \approx 0.55$, where the periodically ordered clusters consisting of 3 particles are separated by 3 empty sites. In the GCE $p(\rho)$ increases monotonically, although for $\rho \approx 0.55$ the slope is very large, and an inflection point is present. We should stress that in the CE N_0 is fixed and the density changes because of the change of L. In contrast, in the GCE L is fixed, and the density changes because μ, and as a result $\langle N\rangle$, changes. In the GCE there are different branches of $p(\rho)$ for different L. One may interpret the nonmonotonic $p(\rho)$ in the CE as a consequence of the jumps between

the different branches of $p(\rho)$ in the GCE for L and $L-1$.

In order to separate the effect of the fluctuation of the number of particles and the effect of the method by which the density changes, we compare the $p(L)$ curves in the CE with N_0 particles and in the GCE with $\langle N\rangle = N_0$. In Fig. 3.19 the pressure is shown as a function of L for the CE with $N_0 = 21$ and for the GCE with $\langle N\rangle = 21$. The GCE curve was obtained by finding for each system size L the value of the chemical potential μ_0 such that $\rho(\mu_0) \approx N_0/L$. We used the exact expression for density obtained in Sec. 3.1. For such chemical potential the pressure was computed from the approximate formula $\beta p = -\ln\Xi(\mu_0, L+1, T) + \ln\Xi(\mu_0, L, T)$, which is the 1d lattice version of the standard expresion $p = -(\partial\Omega/\partial V)_{\mu,T}$. We also present the density profiles for $L = 35, 36, 37, 38$, where p changes rapidly in a nonmonotonic way. In the case of attractive surfaces the periodic structure where three occupied sites are separated by three empty sites is possible for $L = 39$, and corresponds to seven clusters. For $L < 39$ either the clusters are bigger, or the distances between them are smaller. In both cases the repulsion between the particles is present, and pressure increases. In Fig.3.19 we can see six clusters for $L < 37$, and seven clusters for $37 \leq L \leq 42$. Note that the nonmonotonic dependence of p on L corresponds to the jump of the number of clusters. The unusual increase of pressure in the expanding system results from the transition to a larger number of smaller clusters. The clusters repel each other for $L < 39$. Upon increase of the system size from $L = 38$ to $L = 39$ the separation between the clusters becomes large enough to put the clusters at the separations larger than the range of repulsion, and the pressure drops.

It is interesting that although both the average densities and density profiles for $L = 42$ in the two ensembles are the same, the pressure is different. The reason is that the pressure depends not on the values of the thermodynamic potentials at a given state, but on their change, and as can be seen on panel (f) of Fig. 3.19, for $L = 43$ the profiles differ significantly.

We conclude that the mechanical properties of a confined self-assembling system depend significantly on whether the system expands for given (fixed) number of particles, or the separation between the system boundaries is fixed, and the number of particles decreases due to a change of the chemical potential. In both cases we can have the same change of density, but different changes of pressure. The unusual increase of pressure upon system expansion is found only in the case of fixed (average)

number of particles, and is connected with a significant structural reorganization.

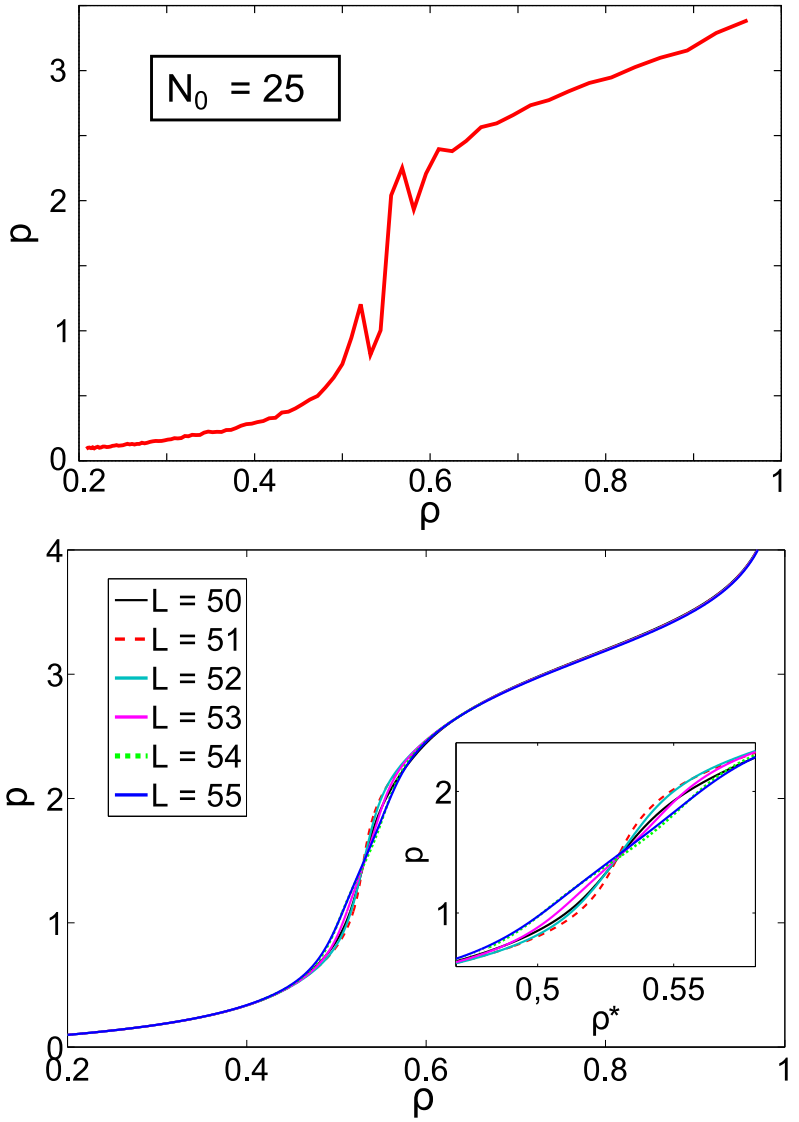

FIG. 3.18: Reduced pressure as a function of density for $J^* = 3$, $T^* = 0.5$ and attractive walls ($h_1^* = h_L^* = -1$). Upper panel: Canonical Monte Carlo (CMC) simulation for the number of particles $N_0 = 25$ and different system sizes L, obtained via virtual insertion method. Lower panel: GCE exact results for pressure vs. density for different system sizes, $L = 50, 51, 52, 53, 54, 55$.

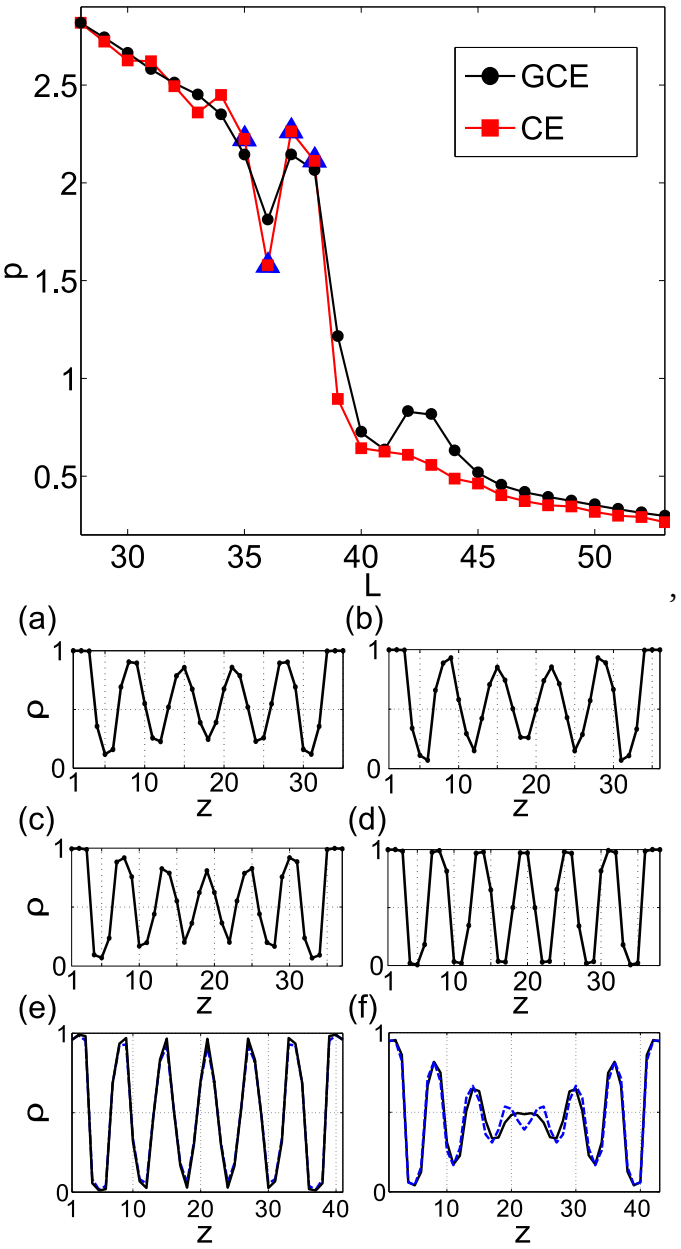

FIG. 3.19: Upper panel: reduced pressure as a function of the system size L for $J^* = 3$ and $T^* = 0.5$ in the case of attractive walls ($h_1^* = h_L^* = -1$). Red curve with squares: Canonical Monte Carlo (CMC) simulation for 21 particles. Black curve with bullets: exact results in the GCE with the average number of particles equal to 21. Lower panels: (a-d) CE density profiles in systems with $L = 35$ (a), $L = 36$ (b), $L = 37$ (c) and $L = 38$. (indicated on the $p(L)$ plot as blue triangles). Panels (e-f): comparison of the density profiles in CE (solid line) and GCE (dashed line) for $L = 42$ (e) and $L = 43$ (f).

3.2.5 The case of elastic boundaries

In this section we assume that the separation between the system boundaries is not fixed, but can fluctuate around $L = L_0$, as in Sec. 3.1.4.2. The change of the wall separation is associated with the energy cost $\Delta U^* = k^*(L - L_0)^2$. Here k^* denotes the elastic constant in units J_1/σ^2. In Fig.3.20 the average system size $\langle L(N)\rangle$ as a function of the number of particles N is presented. The confining surfaces are kept at the separation L by the spring that is at rest for $L_0 = 21$. We assume attractive walls and $T^* = 0.5$. In a system with rigid boundary conditions, attractive walls and $L = 21$, the periodic structure made of 12 particles is energetically favorable. Thus, for $N \leq 12$ only for small values of the spring constant (e.g. $k^* = 0.1$) significant deviations of the average system size from the reference value are present. For $N > 12$ the internal stress of the fluid competes with the elastic forces and $\langle L\rangle > L_0$ even for $k^* = 1$.

We can distinguish two limiting cases: (i) stiff spring, where the system size saturates and the particles become densely packed when N increases, and (ii) soft spring, where the average system size increases with increasing N, and the clusters are separated by empty sites. If k^* is small enough, then the slope of $\langle L(N)\rangle$ increases when a new cluster made of 3 particles is introduced to the system (see panels (a)-(f) of Fig. 3.20). On the other hand, for larger values of k the elastic forces are stronger, and the system tends to modify the structure of the fluid rather then the system size. Between the two limiting cases there is an interesting region where the elastic and the solvation force are comparable and compete.

In Fig.3.21 we show $\langle L(N)\rangle$ for $L_0 = 21$ and $k^* = 0.2$ for several temperatures. At low temperatures three regimes with significantly different slopes of the lines $\langle L(N)\rangle$ can be distinguished. For $N \lesssim 12$ the slope of the line $\langle L(N)\rangle$ is small, because in this case the separation between the clusters ensures no repulsion between them. For $12 \lesssim N \lesssim 15$ the system expands significantly upon addition of particles, because for $N = 14$ an additional cluster appears. In this region the average size of the clusters and the distance between the them is 3. For $N \gtrsim 15$ the slope is small again. Here the elastic stress dominates and the cluster average size increases until the system becomes densely packed. Note that in this region and at low T, before the system gets filled with particles, we obtain an oscillatory dependence of $\langle L(N)\rangle$ on N, with the minima occuring when the number of particles is a multiple of 3. Note also that

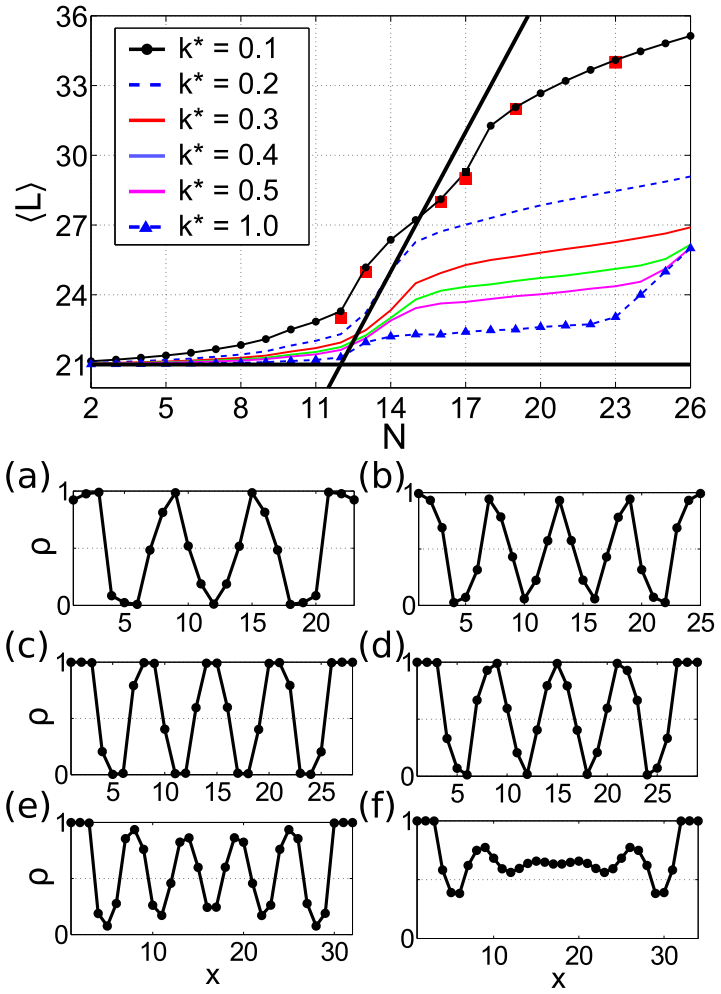

FIG. 3.20: Average system size as a function of the number of particles for different spring constants k^*. The walls are attractive, $h_L^* = h_1^* = -1$, $J^* = 3$, $T^* = 0.5$ and $L_0 = 21$. Thick solid black lines, $L = L_0$ and $L = 2N - 3$, correspond to rigid walls and to walls fully adapting to the optimal structure respectively. In the panels (a-f) the density profiles for the number of particls and the system size marked by the red squares along the black solid curve ($k^* = 0.1$) are shown. (a) $L = 23$ and $N = 12$, (b) $N = 13$ and $L = 25$, (c) $L = 28$ and $N = 16$, (d) $L = 29$ and $N = 17$, (e) $L = 32$ and $N = 19$, (f) $L = 34$ and $N = 23$.

for a given N, $\langle L \rangle$ increases with temperature except from $13 < N < 21$, where for $L = L_0$ the density is between the density of the periodic and the closely packed structures.We verified that the anomalous contraction of the heated system is no longer observed at high T. Finally, note that there is some similarity of the shapes of the $\langle L(N) \rangle$ and $p(\rho)$ lines (Figs.3.21 and 3.18).

The average wall separation and the average density profile give insufficient information about the system behavior. In Figs.3.22 and 3.23 we present histograms for

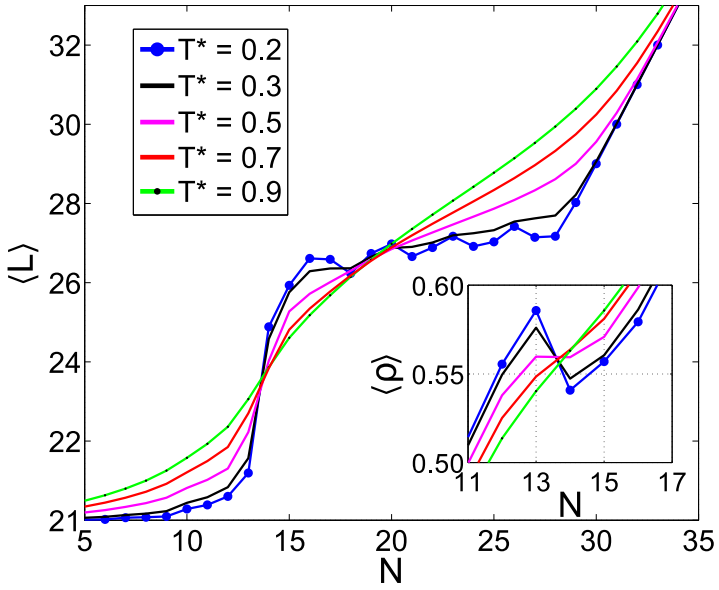

FIG. 3.21: Average system size as a function of the number of particles for different temperatures. Attracting walls assumed ($h_1^* = h_L^* = -1$), $J^* = 3$, spring constant $k^* = 0.2$ and $L_0 = 21$. The inset presents the average density $\langle\rho\rangle \equiv N/\langle L\rangle$ as a function the number of particles.

the wall separation. Two cases can be distinguished - a single maximum in the probability of the appearance of the wall separation L, and a bistability with two maxima in this probability, separated by $\Delta L = 3$.

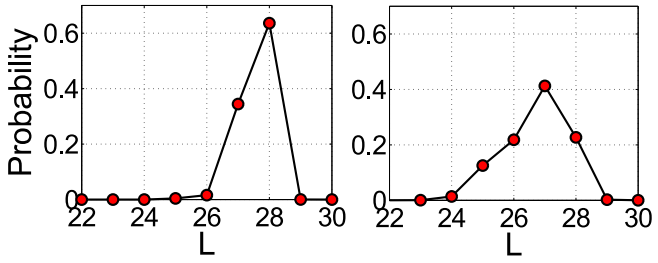

FIG. 3.22: The histograms for the wall separation in the case of elastic boundaries with the spring constant $k^* = 0.2$, $N = 16$, $L_0 = 21$, $J^* = 3$ and attractive walls ($h_1^* = h_L^* = -1$) for $T^* = 0.2$ (left panel), and $T^* = 0.5$ (right panel).

In order to understand the energetics associated with the bistability, let us consider the GS for $L_0 = 10$ and $N = 7$. The microstates shown in Fig. 3.24 correspond to the same energy of the confined system (3.20), when $J^* = 3$ and $k^* = 2/9$. Two different system sizes in the GS can occur when N is not a multiple of 3, and for $L = L_0$ an intra-cluster repulsion is present. The expansion is associated with a simultaneous increase of elastic energy of the walls, and decrease of the internal energy of the particles, when the separations between them are such that the repulsion is absent.

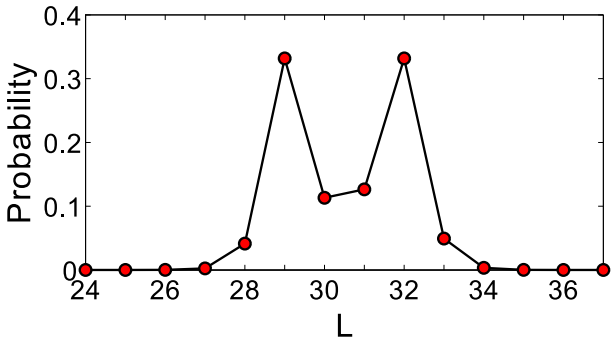

FIG. 3.23: The histogram for the wall separation in the case of elastic boundaries with the spring constant $k^* = 0.06607$. $J^* = 3$, $T^* = 0.5$, $N = 17$, $L_0 = 19$, attractive walls ($h_1^* = h_L^* = -1$).

Each microstate in Fig. 3.24 occurs with the same probability, but because of the difference in the degeneracy for $L = L_0$ and $L = L_0 + 3$, the probability ratio for the two lengths is $p(L_0+3)/p(L_0) = 3$. To estimate the spring constant leading in the above example to equal probability of L_0 and $L_0 + 3$ for low T^*, we take into account only the microstates shown in Fig. 3.24, and require that $\exp(-\beta^*(-5 + J^*)) = 3\exp(-\beta^*(-4+9k^*))$ (see (3.20) for $L = L_0, L_0+3$). For $T^* = 0.2$ we obtain $k^* \approx 2/9+0.0244136$ in very good agreement with the results of simulations shown in Fig. 3.24.

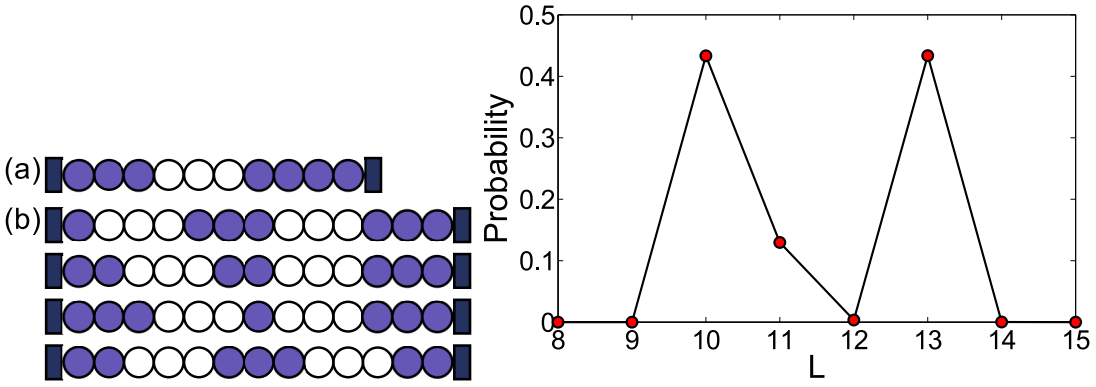

FIG. 3.24: Left panel: The microstates in the GS of a system consisting of 7 particles with the repulsion to attraction ratio $J^* = 3$, confined by attractive walls ($h_1^* = h_L^* = -1$) on a spring with the spring constant $k^* = 2/9$ that is at rest for $L_0 = 10$. In panel (a) $L = L_0$ while in panel (b) $L = L_0 + 3$. Note that the microstates symmetric to those also have the same energy, hence for $L = 10$ there are 2 different microstates with the same energy, and for $L = 13$ there are 6. These microstates correspond to the maxima of the probability shown in the right panel, in which we present the histogram for the wall separation in the above system in the case of $T^* = 0.2$ and elastic boundaries with the spring constant $k^* = 2/9 + 0.0244135$.

3.3 The role of fluctuating number of confined particles

We have studied the effect of various constraints on colloidal self-assembly in thermodynamic states that correspond to self-assembly into small clusters separated by voids. In our model system small clusters with no intra-cluster repulsion yield a negative contribution to the internal energy, and do not interact with one another if the separation between them is larger than the range of repulsion. The positions, the size and the number of clusters can fluctuate and different deformations of the bulk structure are possible in confinement. In order to determine the role of constraints imposed on the number of particles, we have compared density profiles, equations of state, and effects of elastic boundary conditions.

Structure: *If the number of particles in the CE (fixed N) is too small for formation of the bulk structure, then one more cluster can be present in the GCE (fixed μ) despite the same average number of particles* (Fig 3.15). Interestingly, the different number of clusters in the two ensembles is observed for thermodynamic states that *do not* correspond to the maximum of the fluctuation of the number of particles. This is because the fluctuations of the number of particles are coupled with the fluctuations of the size of the clusters. Even a small increase of the number of particles in the GCE together with the splitting of the clusters can lead to formation of a larger number of smaller clusters. The qualitative difference between the two ensembles occurs for quite large number of particles. This behavior is different than in simple fluids, where the difference between the two ensembles was observed only for very small number of particles confined in very small pores [113, 114].

Equation of state: In the bulk the isotherms $p(\rho)$ do not depend on the way in which the variation of density is attained. In the confined inhomogeneous systems it is no longer the case: *Different curves $p(\rho)$ are obtained when the size of the system changes with fixed number of particles, or when the number of particles changes at fixed system size.*

The shape of the $p(\rho)$ curve obtained in the GCE with fixed L depends significantly on L, or more precisely on the commensurability of L and the period of the ordered structure (Fig 3.18). In the CE with fixed N we have obtained anomalous decrease

of pressure for increasing density for small density intervals below and above the density of the equilibrium bulk structure (Fig 3.18). Inspection of density profiles shows that *the anomalous increase of pressure for increasing system size with fixed number of particles is accompanied by increased number of clusters* (the larger cluster splits) (Fig 3.19). Recall that at short separations the clusters repel each other, and this leads to the increase of pressure. The pressure rapidly drops when L further increases and the clusters do not repel one another any more. In order to check if the anomalous dependence of pressure on density follows from the fixed number of particles or from the process by which the density varies, we computed the $p(L)$ curve in the GCE with fixed average number of particles. We have obtained similar curves in the two ensembles except for large slits. In both ensembles the anomalous increase of pressure for increasing L is associated with the increasing number of clusters. For some large L the number of clusters increases with the system size in the GCE but not in the CE (Fig.3.19 e,f). In this case a maximum in the $p(L)$ curve is present only in the GCE.

Bistability in elastic confinement: If the width of the slit can vary, then the system tends to equilibrate the competing solvation and elastic forces. We have found that the equilibrium size of the system is not always unique. In Sec. 3.1 we observed a bistability in a system confined by elastic walls with permeable walls (fixed μ). Two different system sizes can be equally probable: one with expanded and the other one with compressed boundaries. The size fluctuations are accompanied by an absorption or evaporation of a whole cluster. In the case of impervious walls (fixed N) considered in Sec. 3.2 a bistability exists too. *In both cases the origin of the bistability is the change of the number of clusters, but the mechanisms which lead to the change are different*. The number of clusters can fluctuate for fixed number of particles, when the state with a smaller number of bigger clusters and the state with a larger number of smaller clusters are equally probable. When the intra-cluster repulsion in large clusters competes with the elastic energy of stretched boundaries, the clusters can split and separate. The difference between the two equilibrium widths of the system is equal to the period of the bulk structure in the case of permeable walls, and to half the period of the bulk structure when the number of particles is constrained.

Our results show that different anomalies in the confined inhomogeneous systems occur when the release of some constraint or a change of the thermodynamic state leads to a change of the number of clusters. In particular thermodynamic states the structure and anomalies depend qualitatively on the ability of the system to interchange particles with its surroundings.

3.4 Summary

We have studied a system interacting with the SALR potential in slits of various widths with electrically neutral surfaces. We have considered different types of confinement: permeable or impervious, as well as rigid or elastic. In the case of permeable confinement, we have solved the model exactly, while for impervious walls Monte Carlo simulations were performed. In the case of rigid confinement we have studied: the distribution of the particles in confinement, the dependence of pressure on the system size or the average density and the effective potential between the confining surfaces. In the case of elastic confinement we have focused on the distribution of the system size. We paid particular attention to the values of the chemical potential and the number of confined particles which correspond to inhomogeneous distribution of the particles in the bulk.

The bistability of the system confined by elastic walls (Figs.3.13 and 3.23) is our most interesting result in this chapter. *The bistability in the system size distribution occurs when the equilibrium between the competing solvation and elastic forces is not unique.* The difference between the two equally probable system sizes depends on whether the confinement is permeable or impervious. In the case of permeable walls the size difference is equal to the period of the bulk structure, while in the case of impervious walls the size difference is equal to half of the period. Hence, the larger is the period, the greater is the distance between the two almost equally probable system sizes. It should be stressed that the period of the bulk structure is determined by the range of attractive and repulsive parts of the effective pair interaction potential and in the case of colloids can be as large as hundreds of nanometers or even micrometers. What is more, since in our 1d system the energy barrier is $\sim k_B T$, spontaneous changes of the system size may be induced by thermal fluctuations. **Thus, a self-assembly of *nano*-objects can lead to spontaneous changes of the**

system size on a micrometer scale. Apart from ranges of the competing interactions, the bistability phenomenon should not depend on the specific shape of the effective interparticle potential as long as it leads to formation of relatively small clusters. On the other hand, we cannot exclude the possibility that for large clusters the fluctuations of the cluster size can suppress the bistability effect.
The confined self-assembling system behaves as a soft elastic material itself (Fig.3.10), and the bistability takes place when its elastic constant is similar to the elastic constant of the boundaries. The elastic constant of the self-assembling system depends on particle concentration inside the pore. **Thus, interestingly, in the case of permeable confinement the bistability can be induced or suppressed by changing the concentration of particles in the surroundings.** On the other hand, if the elastic constant of the boundaries is very small, then the system can accommodate to the bulk structure and hence, the effects related with the incommensurability or particles interactions with the confinement are softened or even they vanish.

In the case of permeable walls the conditions in the surroundings influence also the deformations in the confined system. We found that by changing μ^* we induce changes in the number and size of the layers in the confined system. These structural changes are reflected in "steps" in $\rho(\mu)$. In order to help to interpret simulation results we obtained exact expressions for $\rho(\mu^*)$ in the case of PBC and various system sizes. We obtained steps in $\rho(\mu^*)$ corresponding to the change of the type of defects resulting from the incommensurability. **In order to avoid misinterpretation of $\rho(\mu^*)$ steps as phase transitions, one should verify if the steps disappear for commensurate system sizes, or if their heights decays as $\sim 1/L$ for increasing system size L.**

The confined simple fluids and the SALR systems differ significantly. Packing effects of molecules or clusters play important role in both cases, especially for the solvation force that exhibits oscillatory decay on the corresponding length scale in each case. However, the clusters can split or merge, unlike the molecules. This leads to qualitative differences between the ensembles, the bistability of the system size and anomalies in the $p(\rho)$ and the $\langle L(N)\rangle$ curves. **The $p(\rho)$ curve is nonmonotonic for both the imperious and the permeable confinement (Fig. 3.19), while the $\langle L(N)\rangle$ curves show that in some ranges of N and T the system may shrink upon**

heating in the case of impervious walls (Fig. 3.21).

We expect that different shapes of the SALR potential will lead to similar results, provided that the clusters contain only a few particles. In the case of the SALR potential leading to large clusters, as those studied in Ref.[38], the effects of confinement may be different because of the cluster-size fluctuations. This expectation is based on the observation that quite different effects of confinement were observed in the case of small- and large-periods of the bulk structure in systems containing amphiphilic molecules [48]. Based on similarities between amphiphilic and SALR systems discussed in Chapter 2, we expect that the effects of confinement in the SALR and in the amphiphilic systems are similar too, but this expectation should be verified.

Chapter 4

Effects of confinement in the two-dimensional model of colloidal self-assembly

In this chapter we study the effect of imposing rigid boundary conditions on the system of particles interacting *via* the SALR potential on a two dimensional triangular lattice. In particular, we will consider self-assembly of particles on the surface of a cylinder. In the first step, the influence of the confinement on the ground state will be studied. In particular, we will characterize the effects of confinement for slit widths optimal and not optimal for the bulk structures to stabilize. Since the model is only virtually infinite (via periodic boundary conditions in one of the directions), therefore from a strict thermodynamic point of view, at $T > 0$ we should not expect real thermodynamic transitions. Nevertheless, the fact that the bulk system exhibits different thermodynamic phases, might produce significant changes of the properties of the confined system when varying the temperature or the chemical potential.

4.1 The model

We continue the study of colloidal self-assembly driven by competing interaction potential, hence we assume the same form of the potential as in Sec. 2.2, that is: the attractive interactions between first neighbors on the triangular lattice, and repulsive interaction between third neighbors. In order to mimic the topology of a cylinder, we assume periodic boundary conditions in the $\mathbf{e}_1$ direction, while rigid boundary conditions are considered in the direction perpendicular to $\mathbf{e}_1$ (see Fig. 4.1). The length of the system in the $\mathbf{e}_1$ direction we denote by L_1. In what follows, we focus on the impact of the wall-wall separation on the self-assembling structures, hence we will choose only such L_1 that are commensurate with the period of the stable structures in the $\mathbf{e}_1$ direction. As in Chap. 3, we assume that the confinement is electrically neutral, therefore the walls interact only with the particles that occupy the nearest neighboring sites of the walls. Thus, if we denote the distance between the confining walls by L_2, then the walls interact only with the particles which (x_1, x_2) position has $x_2 = 1$ or $x_2 = L_2$ (in Fig. 4.1 we chose $L_2 = 8$). We assume that the energy of the particle-wall interaction, h, is independent of the particle position in the $\mathbf{e}_1$ direction and is equal for both walls. With such assumptions the grand-canonical Hamiltonian can be written as

$$\begin{aligned} H_{W2d}[\{\hat{\rho}\}] &= \frac{1}{2}\sum_{\mathbf{x}}\sum_{\mathbf{x}'}\hat{\rho}(\mathbf{x})V(\mathbf{x}-\mathbf{x}')\hat{\rho}(\mathbf{x}')-\sum_{\mathbf{x}}\mu\hat{\rho}(\mathbf{x}) \\ &\quad +h\sum_{x_1=1}^{L_1}(\hat{\rho}(x_1,1)+\hat{\rho}(x_1,L_2)), \end{aligned} \tag{4.1}$$

where the pair interaction potential V is given by Eq. (2.84). As previously, we will use reduced units $X^* \equiv X/J_1$.

Along this chapter we used the simulation techniques described in Sec. 2.2.4.1 for the colloidal self-assembly in the bulk, that is: Metropolis Monte Carlo, thermodynamic integration and parallel tempering technique.

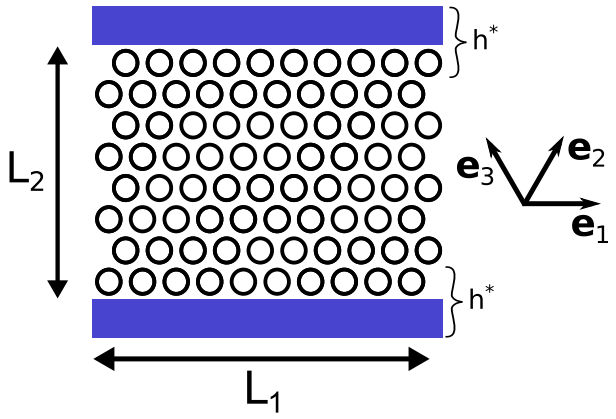

FIG. 4.1: Sketch of the two-dimensional triangular lattice with the slit boundary conditions. L_1 is the length of the system in direction $\mathbf{e}_1$ (in this direction periodic boundary conditions are assumed), whereas L_2 is the distance between the confining walls (measured in number of layers). The walls interact only with the particles which occupy the first neighboring row of the wall.

4.2 The ground state

In this section we present how the bulk ground state is modified by imposing rigid boundary conditions in one of the principal directions[1]. Firstly, we focus on the impact of the particle-wall attraction. Hence, we consider the wall-wall separations, L_2, that are energetically optimal for the bulk structures i. e. the bulk structures can stabilize in the interior of the slit. In such a case analytical calculations of the ground state are performed. Secondly, we investigate the effect of the wall-wall separation. For this second case, in order to focus attention, we consider only $\mu^* = 6$ and $J^* = 3$, which in the bulk GS corresponds to the stability region of the lamellar phase. The impact of L_2 is analyzed by means of MC simulations.

4.2.1 Effect of attractive walls

In order to study the effect of attractive walls on the ground state structures we assumed that the wall-wall separation is so large, that in the middle of the slit and far from the confining walls there is enough space for the bulk structures to stabilize. We have found that for $h^* = -1$, fixed L_2 and upon a change of the chemical potential the system exhibits phase transitions that are not present in the bulk. Namely, some of the transitions are associated with a change of the particle distribution only in the close neighborhood of the confining walls, i. e. some of the found transitions

[1]The bulk ground state in (J^*, μ^*) variables is presented in Fig. 2.43.

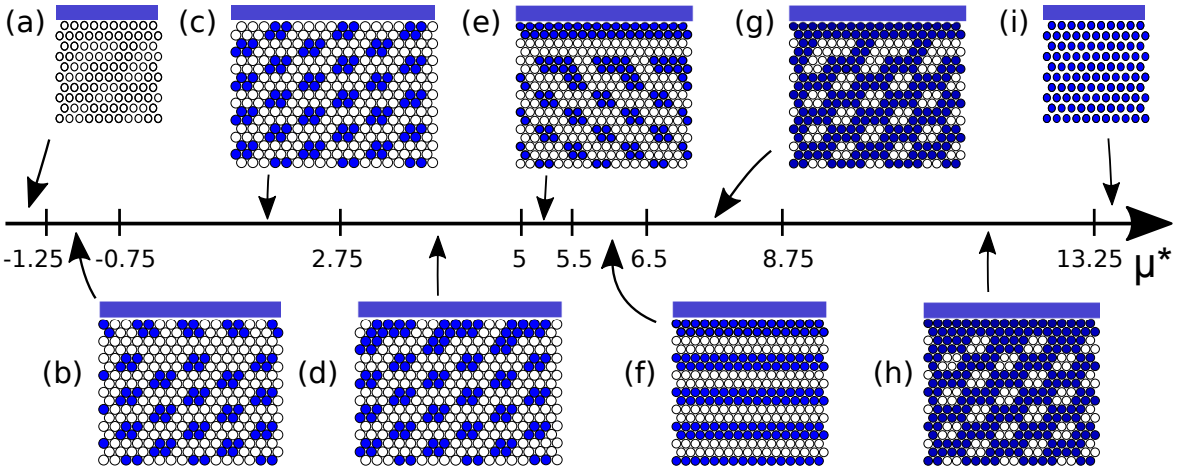

FIG. 4.2: Ground state for $J^* = 3$, $h = -1$ and $L_2 = 2n$, with $n \to \infty$. Panels (a-i) present only a region of the slit close to one of the confining walls. The configurations close to the opposite wall can be obtained by rotation of the presented structures by 180°, with the axis of rotation perpendicular to the lattice surface.

are only *surface phase transitions*. In Fig. 4.2 we present the ground state as a function of μ^* for $J^* = 3$ and for $L_2 \gg 1$ that is optimal for the bulk structures in the $\mathbf{e}_2$ direction. The loci of phase transitions were found by comparison of the grand canonical energy per lattice site, $H_{W2d}/(L_1 L_2)$, of the structures determined by parallel tempering Monte Carlo simulations. The reduced chemical potentials at particular transitions as a function of J^*, L_2 and h^* are given by the following expressions

$$\mu^*_{ab} = \frac{5L_2 - 10 - 12h^*}{8 - 4L_2} \xrightarrow[L_2\to\infty]{} -1.25, \tag{4.2}$$

$$\mu^*_{bc} = -\frac{1}{4}(5 + 2h^*), \tag{4.3}$$

$$\mu^*_{cd} = \frac{1}{4}(8J^* + 2h^* - 11), \tag{4.4}$$

$$\mu^*_{de} = \frac{1}{4}(-14 + 12J^* + 2h^*), \tag{4.5}$$

$$\mu^*_{ef} = \frac{3.5L_2 - 38 + 34J^* - 3J^*L_2}{10 - L_2} \xrightarrow[L_2\to\infty]{} 3J^* - 3.5, \tag{4.6}$$

$$\mu^*_{fg} = \frac{-18J^* - 12 + 3L_2J^* - 2.5L_2}{L_2 - 6} \xrightarrow[L_2\to\infty]{} 3J^* - 2.5, \tag{4.7}$$

$$\mu^*_{gh} = 4J^* - 13/4, \tag{4.8}$$

$$\mu^*_{hi} = 6J^* - 19/4, \tag{4.9}$$

where μ^*_{xy} corresponds to the value of μ^* at the coexistence between the phases presented on panels (x) and (y) of Fig. 4.2. Since at the coexistence with the lamellar phase, L_2 has to be commensurate with the period of the lamellar and the rhomboidal or the bubble phases, the formulas for μ^*_{ef} and μ^*_{fg} are valid only for $L_2 = 4n+2$ with $n > 3$. In the other cases L_2 only needs to be even and large enough in order to avoid interference between the local structures which are adsorbed at the opposite walls. Note, however that not all μ^*_{xy} depend on L_2. We have found that the loci of the surface phase transitions are independent of L_2, if the transition occurs between structures which differ exclusively by the particle arrangement in the neighborhood of the walls. On the other hand, μ^*_{xy} depends on the strength of the particle-wall interaction, h^*, only if the transition takes place between phases with structures that differ at sites that are nearest neighbors of the walls. Interestingly, the increase of the chemical potential not always results in an increase of the walls adsorption (see panels (b) and (d) of Fig. 4.2). The range of validity of the GS phases shown in Fig. 4.2 with respect to variations of the wall attraction has not been checked. However, based on the results for the 2d system (Fig. 3.9) one should expect that for attraction stronger than $h^* = -1$ a surface phase transition between the vacuum and a phase with either only monomers or only rhomboidal clusters adsorbed at the walls should appear.

These results show that if the distance between the confining walls is optimal for the bulk phase stable at the corresponding thermodynamic conditions, then at $T^* = 0$ *the confinement may influence the stable morphologies only locally*.

4.2.2 Effect of the slit width on the lamellar phase

The effects of incommensurability between L_2 and the period of the bulk structures in $\mathbf{e}_2$ direction, were studied only for the case of $\mu^* = 6$, which corresponds to stability of the lamellar phase. The ground states for $\mu^* = 6$ and different wall-wall separations were obtained with the following procedure: for given values of L_2 and h^* we proceed by applying the parallel tempering Monte Carlo for different system lengths, L_1. We typically took 151 values of the reverse temperature β^*, given as $\beta^*_i = i\Delta\beta^*$; with $i = 0, 1, \cdots 150$, and $\Delta\beta^* = 0.10$. The GS configuration and the GS energy are taken as those corresponding to the value L_1 which minimizes the grand canonical energy per site, $H_{W2d}/(L_1 L_2)$.

If the confining surfaces strongly attract particles, then energetically favorable configurations will have double layers (stripes) of particles adsorbed onto the walls. The configuration of the particles between the adsorbed stripes will depend upon the distance between the confining walls, L_2. If $L_2 = 4n+2$, where n is a positive integer, then the distance is commensurate with the period of the bulk structure and the straight lamella (see panel (f) of Fig. 4.2) has the lowest energy. Note that in the case of the straight lamella no degeneracy of the GS is present.

For L_2 incommensurate with the period of the bulk structure *defects*, consisting of a few additional particles, appear in the adsorbed stripes (see Fig. 4.3). In order to avoid excess repulsion, the nearest stripe (second from the wall) has to bypass the defect. The turns of the nearest stripe entail turns of the other stripes inside the slit in such a way that it is energetically favorable to build a defect at the opposite wall. Such construction ensures that the distance between every two defects is the same, hence three consecutive defects in the $\mathbf{e_1}$ direction form an equilateral triangle (Fig. 4.4).

The shape of the defect envelope depends not only on the size of the defect, but also on L_2. Defects consisting of two particles indicate a shift of the nearest stripe by one row in direction perpendicular to the walls if $L_2 = 4n-1$, or by two rows if $L_2 = 4n$. A trapezoidal defect which can occur if $L_2 = 4n+1$ indicates a shift of the nearest stripe by three rows. Such shifts allow the lamellar stripes inside the slit to adjust their positions to the stripe adsorbed at the opposite wall and minimize the effect of the incommensurability.

Note that only for large enough L_2 (> 13) the shape of the defect is determined by $\mod(L_2, 4)$. That is because for narrow slits and positive value of the chemical potential, enlarging the defects and the size of the unit cell may result in decrease of the grand canonical energy per lattice site. But for large enough slit width the distance L_2 determines the shape and the position of the defects, hence having L_2 one can also tell the size of the unit cell in the $\mathbf{e}_1$ direction, L_1, which is given by the following formula

$$L_1 = \begin{cases} L_2 - 1 & \text{if } L_2 = 4n-1 \\ L_2 - 4 & \text{if } L_2 = 4n \\ L_2 - 3 & \text{if } L_2 = 4n+1. \end{cases}$$

We cannot tell, however, if for large wall-wall separations (e. g. $L_2 > 30$) L_1 is still determined uniquely by L_2.

In comparison to the bulk, stripes in the slit confinement are allowed to turn not only in one, but in two directions. Thanks to this additional degree of freedom the confined system is also able to stabilize in a lamellar structure, however this time the segments of the lamella are parallel not only to the two main lattice directions, but to all the three directions. Nevertheless, the presence of the confining walls removes the degeneracy of the GS. Note, however, that in the case of periodic boundary conditions in both directions the lamellar phase may consist of just one stripe wrapped around the torus, while in the case of a slit with the cylindrical geometry there are always many parallel stripes wrapped around the cylinder, and this is a qualitative difference.

4.2.3 Effect of the wall-particle repulsion on the lamellar phase

For the case of attractive walls, we have seen that the slit geommetry favours the formation of stripes that are roughly parallel to the walls. In what follows we will try to elucidate whether this behavior occurs for neutral and/or repulsive walls. To this aim, we will consider, as above, $\mu^* = 6$, and systems with $L_2 = 16$. We will look at the GS behavior for different wall-particle interactions.

In the case of attractive walls, with $h^* = -1$, the GS is shown in Fig. 4.3. Two lamellar stripes are close to the walls, and two *undulating* stripes appear in the inner region of the slit. The periodicty length of the GS configurations is $L_1 = 12$. For $h^* = 0$ the GS configurations varies, exhibiting $L_1 = 16$ (Left panel of Fig. 4.5). Some empty sites appear at the rows that are nearest neighbors of the walls, but the general structure of the system is quite similar to the one corresponding to attractive walls. The same ground state persists for slightly repulsive walls: $h^* = 1$ and $h^* = 2$. On increasing the repulsive character of the walls, at $h^* = 3$ the particles are expelled from the bottom and top rows of the slit, and the GS configuration resembles that of $L_2 = 14$ and attractive walls, with four parallel straight stripes that do not interact with the walls (Right panel of Fig. 4.5). Hence having the wall separation $L_2 = 4n$ one can remove the defects by changing the particle-wall interaction from attractive to strongly repulsive. We expect that the defects present for $L_2 = 4n - 1$ would be removed if one of the walls would be attractive and the opposite wall would be

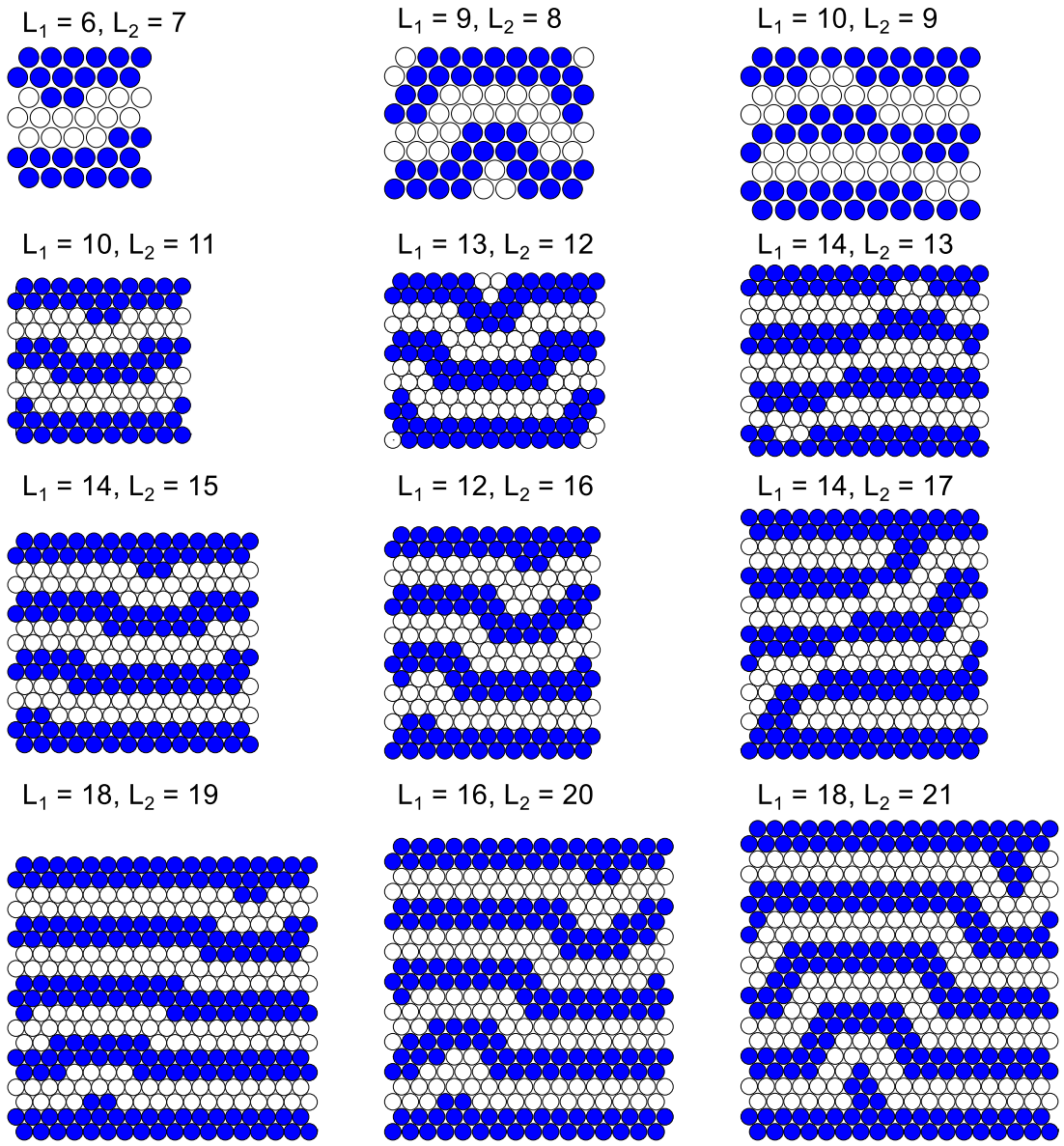

FIG. 4.3: The ground state ($T = 0$) configurations for $L_2 = 4n - 1$ (left column) $L_2 = 4n$ (center column) and $L_2 = 4n + 1$ (right column), where $n = 2, 3, 4, 5$. The confinement attracts the particles with $h^* = -1$. For the sake of figure clarity the walls are not shown.

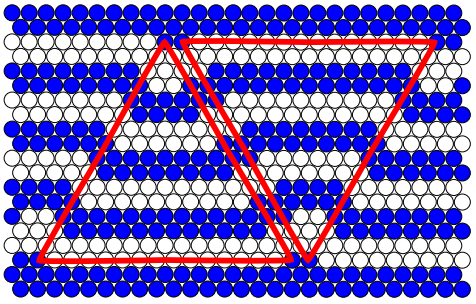

FIG. 4.4: The defects are in the vertices of the equilataral triangle.

strongly repulsive, while in the case of $L_2 = 4n + 1$ in order to remove the defects different wall-particle interaction range would be necessary.

Thus, the presence of defects in the GS structures depends not only on the wall separation, but also on the wall-particle interaction which sufficiently tuned may help to remove the defects.

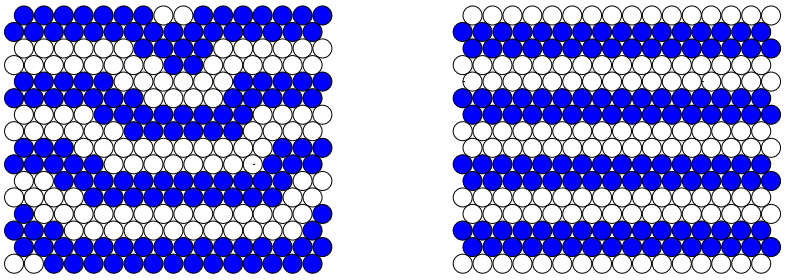

FIG. 4.5: Ground state configuration for $L_2 = 16$ for different interactions with the walls. Left panel: $h^* = 0$, right panel: $h^* = 3$.

4.3 Effective interaction between the walls

We start the investigation of the model at $T^* > 0$ by computing the effective interaction between the confining walls, $\Psi(L_2)$ (see Eq. 3.8). In order to compute $\Psi(L_2)$ we have applied the MC thermodynamic integration procedure for fixed chemical potential, which was previously used for the bulk system (Sec. 2.2.4).

The grand potentials per lattice site for the bulk and the slit system, necessary for the calculation of the excess grand potential (see Eq. (3.8)) were computed using the following relation

$$\beta\tilde{\Omega}(\beta,\mu) = -\ln 2 + \int_0^\beta \frac{\langle \mathcal{H}(\beta',\mu)\rangle}{L_1 L_2}\, \mathrm{d}\beta', \tag{4.10}$$

where $\mathcal{H}$ is the grand canonical Hamiltonian of the corresponding model given by Eq. (2.83) in the case of the bulk, and by Eq. (4.1) in the case of the slit, and the term $-\ln 2$ results from the assumption that at infinite temperature our model acts like an ideal lattice gas. To obtain $\Psi(L_2)$ out of Ω_{ex}, we note that these two quantities at fixed temperature differ only by a constant (see Eq. (1.13) in introduction). Since $\lim_{L_2\to\infty} \Psi(L_2) = 0$, we have estimated the constant by the value of Ω_{ex} for which the curve reaches a plateau.

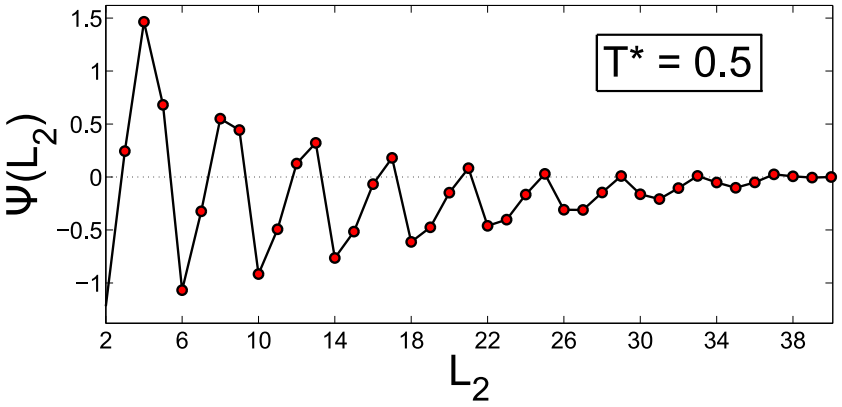

FIG. 4.6: The effective wall-wall interaction potential as a function of the wall-wall separation , $\Psi(L_2)$ at temperature $T^* = 0.5$ for $L_1 = 120$, $\mu = 6$ and attractive walls with $h^* = -1$.

The simulations were carried out with the following model parameters: for the bulk system we used a square lattice with $L = 120$, whereas for the slit we considered a lateral length $L_1 = 120$, and different slit widths L_2, ($L_2 \leq 40$). We used temperatures ranging from $\beta^* = 0$ up to, typically $\beta^* = 4$ or $\beta^* = 5$ with a grid constant $\Delta\beta^* = 0.01$. As usual, the initial configurations for all the replicas were built by assigning at random to each site one of its possible states: 0 or 1.

A typical shape of $\Psi(L_2)$ is shown in Fig. 4.6. It can be observed that the effective potential between the walls exhibits a significant decay length, with an oscillatory behavior. In addition, slit widths that fulfill $L_2 = 4n + 2$, with $n = 1, 2, \ldots 5$ correspond to local minima of $\Psi(L_2)$. We can anticipate that this effect is due to the good fitting of the straight lamellar stripe structures to those widths. Note, however, that for $L_2 > 22$ the minima are located at $L_2 = 31$ and $L_2 = 35$, which do not correspond to the wall separation optimal for the straight lamella structure.

The shape of $\Psi(L_2)$ is very similar to the shape of Ψ obtained for the 1d model (Fig. 3.4). The similarity follows from the fact that the lamellar phase is periodic only in direction perpendicular to the walls. Thus, the density profile of the slit cross-section averaged over $\mathbf{e}_1$ defined as

$$\rho(x_2^0) \equiv \frac{1}{L_1} \sum_{x_1=1}^{L_1} \hat{\rho}(x_1, x_2^0) \tag{4.11}$$

resembles the density profiles of the one-dimensional cluster phase (see Fig. 4.7 and Fig. 3.15). Since in the 1d model, the oscillatory behavior of Ψ leads to bistability in the system size distribution, we predict that a similar phenomenon can occur also

in the 2d slit.

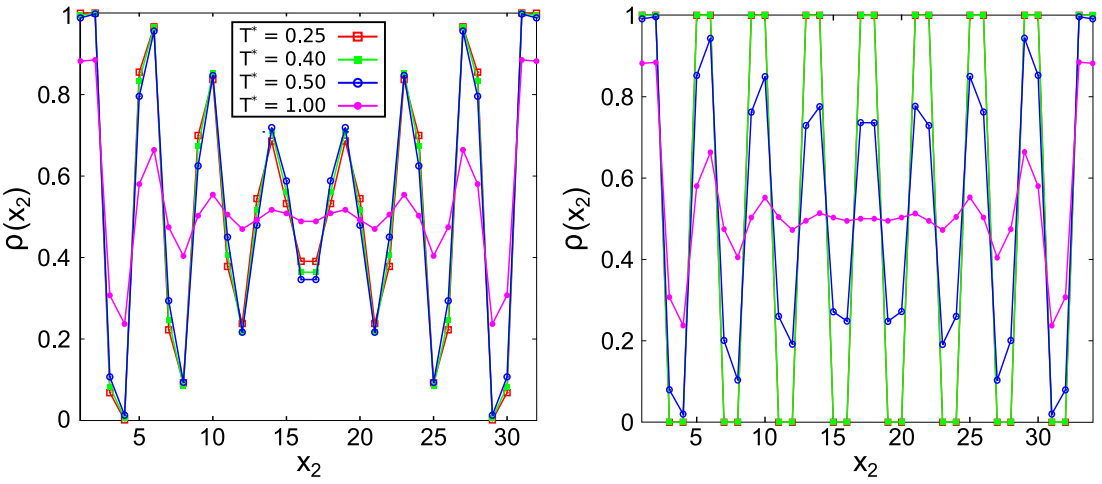

FIG. 4.7: The density profiles in the cross-section of the slit given by Eq. (4.11) for several temperatures. Left panel: $L_2 = 32$, right panel: $L_2 = 34$. The color code is the same in both panels. The walls are attractive with $h^* = -1$.

In order to gain some intuition about the structural changes that happen within one period of $\Psi(L_2)$, in Fig. 4.8 we show some representative configurations for slits widths $L_2 = 30, 31, 32, 33, 34$, with $L_1 = 120$, and at $T^* = 0.25$. For $L_2 = 30$ and $L_2 = 34$ the system presents respectively eight and nine straight stripes, which are parallel to the walls. The periodicity of the system in direction perpendicular to the walls is four, and the top and bottom stripes are located close to the walls. For $30 < L_2 < 34$ the structure of the system can be described as composed by eight stripes, but the stripes that are not close to the walls are no longer straight, showing some cooperative corrugation. The corrugation seems to exhibit some local order in direction $\mathbf{e}_1$, similar to the way the defects in the ground state spread.

The effect of the temperature is shown for $L_2 = 32$ in Fig. 4.9. Obviously, the higher temperature is the more defects in the lamellar structure occur. It is not clear, however, if the defects appear in a specific manner or not. Another question is, if a separate phase, like the molten lamella phase in the bulk, stabilizes at intermediate temperatures. In the following section we will propose a quantitative description of the effects of temperature on the system.

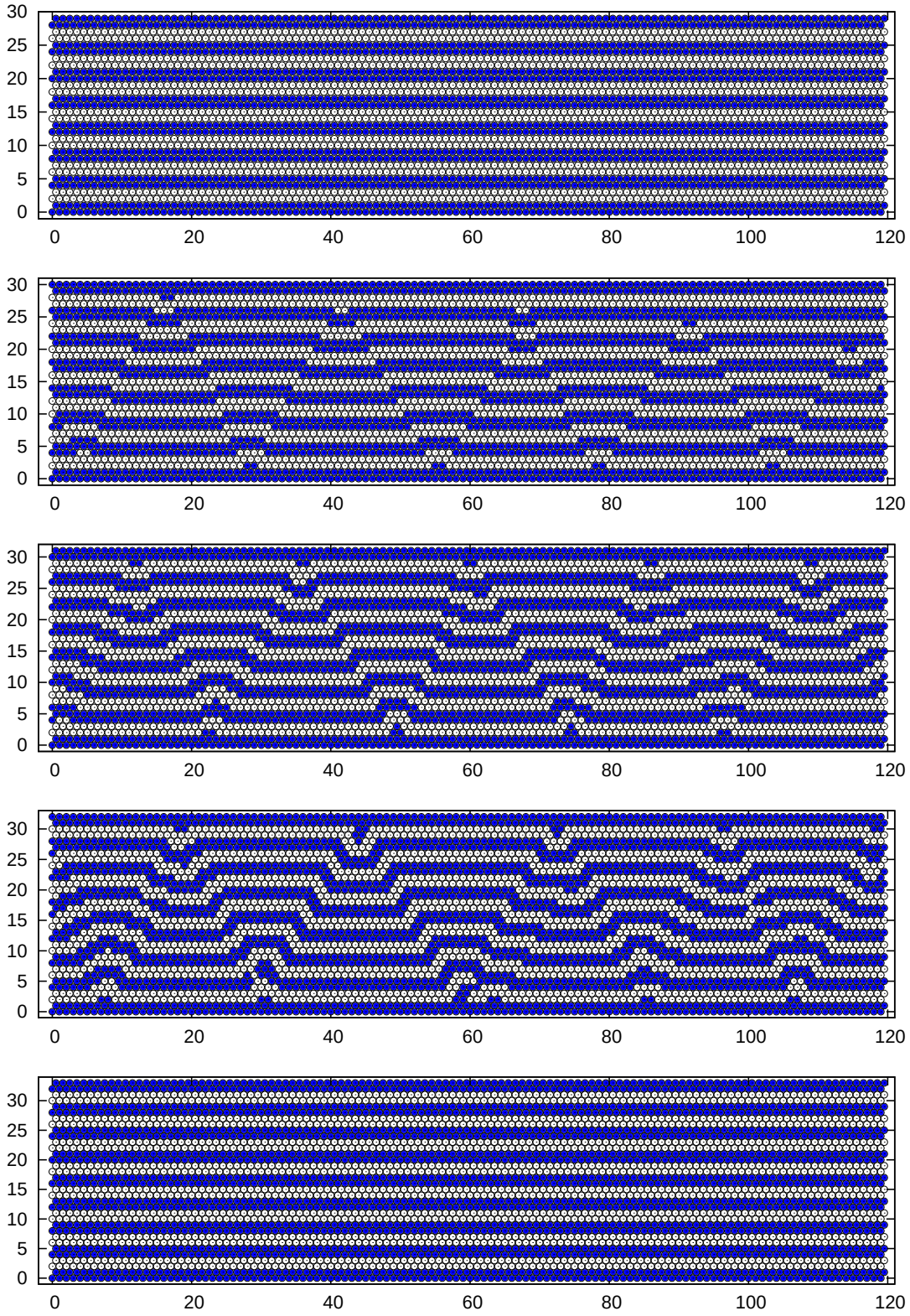

FIG. 4.8: Representative configurations of the systems with attractive walls ($h^* = -1$), at low temperature $T^* = 0.25$, and different pore widths. Form top to bottom: $L_2 = 30$, $L_2 = 31$, $L_2 = 32$, $L_2 = 33$, and $L_2 = 34$. Only the system sites are plotted.

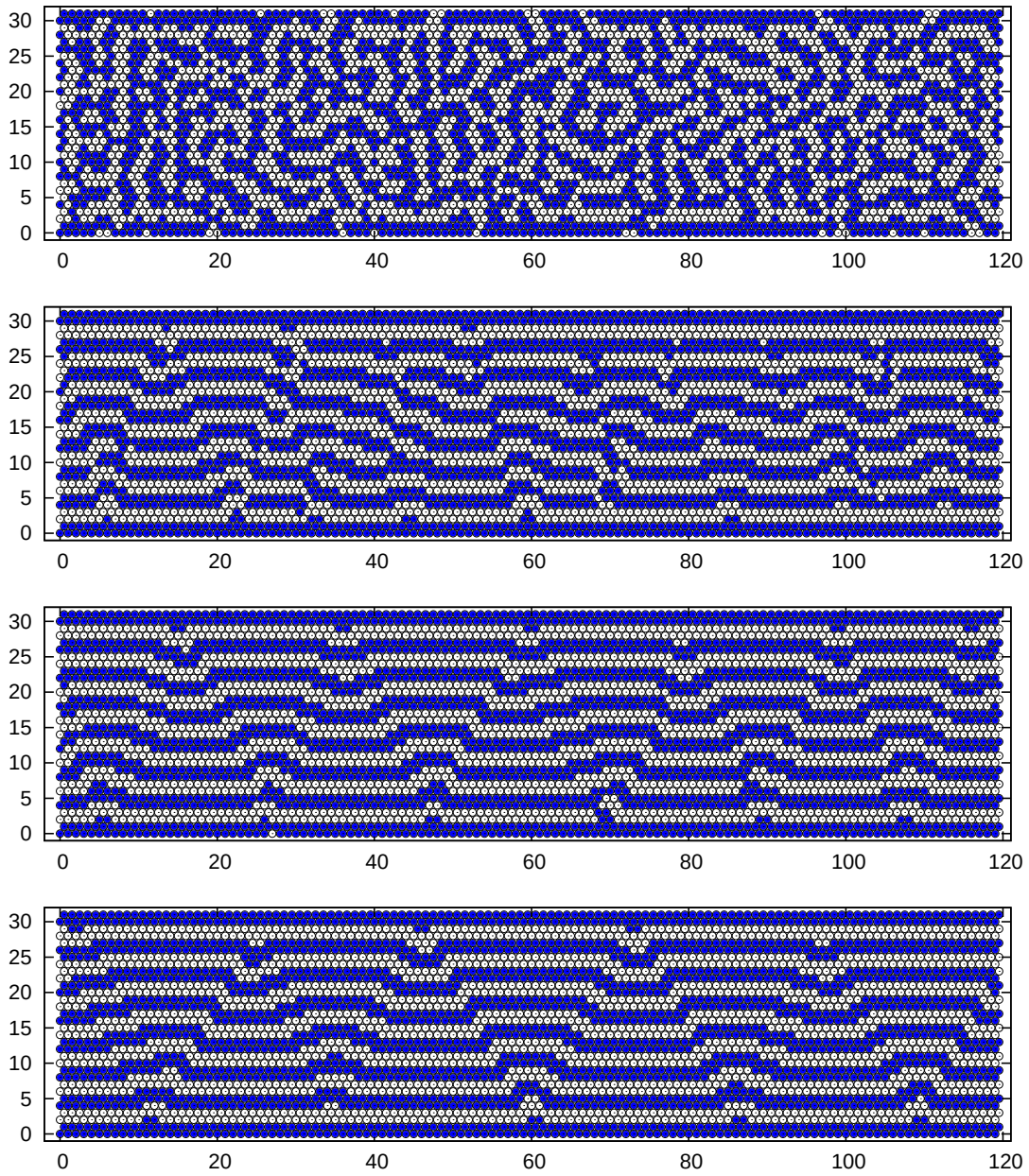

FIG. 4.9: Representative configurations of the system with attractive walls ($h^* = -1$) and $L_2 = 32$ ($L_1 = 120$) and several temperatures. Form top to bottom: $T^* = 1.00$, $T^* = 0.50$, $T^* = 0.40$, and $T^* = 0.25$.

4.4 Spatial correlation functions

By inspection of the low temperature configurations presented in Fig. 4.8, it seems that the system exhibits large correlation at relative large distances in the $\mathbf{e}_1$ direction. Since the system self-assembles in an almost periodic structure, in order to compute an *average* period in direction $\mathbf{e}_1$ we have considered a global correlation function along the confining walls. We define the density correlation function along the direction $\mathbf{e}_1$ as

$$g_0(x_1) \equiv \frac{1}{L_2} \sum_{x_1^0=1}^{L_1} \left[\langle \vec{\rho}(x_1^0) \cdot \vec{\rho}(x_1^0 + x_1) \rangle - \langle \vec{\rho}(x_1^0) \rangle \cdot \langle \vec{\rho}(x_1^0) \rangle \right], \tag{4.12}$$

where $\vec{\rho}(x_1^0) \equiv (\hat{\rho}(x_1^0, 1), \ldots, \hat{\rho}(x_1^0, L_2))$, is a vector containing the densities of the sites belonging to a compact line of sites in the direction $\mathbf{e}_2$ (see Fig. 4.10), $\cdot$ is the standard scalar product, and $\langle \cdots \rangle$ indicates an average over a number N_c of different system configurations. From $g_0(x_1)$ we can define a normalized correlation function:

$$g(x_1) \equiv g_0(x_1)/g_0(0). \tag{4.13}$$

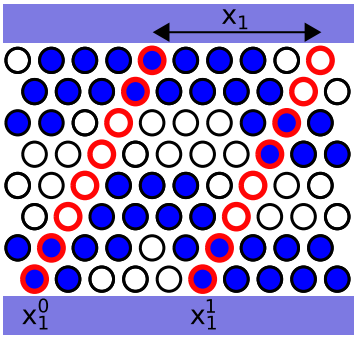

FIG. 4.10: Sketch of the definition of the density vectors, $\vec{\rho}$, used in the definition of the global correlation function $g_0(x_1)$. Here the vectors are oriented in the $\mathbf{e}_2$ direction. The red rings connect the sites which belong to one density vector. In the scheme two density vectors are depicted: $\vec{\rho}(x_1^0) = (1,1,0,0,0,0,1,1)$ and $\vec{\rho}(x_1^1) = (1,1,0,0,1,1,0,0)$, with $x_1 = x_1^1 - x_1^0$.

The correlation function $g(x_1)$ is shown in the upper panel of Fig. 4.11 for $L_2 = 32$ at several temperatures. We found substantial dependence of the correlation functions $g(x_1)$ on the temperature for $L_2 = 32$. It is found that the damping of the oscillations with the distance decreases on cooling the system. More interestingly, the apparent wavelength increases. In order to quantify the shape of the correlation function

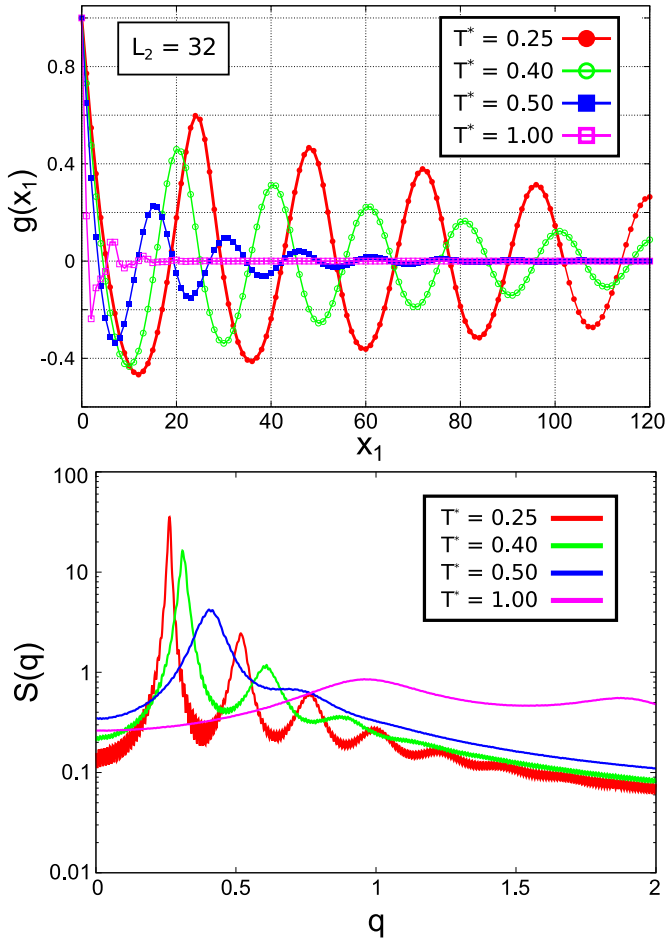

FIG. 4.11: Upper panel: the correlation function $g(x_1)$ for $L_2 = 32$. Lower panel: Fourier transforms $S(q)$ for $L_2 = 32$. The pseudo-periodicity parameter $x_1^p(T) \equiv 2\pi/q_{max}$ takes the values: $x_1^p = 23.9$ (for $T^* = 0.25$); $x_1^p = 20.3$ (for $T^* = 0.40$); $x_1^p = 15.6$ (for $T^* = 0.50$); and $x_1^p = 6.6$ (for $T^* = 1.00$).

$g(x_1)$ we have carried out a Fourier-like analysis of the results. The Fourier integral applied to the lattice was taken as:

$$\tilde{S}(q) = \frac{1}{\sqrt{2\pi}}\left[g(0) + 2\sum_{x_1=1}^{L_1/4} g(x_1)\cos(qx_1)\right]. \tag{4.14}$$

Examples of the results can be found in the lower panel of Fig. 4.11. Defining q_{max} as the value of q that maximizes $S(q)$ we can compute a length $x_1^p = 2\pi/q_{max}$, which characterizes the typical wavelength of the oscillations in $g(x_1)$. In the caption of Fig. 4.11 we collect the corresponding values for slits with $L_2 = 32$ and different temperatures. The results for x_1^p are consistent with the position of the second maximum of $g(x_1)$. From the trends of the correlation functions $g(x_1)$ shown in Fig. 4.11 one should expect an ordered structure at the ground state, with periodicity

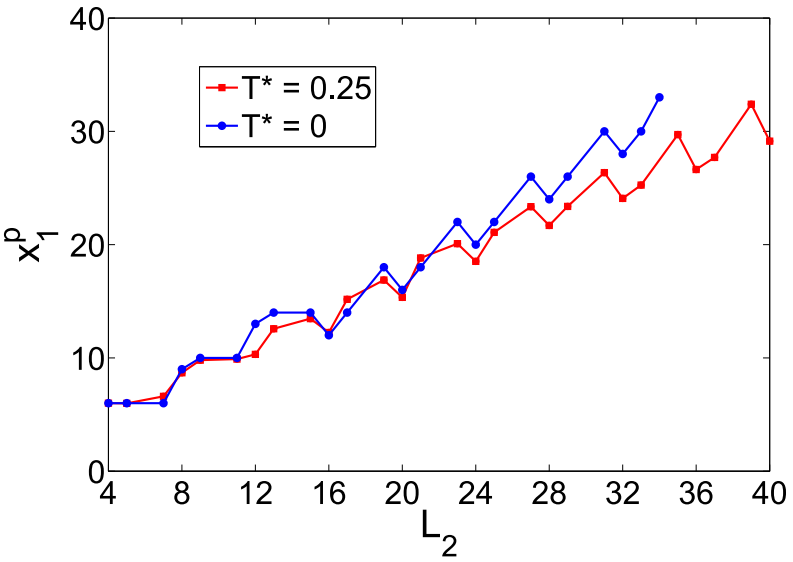

FIG. 4.12: Pseudo-periodicity parameter x_1^p as a function of the slit width at $T^* = 0.25$ (red line) and $T^* = 0$ (blue line). The walls are attractive with $h^* = -1$.

in the direction $\mathbf{e}_1$. This result is consistent with the ground state presented in Fig. 4.3.

It seems interesting to analyze the dependence of x_1^p at low temperature on the pore width. In this analysis the pore widths fulfilling $L_2 = 4n + 2$ (n positive integer number) are not considered, since no bending of the lamellar stripes occur at low temperature for such wall separations. The results for $T^* = 0.25$ are shown in Fig. 4.12 and are compared with the period of the ground state configuration in the $\mathbf{e}_1$ direction. We can see that x_1^p shows some oscillation with L_2, but the general trend is to increase with L_2.

The results presented in this section come from simulation of systems of different slit widths, using a quite large value of the lateral length, namely $L_1 = 2520$. Such large values of L_1 are required to reduce the possible effects of incommensurability of the system size with possible quasi-ordered structures that can appear at low temperature.

4.5 Pseudo-phase transitions

We shall not expect thermodynamic phase transitions in slit systems at $T^* > 0$, given the fact that the system is *virtually* macroscopic in only one direction of the space. However, as the slit width grows, we can expect the presence of some signatures of

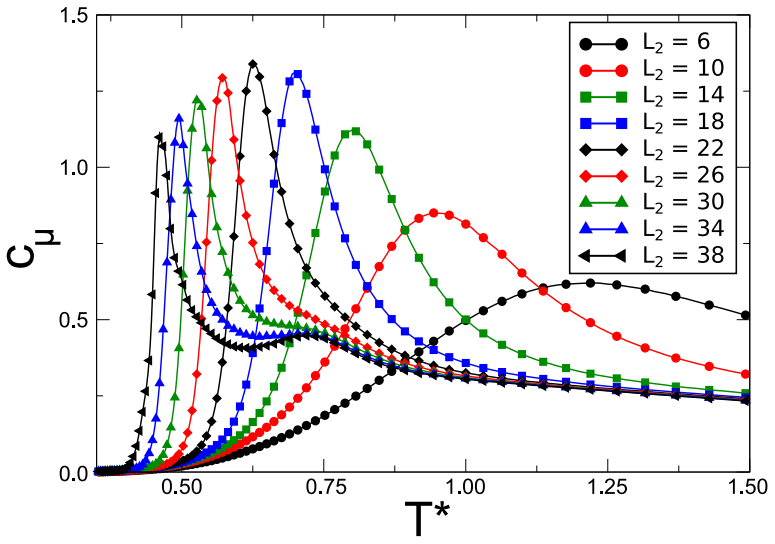

FIG. 4.13: Heat capacity, $c_\mu(T)$ for $\mu^* = 6$, $h^* = -1$ and different pore widths. $c_\mu(T)$ exhibits two maxima for $L_2 > 30$.

the two-dimensional bulk transitions. In order to test these expectations, we study the behavior of the heat capacity c_μ, defined as:

$$c_\mu = \frac{1}{V}\left(\frac{\partial \langle H_{W2d}\rangle}{\partial T}\right)_{V,\mu}, \tag{4.15}$$

where $V \equiv L_1 \times L_2$, and the angular brackets represent the average of a corresponding quantity for given conditions in the grand canonical ensemble. In particular, we take $h^* = -1$, $\mu^* = 6$ and the pore widths $L_2 = 6, 10, 14, 18, \cdots, 38$ (i.e. those sizes whose GS present straight stripes). In Figure 4.13 we show c_μ as a function of the temperature. For the narrowest slits only one maximum of $c_\mu(T)$ appears, whereas for the largest values of L_2 (say, $L_2 \geq 30$) there are two maxima. One of then, is located at $T^* \simeq 0.75$, and can be related with the fluid - molten lamella transition of the bulk. The second peak appears at lower temperature and can be thought as due to the *melting* of the ordered structure of the GS.

4.6 Summary

A long range arrangement of lamellar structures made of electrically conductive particles is one of the goals in the industry aimed at device miniaturization. Hence, description of the way in which the defects may occur in such self-assembling structures is an important issue. In this chapter, we have made an attempt to describe

the way the defects appear in the template-assisted self-assembling systems with competing interactions. Namely, we have studied a model system for colloidal self-assembly in the two-dimensional slit geometry on a triangular lattice. We have paid particular attention to confinement induced defects in the lamellar morphologies. We have described the way the defects spread in the ground state stable structures and we have studied the effect of the temperature. In particular, we have analyzed correlations between the density profiles of the slit cross-sections, and the heat capacity.

The ground state of the model, was firstly studied for the case of slit widths, L_2, optimal for the bulk structures at the corresponding thermodynamic conditions, and for a broad range of the chemical potential (Fig. 4.2). We have found that, if L_2 is large and appropriate for the bulk structures to stabilize, then the presence of confinement does not induce any *global* changes in the bulk morphologies. However, in such a case upon the change of the chemical potential the system exhibits *local* changes in the bulk morphologies, that is **surface phase transitions**. We have shown analytically that the value of the chemical potential at phase coexistences depends on the strength of the wall-particle interactions only for the cluster or lamellar structures. For transitions between the phases with the same structure in the interior, the chemical potential at the transition is independent of the wall separation. The structures for the chemical potential values corresponding to the coexistence between two different phases has not been investigated yet.
For the chemical potential corresponding to the lamellar phase in the bulk, we have studied the dependence of the ground state on L_2. We have found that if L_2 and the wall-particle interaction are *not* favorable for the bulk structure to stabilize, then *global* changes in the bulk lamellar phase may occur. The changes in the bulk lamellar pattern, we call *defects*. We have found that, *the defects appear in an organized manner,* and for large enough L_2 their shape and position depend only on the remainder from the division of L_2 by the period of the bulk lamellar phase. Interestingly, similar shape of the lamellar phases with defects was found in the oil-water-surfactant confined system (see Fig. 1.9). The presence of the defects strictly depends on the particle-wall interaction. We have shown that *the properly tuned wall-particle interaction can remove the defects.* What is more, the confinement removes the infinite degeneracy of the lamellar phase present in the bulk ground state.

Thus, although the confinement leads to stabilization of new complex structures, it has an ordering effect on the system.

We conclude that at $T^* = 0$ the changes in the bulk stable structures induced by confinement are either local (Fig. 4.2) or global (Fig. 4.3). The global changes, however, can be suppressed by matching between the wall separation, and the particle-wall interactions. Although in the presence of confinement new complex patterns are stabilized, the confinement has an ordering effect since it removes the infinite degeneracy of the bulk lamellar phase.

At $T > 0$ we have focused on the description of the defects only in the lamellar phase. We have computed the effective wall-wall interaction Ψ, the density correlation function along the slit $g(x_1)$, and the heat capacity c_μ.

The study of Ψ showed that the effective wall-wall interaction potential as a function of the slit width exhibits damped oscillations. At low temperature and relatively narrow slits the minima of Ψ correspond to L_2 optimal for the ground state straight lamellar phase. Interestingly, at higher temperature ($T^* = 0.5$) the local minima of Ψ can correspond to wall separations not suitable for the straight lamellar stripes. Similar phenomenon, with minima of Ψ corresponding to the system size not appropriate for the bulk ground-state periodic phase was previously noticed in the 1d model when $T^* > 0$ (see Fig. 3.11) by exact calculations. In both cases the mismatch results from the thermal fluctuations which lead to incommensurability of the lattice constant and the period of the average structure.

The spatial arrangement of the defects in the lamellar structures was studied with the density correlation function, $g(x_1)$, defined in such a way that it describes the correlations along the confining walls. We have found that $g(x_1)$ is an oscillatory decaying function, which period depends on the temperature and the wall separation. Fourier analysis of $g(x_1)$ allowed to determine the pseudo-periodicity parameter, x_1^p, which value reflects the concentration of the defects in the system[2]. We have shown that the x_1^p exhibits oscillations superimposed on an increasing function of the wall separation and that for large separations is an increasing function of the temperature. In the future it would be interesting to check whether the number of defects

[2]Note that at $T = 0$ the pseudo-periodicity parameter x_1^p is equal to the size of the ground state unit cell in the $\mathbf{e}_1$ direction, and that the larger is the cell the less defects there are in the system.

in the slit can be quantitatively expressed as a function of the temperature. Since defects are undesirable in nano-devices, such a result should be of interest.

Finally, we have computed the heat capacity of the system as a function of the temperature. Although we do not expect phase transitions in the confined system at $T > 0$, we note that the heat capacity exhibits two maxima if the slit is wide enough. We interpret these maxima as a possible sign of the transitions present in the bulk, thus we do not exclude the possibility that some analogue of the molten lamella phase stabilizes.

To conclude, we note that even when the slit width and particle-wall interactions are not favorable for defectless structures, the defects appear in an organized manner with a given periodicity, leading to an ordered pattern.

Chapter 5

Thesis summary

We have studied effects of boundary conditions on self-assembly. The study started with determination of bulk properties of two types of self-assembling systems: the system of amphiphilic molecules which represents self-assembly driven by anisotropic pair interactions, and the system of particles interacting *via* competing potential which represents self-assembly induced by isotropic interactions (Sec. 2.1). The amphiphilic interactions are characteristic for surfactants, lipids in water or block copolymers, while the competing interaction potential with short range attraction and long range repulsion, can be observed in systems such as colloidal suspensions, protein solutions or quantum dots. We have introduced one-dimensional lattice models for both systems. The models were solved exactly by the transfer matrix method. The study of the models was based on the exact solutions in the grand canonical ensemble, but also Monte Carlo simulations in the canonical ensemble and theoretical calculations within the mean-field theory were performed. We found strong similarities between mechanical, structural and thermal properties of the two systems. For this reason further studies in the two-dimensional space were carried out only for the model with the isotropic competing interaction potential (Sec. 2.2). The studies of the bulk properties in the two-dimensional discrete space were based on analytical calculations at $T = 0$, Monte Carlo simulation techniques and numerical calculations of mean-field type. In particular, for the first time the complete

phase diagram of the system with isotropic competing interactions was found (Fig. 2.52). After investigation of the bulk properties, the next step was to describe the effects of confinement on the self-assembling systems. Firstly, we have considered one-dimensional systems and the effects of rigid or elastic walls that can be either permeable or impervious (Chap. 3). In the case of permeable walls, which allow the particles to adsorb or desorb, we have found the exact solution of the model, while in the case of impervious walls the study was based on the MC simulation. Finally, we have studied a two-dimensional system of slit geometry, that is a system with the rigid boundary conditions in one direction and the periodic boundary conditions in the other direction (Chap. 4). In this case we have studied the ground state ($T^* = 0$) of the system, and the spatial organization of defects in the lamellar phase at low temperatures. In what follows we summarize the main results of the thesis.

1. Common properties of amphiphilic and colloidal systems at low temperature. Our study of generic models for the two classes of the self-assembling systems revealed striking similarities between them at low temperature. We have shown by exact calculations that although for both models at $T > 0$ only the disordered phase is stable in 1d, both systems can exhibit quasi-long range order manifested by an oscillatory decay of the correlation function with the correlation length a few orders of magnitude larger than the particle size (Figs. 2.15 and 2.35). This means that, in contrast to simple fluids, the self-assembly of *nano*-objects can induce inhomogeneities correlated on the length scale of micrometers. We have found that, in the range of thermodynamic variables corresponding to these inhomogeneous structures, the $p(\rho)$ isotherms have a step-like shape (Figs. 2.14 and 2.32), i. e. a sequence of very large, very small and again very large compressibility for increasing ρ occurs. What is more, we have shown that at the density corresponding to the ground state periodic phases the heat capacity as a function of temperature has two maxima in both models (Fig. 2.40), in spite of the fact that for our 1d models phase transitions can occur only at $T = 0$. Thus, in the case of complex self-assembling systems, the heat capacity may have a maximum which does not indicate a phase transition.

The $T^* = 0$ phase diagrams of the models for colloidal (Fig. 2.2) and amphiphilic (Fig. 2.26) self-assembly have the same topology, i. e. phases with oscillatory density or concentration occur when the repulsion in the case of colloids or attraction

between water and properly oriented amphiphilic molecules are strong. Surprisingly, not only the topology is shared. In the case of both one-dimensional models as well as for the two-dimensional model for colloidal self-assembly (Fig. 2.43), we have found analytically that at some phase coexistences the ground state is strongly degenerated and the entropy per lattice site does not vanish. The degeneracy results in vanishing of the surface tension between the coexisting phases. The universality of this results, leads us to the conclusion that the vanishing surface tension at the ground state coexistence may be a general property of self-assembling systems. Note that the lack of the surface tension indicates that macroscopic phase separation is unfavorable and leads to disordered structures, which can be interpreted as a disordered phase that is strongly inhomogeneous (Fig. 2.44).

2. Phase behavior of colloidal systems with the SALR potential in the bulk. We have found the first complete phase diagram of the system with isotropic short range attraction and long range repulsion interparticle potential (Fig. 2.52). Previously only very rough sketches of the phase diagram, or mean-field results were obtained (Figs. 1.5 and 1.6). In particular, we have found that the lamellar phase, which consists of identical stripes, looses the *translational* order at some T. The *orientational* order, however, remains present until the stripes melt at higher T into the fluid phase with no global order. Stability of the lamellar phase with the orientational order, but without the translational order, called the "molten lamella" phase is a novelty [1]. In addition, we have found reentrant melting in the (μ^*, T^*) representation of the phase diagram. Namely, at constant chemical potential a counterintuitive sequence of phases: fluid-periodic-fluid can be observed upon increase of temperature. Similar phase behavior was observed in the mean-field phase diagram of the one-dimensional model (Fig. 2.8). When in systems with competing interactions the repulsion is too weak to suppress the ground state phase separation, the inhomogeneities may still appear as a compromise between the macroscopic phase separation (that is energetically favorable but entropically unfavorable), and the disordered structure (that is favorable entropically and unfavorable energetically).

[1] We should mention that a similar phase called "nematic phase" was discovered independently in thin magnetic layers [115].

3. The role of the mean-field approximation. In order to verify the accuracy of approximate theories for complex self-assembling systems, we have applied the self-consistent mean-field theory to our models. We have found that although in the one-dimensional systems the MF theory incorrectly predicts phase transitions, it still carries a lot of information that is related to exact results. For instance, in the region of the MF phase diagram corresponding to stability of the periodic phase, the exact result for the correlation function has damped oscillations with a very large correlation length (Fig. 2.15). This indicates that although the system is disordered, if one would fix a particle to its position a very long range of correlations would occur. What is more, when the MF predicts stability of the disordered phase, the correlation function decays monotonically. Even when upon heating the MF predicts a phase transition from homogeneous to periodic phase, the correlation function also changes from monotonic to oscillatory, but with a much shorter correlation length (Fig. 2.21). Although the MF approximation to some extent can be a support for exact studies of one-dimensional systems, it fails to predict correct phase diagram in two dimensions, where phase transitions are present. Among many differences between the MF and the MC phase diagrams of the SALR system discussed in Sec. 2.2.5, the most pronounced difference is that in the MF phase diagram (Fig. 2.49) there is reentrant melting at constant temperature neither upon increasing the chemical potential nor upon increasing the density, which are both present in the MC result (Fig. 2.52). What is more the MF predicts stability of phases which are not present in the MC results, such as the cluster phase with positional, but without orientational order.

However, if we interpret the 1d model with SALR potential as a model of properties of the lamellar phase in a two-dimensional system, then the MF approximation applied to 1d model correctly predicts some of the features of the 2d phase diagram obtained by MC simulations. In particular, the 1d MF phase diagram for strong repulsion (Fig. 2.8) predicts coexistence of two ordered phases with different degree of order, what can reflect the coexistence of the more ordered lamellar phase with the less ordered molten lamella. Moreover, the MF prediction of the reentrant melting phenomenon for the constant chemical potential and upon increase of the temperature also agrees with the 2d phase diagram obtained by MC simulations.

4. Confinement induced anomalies.
Our study of confined self-assembling systems revealed that in thermodynamic conditions corresponding to the self-assembly of inhomogeneous structures many anomalies, absent in simple fluids occur. These are few among them:
(i) We have found nonmonotonic $p(\rho)$ isotherms for both the impervious and the permeable rigid confinement (Fig. 3.18 and Fig. 3.19). It means that in the case of inhomogeneous structures the increase of density may lower the pressure. The reason is that the increase of density may result in the increase of the average cluster size, but decrease of the number of clusters. The clusters repel each other when the distance between them is short, and this effective repulsion determines the pressure.
(ii) In the case of elastic and impervious walls the analysis of $\langle L(N)\rangle$ has shown that in some ranges of N and T the system may shrink upon heating (Fig. 3.21).
(iii) We have shown that the average number of clusters in the canonical and the grand canonical ensembles may differ even if the average number of particles is the same. Moreover, the inequivalence of the canonical and the grand canonical ensembles is not most pronounced at the maximum of fluctuation in the number of particles as it does for simple fluids, and is rather related with fluctuations in the cluster size and the number of clusters (Sec. 3.2.3). Hence, in the case of complex systems, one should take an advantage from the ensemble equivalence with a special care.
(iv) Finally, the solvation potential, which describes the effective interactions between the confining walls, exhibits oscillatory decay on a length scale which is a few orders of magnitude larger than the particle diameter, and the period equal to a double size of the cluster (Fig. 3.11). Thus, the solvation potential is nonzero at much larger length scales than it is for simple fluids.

5.Equilibrium size of the self-assembling system confined by elastic walls. From the oscillatory behavior of the solvation potential (Fig. 3.11) it follows that to some extent our system can be treated like a soft elastic material. If the confining walls are also elastic, then the system size is determined by a mechanical equilibrium between the solvation force of the fluid and the elastic force of the confinement. We have found that if thermodynamic conditions favor self-assembly into structures that are periodic in direction in which the system size is allowed to vary, then the equilibrium system size may not be unique (Sec. 3.1.4.2, Sec. 3.2.5 and Sec. 4.3). Namely,

in such a case we have found a bistability in the system size distribution (Fig. 3.13 and Fig. 3.23). Interestingly, since the hight of the energy barrier is of order of $k_B T$ in one-dimension, the changes of the wall-wall distance may by thermally induced. The difference between the system sizes corresponding to the two maxima of the probability of the system size depends on whether the walls are impervious or permeable. In the case of impervious walls the distance is equal to the half of the pattern period, while in the case of permeable walls the distance is the pattern period. Note that the period is determined by the ranges of the attractive and repulsive terms of the effective potential, hence in the case of colloidal systems it can be of order of even a micrometer. Taking it all into account, we conclude that, we have found a way in which self-assembly of nanoscale objects can lead to spontaneous changes of the system size on a micrometer scale.

6. Organizing effect of the slit. The presence of confinement in the two-dimensional system may induce stabilization of structures which are much more complex than those stable in the bulk (Chap. 4). However, the general impact of the confinement is ordering. In particular, out of the phase coexistences the confinement removes the infinite degeneracy of the lamellar phase that was present in the bulk ground state, thus the ground state in the slit is unique. Since in the nano-industry structures without defects are desirable, we have considered the way the defects induced by the confinement appear in the system. We have found that at $T = 0$ the presence of defects is strictly determined by the wall-wall distance and the wall-particle interactions. In the case of wall separation suitable for periodic structures with no defects, the effects of confinement are only local or do not appear at all. The local changes are present only in the cluster phase and in the close neighborhood of the walls. Their appearance upon a change of the chemical potential is associated with surface phase transitions (Fig. 4.2). The case of the wall separation and the wall-particle interactions which are unfavorable for the bulk structures, was analyzed only for the chemical potential value corresponding to the lamellar phase. It turned out that in such a case the defects appear globally along the whole slit (Fig. 4.3). However, we have found that the defects appear in an organized manner with a given periodicity in the direction parallel to the walls. Interestingly, the periodicity is present not only at $T = 0$, but also at low $T > 0$ (Fig. 4.9).

The universality of the conclusions. The patterns emerging in the colloidal and amphiphilic self-assembly are very similar. Our study confirmed that the similarity is strong not only at high, but also at low and zero temperature. Based on the similarity between the two types of self-assembly, we can expect that our results on systems with isotropically interacting particles may also concern amphiphilic systems, at least on a qualitative level. We also expect that magnetic systems with competing interactions [116–119] may have very similar properties in confinement as well.

Chapter 6

Appendices

6.1 Derivation of the approximation for the internal energy.

We derive an approximate expression for the internal energy $\mathcal{U}$ when the local density (or volume fraction) varies on a mesoscopic length scale, i.e. for small gradients of $\rho(\mathbf{r})$. When $\rho(\mathbf{r}+\Delta\mathbf{r})$ is approximated by a truncated Taylor series, Eq.(1.6) takes the approximate form

$$\mathcal{U} = \frac{1}{2}\int d\mathbf{r}\int d\Delta\mathbf{r}\; V(\Delta r)g(\Delta r)\rho(\mathbf{r})\Big[\rho(\mathbf{r}) + \Delta r_i\frac{\partial\rho}{\partial r_i} + \frac{1}{2}\Delta r_i\frac{\partial^2\rho}{\partial r_i\partial r_j}\Delta r_j + ...\Big] \quad (6.1)$$

where $\mathbf{r} = (r_1, r_2, r_3)$ and summation convention for repeated indexes is used. The above can be written in the form

$$\mathcal{U} = \int d\mathbf{r}\Big[V_0 v^2\rho(\mathbf{r})^2 - \frac{V_2 v^2}{2}\rho(\mathbf{r})\sum_{i=1}^{3}\frac{\partial^2\rho}{\partial r_i^2} + ...\Big] \quad (6.2)$$

where $V_0 v^2 = \int d\mathbf{r}V(r)g(r)/2$ and $-V_2 v^2 = \int d\mathbf{r}r_i^2 V(r)g(r)/2$. In derivation of the above we took into account that an integral over R^3 of an odd function, $V(r)g(r)r_i$

and $V(r)g(r)r_i r_j$ with $i \neq j$, vanishes. When the second term in (6.2) is integrated by parts and the boundary term is neglected, we obtain for $\mathcal{U}$ Eq.(1.9). Next we take into account that the integration over the angles in spherical variables for any function $f(r)$ of $r = |\mathbf{r}|$ gives

$$\int d\mathbf{r} f(r) = 4\pi \int_0^\infty dr r^2 f(r) \tag{6.3}$$

and

$$\int d\mathbf{r} f(r) r_i^2 = \frac{4\pi}{3} \int_0^\infty dr r^4 f(r), \tag{6.4}$$

and for V_0 and V_2 defined above we obtain Eq.(1.8).

When $V_2 < 0$, the functional in Eq.(1.9) is unstable, and the Taylor expansion in (6.1) must be truncated at the fourth order term. The term associated with the third-order derivative vanishes, because the integrand is an odd function. In order to evaluate the fourth-order term, we perform the integration over the angles in spherical variables of the integrands of the form $V(r)g(r)r_i^2 r_j^2$ and integrate by parts twice the expressions

$$\int d\mathbf{r} \rho(\mathbf{r}) \frac{\partial^4 \rho}{\partial r_i^2 \partial r_j^2} \tag{6.5}$$

with $i = j$ as well as $i \neq j$. We neglect the boundary terms, and after some algebra we finally obtain Eqs.(1.9) and (1.8).

6.2 TCP in the 1d model for colloidal self-assembly

In what follows we will derive the expression for the tricritical point in the MF phase diagram of the 1d model for colloidal self-assembly in the bulk (Sec.2.1.1.3).

We assume that when the continuous transition to the homogeneous phase with density $\bar{\rho}_0(\mu^*, T^*)$ is approached, the density in the periodic phase has the form $\bar{\rho}(x) = \bar{\rho}_0 + \Delta\rho(x)$ with

$$\Delta\rho(x) = \delta\rho + \phi \cos(k_b x). \tag{6.6}$$

The continuous transition coincides with the λ-line, and at the λ-line $\delta\rho = \phi = 0$. The difference between the grand potential in the periodic and the homogeneous phases, $\Delta\Omega = \Delta\omega L$, is a function of $\delta\rho$ and ϕ and $\Delta\omega$ can be Taylor expanded for $\delta\rho \to 0$ and $\phi \to 0$. When $2\pi/k_b$ is not integer, in calculating $\Delta\omega$ (see (2.11)) we choose $n \to \infty$ such that $L \approx 2n\pi/k_b$ and make the approximation

$$\frac{1}{L}\sum_{x=1}^{L}\cos(k_b x)^m \approx \frac{1}{2\pi}\int_0^{2\pi}\cos z^m dz. \tag{6.7}$$

The second derivative of $\Delta\omega$ with respect to ϕ vanishes at the continuous transition, while the second derivative with respect to $\delta\rho$ is positive. From the extremum condition $\partial\Delta\omega/\partial\delta\rho = 0$ we obtain

$$\delta\rho = -\frac{A_3(\rho_0)}{4(\beta^*\tilde{V}(0) + A_2(\rho_0))}\phi^2 + O(\phi^4) \tag{6.8}$$

and

$$\beta\Delta\omega = a_2\phi^2 + a_4\phi^4 + O(\phi^6) \tag{6.9}$$

where

$$a_2 = \frac{\beta^*\tilde{V}(k_b) + A_2(\rho_0)}{4} \tag{6.10}$$

$$a_4 = \frac{1}{32}\left(\frac{A_4(\rho_0)}{2} - \frac{A_3(\rho_0)^2}{\beta^*\tilde{V}(0) + A_2(\rho_0)}\right) \tag{6.11}$$

and $A_n(\rho) = d^n\beta f_h(\rho)/d\rho^n$ with f_h given in Eq.(2.12). The transition is continuous for $a_4 > 0$, and becomes first order at the tricritical point (TCP) given by $a_2 = a_4 = 0$. We obtain for the density and temperature at the TCP the following expressions

$$\bar{\rho}_0^{tcp} = \frac{1}{2}\left[1 \pm \sqrt{\frac{\tilde{V}(k_b) - \tilde{V}(0)}{\tilde{V}(k_b) + 3\tilde{V}(0)}}\right], \tag{6.12}$$

$$T^*_{tcp} = \frac{-\tilde{V}(k_b)\tilde{V}(0)}{\tilde{V}(k_b) + 3\tilde{V}(0)}. \tag{6.13}$$

Real positive solutions for $\bar{\rho}_0^{tcp}$ exist for $1/9 < J^* < 1$, ie. when the lines of instability intersect and form a loop.

6.3 Grand potential for weakly ordered periodic phases in MF approximation for the 2d model for colloidal self-assembly

The normalized functions g_p satisfy the equations

$$\frac{1}{V_u}\sum_{\mathbf{x}\in V_u} g_p(\mathbf{x}) = 0 \tag{6.14}$$

and

$$\frac{1}{V_u}\sum_{\mathbf{x}\in V_u} g_p^2(\mathbf{x}) = 1. \tag{6.15}$$

In the above equations the summation is over the unit cell of the ordered structure with the area V_u. The length of the unit cell in our case is $2\pi/k_b$. The functions g_p for the lamellar and hexagonal phases have the forms

$$g_l(\mathbf{x}) = \sqrt{2}\cos(k_b \mathbf{x}\cdot\mathbf{e}_i) \tag{6.16}$$

and

$$g_h(\mathbf{x}) = \sqrt{\frac{2}{3}}\sum_{i=1}^{3}\cos(k_b \mathbf{x}\cdot\mathbf{e}_i) \tag{6.17}$$

where k_b is given in Eq.(2.90). In the case of noninteger $2\pi/k_b$, in order to calculate Eqs.(6.14) and (6.15), we make the approximation

$$\frac{1}{V_u}\sum_{\mathbf{x}\in V_u} f(k_b\mathbf{x}) \simeq \int_0^{2\pi}\frac{dz_1}{(2\pi)}\int_0^{2\pi}\frac{dz_2}{(2\pi)} f(\mathbf{z}), \tag{6.18}$$

where $z_i = k_b x_i$.

From the condition $\partial\Delta\Omega/\partial\delta\rho_p = 0$ we obtain for $\Phi_p \ll 1$

$$\delta\rho_p \cong -\frac{A_3\Phi_p^2}{2(\beta^*\tilde{V}^*(0)+A_2)}, \tag{6.19}$$

where $A_n = \frac{d^n \beta f_h(\rho)}{d\rho^n}$ with f_h defined in Eq.(2.12), and $\beta^* \tilde{V}^*(0)\rho_0 + A_1 - \beta^* \mu^* = 0$. After some algebra we obtain the approximate expression

$$\beta^* \Delta\Omega_p^* = \Phi_p^2 \frac{\beta^* \tilde{V}^*(\mathbf{k}_b) + A_2}{2} + \Phi_p^3 \frac{A_3 \kappa_3^p}{3!} + \Phi_p^4 \Big[\frac{A_4 \kappa_4^p}{4!} - \frac{A_3^2}{8(\beta^* \tilde{V}^*(0) + A_2)} \Big] + O(\Phi_p^5), \tag{6.20}$$

where the geometric factors are defined as $\kappa_n^p = \frac{1}{V_u} \sum_{V_u} g_p(\mathbf{x})^n$ and take the following values $\kappa_3^l = 0$, $\kappa_4^l = \frac{3}{2}$, $\kappa_3^h = \sqrt{\frac{2}{3}}$, $\kappa_4^h = \frac{5}{2}$ [42]. From $\partial \Delta\Omega / \partial \delta\Phi_p = 0$ we obtain the amplitude Φ_p, and after inserting it to (6.20), the value of $\beta \Delta\Omega_p^*$ for given T^* and ρ_0.

6.4 Asymptotic expressions for the one-dimensional model with rigid boundary conditions

6.4.1 Average density

We introduce the notation:

$$a_r + i b_r \equiv \sum_{\hat{S}(1)} e^{\beta^* \hat{\rho}(1) h_1^*} P_r(\hat{S}(1)) P_r^{-1}(\hat{S}(n)), \tag{6.21}$$

$$c_r + i d_r \equiv \sum_{\hat{S}(M)}{}' e^{\beta^* \hat{\rho}(L) h_L^*} e^{\beta H_j^*(\hat{S}(M))} P_r(\hat{S}(n)) P_r^{-1}(\hat{S}(M)) \tag{6.22}$$

where $r = 1, \ldots, 8$ and $i = \sqrt{-1}$. The dependence of a_r, b_r, c_r and d_r on $\hat{S}(n)$ is not indicated for clarity of notation. The parameters c_r and d_r depend also on $j = \mathrm{mod}\,(L, 3)$. Then Eq. (3.7) takes form

$$\langle \hat{\rho}(3n+l) \rangle = \frac{\lambda_1^{M-1}}{\Xi} \sum_{\hat{S}(n)} \hat{\rho}(3n+l) \Big(\sum_{r=1}^{8} \Big(\frac{\lambda_r}{\lambda_1} \Big)^n (a_r + i b_r) \Big) \Big(\sum_{r=1}^{8} \Big(\frac{\lambda_r}{\lambda_1} \Big)^{M-n-1} (c_r + i d_r) \Big), \tag{6.23}$$

where $\lambda_1 \in \mathbb{R}$ is the eigenvalue with the largest absolute value Our aim is to obtain an asymptotic expression for $\langle \hat{\rho}(x) \rangle$ for $M \to \infty$ and $n \sim M/2$. We sort the eigenvalues in the descending order of their absolute values and neglect in Eq.(3.7) all the eigenvalues except from the first 3 of them. We limit ourselves to the two cases: 1) $\lambda_2 = \bar{\lambda}_3 = |\lambda_2| e^{i\lambda}$ and 2) $\lambda_2, \lambda_3 \in \mathbb{R}$ with $|\lambda_3/\lambda_2|^n \ll 1$ for $n \gg 1$.

If $\lambda_2 = \bar{\lambda}_3$ then after some algebra we obtain

$$\langle\hat{\rho}(3n+l)\rangle \simeq \frac{\lambda_1^{M-1}}{\Xi}\sum_{\hat{S}(n)}\hat{\rho}(3n+l)\Big(a_1c_1+2c_1\left(\frac{|\lambda_2|}{\lambda_1}\right)^n(a_2\cos(n\lambda)-b_2\sin(n\lambda)) \quad (6.24)$$
$$+2a_1\left(\frac{|\lambda_2|}{\lambda_1}\right)^{M-n-1}(c_2\cos((M-n-1)\lambda)-d_2\sin((M-n-1)\lambda))\Big)$$

In deriving (6.24) we took into account that $\left(\frac{|\lambda_2|}{\lambda_1}\right)^n \cdot \left(\frac{|\lambda_2|}{\lambda_1}\right)^{(M-n-1)} \ll \left(\frac{|\lambda_2|}{\lambda_1}\right)^{M-n-1}$ for $M \gg 1$ and $n \sim M/2$. Eq.(6.24) can be written in the form (3.15) with ξ defined in Eq.(3.16), λ defined below Eq.(3.16), and with the following expressions for the remaining parameters:

$$\bar{\rho} \equiv \frac{\lambda_1^{M-1}}{\Xi}\sum_{\hat{S}(n)}\hat{\rho}(3n+l)a_1c_1, \quad (6.25)$$

$$A_1(l) = \begin{cases} w_2 & \text{if } \lambda_2, \lambda_3 \in \mathbb{R} \text{ and } |\lambda_3/\lambda_2|^n \ll 1 \\ \frac{w_2}{\cos\theta_1(l)} & \text{if } \lambda_2 = \bar{\lambda}_3 \end{cases}$$

$$A_L(l) = \begin{cases} w_4 & \text{if } \lambda_2, \lambda_3 \in \mathbb{R} \text{ and } |\lambda_3/\lambda_2|^n \ll 1 \\ \frac{w_4\exp(3/\xi)}{\cos\theta_L(l)} & \text{if } \lambda_2 = \bar{\lambda}_3 \end{cases}$$

$$\theta_1(l) \equiv \arctan\frac{w_3}{w_2}, \qquad \theta_L(l) \equiv \arctan\frac{w_5}{w_4} - \lambda$$

where

$$w_2 \equiv \frac{2\lambda_1^{M-1}}{\Xi}\sum_{\hat{S}(n)}\hat{\rho}(3n+l)a_2c_1, w_3 \equiv \frac{2\lambda_1^{M-1}}{\Xi}\sum_{\hat{S}(n)}\hat{\rho}(3n+l)b_2c_1, \quad (6.26)$$

$$w_4 \equiv \frac{2\lambda_1^{M-1}}{\Xi}\sum_{\hat{S}(n)}\hat{\rho}(3n+l)a_1c_2, w_5 \equiv \frac{2\lambda_1^{M-1}}{\Xi}\sum_{\hat{S}(n)}\hat{\rho}(3n+l)a_1d_2, \quad (6.27)$$

The above asymptotic expressions are not valid when λ_2 and λ_3 are both real, and $|\lambda_3/\lambda_2|^n = O(1)$. For the range of parameters studied in this article, however, λ_2 and λ_3 are complex conjugate numbers.

6.4.2 The effective interaction between the confining walls

In the asymptotic region of $M \to \infty$ the exact expression for $\Psi(L)$ (Eq. (3.14)) takes the asymptotic form given in Eq.(3.17) with $\phi(j) = \phi_2(j) - \lambda$ and with

$$A(j) = \begin{cases} C_2^a(j)e^{3/\xi} & \text{if } \lambda_2, \lambda_3 \in \mathbb{R} \text{ and } |\lambda_3/\lambda_2|^M \ll 1 \\ 2C_2^a(j)e^{3/\xi} & \text{if } \lambda_2 = \bar{\lambda}_3 \end{cases},$$

where $C_r^a(j)e^{i\phi_r(j)} = -\frac{C_r(j)}{C_1(j)}$, and $C_r(j)$ are given by Eq. (3.11).

6.5 Microstates obtained by the virtual expansion of the system

In what follows we show that the virtual expansion scheme described in 3.2.2 is not biased, i.e. it generates all possible microstates of the system of the given size with the same probability.

We consider N indistinguishable particles and L lattice sites. Each site can be empty or occupied by one particle, thus there are $\binom{L}{N}$ distinguishable microstates. We will show that the virtual expansion procedure of building configurations of the system with $L+1$ sites by inserting an empty site at a random position in a system with L sites is not biased by the insertion procedure. Let us consider two sets of particle configurations. The elements of the first set are the microstates of a system of size L with N occupied sites with a distinguished position in which a new site can be inserted. Since the new site can be inserted in $L+1$ places, the first set contains $(L+1)\binom{L}{N}$ different elements. In the second set each of the elements corresponds to one of the microstates of a system of $L+1$ sites with N occupied sites, and with one of its $L+1-N$ empty sites marked as removable. The number of elements of the second set is $(L+1-N)\binom{L+1}{N}$. Because $(L+1)\binom{L}{N} = (L+1-N)\binom{L+1}{N}$, the two sets are equinumerous. We define a one-to-one correspondence between the elements of the two sets by identifying the location of the insertion point in an element of the first set with the location of the removable site in the element of the second set, and by requiring that the same sites are occupied. Note that each microstate of the system with $L+1$ sites can be obtained in $L+1-N$ ways from the elements of the second

set by removing the mark “removable”. Because of the one-to-one correspondence between the elements of the two sets, each microstate of the system with $L+1$ sites is obtained $L+1-N$ times by the above procedure.

It follows that the proposed procedures of building configurations of the system with $L+1$ sites by inserting an empty site at a random position on the configurations of a system with L sites are not biased by the insertion procedure. The same lack of bias applies in the reverse procedure.

For an illustration let us consider $L = 2$ and $N = 1$. There are 2 microstates, [1,0] and [0,1]. After insertion of an empty site in 3 possible places, we obtain from the first microstate [0,1,0], [1,0,0], [1,0,0], and from the second microstate [0,0,1],[0,0,1], [0,1,0]. One can easily see that after this procedure we obtained each microstate in the system of size $L+1 = 3$ containing $N = 1$ particle $L+1-N = 2$ times.

Bibliography

[1] G. M. Whitesides and B. Grzybowski. Self-assembly at all scales. *Science*, 295:2418, 2002.

[2] G. M. Whitesides and M. Boncheva. Beyond molecules: Self-assembly of mesoscopic and macroscopic components. *Proc. Nat. Acad. Sci. USA*, 99:4769, 2002.

[3] A. van Blaaderen, R. Ruel, and P. Wiltzius. Template-directed colloidal crystallization. *Nature*, 385:321, 1997.

[4] Y. Xia, B. Gates, Y. Yin, and Y. Lu. Monodispersed colloidal spheres: old materials with new applications. *Adv. Mater.*, 12:693, 2000.

[5] C. De Rosa, C. Park, E. L. Thomas, and B. Lotz. Microdomain patterns from directional eutectic solidification and epitaxy. *Nature.*, 405:433, 2000.

[6] M. N. Jones nad D. Chapman. *Micells, Monolayers and Biomembranes*. Wiley-Liss, New York, 1995.

[7] A. Stradner, H. Sedgwick, F. Cardinaux, W.C.K. Poon, S.U. Egelhaaf, and P. Schurtenberger. Equilibrium cluster formation in concentrated protein solutions and colloids. *Nature*, 432:492, 2004.

[8] J. S. Pedersen, S. Hansen, and R. Bauer. The aggregation behavior of zinc-free insulin studied by small-angle neutron scattering. *Eur. Biophys. J.*, 22(6):379–389, 1994.

[9] F. S. Bates and G. H. Fredrickson. Block copolymers designer soft materials. *Physics Today*, 52:32, 1999.

[10] J.-C. Loudet, P. Barois, and P. Poulin. Colloidal ordering from phase separation in a liquid-crystalline continuous phase. *Nature*, 407:611, 2000.

[11] S. Guillot, M. Delsanti, S. Désert, and D. Langevin. Surfactant-induced collapse of polymer chains and monodisperse growth of aggregates near the precipitation boundary in carboxymethylcellulose-dtab aqueous solutions. *Langmuir*, 19(2):230–237, 2003.

[12] M. Seul and D. Andelman. Domain shapes and patterns: the phenomenology of modulated phases. *Science*, 267:476, 1995.

[13] R. M. Weis and H. M. McConnell. Cholesterol stabilizes the crystal-liquid interface in phospholipid monolayers. *J. Chem. Phys.*, 89:4453, 1985.

[14] R. M. Weis and H. M. McConnell. Two-dimensional chiral crystals of phospholipid. *Nature*, 310:47, 1984.

[15] M. Losche and H. Mohwald. Impurity controlled phase transitions of phospholipid monolayers. *Eur. Biophys. J.*, 11(1):35–42, 1984.

[16] T. Witten. Structured fluids. *Phys. Today*, 43:21, 1990.

[17] H. Hasegawa and T. Hashimoto. Morphology of block copolymers and mixtures of block copolymers at free surfaces. *Polymer*, 33:475, 1992.

[18] J. Bang, U. Jeong, D. Y. Ryu, T. P. Russell, and C. J. Hawker. Block copolymer nanolithography: translation of molecular level control to nanoscale patterns. *Adv. Mater.*, 21(47):4769–4792, 2009.

[19] J. N. Israelachvili, D. J. Mitchell, and B. W. Ninham. Thermodynamics of amphiphilic association structures. *J. Chem. Soc. Faraday Trans. 2*, 72:1525, 1976.

[20] D. J Beltran-Villegas, B. A Schultz, N. HP Nguyen, S. C Glotzer, and R. G Larson. Phase behavior of Janus colloids determined by sedimentation equilibrium. *Soft Matter*, 10(26):4593–4602, 2014.

[21] L. Leibler. Theory of microphase separation in block copolymers. *Macromolecules*, 13:1602, 1980.

[22] G. H. Fredrickson and E. Helfand. Fluctuation effects in the theory of microphase separation in block copolymers. *J. Chem. Phys.*, 87:67, 1987.

[23] Gerhard Gommper and Michael Schick. *Self-Assembling Amphiphilic Systems*, volume 16 of *Phase Transitions and Critical Phenomena*. Academic Press, first edition, 1994.

[24] A. Ciach and W. T. Góźdź. Nonelectrolyte solutions exhibiting structure on the nanoscale. *Annu. Rep.Prog. Chem., Sect.C*, 97:269, 2001. and references therein.

[25] S. A. Brazovskii. Phase transition of an isotropic system to a nonuniform state. *Sov. Phys. JETP*, 41:85, 1975.

[26] A. K. Khandpur, S. Foerster, F. S. Bates, I. W. Hamley, A. J. Ryan, W. Bras, K. Almdal, and K. Mortensen. Polyisoprene-polystyrene diblock copolymer phase diagram near the order-disorder transition. *Macromolecules*, 28(26):8796–8806, 1995.

[27] S. Qi and Z.-G. Wang. Kinetics of phase transitions in weakly segregated block copolymers: Pseudostable and transient states. *Phys. Rev. E*, 55(2):1682, 1997.

[28] D. A. Hajduk, H. Takenouchi, M. A. Hillmyer, F. S. Bates, M. E. Vigild, and K. Almdal. Stability of the perforated layer (PL) phase in diblock copolymer melts. *Macromolecules*, 30(13):3788–3795, 1997.

[29] IBM brings nature to computer chip manufacturing. *Am. Ceram. Soc. Bull.*, 2007. http://www-03.ibm.com/press/us/en/pressrelease/21473.wss.

[30] A. Saric and A. Cacciuto. Self-assembly of nanoparticles adsorbed on fluid and elastic membranes. *Soft Matter*, 9:6677–6695, 2013.

[31] A. Sanchez-Iglesias, M. Grzelczak, T. Altantzis, B. Goris, J. Perez-Juste, S. Bals, G. Van Tondeloo, S. H. Donaldson, B. F. Chmelka, J. N. Israelachvili, and L. M. Liz-Marzan. Hydrophobic interactions modulate self-assembly of nanoparticles. *ACS Nano*, 6:11059, 2012.

[32] A. I. Campbell, V. J.Anderson, J. S. van Duijneveldt, and P. Bartlett. Dynamical arrest in attractive colloids: The effect of long-range repulsion. *Phys. Rev. Lett.*, 94:208301, 2005.

[33] R. P. Sear and W. M. Gelbart. Condensed phase dynamics, structure, and thermodynamics: Spectroscopy, reactions, and relaxation-microphase separation versus the vapor-liquid transition in systems of spherical particles. *J. Chem. Phys.*, 110:4582, 1999.

[34] A. Imperio and L. Reatto. A bidimensional fluid system with competing interactions: spontaneous and induced pattern formation. *J. Phys.: Condens. Mat.*, 16:S3769, 2004.

[35] A. Imperio and L. Reatto. Microphase separation in two-dimensional systems with competing interactions. *J. Chem. Phys.*, 124:164712, 2006.

[36] A. Imperio and L. Reatto. Microphase morphology in two-dimensional fluids under lateral confinement. *Phys. Rev. E*, 76:040402, 2007.

[37] A. J. Archer, D. Pini, R. Evans, and L. Reatto. Model colloidal fluid with competing interactions: Bulk and interfacial properties. *J. Chem. Phys.*, 126:014104, 2007.

[38] A. J. Archer and N. B. Wilding. Phase behavior of a fluid with competing attractive and repulsive interactions. *Phys. Rev. E*, 76:031501, 2007.

[39] A. J. Archer. Two-dimensional fluid with competing interactions exhibiting microphase separation: Theory for bulk and interfacial properties. *Phys. Rev. E*, 78:031402, 2008.

[40] A. Archer, Ionescu, D. Pini, and L. Reatto. Theory for the phase behaviour of a colloidal fluid with competing interactions. *J. Phys.: Condens. Mat.*, 20:415106, 2008.

[41] A. Ciach. Universal sequence of ordered structures obtained from mesoscopic description of self-assembly. *Phys. Rev. E*, 78:061505, 2008.

[42] A. Ciach and W. T. Góźdź. Mesoscopic description of network-forming clusters of weakly charged colloids. *Condens. Matter Phys.*, 13:23603, 2010.

[43] A. Ciach, J. Pękalski, and W. T. Góźdź. Origin of similarity of phase diagrams in amphiphilic and colloidal systems with competing interactions. *Soft Matter*, 9:6301, 2013.

[44] J. L. Barrat and J.-P. Hansen. *Basic Concepts for Simple and Complex Liquids*. Cambridge University Press, 2003.

[45] P. Huber. Soft matter in hard confinement: phase transition thermodynamics, structure, texture, diffusion and flow in nanoporous media. *J. Phys.: Conden. Mat.*, 27(10):103102, 2015.

[46] R. Evans. Fluids adsorbed in narrow pores: phase equilibria and structure. *J. Phys.: Condens. Mat.*, 2:8989, 1990.

[47] J. N. Israelachvili. *Intermolecular and Surface Forces, Third Edition*. Academic Press, 2011.

[48] M.Tasinkevych and A.Ciach. Structural transformations in confined lamellar phases in oil-water-surfactant mixtures. *J. Chem. Phys.*, 115:8705, 2001.

[49] A. Ciach. Phase transitions in confined lamellar phases. *Bull. Pol. Acad. Sci. Tech. Sci*, 55(2):179, 2007.

[50] P. Kékicheff and H. K. Christenson. Forces measured in a swollen lyotropic lamellar mesophase confined between solid surfaces. *Phys. Rev. Lett.*, 63:2823–2826, 1989.

[51] D. A. Antelmi, P. Kékicheff, and P. Richetti. Measurement of the interactions between macroscopic surfaces inducing a first-order phase transitions: the sponge-lamellar transformation. *J. Phys. II France*, 5:103, 1995.

[52] M. W. Matsen and F. S. Bates. Unifying weak and strong-segregation block copolymer theories. *Macromolecules*, 29:1091, 1996.

[53] M. W. Matsen. Thin films of block copolymer. *J. Chem. Phys.*, 106:7781, 1997.

[54] M. Tasinkevych and A. Ciach. Lattice model results for lamellar phases in slits. *Phys. Rev. E*, 60:7088, 1999.

[55] V. Babin, A. Ciach, and M. Tasinkevych. Capillary condensation of periodic phases in self-assembling systems. *J. Chem. Phys.*, 114:9585, 2001.

[56] V. Babin and A. Ciach. Response of the bicontinuous cubic d phase in amphiphilic systems to compression or expansion. *J. Chem. Phys.*, 119:6217, 2003.

[57] P. Chi, Z. Wang, B. Li, and A.-C. Shi. Soft confinement-induced morphologies of diblock copolymers. *Langmuir*, 27(18):11683–11689, 2011.

[58] A. Ciach, J. S. Høye, and G. Stell. Microscopic model for microemulsions. *J Phys A*, 21:L777, 1988.

[59] M. Tasinkevych and A. Ciach. Swollen lamellar phases confined in capillary-like pores. *Phys. Rev. E*, 72:061704, 2005.

[60] B. Yu, P. Sun, T. Chen, Q. Jin, D. Ding, B. Li, and A.-C. Shi. Confinement-induced novel morphologies of block copolymers. *Phys. Rev. Lett*, 96(13):138306, 2006.

[61] I. Carmesin and K. Kremer. The bond fluctuation method: a new effective algorithm for the dynamics of polymers in all spatial dimensions. *Macromolecules*, 21(9):2819–2823, 1988.

[62] R.G. Larson. Self-assembly of surfactant liquid crystalline phases by Monte Carlo simulation. *J. Chem. Phys.*, 91(4):2479–2488, 1989.

[63] B. Yu, P. Sun, T. Chen, Q. Jin, D. Ding, B. Li, and A.-C. Shi. Self-assembled morphologies of diblock copolymers confined in nanochannels: Effects of confinement geometry. *J. Chem. Phys.*, 126(20):204903, 2007.

[64] B. Yu, Q. Jin, D. Ding, B. Li, and A.-C. Shi. Confinement-induced morphologies of cylinder-forming asymmetric diblock copolymers. *Macromolecules*, 41(11):4042–4054, 2008.

[65] J. Pękalski. *Lattice model with interactions attractive on short and repulsive on long distances*. *University of Warsaw*, 2012. Master thesis.

[66] A. Shukla, E. Mylonas, E. Di Cola, S. Finet, P. Timmins, T. Narayanan, and D. I. Svergun. Absence of equilibrium cluster phase in concentrated lysozyme solutions. *Proc. Nat. Acad. Sci. USA*, 105:5075, 2008.

[67] A. Ciach, J. S. Høye, and G. Stell. Microscopic model for microemulsions. I. Ground state properties. *J. Chem. Phys.*, 90:1214, 1989.

[68] A. Ciach. Simple lattice models of complex systems. *J. Mol. Liquids*, 164:74, 2011.

[69] A. Ciach, W. T. Góźdź, and R.Evans. Effect of a nearby charge-ordered phase on correlation functions in ionic systems. *J. Chem. Phys.*, 118:3702, 2003.

[70] M. C. Barbosa. Ising model with isotropic competing interactions in the presence of a field: A tricritical-Lifshitz-point realization. *Phys. Rev. E*, 48:1744, 1993.

[71] P. C. Royall, M. E. Leunissen, A.-P. Hynninen, M. Dijkstra, and A. van Blaaderen. Re-entrant melting and freezing in a model system of charged colloids. *J. Chem. Phys.*, 124:244706, 2006.

[72] D. El Masri, T. Vissers, S. Badaire, J. C. P. Stiefelhagen, H. R. Vutukuri, P. Helfferich, T. H. Zhang, W. K. Kegel, A. Imhof, and A. van Blaaderen. A qualitative confocal microscopy study on a range of colloidal processes by simulating microgravity conditions through slow rotations. *Soft Matter*, 8:2979, 2012.

[73] D. Andelman, F. Brochard, and J.-F. Joanny. Modulated structures and competing interactions in amphiphilic monolayers. *Proc. Nat. Acad. Sci. USA*, 84:4717, 1987.

[74] O. Perron. Zur theorie der matrices. *Math. Ann.*, 64(2):248–263, 1907.

[75] W. Selke. The ANNNI model-theoretical analysis and experimental application. *Phys. Rep.*, 170:213, 1988.

[76] D. Pini, A. Parola, and L. Reatto. Freezing and correlations in fluids with competing interactions. *J. Phys.: Condens. Mat.*, 18:S2305, 2006.

[77] D. Pini, G. Jialin, A. Parola, and L. Reatto. Enhanced density fluctuations in fluid systems with competing interactions. *Chem. Phys. Lett.*, 327:209, 2000.

[78] L. D. Landau and E. M. Lifshitz. *Statistical Physics*. Pergamon Press, 3 edition, 1989.

[79] D. P. Landau and K. Binder. *A Guide to Monte Carlo Simulations in Statistical Physics (2nd edition)*. Cambridge University Press, 2005.

[80] N. G. Almarza, J. A. Capitán, J. A. Cuesta, and E. Lomba. Phase diagram of a two-dimensional lattice gas model of a ramp system. *J. Chem. Phys.*, 131:124506, 2009.

[81] I. Brovchenko and A. Oleinikova. Multiple phases of liquid water. *ChemPhysChem*, 9:2660, 2008.

[82] J. Jirsak and I. Nezbeda. Molecular-based equation of state for tip4p water. *J. Mol. Liq.*, 136:310, 2007.

[83] I. Nezbeda and J. Jirsak. Water and aqueous solutions: simple non-speculative model approach. *Phys. Chem. Chem. Phys.*, 13:19689, 2011.

[84] A. Ciach, W. T. Góźdź, and A. Perera. Simple three-state lattice model for liquid water. *Phys. Rev. E*, 78:021203, 2008.

[85] A. Perera and B. Kezic. Fluctuations and micro-heterogeneity in mixtures of complex liquids. *Faraday Discuss.*, 167:145, 2013.

[86] J. Kolafa and I. Nezbeda. Monte carlo simulations on primitive models of water and methanol. *Mol. Phys.*, 61:161, 1987.

[87] G. H. Wannier. Antiferromagnetism. The Triangular Ising Net. *Phys. Rev.*, 79:357, 1950.

[88] R. M. F. Houtappel. Order-disorder in hexagonal lattices. *Physica*, 16:425, 1950. doi: 10.1016/0031-8914(50)90130-3.

[89] M. Kaburagi and J. Kanamori. Ground state structure of triangular lattice gas model with up to 3rd neighbor interactions. 44:718–727, 1978. doi: 10.1143/JPSJ.44.718.

[90] U. Brandt and J. Stolze. Ground states of the Triangular Ising model with two-and three-spin interactions. *Z. Phys. B Con. Mat.*, 64:481–490, 1986.

[91] Yu. I. Dublenych. Ground states of lattice-gas models on the triangular and honeycomb lattices: Devil's step and quasicrystals. *Phys. Rev. E*, 80:011123, 2009.

[92] Yu. I. Dublenych. Ground states of the lattice-gas model on the triangular lattice with nearest- and next-nearest-neighbor pairwise interactions and with three-particle interaction: Ground states at boundaries of full-dimensional regions. *Phys. Rev. E*, 84:061102, 2011.

[93] Yu. I. Dublenych. Continuum of ground states and aperiodic structures in a

lattice gas on the triangular lattice with finite-range interactions. *Phys. Rev. E,* 86:014201, 2012.

[94] R. Evans. The nature of the liquid-vapour interface and other topics in the statistical mechanics of non-uniform, classical fluids. *Adv. Phys.*, 28:143, 1979.

[95] M. P. Allen and D. J. Tildesley. *Computer Simulation of Liquids*. Oxford University Press, 1987.

[96] D. Frenkel and B. Smit. *Understanding Molecular Simulation. From Algorithms to Applications*. Academic Press, Boston, 1996.

[97] N. Metropolis, A. W. Rosenbluth, M. N. Rosenbluth, A. H. Teller, and E. Teller. Equation of state calculations by fast computing machines. *J. Chem. Phys.*, 21:1087, 1953.

[98] N. G. Almarza, J. M. Tavares, E. G. Noya, and M. M. Telo da Gama. Three-dimensional patchy lattice model for empty fluids. *J. Chem. Phys.*, 137(24):244902, 2012.

[99] R. H. Swendsen and J.-S. Wang. Replica Monte Carlo Simulation of Spin-Glasses. *Phys. Rev. Lett.*, 57:2607–2609, Nov 1986.

[100] D. J. Earl and M. W. Deem. Parallel tempering: Theory, applications, and new perspectives. *Phys. Chem. Chem. Phys.*, 7:3910–3916, 2005.

[101] J. S. Hoye, E. Lomba, and N. G. Almarza. One-and three-dimensional lattice models with two repulsive ranges: simple systems with complex phase behaviour. *Mol. Phys.*, 107:321, 2009.

[102] S. Torquato. *Random Heterogeneous Materials, Microstructures and Macroscopic Properties*. Springer-Verlag, New York, 2002.

[103] K. Nakanishi. Modulated Structure of an Spin System on a Triangular Lattice. II. Complete Devil's Staircase. *J. Phys. Soc. Jpn.*, 52(7):2449–2458, 1983.

[104] M. E Fisher and W. Selke. Infinitely many commensurate phases in a simple Ising model. *Phys. Rev. Lett.*, 44(23):1502, 1980.

[105] W. Selke and M. E. Fisher. Two-dimensional Ising models with competing interaction a Monte Carlo study. *Z. Phys. B*, 40(1):71–77, 1980.

[106] P. Bak. Commensurate phases, incommensurate phases and the devil's staircase. *Rep. Prog. Phys.*, 45:587, 1982.

[107] A. de Candia, E. Del Gado, A. Fierro, N. Sator, M. Tarzia, and A. Coniglio. Columnar and lamellar phases in attractive colloidal systems. *Phys. Rev. E,* 74:010403(R), 2006.

[108] A. Ciach and O. Patsahan. Effect of mesoscopic fluctuations on equation of state in cluster-forming systems. *Condens. Matter Phys.*, 15:23604, 2012.

[109] C. J. Olson Reichhardt, C. Reichhardt, and A. R. Bishop. Structural transitions, melting, and intermediate phases for stripe- and clump-forming systems. *Phys. Rev. E*, 82:041502, 2010.

[110] M. Tasinkevych and A. Ciach. Ternary surfactant mixtures in semi-infinite geometry. *J. Chem. Phys.*, 110:7548, 1999.

[111] A. Ciach and V. Babin. Landau functional for confined amphiphilic systems. *J. Mol. Liq*, 112:37, 2004.

[112] F. Schmid and M. Schick. Phase transitions of a confined complex fluid. *Phys. Rev. E*, 48:1882, 1993.

[113] A. Gonzalez, J. A. White, F. L. Roman, and R. Evans. How the structure of a confined fluid depends on the ensemble: Hard spheres in a spherical cavity. *J. Chem. Phys.*, 109:3637, 1998.

[114] Y. W. Kim, S. C. Kim, and S. H. Suh. Highly charged colloidal suspensions in planar slits. *J. Chem. Phys.*, 110:1230, 1999.

[115] D. G. Barci, A. Mendoza-Coto, and D. A. Stariolo. Nematic phase in stripe-forming systems within the self-consistent screening approximation. *Phys. Rev. E*, 88:062140, 2013.

[116] S. A. Cannas, M. F. Michelon, D. A. Stariolo, and F. A. Tamarit. Ising nematic phase in ultrathin magnetic films: a Monte Carlo study. *Phys. Rev. B*, 73:184425, 2006.

[117] S. A. Cannas, M. Carubelli, O. V. Billoni, and D. A. Stariolo. Inverse transition in a two-dimensional dipolar frustrated ferromagnet. *Phys. Rev. B*, 84:014404, 2011.

[118] D. G. Barci and D. A. Stariolo. Competing interactions, the renormalization group, and the isotropic-nematic phase transition. *Phys. Rev. Lett.*, 98:200604, 2007.

[119] D. G. Barci and D. A. Stariolo. Orientational order in two dimensions from competing interactions at different scales. *Phys. Rev. B*, 79(7):075437, 2009.